Silesian University of Technology

Faculty of Mechanical Engineering

Department of Engineering Materials and Biomaterials

DOCTORAL DISSERTATION

Towards Digital Twins for Quantifying Laser-Microstructure Interface in Multicomponent Alloys Using Thermodynamic Tensor Model

in the form of a collection of thematically related articles published in scientific journals

Upadesh Subedi, M.Sc., Eng.

Scientific discipline: Materials Engineering

Supervisor: **Tomasz Tański, Ph.D., D.Sc., Eng., prof. SUT**

Auxiliary Supervisor: **Anil Kunwar, Ph.D., Eng.**

Silesian University of Technology

Faculty of Mechanical Engineering

Gliwice, 2026

ACKNOWLEDGEMENTS

I would like to express my sincere gratitude to my supervisor, Professor Tomasz Tański, for his guidance, support, and trust throughout my doctoral studies. His supervision helped shape the direction of this dissertation and provided the academic foundation needed to complete this work.

I am deeply grateful to my co-supervisor, Anil Kunwar, Ph.D., for his continuous scientific guidance, technical support, and encouragement during the development of this research. His insight and involvement were central to the progress of my doctoral work.

I would also like to sincerely thank Professor Nele Moelans at KU Leuven for her valuable guidance, scientific discussions, and support. I am especially grateful for the opportunity to work as a visiting scholar in her research group, and for providing access to the Vlaams Supercomputer Centrum, which significantly supported the computational part of this research.

I gratefully acknowledge the Doctoral School of Silesian University of Technology for the scholarship and continuous support provided during my Ph.D. studies. I also acknowledge the financial support received through two National Science Centre, Poland-funded projects during my doctoral work: UMO-2021/42/E/ST5/00339 and UMO-2023/51/I/ST11/02716. These institutional and project-based supports provided an important scientific and research environment for carrying out this dissertation.

I would like to thank all my co-authors in the research papers published during my Ph.D. Their collaboration, discussions, and contributions helped strengthen the scientific quality of the work included in this dissertation.

My deepest gratitude goes to my parents, Professor Nutan Subedee, and Saraswoti Sharma, and to my sister, Aastha Subedi, for their unconditional love, patience, and support. Their belief in me has been a constant source of strength throughout this journey.

Finally, I am grateful for the resilience, perseverance, and persistence that this Ph.D. journey taught me. The path demanded discipline, sacrifice, and endurance, and I am thankful for having found the strength to continue and bring this work to completion.

ABSTRACT

Laser processing and microstructural evolution in alloy systems involve coupled heat transfer, phase transformation, diffusion, interfacial reactions, and meltpool dynamics. In this dissertation, the laser-microstructure ($\mathscr{L}$-$\mathscr{M}$) interface is treated as a dynamic region where thermal history, composition, free-energy landscape, and morphology evolve together. The main objective is to represent, quantify, compress, reconstruct, and predict this interface using thermodynamically informed computational and data-driven models.

The dissertation develops a computational framework based on phase-field modeling, thermodynamic tensor representation, and physics-informed machine learning. Across the studied alloy systems, microstructural evolution is analyzed through phase-field simulations and represented using physically meaningful descriptors. Building on these simulations, this evolution is further encoded as high-dimensional tensor data, enabling tensor sparsification, decomposition, and reconstruction while preserving essential morphological and interfacial information. This establishes the **Thermodynamic Tensor Representation** as a compact and physically meaningful form for storing and reconstructing simulation-based microstructure data.

The second part extends the framework toward **laser-processed alloy systems**. In the multicomponent Cu_x*(Ti-6Al-4V)*$_y$ system, finite-element heat-transfer simulations and phase-field modeling are used to describe laser-induced Ti_2Cu intermetallic growth in the matrix. In the *Ti-Au* system, a non-isothermal multiphase-field model is developed to resolve meltpool formation, Ti_3Au intermetallic evolution, interdiffusion, and the interaction between thermal and chemical fronts. The model includes temperature- and composition-dependent free-energy functions, KKS-type phase-equilibrium constraints, and coupled heat-transfer and fluid-flow effects. In the unary Au system, different laser beam profiles and free-energy descriptions are compared to study their influence on meltpool morphology, phase evolution, and Marangoni-driven flow.

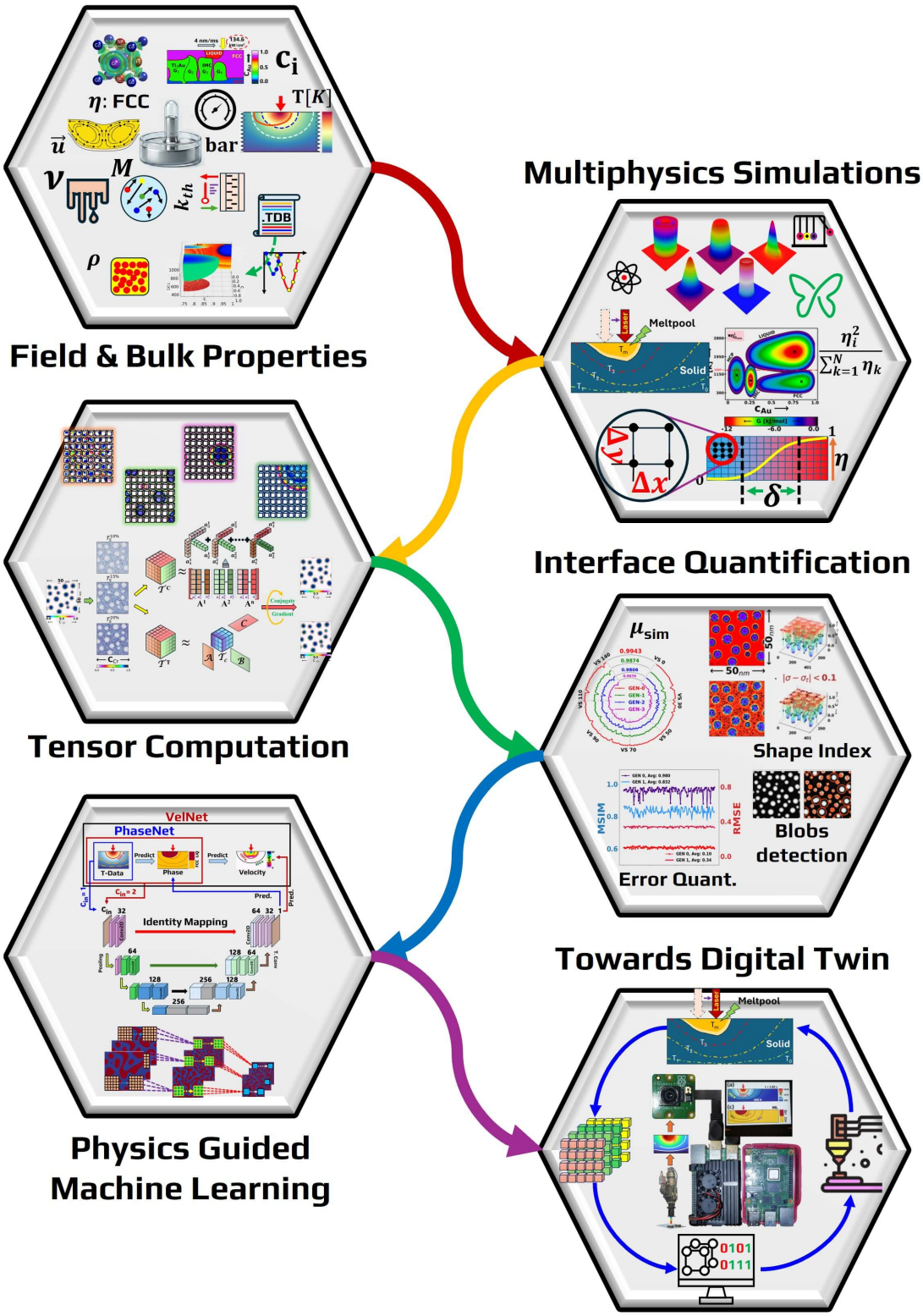
The final part develops **machine learning models for computational acceleration**. Conv-LSTM models predict multi-generational microstructural evolution in binary alloy systems, including Pd-Rh and Cu-Mn examples, while U-Net-based MicroTwin and FlowTwin models predict phase and velocity fields from temperature data in laser-processed Au. The predictions are evaluated using interface-sensitive descriptors such as microstructural similarity, shape index, blob detection, meltpool geometry, and velocity fields.

Overall, the dissertation shows that the $\mathscr{L}$-$\mathscr{M}$ interface can be described through a thermodynamically grounded tensor framework supported by multiphysics simulations and physics-informed learning models. The developed methodology provides a route **Toward Digital Twin** construction for laser-processed multicomponent alloys.

STRESZCZENIE

Procesy laserowego obróbki materiałów prowadzą do złożonych zmian mikrostrukturalnych wynikających ze współoddziaływania transportu ciepła, przemian fazowych, dyfuzji składników stopowych, reakcji międzyfazowych oraz zjawisk zachodzących w jeziorku ciekłego metalu. Zrozumienie mechanizmów odpowiedzialnych za przebieg tych procesów oraz ich ilościowy opis mają kluczowe znaczenie dla projektowania nowoczesnych materiałów i technologii wytwarzania. Głównym celem rozprawy było opracowanie metod opisu, analizy i prognozowania ewolucji mikrostruktury podczas laserowej obróbki stopów metali z wykorzystaniem modeli obliczeniowych, obliczeń termodynamicznych oraz metod uczenia maszynowego. Szczególną uwagę poświęcono opracowaniu termodynamicznego modelu tensorowego umożliwiającego efektywne odwzorowanie, przechowywanie oraz odtwarzanie informacji o ewolucji mikrostruktury i jej wykorzystanie w modelach predykcyjnych. W pierwszej części pracy rozwinięto metodykę opartą na modelowaniu pola fazowego oraz termodynamicznym modelu tensorowym. Wyniki symulacji mikrostruktury zapisano w postaci wielowymiarowych struktur danych, które poddano procesom redukcji, dekompozycji i rekonstrukcji przy zachowaniu najważniejszych cech morfologicznych oraz informacji o granicach międzyfazowych. Pozwoliło to na opracowanie zwartego i fizycznie uzasadnionego sposobu reprezentacji danych generowanych w obliczeniach wielkoskalowych. W dalszej części rozprawy opracowaną metodykę zastosowano do analizy stopów poddawanych obróbce laserowej. Dla układu $Cu_x(Ti\text{-}6Al\text{-}4V)_y$, przeprowadzono modelowanie wymiany ciepła oraz wzrostu faz międzymetalicznych indukowanych oddziaływaniem wiązki laserowej. Dla układu *Ti-Au* opracowano nieizotermiczny wielofazowy model umożliwiający opis tworzenia jeziorka ciekłego metalu, wzrostu fazy Ti_3Au, procesów dyfuzji oraz wzajemnego oddziaływania pól cieplnych i obszarów chemicznych. W układzie Au przeanalizowano wpływ parametrów wiązki laserowej oraz opisu termodynamicznego materiału na geometrię jeziorka, przebieg przemian fazowych i przepływy wywołane efektem Marangoniego. Ostatnią część pracy poświęcono wykorzystaniu metod uczenia maszynowego do przyspieszenia obliczeń. Opracowane modele Conv-LSTM umożliwiły prognozowanie ewolucji mikrostruktury w wybranych układach stopowych, natomiast modele MicroTwin i FlowTwin bazujące na architekturze U-Net pozwoliły na przewidywanie rozkładów faz oraz pól prędkości na podstawie danych temperaturowych. Trafność prognoz oceniano z wykorzystaniem parametrów opisujących podobieństwo mikrostruktur, geometrię jeziorka ciekłego metalu oraz charakterystykę pól przepływu. Uzyskane wyniki potwierdzają możliwość integracji modeli wielofizycznych, obliczeń termodynamicznych oraz algorytmów uczenia maszynowego w ramach jednolitego środowiska obliczeniowego. Opracowana metodyka stanowi podstawę do budowy cyfrowych bliźniaków procesów laserowego przetwarzania wieloskładnikowych stopów metali.

GRAPHICAL ABSTRACT



LIST OF PUBLICATIONS

This Ph.D. thesis is presented as a collection of thematically related research articles published during the course of the doctoral studies. The full texts of these papers are included in **Appendix A**, on pages **54** – **140**. The publications forming the basis of this thesis are listed below:

I. **U. Subedi***, N. Moelans, T. Tański and A. Kunwar, "Rapid portabilization of elasto-chemical evolution data for dental Ti-Cr alloy microstructure through sparsification and tensor computation." *Scripta Materialia*, 2024, [1]

DOI: https://doi.org/10.1016/j.scriptamat.2024.116027.

Author's contribution – 71%

CRediT: Conceptualization, Data curation, Formal analysis, Investigation, Methodology, Software, Validation, Visualization, Writing – original draft.

II. H.B. Mamo, **U. Subedi**, T. Poloczek, M. Adamiak, A.N.S. Appiah, M. Skonieczna, P.M. Nuckowski, Y. Geng, B. Haldar, and A. Kunwar "Prototyping Ti2Cu intermetallic grain growth heterogeneously in Ti6Al4V matrix through laser additive manufacturing" *Materials & Design* , 2024, [2]

DOI: https://doi.org/10.1016/j.matdes.2024.113312.

Author's contribution – 16%

CRediT: Writing – review & editing, Visualization, Validation, Software, Methodology, Investigation.

III. **U. Subedi***, N. Moelans, T. Tański and A. Kunwar, "Foretelling microstructural interface with multi-generational convolutional-LSTM framework." *Engineering with Computers*, 2025, [3]

DOI: https://doi.org/10.1007/s00366-025-02117-z.

Author's contribution – 72%

CRediT: Conceptualization, Data curation, Formal analysis, Investigation, Methodology, Software, Validation, Visualization, Writing – original draft.

IV. **U. Subedi***, N. Moelans, T. Tański and A. Kunwar, "A non-isothermal multi-phase field approach to model the meltpool and IMC grains interaction in Ti-Au material" *Computational Materials Science*, 2025, [4]

DOI: https://doi.org/10.1016/j.commatsci.2025.113875.

Author's contribution – 70%

CRediT: Conceptualization, Data curation, Formal analysis, Investigation, Methodology, Software, Validation, Visualization, Writing – original draft.

V. **U. Subedi**[*], A. Bhattarai, N. Moelans, T. Tański and A. Kunwar, "Spatiotemporally learning the morphological and dynamic features of Au meltpool under different heat source types with phase-field informed U-Net framework" *Computational Materials Science*, 2025, [5]
DOI: https://doi.org/10.1016/j.commatsci.2025.114456.
Author's contribution – 60%
CRediT: Conceptualization, Data curation, Formal analysis, Investigation, Methodology, Software, Validation, Visualization, Writing – original draft.

[*] Corresponding Author

SUPPLEMENTARY PUBLICATIONS NOT INCLUDED IN THE DISSERTATION

The following publications are related to the broader scientific and methodological scope of the doctoral work. They demonstrate additional research experience and technical competence in phase-field modeling, microstructural informatics, data-driven materials design, and additive manufacturing. These works provided supplementary knowledge and methodological understanding relevant to the development of the dissertation; however, **they are not included among the selected publications forming the main basis of this dissertation.**

I. S. Poudel, **U. Subedi**, M.O. Hamid, K. Gyanwali, N. Moelans, A. Timofiejczuk and A. Kunwar, "AlloyManufacturingNet for discovery and design of hardness-elongation synergy in multi-principal element alloys" *Engineering Applications of Artificial Intelligence*, 2024
DOI: https://doi.org/10.1016/j.engappai.2024.107902.

II. S. Liang, C. Wei, A. Kunwar, **U. Subedi**, H. Jiang, H. Ma and C. Ke, "Phase field modelling combined with data-driven approach to unravel the orientation influenced growth of interfacial Cu6Sn5 intermetallics under electric current stressing" *Surfaces and Interfaces*, 2023
DOI: https://doi.org/10.1016/j.surfin.2023.102728.

III. M. Dagnaw, S. Poudel, **U. Subedi**, R. Thapa, Ł. Reimann, A.N.S. Appiah, P.M. Nuckowski, M. Król, Z. Brytan, N. Moelans, and A. Kunwar, "Integrating experiments and phase field method through informatics for tailored corrosion performance of additively manufactured steel microstructures" *ChemRxiv*, 2026
DOI: https://doi.org/10.26434/chemrxiv-2025-sk6h5.

TABLE OF CONTENTS

Acknowledgements i

Abstract (Streszczenie) ii

Graphical abstract iv

List of publications v

Supplementary publications not included in the dissertation vii

Table of contents viii

List of tables x

List of figures xi

List of acronyms and abbreviations xii

1. Introduction 1

1.1 Lasers in additive manufacturing 1

1.2 Multicomponent alloys, microstructure, and interface 2

1.3 Challenges in quantification of interface evolution 3

1.4 Digital Twins in materials manufacturing 4

1.5 Computational models 5

1.6 Complexity of high dimensional data 5

1.7 Problem statement 6

2. Objectives 8

2.1 Main objective 8

2.2 Specific objectives 8

3. Scientific problem statement 10

3.1 State of the art 10

3.2 Title definition 11

3.3 Main hypothesis 11

3.4 Specific hypothesis 11

4. Laser-Microstructure interface and interaction 13

4.1 Laser ($\mathscr{L}$) 13

4.1.1 Thermal history and meltpool formation 14

4.1.2 Process parameters 16

4.1.3 Meltpool's kinematic lag 19

4.2 Microstructure ($\mathscr{M}$) 21

4.2.1 Spatio-temporal field variables 21

4.2.2 Free-energy landscapes . . . 23
4.2.3 Interfacial reaction, and intermetallic growth . . . 25
4.2.4 Morphological and interface-sensitive data . . . 27
4.3 Methodology . . . 29
4.3.1 Multiphysics modeling . . . 30
4.3.2 Tensor Model . . . 31
4.3.3 Physics-informed Conv-LSTM and U-Net frameworks . . . 32
4.3.4 Towards Digital Twins of materials models . . . 35
4.4 Hierarchical determinants of $\mathscr{L}$-$\mathscr{M}$ Interaction . . . 37
4.4.1 Laser-side control variables . . . 37
4.4.2 Microstructure response variables . . . 38
4.4.3 Numerically fingerprinting the interfacial dynamics . . . 38
4.5 Multi-level quantification of $\mathscr{L}$-$\mathscr{M}$ Interface . . . 38
4.5.1 Thermodynamic representation of the interface . . . 39
4.5.2 Tensor-based quantification and ML approaches . . . 39
4.6 Major Findings . . . 40
4.6.1 Kinematics of interface attributes . . . 40
4.6.2 Compact representation of $\mathscr{M}_{Global}$ and $\mathscr{M}_{Local}$ . . . 41
4.6.3 Portable information at manifest space . . . 41
4.6.4 $\mathscr{L}$-$\mathscr{M}$ information retention . . . 41
4.7 Integrated outcomes . . . 42
5. Conclusions and future outlooks . . . 43
5.1 Conclusion . . . 43
5.2 Future outlook . . . 44
References . . . 47
Appendix A: Publications . . . 54
Article I . . . 54
Article II . . . 61
Article III . . . 75
Article IV . . . 101
Article V . . . 120
Appendix B: Declaration of Co-Authors . . . 141

LIST OF TABLES

Table 4.1 Temperature response across beam types and free-energy formulations 18
Table 4.2 Microstructural similarity index (μ_{SIM}) across generations 33
Table 4.3 Inference time across platforms 36
Table 4.4 Laser parameter space 37

LIST OF FIGURES

Figure 1.1 Effect of laser parameters on meltpool and IMC evolution 2
Figure 1.2 Intermetallic grain evolution under laser surface alloying 4
Figure 1.3 Conceptual Digital Twin framework for laser processing 5
Figure 4.1 Schematics of laser processing setup and different beam profiles. 15
Figure 4.2 Illustration of laser surface alloying in Cu_x(Ti-6Al-4V)$_y$ 15
Figure 4.3 Thermal history and meltpool velocity profile 16
Figure 4.4 Irradiance dictating IMC thickness and meltpool shape 17
Figure 4.5 Lead-lag dynamics between thermal and phase fronts 19
Figure 4.6 Illustration of τ-$\mathscr{D}$ dynamics and δt_{pos} 20
Figure 4.7 Phase field variables in simulation results 22
Figure 4.8 Free energy landscapes 24
Figure 4.9 Ti_3Au IMC grain morphology comparison 26
Figure 4.10 Geometric quantification tools 27
Figure 4.11 Tensor reconstruction accuracies 28
Figure 4.12 Methodological framework for laser-induced microstructure evolution 30
Figure 4.13 Tensor sparsification, decomposition and reconstruction 32
Figure 4.14 Convolutional-LSTM model architecture 32
Figure 4.15 Multi-generational microstructure prediction 33
Figure 4.16 U-Net machine learning model framework 34
Figure 4.17 Perspective attention-based prediction workflow 35
Figure 4.18 Flow-diagram of conceptualized Digital-Twin Framework 36
Figure 5.1 Future outlook on composition-aware thermo-morphological prediction 45

LIST OF ACRONYMS AND ABBREVIATIONS

AM	:	Additive Manufacturing
CNN	:	Convolutional Neural Network
CCAs	:	Compositionally Complex Alloys
CPD	:	Canonical Polyadic Decomposition
FCC	:	Face-Centered Cubic
FEM	:	Finite Element Method
GRU	:	Gated Recurrent Unit
HEAs	:	High Entropy Alloys
HCP	:	Hexagonal Closed-Packed
IMC	:	Intermetallic Compounds
LPBF	:	Laser Powder Bed Fusion
LSTM	:	Long Short-Term Memory
MOOSE	:	Multiphysics Object Oriented Simulation Environment
MPEAs	:	Multi-Principal Element Alloys
PFM	:	Phase Field Method
RNN	:	Recurrent Neural Network
SLM	:	Selective Laser Melting
TDB	:	Thermodynamic Data-Base
TRL	:	Technology Readiness Level
VED	:	Volumetric Energy Density

CHAPTER I

INTRODUCTION

This chapter introduces the fundamentals of laser-microstructure ($\mathscr{L}$-$\mathscr{M}$) interaction in multicomponent alloys and establishes the context of this work. It outlines how laser processing influences microstructural evolution, why interface behavior governs material properties, and why its quantification remains challenging under coupled thermal and chemical conditions.

To address these challenges, the need for computational frameworks that connect high-fidelity multiphysics modeling with scalable predictive approaches is highlighted. The concept of a Digital Twin is introduced as a pathway for near real-time prediction of microstructure evolution. Multiphysics phase-field modeling is presented as a physically consistent approach, along with its computational limitations. A thermodynamically consistent tensor-based representation is then introduced to enable structured handling of microstructural data and its integration with machine learning. The chapter concludes with the formulation of the problem addressed in this dissertation.

In this dissertation, the term $\mathscr{L}$-$\mathscr{M}$ interface is used as the central connecting concept across all included articles. It refers not only to a geometrical phase boundary, but to the coupled zone where laser-induced thermal history is converted into microstructural change through composition-dependent thermodynamics, diffusion, phase transformation, interfacial motion, and meltpool flow. The Thermodynamic Tensor Model provides the structured representation of this evolving information, while machine learning provides the predictive route required for Digital Twin development. Therefore, the dissertation links the five published articles through a single guiding question of how laser-induced microstructural interface evolution can be represented, quantified, compressed, and predicted in a physically meaningful form.

1.1 Lasers in additive manufacturing

Laser-based additive manufacturing relies on localized thermal energy to induce melting and solidification [4–9]. The interaction between a moving laser heat source and the material generates a transient meltpool, whose geometry and evolution depend on processing parameters such as laser power, scan speed, beam profile, and composition of the alloy [5, 10, 11].

As illustrated in Figure 1.1 (**Article IV**), variations in scan speed and irradiance alter both meltpool shape and intermetallic growth. Figures 1.1 **(a-b)** show differences in IMC morphology with scan speed, while Figure 1.1 **(c-d)** quantify intermetallic compounds' (IMC) thickness, meltpool depth, and surface width under varying irradiance. These variations directly influence thermal gradients, which govern phase transformation and interfacial evolution. Even small changes in processing

conditions lead to significant differences in meltpool geometry and microstructure, highlighting the strong coupling between laser parameters and material response [4, 5].

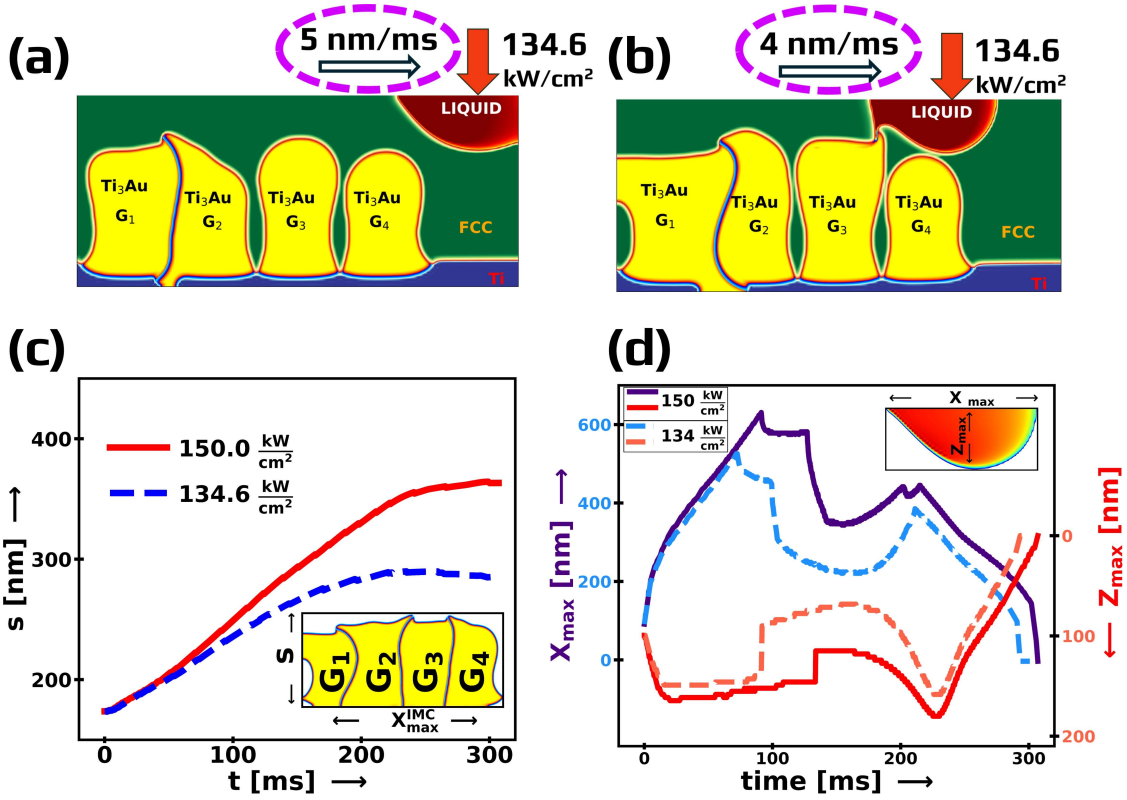


Figure 1.1 Multiphysics phase-field simulation of laser processing in a *Ti-Au* system. **(a-b)** Phase evolution showing intermetallic (IMC) growth under different scan speeds (5 nm/ms and 4 nm/ms). **(c)** Time evolution of average IMC thickness for two irradiance levels (150 and 134.6 kW/cm^2). **(d)** Meltpool depth and surface width as functions of time under the same irradiance conditions **[4]**.

1.2 Multicomponent alloys, microstructure, and interface

Multicomponent alloys, as considered in this work, consist of two or more interacting chemical species whose spatial redistribution under thermal processing governs phase evolution and interfacial reactions. In systems such as *Ti-Cr*, *Ti-Au*, and $Cu_x(Ti\text{-}6Al\text{-}4V)_y$, the presence of multiple elements enables the formation of intermetallic compounds, and phase transformations during laser processing, making the microstructural response inherently composition dependent [2, 4].

A microstructure is not a static arrangement of phases, but a thermodynamically unstable configuration that evolves in time toward equilibrium [12]. Within the diffuse-interface framework, it is represented using phase-field variables that vary continuously in space and time, capturing the evolution of composition, phase distribution, and morphology under coupled thermal and chemical driving forces [13–18]. In the multicomponent systems considered in this work, this evolving microstructure manifests through the formation and interaction of distinct phases such as LIQUID, Face-Centered Cubic (FCC), Hexagonal Closed-Packed (HCP), and IMCs. These IMCs include phases such as Ti_2Cu and Ti_3Au, which nucleate and grow at interfaces under non-isothermal con-

ditions [2, 4]. The spatial distribution, morphology, and connectivity of these phases define the microstructure and its evolution during laser processing.

The interface is the region separating distinct phases, characterized by a finite thickness in diffuse-interface descriptions. In the phase-field framework, it is defined as a narrow region where the phase-field variables vary continuously between their equilibrium values in neighboring phases, rather than forming a sharp boundary [12]. The evolution of the interface is therefore not tracked explicitly but is implicitly determined by the temporal evolution of these phase-field variables, which govern the shape, position, and motion of the interface over time. Physically, this region is where interdiffusion, phase transformation, and interfacial energy effects occur simultaneously [4, 19–22]. Under laser processing, strong thermal gradients and non-equilibrium conditions drive rapid interface migration, controlling the formation and growth of intermetallic phases and the resulting microstructural morphology.

As shown in Figure 1.2 (**Article II**), intermetallic grains grow under laser surface alloying. Figure **(a)** shows uniform growth from homogeneous initial morphology, while **(b)** shows heterogeneous growth where larger grains grow faster due to differences in initial morphology. The spatio-temporal evolution of such grains, heterogeneous growth, and shrinkage, has been extensively studied using phase-field modeling approaches [4]. Experimental investigations further confirm the formation and growth of intermetallic phases such as Ti_2Cu during laser processing [2]. Similarly, Ti_3Au formation in *Ti-Au* systems exhibit significantly increased hardness compared to pure Ti and steel alloys [23, 24].

These observations show that microstructure and interface evolution directly govern material properties. Interfaces act as active regions where diffusion and phase transformation occur simultaneously, and their morphology, thickness, and dynamics determine the resulting mechanical behavior of the material. Therefore, understanding and quantifying the evolution of interfaces in multicomponent systems is essential for controlling properties in laser-based manufacturing.

1.3 Challenges in quantification of interface evolution

Despite its importance, quantifying interface evolution remains challenging due to the coupled and nonlinear nature of heat transfer, diffusion, phase transformation, and morphology [25–27]. Phase-field modeling provides a thermodynamically consistent framework for simulating these processes [4, 19], capturing microstructural evolution with high spatial and temporal resolution. However, its computational cost limits its application to large-scale and real-time scenarios [28, 29].

Data-driven approaches offer computational efficiency and rapid prediction capabilities. For example, RNN-, GRU-, and LSTM-based models have been used to predict microstructural evolution

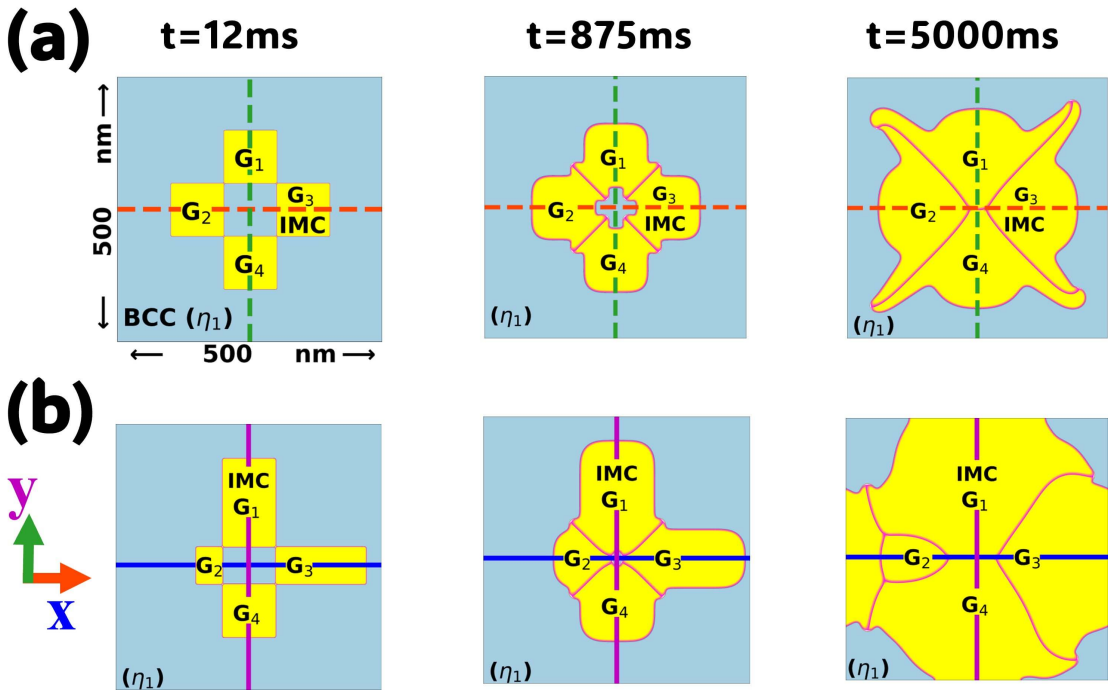


Figure 1.2 Time-resolved evolution of intermetallic grains under laser surface alloying. **(a)** Uniform growth from homogeneous initial morphology. **(b)** Heterogeneous growth showing non-linear grain evolution influenced by initial morphology, highlighting interface-driven microstructural dynamics **[2]**.

[30], and PredRNN has been applied to *FeCrCo* systems [31]. Despite these advances, such approaches operate in reduced representations, leading to loss of spatial and interfacial information [3]. This creates a gap between high-fidelity simulations and scalable predictive models.

1.4 Digital Twins in materials manufacturing

The concept of a Digital Twin provides a pathway to bridge detailed physical modeling with predictive capability. In materials manufacturing, a Digital Twin represents a computational system capable of predicting microstructural evolution under varying processing conditions. As shown in Figure 1.3, the framework developed in this work integrates multiphysics simulations, tensor-based representation, and machine learning models [5]. Phase-field simulations generate thermodynamically consistent datasets, which are encoded into tensor form and used to train predictive models capable of estimating meltpool geometry, phase distribution, and velocity fields [5].

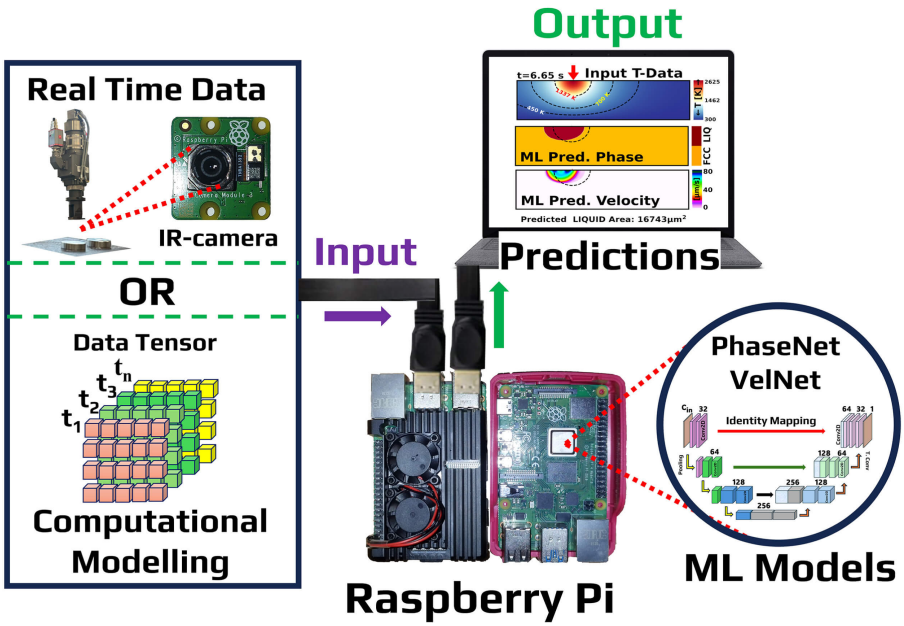


Figure 1.3 Conceptual Digital Twin framework integrating multiphysics simulations, tensor-based data representation, and machine learning models for prediction and feedback control of microstructure evolution. Phase-field data are used to train predictive models, which operate on simulation or real-time inputs to estimate meltpool behavior and enable adaptive process control **[5]**.

This integration enables rapid prediction while maintaining physical consistency. The inclusion of feedback mechanisms further allows adaptive control of process parameters such as laser power, scan speed, and beam characteristics, forming the basis of a scalable Digital Twin framework [5].

1.5 Computational models

Accurate modeling of $\mathscr{L}$-$\mathscr{M}$ interaction requires a multiphysics framework that integrates heat transfer, diffusion, meltpool flow, and phase transformation. Phase-field modeling provides a thermodynamically consistent approach based on free-energy formulations [32–34]. In non-isothermal systems, temperature- and composition-dependent free-energy functionals govern phase stability and transformation kinetics [4, 35, 36]. The evolution of conserved and non-conserved variables is described through convection-diffusion and Allen-Cahn type equations [33, 37]. These models have been successfully applied to simulate meltpool dynamics, interdiffusion, and intermetallic growth [2, 4]. However, their computational cost remains a major limitation for large-scale and real-time applications.

1.6 Complexity of high dimensional data

To bridge the gap between high-fidelity simulations and scalable predictive models, a structured representation of microstructural evolution is required [28]. In this work, a thermodynamically consistent tensor-based representation, referred to as the "*Thermodynamic Tensor Model*", is introduced. Microstructural evolution is governed by coupled spatio-temporal fields such as compo-

sition distribution, temperature, phase-fraction, and thermodynamic potentials derived from Gibbs free energy formulations [4, 5]. These fields evolve continuously and are strongly interdependent. The tensor framework encodes these fields into a multi-dimensional structure, preserving spatial and temporal correlations. Tensor decomposition and reconstruction enable efficient handling of large datasets while retaining essential interface features [1]. This provides a structured representation suitable for predictive modeling.

1.7 Problem statement

The preceding sections show that the central difficulty in laser processing of compositionally complex alloys (CCAs) is not only the simulation of temperature or phase evolution, but the consistent quantification of the $\mathscr{L}$-$\mathscr{M}$ interface where thermal input, chemical redistribution, and phase transformation meet. Phase-field models can resolve this physics with high fidelity, but their computational cost makes repeated exploration of processing and composition space impractical. At the same time, data-driven models can accelerate prediction, but they often lose the thermodynamic and interfacial meaning required for reliable interpretation.

Therefore, the scientific problem addressed in this dissertation is the absence of a unified framework that can preserve the physical content of multiphysics simulations, transform high-dimensional microstructural fields into compact tensor representations, and use this information for scalable prediction of interface evolution. This problem is especially important for multi-principal element alloys (MPEAs), where the same laser condition may produce different microstructural responses because composition modifies the free-energy landscape, diffusion kinetics, interfacial energy, and meltpool morphology.

This gap arises from several specific limitations in current computational and data-driven approaches, outlined below.

(i) **Interface evolution is difficult to quantify under coupled laser conditions**

The $\mathscr{L}$-$\mathscr{M}$ interface evolves through the simultaneous action of heat transfer, chemical diffusion, phase transformation, and meltpool flow. Existing approaches often describe these phenomena separately, which makes it difficult to quantify how thermal history, phase-front motion, and compositional redistribution jointly control interface evolution.

(ii) **High-fidelity phase-field simulations are computationally expensive**

Multiphysics phase-field models can capture laser-induced melting, solidification, interdiffusion, and intermetallic growth, but their repeated use over different laser parameters, compositions, and thermodynamic conditions is computationally demanding. This limits their direct use for rapid process exploration and Digital Twin oriented prediction.

(iii) **High-dimensional microstructural data lack compact physical representation**

Phase-field simulations generate large spatio-temporal datasets containing temperature, phase, composition, velocity, and interface information. Without a compact tensor-based representation, these datasets remain difficult to store, transfer, reconstruct, compare, and use as structured inputs for predictive modeling.

(iv) **Thermodynamic consistency is weakly connected to machine learning prediction**

Data-driven models can predict microstructural fields rapidly, but many reduced-order or image-based approaches do not explicitly preserve the thermodynamic meaning of phase stability, free-energy differences, interface motion, and composition-dependent driving forces. This weakens their reliability when applied beyond a narrow training condition.

(v) **Digital Twin frameworks require a stronger bridge between physics and prediction**

A practical Digital Twin for laser-processed multicomponent alloys requires more than fast prediction. It must connect laser parameters, thermodynamic tensors, multiphysics phase-field outputs, interface descriptors, and surrogate models within a single interpretable workflow. Such a bridge is still missing for composition-sensitive laser-microstructure interaction.

CHAPTER II

OBJECTIVES

The limitations discussed in Chapter I show that accurate quantification of $\mathscr{L}$-$\mathscr{M}$ interaction requires the integration of multiple approaches. Multiphysics phase-field simulations provide physically consistent descriptions of meltpool evolution, interdiffusion, and interfacial phase growth [4, 5], but their computational cost limits scalability. Experimental studies confirm the occurrence of complex interfacial reactions and microstructural transformations, yet they do not provide complete spatio-temporal descriptions of the underlying mechanisms [2]. Machine learning models enable rapid prediction, but their reliability depends on physically meaningful and thermodynamically consistent data representations [1, 3, 5]. Therefore, the objectives of this dissertation are defined to connect physics-based modeling, tensor-based representation, and machine learning into a unified framework that enables scalable prediction and supports the development of Digital Twin methodologies for multicomponent alloy systems.

2.1 Main objective

The main objective of this dissertation is **to develop a unified, thermodynamically consistent framework for quantifying and predicting laser-microstructure interface evolution in multicomponent alloys** by integrating multiphysics phase-field modeling, tensor-based data representation, and machine learning, enabling scalable Digital Twin systems.

2.2 Specific objectives

(i) **Development of thermodynamic tensor representation for microstructural evolution**
To construct a structured tensor representation of spatio-temporal microstructural fields, including phase distribution, temperature, and composition, enabling efficient storage, reconstruction, and integration with data-driven models.

(ii) **Formulation of multiphysics non-isothermal phase-field models**
To develop thermodynamically consistent phase-field models for simulating meltpool evolution, interdiffusion, and phase transformation under non-isothermal conditions.

(iii) **Quantitative characterization of interface evolution**
To establish methods for quantifying microstructural interfaces through measurable descriptors such as meltpool depth and width, intermetallic layer thickness, phase fraction, and interface-sensitive metrics including shape, and similarity index, using spatio-temporal simulation data and experimental validation.

(iv) **Development of physics-informed machine learning models**

To design and implement machine learning architectures, including Conv-LSTM and U-Net, for predicting microstructural evolution and meltpool behavior while preserving spatial and interfacial features.

(v) **Integration toward a Digital Twin framework**

To combine multiphysics simulations, tensor representations, and machine learning models into a scalable framework for rapid prediction of $\mathscr{L}$-$\mathscr{M}$ interaction, forming the basis of a computational Digital Twin system.

(vi) **Extension to materials informatics and property prediction**

To apply the developed framework to structure-property prediction and data-driven materials design in multicomponent alloy systems.

CHAPTER III

SCIENTIFIC PROBLEM STATEMENT

3.1 State of the art

Laser-based additive manufacturing of multicomponent alloys involves coupled interactions between thermal fields, chemical diffusion, and phase transformations, which govern meltpool dynamics, interdiffusion, and intermetallic formation at microstructural interfaces [38–40]. Multiphysics phase-field modeling provides a thermodynamically consistent framework to resolve these processes, enabling spatio-temporal prediction of phase evolution [41]. Recent non-isothermal multiphase-field models capture meltpool-intermetallic interactions, temperature-dependent phase stability, and interfacial growth kinetics [29]. For example, **Article IV** shows that variations in laser irradiance and scan speed significantly affect meltpool geometry and intermetallic grain thickness, while **Article V** demonstrates that different beam profiles, even under identical laser power and radius, lead to distinct heat distributions and microstructural pathways. These results align with experimental observations of intermetallic formation, such as Ti_2Cu and Ti_3Au, driven by thermodynamic forces [2, 38].

Together, these studies show that laser-induced microstructural evolution can be described through coupled fields rather than through isolated process parameters. In **Article IV**, the non-isothermal multiphase-field formulation resolves the spatio-temporal evolution of temperature, phase state, composition, meltpool geometry, and interfacial growth under a defined laser-processing window. In **Article V**, the physics-informed learning framework further predicts phase and velocity fields from temperature data, while retaining the influence of thermodynamic driving force, heat-source type, and meltpool-flow response.

Despite their accuracy, phase-field models remain computationally expensive, limiting large-scale and real-time applications [42, 43]. Machine learning approaches, including RNN, GRU, and LSTM models, have been introduced to accelerate prediction [30, 31]. However, these methods typically rely on reduced or latent representations, which do not preserve interface-level information and lack thermodynamic consistency, limiting generalization across systems [3]. To address this, manifest-space prediction has been proposed, where microstructure evolution is learned directly in the spatio-temporal domain. **Article III** and **Article V** demonstrate this using Conv-LSTM and U-Net architectures, enabling multi-generational prediction of microstructure and meltpool behavior while preserving spatial fidelity.

In parallel, tensor-based representations have been explored for handling high-dimensional microstructural data [28]. Techniques such as sparsification and reconstruction enable compression

of spatio-temporal datasets while retaining structural information [1, 44]. However, their integration with thermodynamically consistent simulations and predictive models remains limited. Similarly, materials informatics approaches show potential for predicting structure-property relationships [45, 46], but are often decoupled from process-level microstructural evolution. Therefore, despite advances in modeling, learning, and data representation, existing approaches remain fragmented, lacking a unified framework that combines thermodynamic consistency, interface-level quantification, and scalable prediction.

3.2 Title definition

The title of this dissertation reflects the integration of interface physics, structured data representation, and predictive modeling. The **Laser-Microstructure Interface** is the evolving boundary between phases under laser-induced thermal fields, where interdiffusion, phase transformation, and intermetallic growth occur simultaneously, governed by temperature- and composition-dependent free-energy functionals [2, 4, 5]. The **Thermodynamic Tensor Model** represents microstructural evolution as a structured spatio-temporal dataset, where phase distribution, temperature, composition, and thermodynamic descriptors are encoded into a multi-dimensional tensor framework, preserving the coupling between thermal, chemical, and interfacial processes [1, 5]. The **Digital Twin** is defined as a computational framework capable of predicting microstructural evolution under varying processing conditions by integrating multiphysics modeling, tensor representation, and machine learning [3, 5]. Together, these components define a unified framework for quantifying and predicting laser-induced microstructural evolution in multicomponent alloys.

3.3 Main hypothesis

The central hypothesis of this dissertation is that a thermodynamic tensor representation can preserve thermodynamic, spatial, and interfacial information sufficiently to enable accurate machine-learning prediction of laser-induced microstructural evolution in multicomponent alloys, thereby supporting the development of digital-twin frameworks for quantifying laser-microstructure interactions.

3.4 Specific hypothesis

(I) **Thermodynamic consistency enables accurate interface evolution**

Accurate prediction of interfacial and microstructural evolution requires temperature- and composition-dependent free-energy formulations in multiphysics phase-field models.

(II) **Tensor representation preserves interface-level information**

Representing spatio-temporal microstructural evolution in tensor form preserves spatial and

interfacial features more effectively than reduced representations, enabling improved reconstruction and learning of interface dynamics.

(III) **Manifest-space learning enables predictive evolution**

Machine learning models trained on thermodynamically consistent tensor data can predict multi-generational microstructural evolution and meltpool behavior directly in the spatio-temporal domain while preserving interface characteristics.

(IV) **Integrated framework enables scalable digital twin development**

Integrating multiphysics modeling, tensor representation, and machine learning enables scalable prediction of $\mathscr{L}$-$\mathscr{M}$ interaction under varying processing conditions in near real-time.

(V) **Coupled physics-data framework improves process-structure understanding**

Combining physics-based simulations with data-driven models improves prediction and interpretation of process-structure relationships in multicomponent alloys.

CHAPTER IV

LASER-MICROSTRUCTURE INTERFACE AND INTERACTION

This chapter presents the central scientific theme of the dissertation by bringing together the physical, thermodynamic, representational, and predictive components developed across the included studies. While Chapters 1-3 established the background, objectives, and scientific hypotheses, the present chapter explains how laser-induced thermal fields, interfacial phase evolution, thermodynamic driving forces, tensor-based representation, and machine learning prediction collectively define the laser-microstructure ($\mathscr{L}$-$\mathscr{M}$) interface problem addressed in this thesis. **The discussion begins with the laser as the external driver of heat deposition and process variability, then proceeds to microstructure as the evolving material response, followed by the integrated methodological framework based on multiphysics phase-field modeling, thermodynamic tensor representation, and physics-informed learning, and finally synthesizes the findings to establish the route from interface physics to Digital Twin prediction.** The chapter further identifies the major determinants controlling interface evolution and formulates the quantitative descriptors used to characterize meltpool behavior, intermetallic growth, phase distribution, and interface-sensitive morphological evolution.

4.1 Laser ($\mathscr{L}$)

The laser is the initiating element of the entire $\mathscr{L}$-$\mathscr{M}$ interaction problem. In the framework developed in this dissertation, it is not treated merely as a source of heat, but as a primary cause that determines how energy is deposited into the materials, how temperature gradients evolve in space and time, and how the materials subsequently responds through melting, diffusion, phase transformation, and interface motion [4]. The significance of $\mathscr{L}$ in this context lies in the fact that even when the material system remains unchanged, variation in laser parameters such as power, irradiance, scan speed, and beam profile can produce substantially different meltpool geometries, interfacial reaction zones, and phase evolution pathways [4, 5].

The laser must therefore be understood at three connected levels. First, it acts as the source of transient thermal loading. Second, it defines the process window within which interfacial reactions become thermodynamically and kinetically possible. Third, it governs the quality and complexity of the data that later enters the machine learning stages of the Digital Twin framework. This interpretation is consistent with the multiphysics studies of unary *Au*, *Ti-Au*, and $Cu_x(Ti\text{-}6Al\text{-}4V)_y$ systems, where the imposed laser conditions directly altered meltpool depth, meltpool width, phase-front propagation, and microstructural transformation pathways [2, 4, 5].

4.1.1 Thermal history and meltpool formation

Laser-induced microstructural evolution begins with the spatially localized deposition of energy into the material domain. This deposition gives rise to rapid temperature rise, transient thermal gradients, and local melting, which together establish the conditions under which phase transformation and interfacial diffusion take place. In the numerical frameworks used throughout this work, the thermal field is governed by the transient heat-transfer equation with an external laser source term. In its general form, the heat-transfer problem is expressed as [2, 4, 5]:

$$\rho_i \langle T \rangle C_{p,i} \langle T \rangle \left(\frac{\partial T}{\partial t} + \vec{u} \cdot \nabla T \right) = \nabla \cdot \left(k_{th,i} \langle T \rangle \nabla T \right) + Q_{laser} \qquad \text{Equation 4.1}$$

where ρ_i, $C_{p,i}$, and $k_{th,i}$ represent the density, specific heat capacity, and thermal conductivity of phase 'i', respectively, all expressed as temperature-dependent quantities denoted by $\langle T \rangle$. The term $\vec{u}$ represents the local velocity field within the meltpool, and Q_{laser} denotes the externally imposed laser heat source, which varies depending on beam profile and processing conditions. This equation defines the thermal component of the $\mathscr{L}$-$\mathscr{M}$ interaction by governing the evolution of the temperature field. The general simulation setup of laser processing is illustrated in Figure 4.1**(a)**, where a moving laser source traverses the top surface of the computational domain with a predefined scan speed. Different beam configurations, including Gaussian, Flat-Top, Ring, and Bessel, are shown in Figure 4.1**(b)**, highlighting that even for identical power input, the resulting intensity distribution varies significantly across the domain [5]. The thermal field generated by this moving heat source defines the thermal history of the system. Thermal history is understood as the time-dependent sequence of heating, melting, dwell, and cooling experienced locally within the material. Since microstructural processes such as interdiffusion, phase nucleation, and grain growth are strongly temperature dependent, the thermal history acts as the direct link between the externally applied laser input and the internal material response.

In **Article II**, this thermal description is used to model the transient temperature field in the Cu_x*(Ti-6Al-4V)*$_y$ system during laser surface alloying. The simulation setup and comparison with experimental cross-section are shown in Figure 4.2. The thermal model enables reconstruction of the temperature evolution at the interface, which cannot be directly resolved experimentally, and explains the thermodynamic activation of Ti_2Cu intermetallic formation.

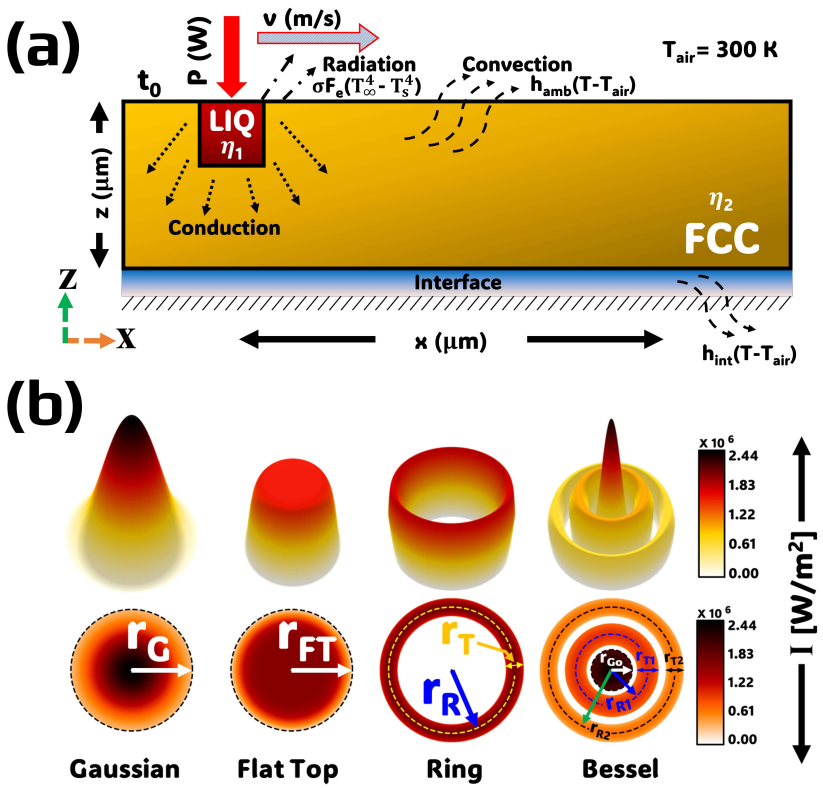


Figure 4.1 **(a)** Schematics diagram of 2D computational domain setup illustrating the laser-induced phase evolution. **(b)** Visualization of four different laser beam profiles: Gaussian, Flat-Top, Ring and Bessel with 3D representation of intensity map and top-view intensity distribution [5].

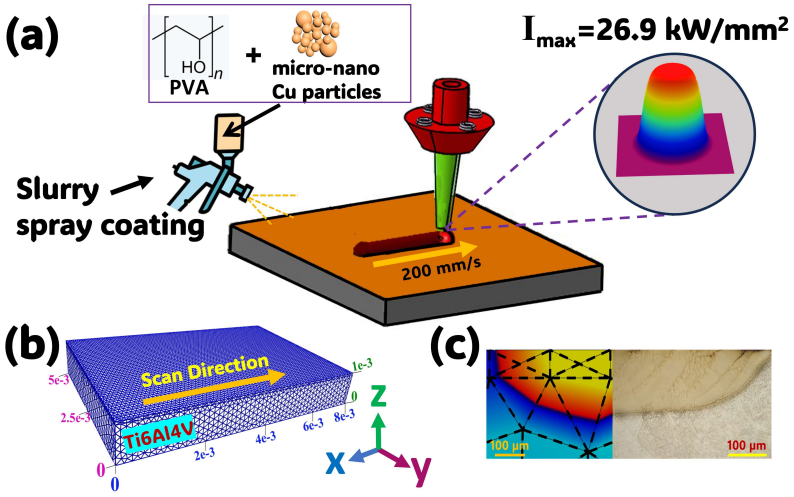


Figure 4.2 **(a)** Schematics of laser surface alloying with Flat-Top laser beam profile. **(b)** Two-layer computational mesh of Ti6Al4V substrate and Cu powder bed. **(c)** Comparison between computational domain and experimental melt-zone cross-section [2].

In **Article IV**, the thermal history is directly coupled with phase evolution in the *Ti-Au* system, where LIQUID, HCP, FCC, and Ti_3Au-IMC phases evolve simultaneously under non-isothermal conditions. The temperature distribution at a fixed simulation time for different scan speeds is shown in Figure 4.3**(a)** and **(b)**, together with time-temperature histories at selected spatial points. These results demonstrate that different locations within the domain experience different thermal

exposure durations above the melting temperature, leading to heterogeneous phase evolution. Melt-

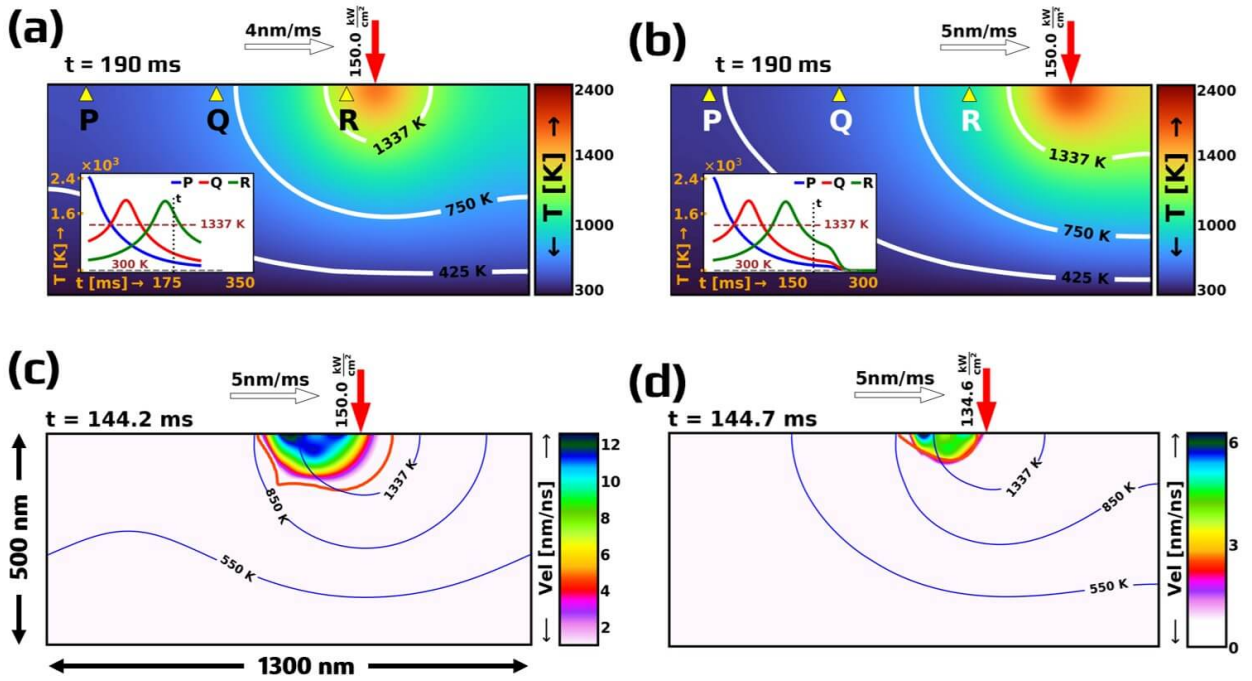


Figure 4.3 Temperature distribution and velocity profiles under different laser conditions. **(a-b)** Temperature field at 190 *ms* for scan speeds of 4 and 5 nm/ms at constant irradiation. **(c-d)** Velocity magnitude inside LIQUID phase for different irradiance levels at constant scan speed **[4]**.

pool formation is the most direct manifestation of this thermal history. The meltpool defines the liquid region in which diffusion, phase mobility, and interfacial reactions are significantly enhanced compared to the surrounding solid. As shown in Figure 4.3**(c)** and **(d)**, the meltpool geometry and flow behavior depend strongly on laser conditions. Higher irradiance leads to increased meltpool depth and width, as well as higher velocity magnitude within the LIQUID phase. In the presented results, the maximum velocity is approximately doubled (12 nm/ms) under higher irradiance conditions, indicating stronger convective transport within the meltpool.

The meltpool therefore defines the spatial domain in which interfacial reactions occur and controls the kinetics of these reactions through fluid flow and enhanced diffusion. In the $Cu_x(Ti\text{-}6Al\text{-}4V)_y$ system, it determines the region where Ti_2Cu form, while in the *Ti-Au* and unary *Au* systems, it governs the evolution of phase fronts that are later used as inputs for predictive models such as **MicroTwin** and **FlowTwin** [2, 4, 5].

4.1.2 Process parameters

The effect of the laser on microstructure does not arise from heat input alone, but from the combined action of multiple processing parameters. Among these, irradiance, scan speed, and beam profile are the most influential variables considered in this work. In the *Ti-Au* study (**Article IV**), higher irradiance produced a deeper meltpool and a thicker Ti_3Au intermetallic grains, demon-

strating that interface evolution is highly sensitive to the energy density imposed by the laser [4]. Specifically, the meltpool depth increased from 158 nm to 180 nm, while IMC thickness increased to 364 nm under maximum heat-flux conditions (max $\dot{Q}$) of 150 kW/cm^2 at 4 nm/ms. This is illustrated in Figure 4.4, where **(a)** shows the accelerated increase in IMC thickness under higher irradiance, and **(b)** shows the corresponding increase in meltpool dimensions (maximum horizontal span: x_{max} and maximum vertical depth: z_{max}), with solid lines representing 150 kW/cm^2 and dashed lines 134.6 kW/cm^2.

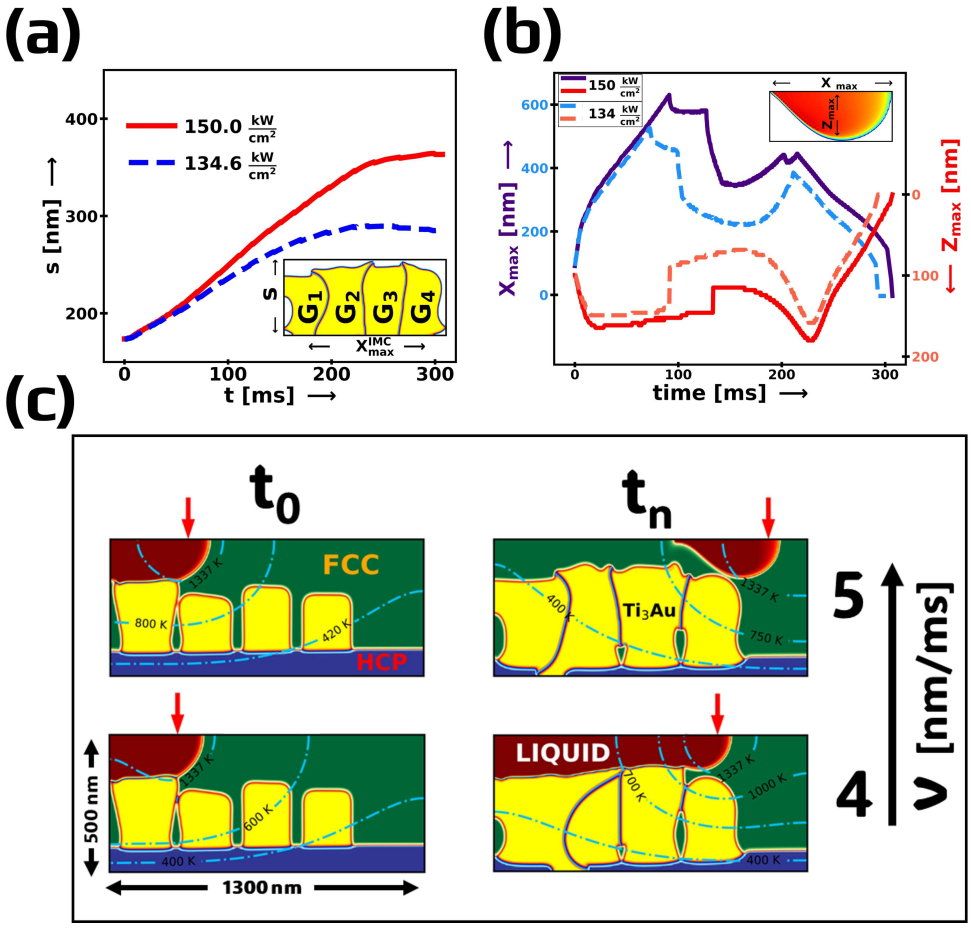


Figure 4.4 In **(a)** graph quantifying the effect of higher (150 kW/cm^2) and lower (134.6 kW/cm^2) irradiance level in temporal evolution of IMC layer thickness at constant scan speed of 5 nm/ms is presented. Similarly **(b)** shows the meltpool's maximum horizontal span (x_{max}) and maximum vertical depth (z_{max}) at two level of irradiance. In **(c)** the phase evolution under two different laser scan speed at a constant irradiance of 150 kW/cm^2 is presented. The top row presents results with laser scan speed of 5 nm/ms at simulation time 40 ms and 200 ms whereas bottom row represents phase morphology with scan speed of 4 nm/ms at same simulation time **[4]**.

Scan speed plays an equally important role because it controls the residence time of the laser over a given material point. A slower scan speed increases local exposure time and allows greater heat accumulation, thereby promoting deeper melting and stronger interfacial evolution. A higher scan speed reduces this interaction time, shortens the thermal exposure window, and may suppress or limit intermetallic growth. As illustrated in Figure 4.4**(c)**, at a constant irradiance of 150 kW/cm^2

the difference in morphological evolution across different phases is linked to the difference in laser scan speed. With a lower scan speed of 4 nm/ms the LIQUID phase is observed to dwell longer compared to that with higher scan speed of 5 nm/ms. This effect is explicit observed in **Article IV**, where scan speed and irradiance jointly control the meltpool geometry and relative propagation of the thermal, and chemical diffusion fronts. In **Article II**, a laser scan speed of 200 mm/s and power of 1000 W defined the thermal cycle governing Ti_2Cu formation in the Cu_x(Ti-6Al-4V)$_y$ system, confirming the process window must be resolved quantitatively rather than descriptively. Beyond power and speed, **Article V** shows that beam profile itself alters the character of $\mathscr{L}$-$\mathscr{M}$ interaction.

A direct quantitative comparison of laser beam profiles reveals that the heat source shape itself significantly alters the meltpool morphology and internal dynamics, even under identical power and scan speed. The Flat-Top beam produces a significantly larger meltpool area (0.016 mm^2) compared to the Ring beam (0.013 mm^2), indicating a transition from spatially extended to confined thermal interaction. In terms of thermal intensity, the Gaussian beam reaches a higher peak temperature (3062 K) than the Bessel beam (2749 K), reflecting stronger energy localization in the Gaussian profile. Similarly, the internal meltpool dynamics differ markedly across beam types: the Bessel beam generates a maximum velocity of 84.65 $\mu m/s$, whereas the Ring beam produces only 20.37 $\mu m/s$, demonstrating a substantial reduction in convective transport [5]. The influence of both beam profile and free energy formulation on the thermal response is summarized in Table 4.1, where the maximum temperature attained under different beam profiles is compared for TDB-based (F_ψ) and fitted (F_θ) free-energy formulations. The consistently higher temperatures predicted by F_θ across all beam types indicate an overestimation of thermal intensity relative to the thermodynamically consistent F_ψ formulation, reinforcing the sensitivity of $\mathscr{L}$-$\mathscr{M}$ interaction to the choice of free-energy description.

Table 4.1 Maximum temperature attained in unary Au system under different laser beam profiles (Gaussian, Flat-Top, Ring, Bessel) for two free-energy formulations: thermodynamically consistent TDB-based (F_ψ) and fitted (F_θ). The comparison highlights the combined influence of beam energy distribution and thermodynamic description on the thermal response, with F_θ consistently predicting higher peak temperatures across all beam types **[5]**.

	Gaussian	**Flat-Top**	**Ring**	**Bessel**
F_ψ	2996 K	2966 K	1883 K	2441 K
F_θ	3062 K	3029 K	2180 K	2749 K

4.1.3 Meltpool's kinematic lag

One of the strongest conceptual advances this thesis presents is that the laser does not generate identical thermal and phase responses. In many simplified computational treatments, the formation of the meltpool is assumed to occur instantaneously once the temperature crosses the melting point [21, 29, 47]. **Article IV** and **Article V** shows that this assumption is physically inadequate, because the thermal diffusion front and the phase (mass) diffusion front do not move together. The TDB-based free-energy formulation (F_ψ) of **Article V** reproduced the physically meaningful lag between thermal advance and phase transformation, whereas simplified fitted forms (F_θ) tended to blur this distinction. This behavior is shown in Figure 4.5, where under F_θ the isotherm front (1337 K) and meltpool phase front overlap (4.5**(a-b)**), whereas under F_ψ a clear separation appears between the isotherm (dotted lines) and the LIQUID phase boundary (red contours) for the same beam profiles (4.5**(c-d)**).

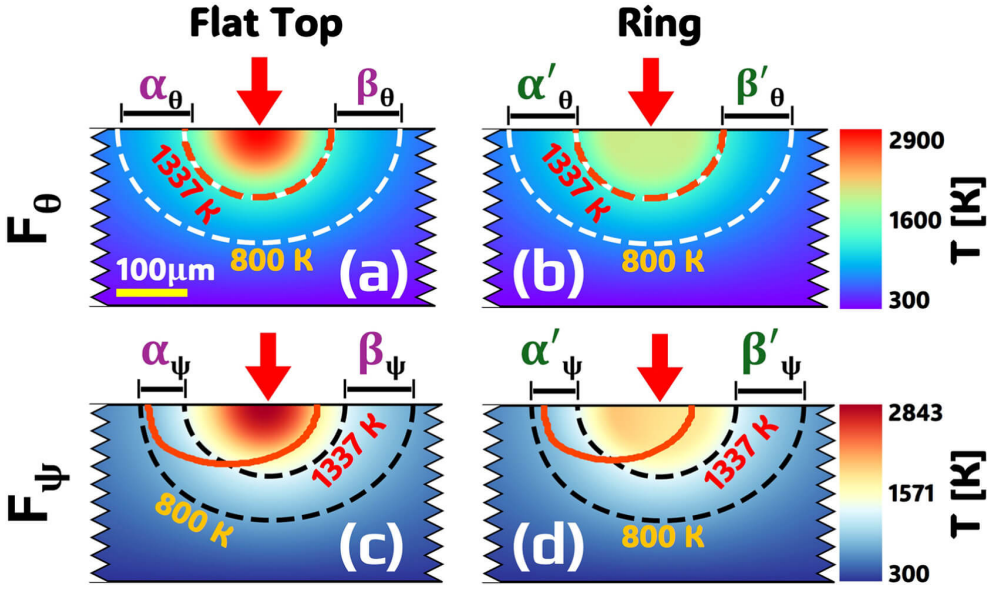


Figure 4.5 Illustration of comparison in temperature distribution and LIQUID phase evolution for Flat-Top and Ring beams with two different free-energy formulations. Subplot **(a)** and **(b)** represents results from fitted free-energy formulation where the lead-lag dynamics between isotherm front and phase front share the same contour line. Similarly, subplot **(c)** and **(d)** highlights the lead-lag dynamics between thermal and phase front which is observed in simulation with TDB based free-energy expression. The red contour line represents the LIQUID phase whereas the dashed line with 1337 K marking represents the thermal front with melting point of the Au-rich FCC phase **[5]**.

In **Article IV** a related interpretation is developed from the perspective of coupled heat and chemical diffusion. There, the relative propagation of the heat-transfer front and the chemical-diffusion front is quantified using the **positional time lag** (δt_{pos}) and dimensionless **Lewis number (Le)** based interpretation, showing that heat transport is faster than interfacial chemical diffusion. This is shown in Figure 4.6**(a-b)** where the evolution of the thermal front (τ) and phase front ($\mathscr{D}$) under $\dot{Q}_{max}$ (150 kW/cm^2 at 4 nm/ms) and $\dot{Q}_{min}$ (134.6 kW/cm^2 at 5 nm/ms) conditions, consistently

showing the thermal front leading the phase boundary. The corresponding quantification is plotted in Figure 4.6(**c**) through the variation of *Le* across different scan speeds and irradiance levels, and in Figure 4.6(**d-e**) through the spatial distribution of δt_{pos} under $\dot{Q}_{min}$ and $\dot{Q}_{max}$ conditions. The

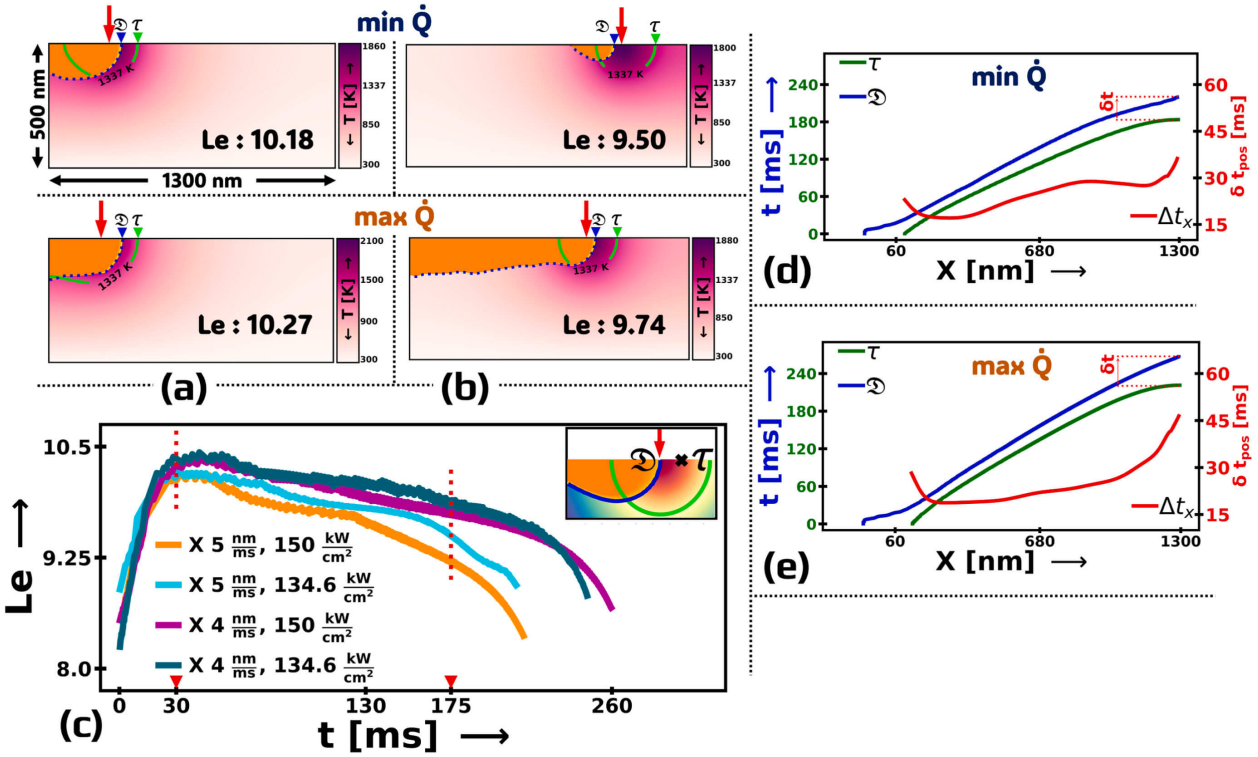


Figure 4.6 Visualization of lead-lag dynamics between thermal, and phase fronts with corresponding Lewis number (*Le*) values and positional time lag between two fronts. Subplot **(a)** and **(b)** represents the evolution of thermal front (τ) and phase front ($\mathscr{D}$) under $\dot{Q}_{min}$ and $\dot{Q}_{max}$ respectively. The *Le* calculated at the displayed laser position is presented within the sub-figures. In **(c)** the plot illustrating the *Le* evolving temporally over the simulation time for four different configurations of laser irradiance level and scan speed is presented. Graphs **(d)** and **(e)** display the *positional time lags* (δt_{pos}) between thermal front (τ) and phase front ($\mathscr{D}$) against the computational domain's horizontal dimension at two different heat flux levels **[4]**.

Lewis number provides a compact way to interpret this difference as: $Le = \alpha/D$, where α $[m^2/s]$ is the thermal diffusivity and D $[m^2/s]$ is mass diffusivity. A large value implies that thermal signal propagates faster than the compositional response, meaning that the laser creates a moving thermodynamic opportunity before the microstructure can fully reorganize to exploit it. The shape, thickness, and stability of the interface therefore depend not only on the magnitude of laser input, but also on the material's microstructure dictating this dynamics between thermal and diffusion fronts. Laser's irradiance, scan speed, and beam profile define the thermal history in the material; that thermal history establishes the meltpool; and the meltpool, together with the associated phase-front lag and transport asymmetry, governs the conditions under which diffusion, phase transformation, and grain growth become possible. Therefore, the 'laser' in $\mathscr{L}$-$\mathscr{M}$ interaction is not a background process variable but the primary driver that determines the boundary condition of interface evolution [2, 4, 5].

4.2 Microstructure ($\mathscr{M}$)

Microstructure is defined as a set of spatially and temporally evolving field variables describing the local thermodynamic state of the material. For a unary system with 'i' phases, it can be expressed as $\mathscr{M}_i(x,t) = \{\eta_1(x,t), \eta_2(x,t), ..., \eta_n(x,t)\}$, while for a multicomponent system with 'j' elements, it extends to $\mathscr{M}_{i,j}(x,t) = \{c_1(x,t), c_2(x,t), ..., c_n(x,t), \eta_1(x,t), \eta_2(x,t), ..., \eta_n(x,t)\}$, where c_j are composition fields and η_i are phase-field order parameters. If the laser defines the external energy input, the microstructure represents the internal material response, evolving under coupled thermal, chemical, and interfacial driving forces. Laser irradiation induces rapid and localized changes in temperature and composition, leading to phase transformation, interdiffusion, and interface migration, where phase boundaries continuously migrate, deform, and sometimes disappear. Within this dissertation, microstructure is interpreted across three connected levels: as a physical field described by phase and composition variables; as a thermodynamic system governed by bulk and interfacial free energy functions that control phase stability and interface motion; and as a quantifiable structure characterized through geometric and informatics-based descriptors, including phase fraction, morphology, intermetallic thickness, microstructure-similarity index, and tensorized spatio-temporal representations [1, 3, 4].

4.2.1 Spatio-temporal field variables

The phase-field approach used throughout the included works represents microstructure as a continuous field rather than a collection of sharp interfaces. This is essential because the laser-treated systems undergo local melting, phase transformation, phase separation, and interfacial reaction under non-equilibrium conditions. A sharp-interface treatment would not be able to capture the continuous redistribution of composition and the gradual motion of phase boundaries with sufficient numerical stability [12].

In the simplest form, the evolving microstructure is described through a conserved variable, usually compositions ($\mathbf{c_i}$), and non-conserved order parameters ($\eta_\mathbf{i}$). The conserved variable describes chemical redistribution, while the non-conserved variable describes phase identity. This framework is illustrated in Figure 4.7: **(a)** shows phase separation in the *Ti-Cr* system (**Article I**) through composition evolution; **(b)** shows coupled composition and order-parameter's evolution in the *Ti-Au* system under laser processing (**Article IV**), where distinct regions of LIQUID, FCC, IMC grains (G_1,G_2, G_3, G_4), and HCP phases grow; **(c)** shows order-parameter based phase evolution in the unary *Au* system with LIQUID and FCC phases (**Article V**); and **(d)** show composition evolution in the $Co_xCr_yFe_zNi_{(1-x-y-z)}$ a multi-principal element alloy under Gaussian laser beam (Authors' own work).

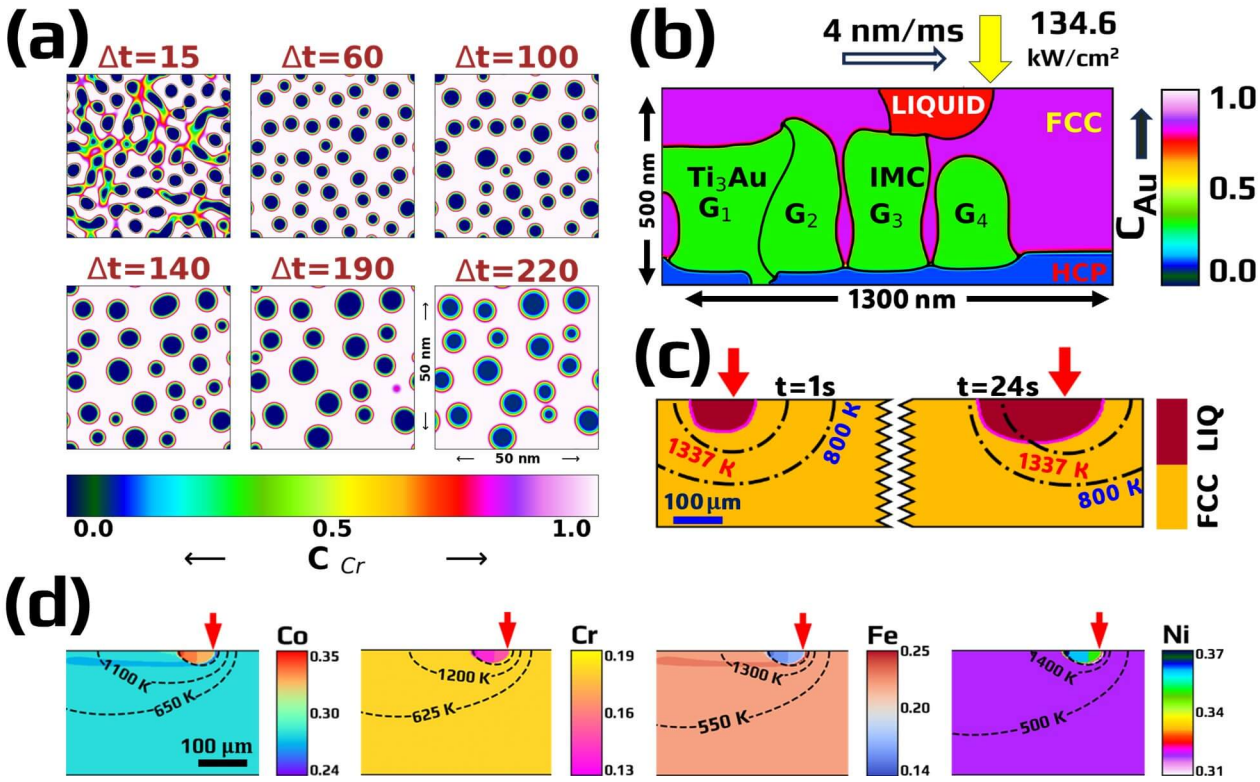


Figure 4.7 Phase field simulation results across different studies presented in the dissertation. In **(a)** the phase separation of *Ti-Cr* alloy system is visualized at six different time stamps representing the compositional distribution of Cr inside the computational domain **[1]**. The conserved variable (composition) evolution in laser processing of *Ti-Au* system is depicted in **(b)** within the four different phases and intermetallic grains **[4]**. **(c)** Highlights the non-conserved variable (order-parameters) in phase field modeling representing the two distinct phases: LIQUID and FCC in unary *Au* system undergoing phase transformation **[5]**. Subplots in **(d)** shows the composition evolution during the laser processing of multicomponent $Co_xCr_yFe_zNi_{(1-x-y-z)}$ alloy system under the Gaussian beam with power 370 W and scan speed 0.5 m/s (Authors' own work).

The evolution of conserved and non-conserved phase-field variables is governed by partial differential equations. The conserved variable follows the multiphase convection-diffusion equation:

$$\frac{\partial c}{\partial t} = \nabla \cdot \left[M\langle T \rangle \nabla \left(\frac{\partial f}{\partial c} \right) \right] - \vec{u} \cdot \nabla c \qquad \text{Equation 4.2}$$

where c is the composition field, $M\langle T \rangle$ is the temperature dependent mobility, f is the bulk free energy density, and $\vec{u}$ is velocity of meltpool whenever applicable. Due to the transient nature of meltpool, a thermal gradient within it creates Marangoni convection which must be accounted for to capture the fluid flow accurately within the meltpool. The expression for thermo-capillary convection coupled with *Navier-Stokes* equation governing the velocity profile is:

$$\vec{n} \cdot \sigma_{LIQUID} = -2H\gamma_{ST}\vec{n} - \nabla_s \gamma_{ST} \qquad \text{Equation 4.3}$$

where σ_{LIQUID} is Cauchy stress tensor for LIQUID phase at free surface, H is the mean surface

curvature, γ_{ST} is the temperature dependent surface tension. Similarly, the temporal evolution of non-conserved phase-field variable (order-parameter) is governed by the Allen-Cahn equation:

$$\frac{\partial \eta}{\partial t} = -L\langle \eta \rangle \left[\frac{\partial f}{\partial \eta_i} - \nabla \cdot \left(\frac{\partial f}{\partial \nabla \eta_i} \right) \right] \qquad \text{Equation 4.4}$$

where η_i represent the order-parameters and $L\langle T \rangle$ is the temperature-dependent interface mobility. Here a thermodynamically consistent interpolation function [48] is required when multiphase coexists within the diffuse interface to swiftly interpolate the related material properties between the relevant phases. The interpolation here is not just a mathematical convenience; it ensures that temperature-dependent properties and phase-dependent free-energy contribution transition smoothly across the interface instead of undergoing unphysical discontinuities.

These governing equations: heat-transfer, multiphase convection-diffusion, Allen-Cahn, Navier-Stokes, along with temperature- and composition-dependent material properties, are coupled into a multiphysics framework that determines microstructure evolution through the underlying free-energy landscape, rather than prescribing it geometrically. The interface is thus treated as a finite-width region, whose morphology emerges from the competition between bulk thermodynamic driving forces and interfacial energy penalties. The results presented in this dissertation are obtained by solving these coupled equations using the Finite Element Method (FEM) within the open source **Multiphysics Object-Oriented Simulation Environment (MOOSE)** framework [49, 50]. The corresponding data and code are available at: https://github.com/subediupadesh

4.2.2 Free-energy landscapes

While multicomponent system's microstructure is defined through composition and phase-field variables, these fields alone do not determine which configurations are stable or how they evolve. A thermodynamic descriptor is required to assign an energetic measure to each possible microstructural state and to provide the driving forces for its transformation. Among thermodynamic quantities, free energy is uniquely suited for this role, as it is formulated as a functional of state variables (such as H, T, and S). For multiphase and multicomponent formulation, '**G**' has composition and phase dependencies. Accordingly, microstructure evolution is governed by gradients of the total free-energy functional under kinetic constraints. The phase-field equations translate this functional into spatio-temporal structural evolution, determining phase stability, interface motion, and the formation of meltpools, decomposition patterns, or intermetallic layers under laser processing. The total free energy is expressed as the sum of bulk and interfacial contributions, where the bulk energy is defined as a weighted combination of phase-specific Gibbs free energies, and the interfacial energy represents the excess energy associated with the diffuse transition between phases (refer

Article IV for detailed formulation).

In the generic binary-alloy system used for the data generation to train the Convolutional-LSTM model (refer **Article III**), the Gibbs free-energy landscape is represented through a double-well function, allowing systematic variation of driving-force parameters and therefore generation of diverse microstructural evolution scenarios for machine learning [3]. The free-energy function is expressed as: $G = \alpha(c - c_{eq})^2 + \beta(c - c_{eq}) + \gamma(c - c_{eq})^4 + \delta$, based on this expression free-energy landscapes for *Cu-Mn* and *Pd-Rh* systems are visualized in Figure 4.8**(a)**, the same subplot illustrates the data generation pipeline for machine learning.

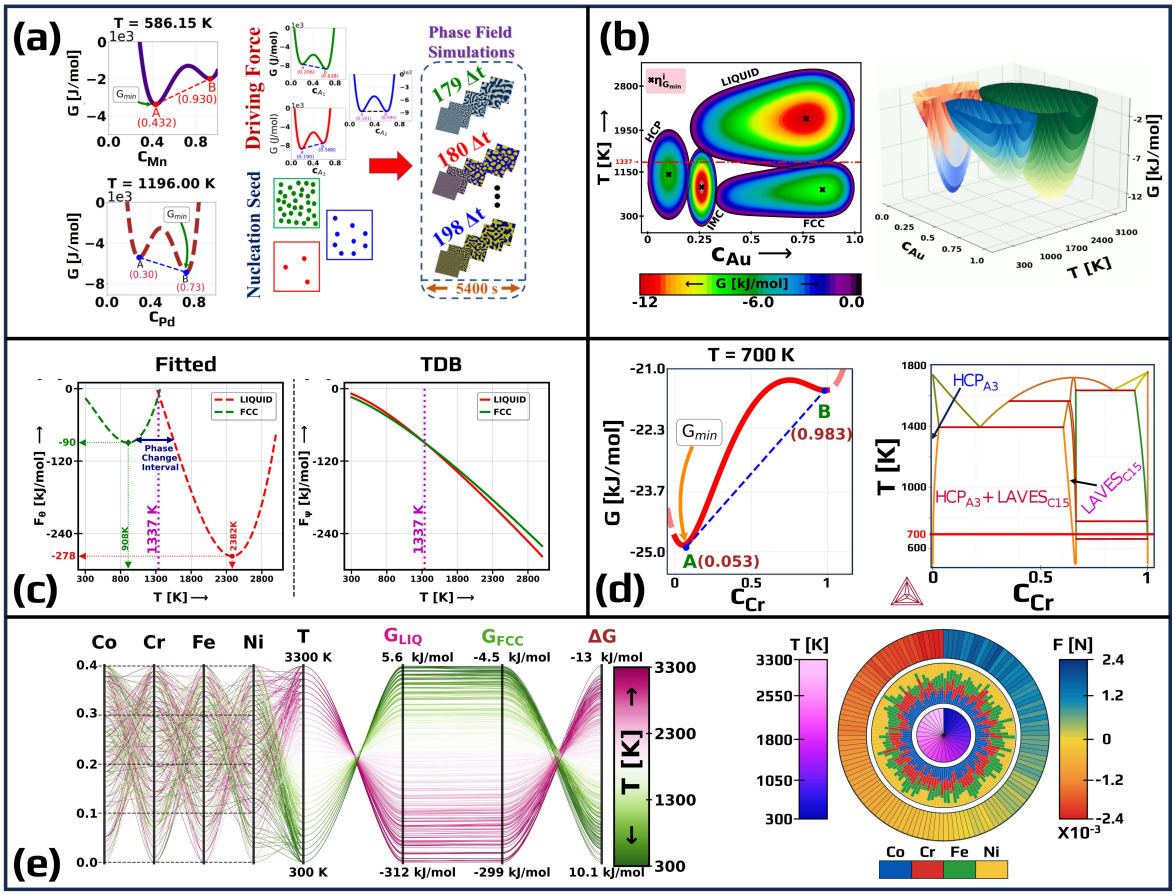


Figure 4.8 Subplot **(a)** illustrates the Gibbs free energy landscape for *Cu-Mn* and *Pd-Rh* alloy system along with the method used to create the phase decomposition dataset to train the machine learning model via multiple simulations setup in **[3]**. Similarly, in **(b)** the 2D and 3D visualization of temperature-composition dependent free energy plots for *Ti-Au* system are presented **[4]**. The visual comparison between polynomial fitted and TDB file extracted free energy expression is presented in **(c)** from the study of unary *Au* phase transformation **[5]**. Subplot **(d)** represents Gibbs free energy landscape and phase stability of the *Ti-Cr* binary alloy. The left plot shows the Gibbs free energy curve at 700 K with local and global minima corresponding to Cr-rich and Ti-rich equilibrium tendencies, while the right graph presents the Ti-Cr phase diagram showing the HCP + LAVES dual-phase region that supports phase separation **[1]**. **(e)** Visualization of the thermodynamic data tensor and phase-transformation driving force for laser-processed $Co_xCr_yFe_zNi_{(1-x-y-z)}$ alloy. The plot on the left shows the composition- and temperature-dependent Gibbs free energies of LIQUID and FCC phases, while the hierarchical sunburst chart maps the corresponding transformation driving force (Authors' own work).

Similarly, in Ti-Au system (**Article IV**), temperature- and composition-dependent Gibbs free energy functions for each of the phases are generated by fitting the free-energy data points from Thermodynamic Database (TDB) file [51]. The 2D and 3D representation of Gibbs free-energy landscape used for the study is visualized in Figure 4.8**(b)**. These free energy functions capture the thermodynamic driving forces for the evolution of intermetallic phases such as Ti_3Au under varying thermal conditions [4]. In unary *Au* system (**Article V**), comparison between fitted (F_θ) and TDB-based (F_ψ) free energy formulations demonstrates that accurate representation of free energy is essential for capturing phase-front dynamics and lag behavior [5]. The plot for F_θ and F_ψ Gibbs free energy landscape is illustrated in Figure 4.8**(c)**.

In system involving compositional heterogeneity, such as *Ti-Cr* (**Article I**), the free energy formulation includes both chemical and elastic contributions with the chemical free energy fitted as a composition-dependent function. Where the elastic strain energy arises due to lattice mismatch between phases and influences the morphology of phase-separated regions. The addition of free energy from elastic response is an important aspect because it explicitly couples phase stability with it, allowing the representation of elasto-chemical evolution data in tensor form [1]. The chemical free energy contribution is shown in Figure 4.8**(d)** at 700 K identifies two thermodynamic minima, indicating the tendency of the system to separate into Ti-rich and Cr-rich regions. The global minimum occurs near Cr composition 0.053, while the local minimum appears near Cr composition 0.983, with corresponding free-energy values of approximately -25 kJ/mol and -21.5 kJ/mol, respectively. This thermodynamic behavior is consistent with the *Ti-Cr* phase diagram, where the coexistence of Ti-rich HCP and Cr-rich LAVES phases confirms the phase separation. Therefore, the free-energy landscape provides the driving force basis for modeling the evolution of Ti-Cr microstructure using the phase-field approach [1]. For the multicomponent system such as *CoCr-FeNi*, the Gibbs free energy is represented as a higher-order thermodynamic tensor corresponding to specific alloy composition, temperature, and phase free-energy state. Direct visualization of this high-dimensional tensor is difficult therefore, the parallel-coordinate plot as shown in Figure 4.8**(e)**, provides a compact projection of the thermodynamic space, while the sunburst chart translates selected tensor entries into the net driving force.

4.2.3 Interfacial reaction, and intermetallic growth

The microstructural interface becomes especially important when two chemically distinct regions are brought into thermal contact under laser irradiation. In such systems, the interface is not merely separating existing phases; it becomes the site of interdiffusion, reaction, and formation of new products. This is dominant situation in the $Cu_x(Ti\text{-}6Al\text{-}4V)_y$ and *Ti-Au* studies.

In the $Cu_x(Ti\text{-}6Al\text{-}4V)_y$ system, laser surface alloying introduces Cu into the near-surface region of the *Ti-6Al-4V* substrate, and the interface responds the formation of Ti_2Cu intermetallic compounds [2]. The combined experimental and computational analysis showed that at an average temperature of 1250 K, the free-energy of the IMC phase is lower than that of the matrix phase, indicating that Ti_2Cu growth is thermodynamically favorable in the region close to the treated surface. The resulting IMC precipitates do not grow as uniform layers only; they nucleate and evolve with irregular size, heterogenous distribution, and curvature-dependent interaction with neighboring grains [2]. This result is clearly visible in Figure 1.2 where the growth of IMC grain follows a homogeneous or heterogenous path depends upon the initial grain morphology at nucleation.

The *Ti-Au* system reveals a more strongly coupled interfacial evolution. There, the intermetallic phase Ti_3Au forms through the reaction: $3Ti + Au \rightarrow Ti_3Au$. The formation enthalpy of Ti_3Au is negative across a wide temperature range, indicating thermodynamic favorability [4]. Under laser irradiation, the interface experiences simultaneous heating, local melting, interdiffusion, and competition between HCP, FCC, LIQUID, and IMC phase. As a result, the Ti_3Au grain does not grow in isolation; its evolution is coupled to the meltpool and to the local temperature- and composition-dependent free-energy hierarchy. The numerical modeling of IMC grain growth is further verified by the experimental work performed by Bialas et al. [38]. Figure 4.9 illustrates the similarity between experimental microstructural image (4.9(**a**)) with Ti_3Au intermetallics formed due to laser treatment of Au-coated Ti film to the phase-field laser processing simulation generated result in Figure 4.9(**b**) in Ti-Au system.

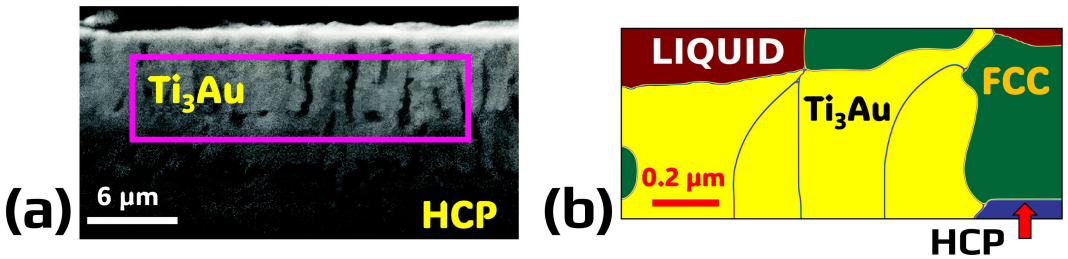


Figure 4.9 **(a)** Experimental image showcasing the microstructural morphology of Ti_3Au IMC grains highlighted inside the magenta box formed as the result of laser treatment of Au-coated Ti film post cooling [38]. **c** Multiphase-field simulation snapshot illustrating the IMC grain evolution as the result of laser processing in Ti-Au system highlighting the formation and growth of irregular and distinct IMC grains aligning the simulation result with experimental findings **[4]**.

In the *Ti-Cr* system, the physical scenario is different, because the key process is phase separation rather than laser-induced intermetallic formation. Even so, the underlying theme is consistent: the microstructure evolves because phase instability drives the materials towards coexisting lower-energy states. The HCP-LAVES separation pattern generated in **Article I** provides the basis for

the later tensor representation, demonstrating that even when the system does not form a laser-produced IMC layer, the interface-rich morphology itself can be encoded and reconstructed as structured microstructural informatics [1].

4.2.4 Morphological and interface-sensitive data

Microstructure in this dissertation is not restricted to phase identity alone. It is also quantified through geometry and morphology. This is necessary because the scientific problem of the thesis is not only to simulate whether a phase exists, but to quantify how interface evolves in shape, size, continuity, and temporal progression. For this reason, the microstructure is characterized through descriptors such as meltpool area, width, depth, IMC thickness, phase-area fraction, shape index, blob features, and microstructural similarity index [3–5].

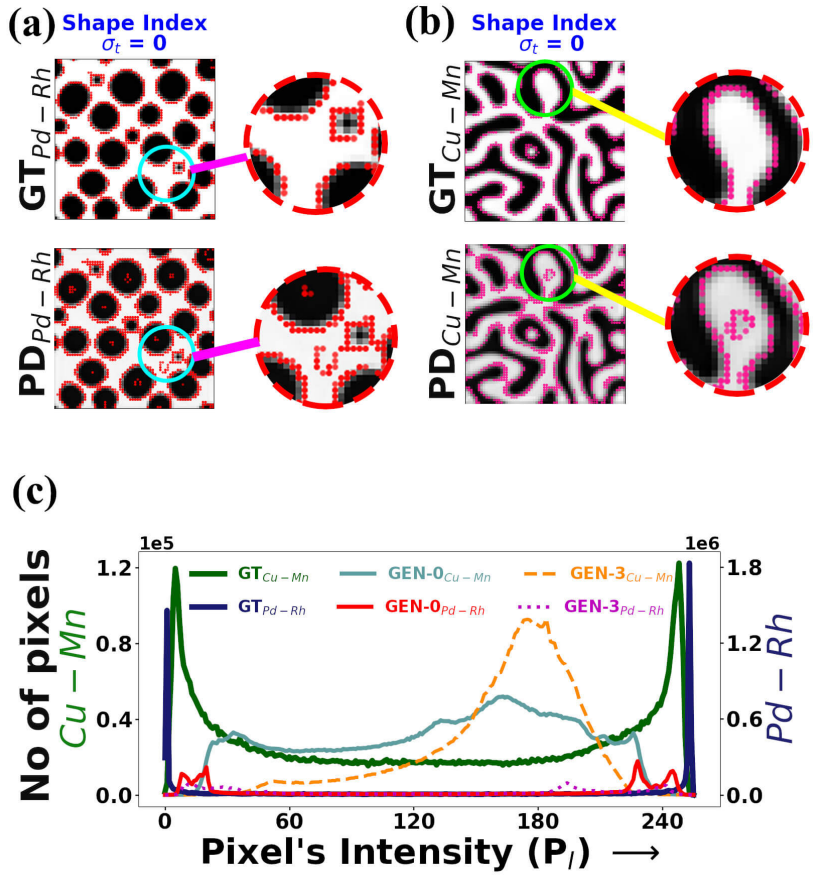


Figure 4.10 Shape index analysis detects and compares microstructural phase-interface in *Pd-Rh* and *Cu-Mn* alloy system between ground truth (GT) and model-predicted (PD) microstructural frames. In *Pd-Rh* **(a)**, predictions show extra interfacial regions (at shape index value $\sigma_t = 0$) and in *Cu-Mn* **(b)**, predictions lag with missing interfaces. Twin histograms **(c)** reveal sharper phase separation in *Pd-Rh* versus broader interfaces in *Cu-Mn* **[4]**.

Article IV quantifies microstructure through the evolving areas of the individual phases, the thickness of the Ti_3Au intermetallic layer, the depth and width of the meltpool under different irradiance, and scan-speed conditions (illustrated in Figure 4.4(**a-b**)). **Article V** quantifies meltpool

morphology and flow by using temperature fields to predict phase shape and flow velocity within the meltpool. **Article II** links microstructural evolution to experimental cross-sectional evidence and shows that the irregular morphology of Ti_2Cu grains is not a secondary detail but a defining characteristic of the laser-interface response.

Article III directly addresses interface-sensitive morphological interpretation by moving beyond pixel-wise similarity and employing metrics such as microstructural similarity index (μ_{SIM}), gray histogram, blob detection, and shape index to preserve interfacial information. This is illustrated in Figure 4.10 **(a-b)**, where the predicted microstructure (PD) appears visually similar to the phase-field ground truth (GT), yet differences become evident when analyzed through curvature-based shape index, which isolates interface regions. Further quantification is provided in 4.10**(c)** through pixel intensity distributions, revealing measurable differences in phase morphology and feature distribution between GT and predicted frames. These descriptors collectively enable an interface-aware characterization of microstructure beyond visual resemblance.

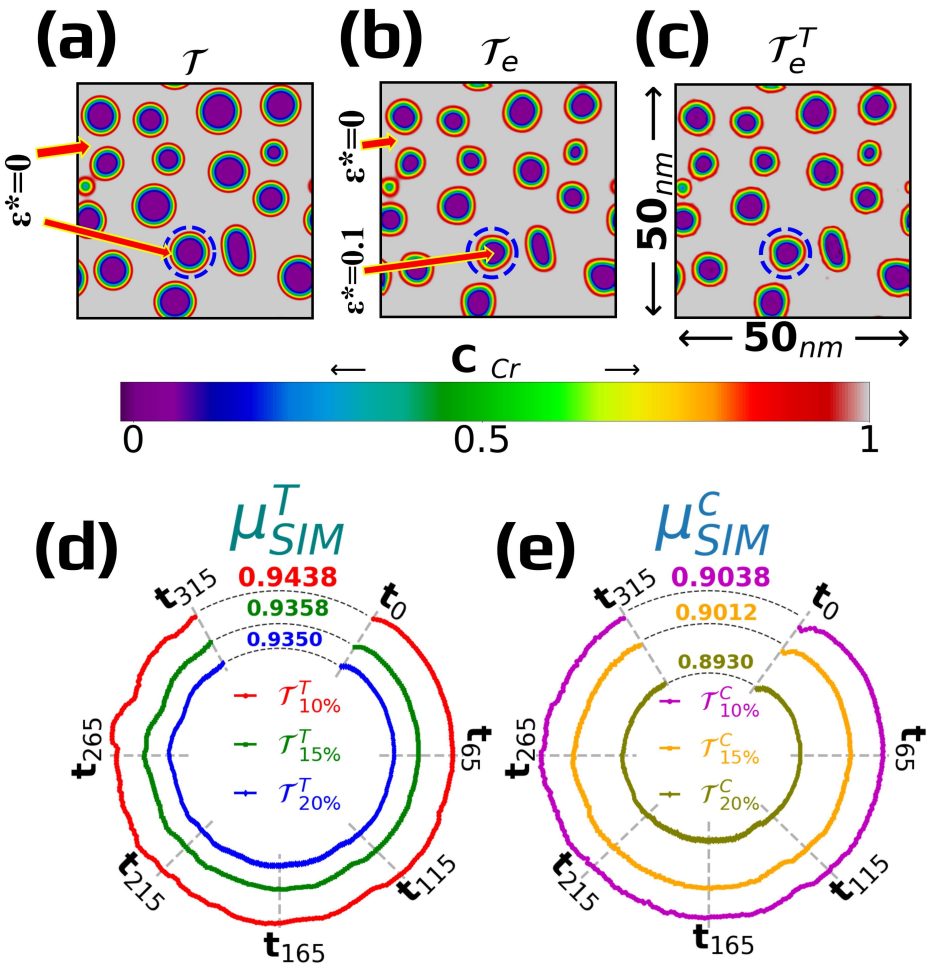


Figure 4.11 **(a)** Elastic effects uneffected microstructural shapshot. **(b)** Deformation from elastic strain ($\varepsilon^* = 0.1$ in α, 0 in β). **(c)** Tucker decomposition reconstruction (at 10% sparsity) preserves composition and deformation. Spider chart **(d)** and **(e)** represents the microstructural similarity index (μ_{SIM}) showing Tucker method (τ^T) excels over CP (τ^C) **[4]**.

Article I provides the final representational layer, where the evolving microstructure are converted into a dense tensor, sparsified, decomposed, and reconstructed, demonstrating the microstructure can be handled not only as a physical field but also as a structured data object without losing the essential interfacial content [1]. As shown in Figure 4.11, the tensor sparsification, decomposition and reconstruction can play a pivotal role in reducing the microstructural data size up to 90% with reconstruction accuracy over 94% using the Tucker decomposition technique while preserving the compositional and elastic-deformation information.

The discussion here shows that microstructure, within this framework, is the thermodynamic and morphological response to laser-controlled energy input. It evolves through coupled composition fields, order parameters, interfacial energies, and temperature-dependent material properties, and it manifests itself as changing phase fractions, meltpool shapes, intermetallic products, and interface morphologies. Because these structural states are both physically meaningful and computationally representable, they can be simulated through multiphysics phase-field models, encoded through tensor-based formats, and later predicted through machine learning architectures [1–5].

4.3 Methodology

The methodology developed in this dissertation provides the structural bridge between the physical processes governing $\mathscr{L}$-$\mathscr{M}$ interaction and the computational framework required for their quantification and prediction. As summarized in Figure 4.12, the framework begins with multiphysics phase-field modeling in **Eulerian frame**, where composition, temperature, phase-field, velocity, and pressure **fields** are solved together under laser irradiation. The model separates material response into **bulk** thermodynamic properties, **interfacial** parameters, and laser **heat-source** terms, while using thermodynamically consistent **interpolation** to transfer bulk properties across diffuse interfaces. This is essential because the $\mathscr{L}$-$\mathscr{M}$ interface is governed by coupled thermal, chemical, kinetic, and interfacial processes that cannot be captured through isolated modeling or purely data-driven approaches. The methodological framework consists of three interconnected layers. The first layer is multiphysics phase-field modeling, which generates thermodynamically consistent spatio-temporal microstructural data under laser irradiation. The second layer is thermodynamic tensor modeling, which encodes the high-dimensional simulation outputs into structured formats suitable for efficient storage, reconstruction, and learning. The third layer is the physics-informed machine learning framework, which uses the tensorized data to predict microstructural evolution, meltpool behavior, and interface dynamics. Together, these layers form the basis of a scalable computational framework that supports Digital Twin development for $\mathscr{L}$-$\mathscr{M}$ interaction [5].

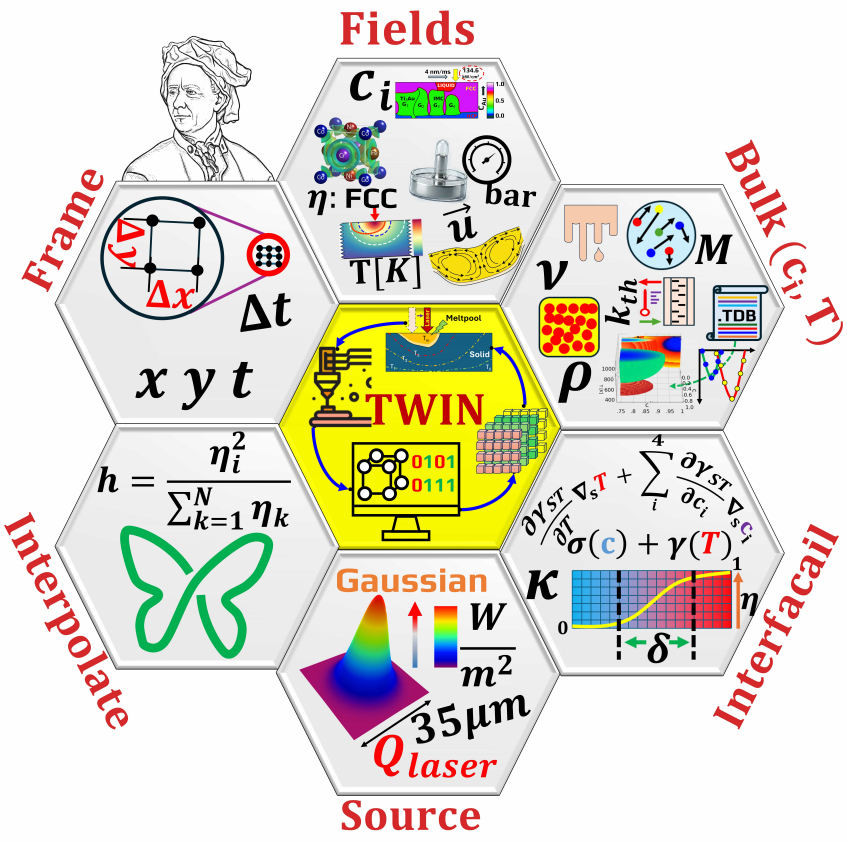


Figure 4.12 Graphical overview of the multiphysics phase-field methodology for laser-induced microstructure evolution in compositionally complex alloys. The framework combines field variables, bulk thermodynamic properties, interfacial parameters, laser heat-source terms, and thermodynamically consistent interpolation to generate physics-based data for tensor modeling, machine learning, and Digital Twin development. (Authors' own work)

4.3.1 Multiphysics modeling

The first stage of the methodology is the generation of high-fidelity microstructural evolution data through coupled physics simulations. These simulations form the foundation of the entire framework because they provide physically consistent descriptions of temperature evolution, phase transformation, interface motion, meltpool-flow dynamics.

Across the included studies, the phase-field method is used to model both conserved and non-conserved fields. The composition field evolves through diffusion-driven processes, while the phase field evolves according to thermodynamic driving forces derived from bulk and interfacial free-energy functions. In the *Ti-Cr* system **Article I**, this approach captures phase separation and elastic effects, generating microstructures with heterogeneous morphology and compositional variation. In the multicomponent $Cu_x(Ti\text{-}6Al\text{-}4V)_y$ system **Article II**, finite-element heat-transfer analysis and phase-field modeling are combined to describe laser-induced Ti_2Cu intermetallic growth in the Ti-6Al-4V matrix. In the *Ti-Au* system **Article IV**, the framework is extended to a non-isothermal, multiphase environment where LIQUID, FCC, HCP, and IMC phases coexist and evolve simultaneously under laser irradiation. In the unary *Au* system **Article V**, the model

further incorporates meltpool dynamics, laser beam profile variation, and flow behavior including Marangoni convection, allowing the simulation of both phase evolution and velocity fields.

The governing partial differential equations for heat transfer, phase evolution, diffusion, and fluid flow, together with temperature- and composition-dependent material properties, are tightly coupled and solved using the Finite Element Method within the **MOOSE** framework [49, 50]. This enables a consistent multiphysics description of the $\mathscr{L}$-$\mathscr{M}$ interaction across phase-separating, interdiffusing, and laser-processed alloy systems.

The key strength of the multiphysics framework lies in its thermodynamic consistency, where evolution is governed by temperature- and composition-dependent free-energy functions. This enables physically grounded phase transformations and interfacial reactions, including the growth of Ti_2Cu and Ti_3Au phases, as well as the lead-lag dynamics between thermal and phase fronts. As a result, the simulations produce not only geometric microstructure but a coupled spatio-temporal dataset comprising temperature, composition, phase distribution, and interface evolution. However, this level of physical fidelity comes with a significant computational cost, often referred to as the curse of dimensionality [28, 52]. The resulting high-dimensional datasets are difficult to store, analyze, and integrate into predictive models, motivating the second stage of the methodology.

4.3.2 Tensor Model

The second stage of the methodology addresses the representation of high-dimensional microstructural evolution data in a structured and computationally efficient form. The microstructural data obtained from phase-field simulations are encoded as multi-dimensional tensors that retain spatial, temporal, and physical correlations. In this formulation, microstructure is treated as a data object defined over space and time, with additional dimensions corresponding to physical variables such as phase, temperature, and composition. This unified representation preserves continuity across fields, unlike conventional approaches that store simulation outputs as independent snapshots.

In the *Ti-Cr* system (**Article I**), this approach is implemented through tensor sparsification, decomposition, and reconstruction. The simulation data are first organized as dense spatio-temporal tensors, which are then sparsified to reduce data size. Decomposition is performed using Canonical Polyadic (CP) and Tucker methods (Figure 4.13 **(a-b)**), followed by reconstruction using conjugate gradient optimization. The results show up to **28-fold data reduction** can be achieved while retaining approximately 94% of the microstructural information, with Tucker decomposition providing higher reconstruction fidelity at lower data densities. An important aspect of this representation is that the encoded data originate from free-energy-driven evolution and therefore retains physical meaning. This allows the tensor to act as a bridge between simulation and predictive modeling,

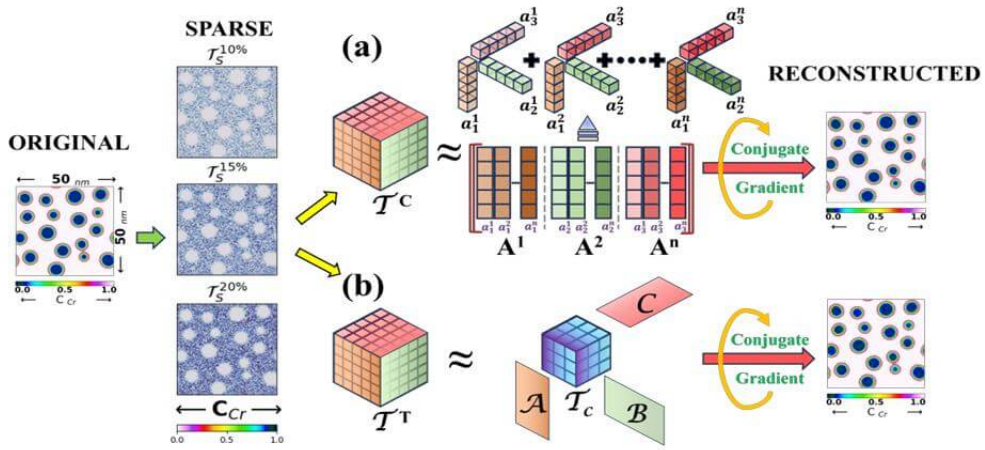


Figure 4.13 Schematics illustrate tensor decomposition and reconstruction from dense phase-field simulation tensor to sparse variants (10%, 15%, 20% of original size). **(a)** CP decomposition factors input $\mathscr{T}_C$ into rank-r matrices A^n. **(b)** Tucker decomposition breaks $\mathscr{T}_T$ into factor matrices A,B,C and a core tensor $\mathscr{T}_C$, similarly optimized. Rightmost column shows reconstructed slices (top: CP; bottom:Tucker) optimized iteratively via conjugate gradient method **[1]**.

rather than as a purely mathematical data structure. The resulting "*Thermodynamic Tensor Model*" provides a consistent framework for data storage, reconstruction, and subsequent learning tasks.

4.3.3 Physics-informed Conv-LSTM and U-Net frameworks

The third stage of the methodology focuses on machine learning models trained on tensorized outputs from multiphysics simulations. The purpose is to reduce the computational cost of predicting microstructural evolution while retaining the physical information carried by temperature, phase, composition, and interface fields. Three models are used in this dissertation: Conv-LSTM, U-Net, and an Attention-regularized surrogate model.

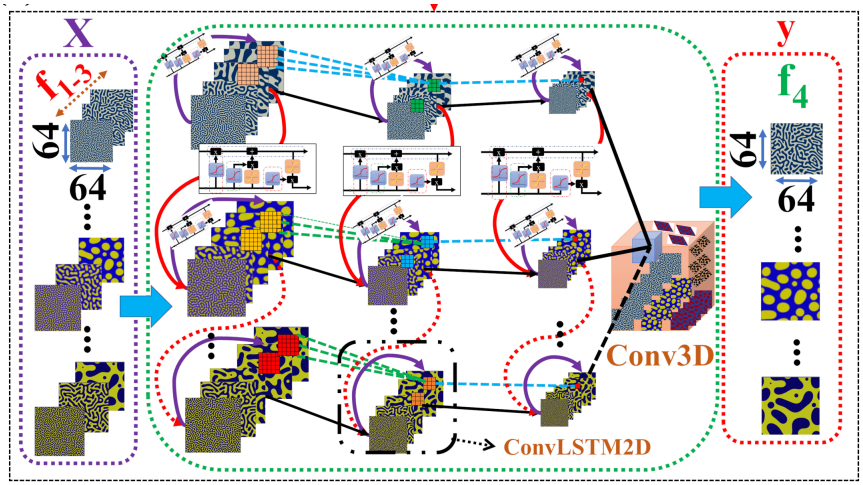


Figure 4.14 A complex model architecture featuring intertwined Convolutional and LSTM layers, forming a unique Conv-LSTM neural network. The model takes three consecutive frames from a microstructural evolution sequence as input and predicts the fourth frame, matching input dimensions. It processes multiple microstructural sequences in batches simultaneously, generating corresponding batches of the next frame as a 3D layer of convolved predictions **[3]**.

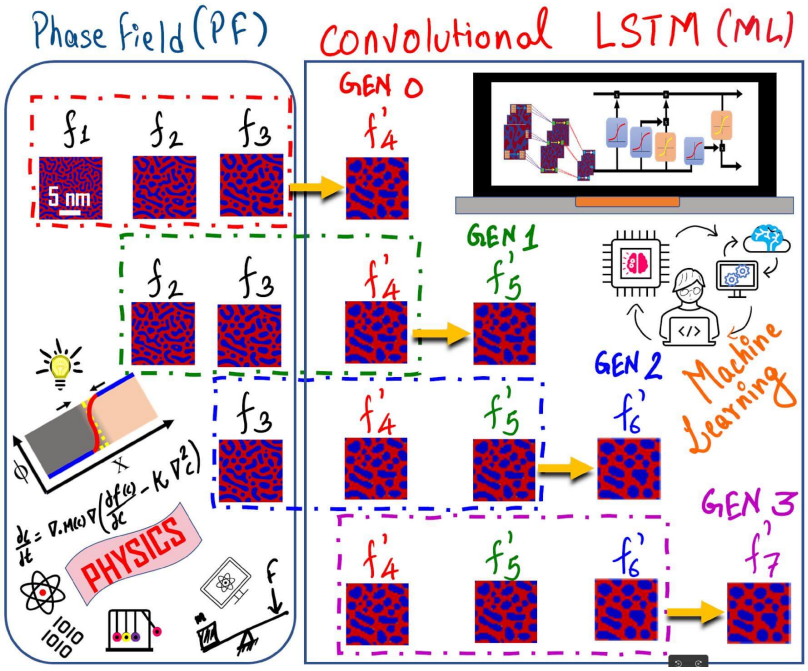


Figure 4.15 A schematic illustrating multi-generational microstructural prediction using a trained Conv-LSTM model. In generation zero (GEN 0), three phase-field-simulated frames are used to predict the fourth frame. In GEN 1, two simulated frames and one predicted frame are used to predict the next step. In GEN 2, the input further shifts to one simulated frame and two predicted frames. By GEN 3, all inputs are fully replaced by previously predicted frames, and the model predicts subsequent microstructural evolution without direct simulation input **[3]**.

The Conv-LSTM framework (**Article III**) is used for spatio-temporal prediction of microstructure evolution. In this model, phase-field simulation frames are treated as ordered temporal inputs, and the network predicts the next microstructural state while preserving spatial morphology, as shown in Figure 4.14. Its multi-generational form, presented in Figure 4.15, progressively replaces simulation-generated inputs with model-predicted frames. This tests whether the model can continue the evolution beyond the original simulation sequence without rapidly losing interfacial information. The prediction quality is summarized in Table 4.2, where the microstructural similarity index (μ_{SIM}) remains high across four generations for *Au-Pt*, *Cu-Mn*, and *Pd-Rh* alloy systems. Because the prediction is performed directly in the physical image space, the output can be evaluated using interface-sensitive descriptors such as μ_{SIM}, shape index, and blob detection.

Table 4.2 μ_{SIM} indices for Conv-LSTM predicted microstructures across four generations for different alloy systems (Au-Pt, Cu-Mn, Pd-Rh). The comparison demonstrates the ability of the model to preserve interfacial features during multi-generational prediction in manifest space **[3]**.

μ_{SIM}	**Au-Pt**	**Cu-Mn**	**Pd-Rh**
GEN 0	0.9943	0.917	0.976
GEN 1	0.9874	0.871	0.958
GEN 2	0.9806	0.829	0.941
GEN 3	0.9676	0.792	0.916

The U-Net framework (**Article V**) is used for phase and meltpool velocity prediction. As shown in Figure 4.16, the first model (**PhaseNet**), maps the temperature field to the phase distribution, while the second model (**VelNet**), uses temperature and predicted phase information to estimate the meltpool velocity field. This two-step structure connects laser-induced thermal history with both phase morphology and meltpool flow. Unlike a purely statistical mapping, the inputs and outputs are generated from coupled phase-field simulations, so the learned relation remains tied to the thermodynamic and kinetic behavior of the modeled system.

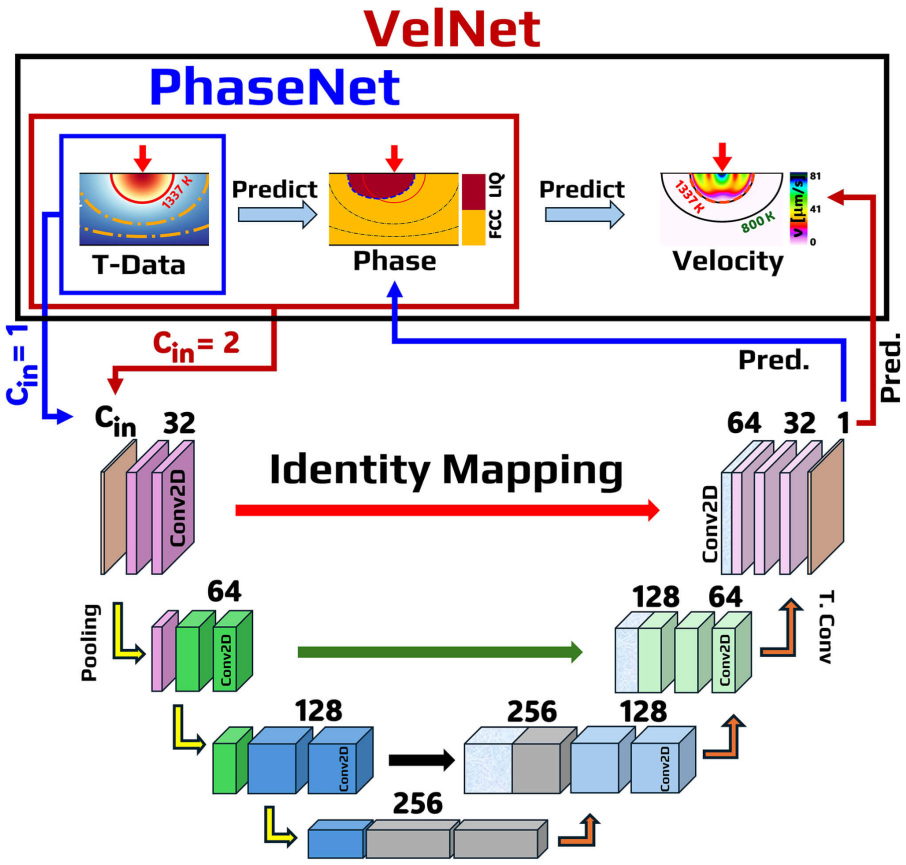


Figure 4.16 Schematic of the customized multi-step U-Net architectures for phase and velocity prediction. **PhaseNet** predicts phase distribution from temperature input, while **VelNet** predicts meltpool velocity using temperature and predicted phase. Both share an encoder-decoder structure, differing in input channels and training objectives **[5]**.

Beyond the Conv-LSTM and U-Net models, the same methodology also provides a pathway toward attention-based physics-informed prediction frameworks, as conceptually summarized in Figure 4.17. In this perspective, the prediction of a new laser-processing condition can be treated as a weighted information-transfer problem, where existing physics-based simulations guide the response at a target condition. The role of attention is not to replace the governing physics, but to organize available simulation data according to process similarity and thermodynamic relevance. Such a direction is consistent with the broader aim of this dissertation: to move from isolated phase-field simulations toward reusable, data-efficient, and physically interpretable Digital Twin components for $\mathscr{L}$-$\mathscr{M}$ interaction.

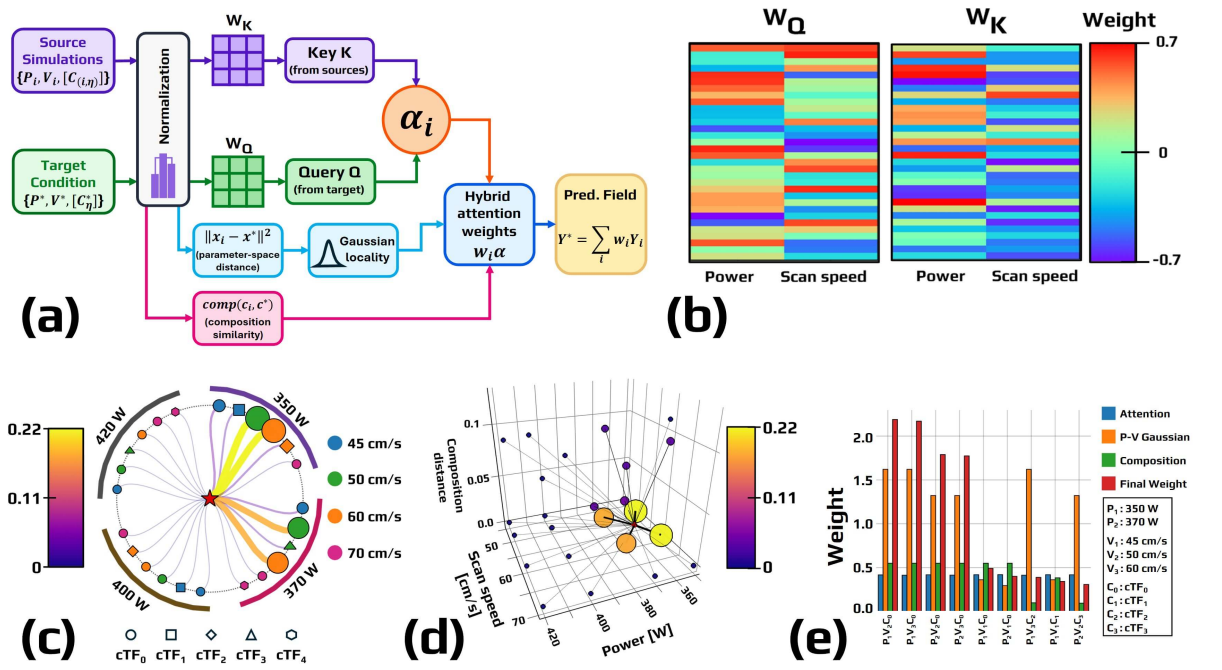


Figure 4.17 Perspective workflow for attention-based physics-informed prediction of laser-induced microstructural response. **(a)** Available simulation cases and a target processing condition are normalized and projected into a common comparison space. **(b)** Query and key projections provide a basis for estimating similarity between source and target conditions. **(c)** Source-to-target relevance can be visualized through weighted connections. **(d)** The position of target and source cases in process-parameter space supports locality-based comparison. **(e)** Final weights combine attention-based relevance with process-parameter proximity, providing a possible route for rapid prediction without repeating full multiphysics simulations. (Authors' own work)

4.3.4 Towards Digital Twins of materials models

The final stage integrates the physics-based, tensor-based, and machine learning components into a unified framework for predicting $\mathscr{L}$-$\mathscr{M}$ interaction. The phase-field model generates high-fidelity data that captures the underlying process physics, which is then organized into tensor form for efficient storage and transformation. This tensorized data is used to train machine learning models that learn the relationship between input fields, such as temperature, and output fields, such as phase distribution and meltpool velocity. Once trained, these models can predict microstructural evolution under new processing conditions without requiring full multiphysics simulations.

This framework is illustrated in Figure 4.18, where the Virtual Digital Twin consists of two hierarchical models: **MicroTwin**, which predicts meltpool morphology and phase from temperature, and **FlowTwin**, which uses this information to estimate velocity fields. Trained in phase-field data, the models operate on temperature inputs obtained from simulations. The predicted outputs are visualized and incorporated into a feedback loop that adjusts laser parameters through a WebApp interface, enabling real-time monitoring and control. The computational efficiency of this framework is summarized in Table 4.3, where the inference time is compared across different computing platforms, including embedded hardware (Raspberry Pi 4), workstation-level systems, and cloud-

based deployment. The results demonstrate that the model achieves sub-second prediction times across all platforms, confirming its suitability for real-time Digital Twin applications.

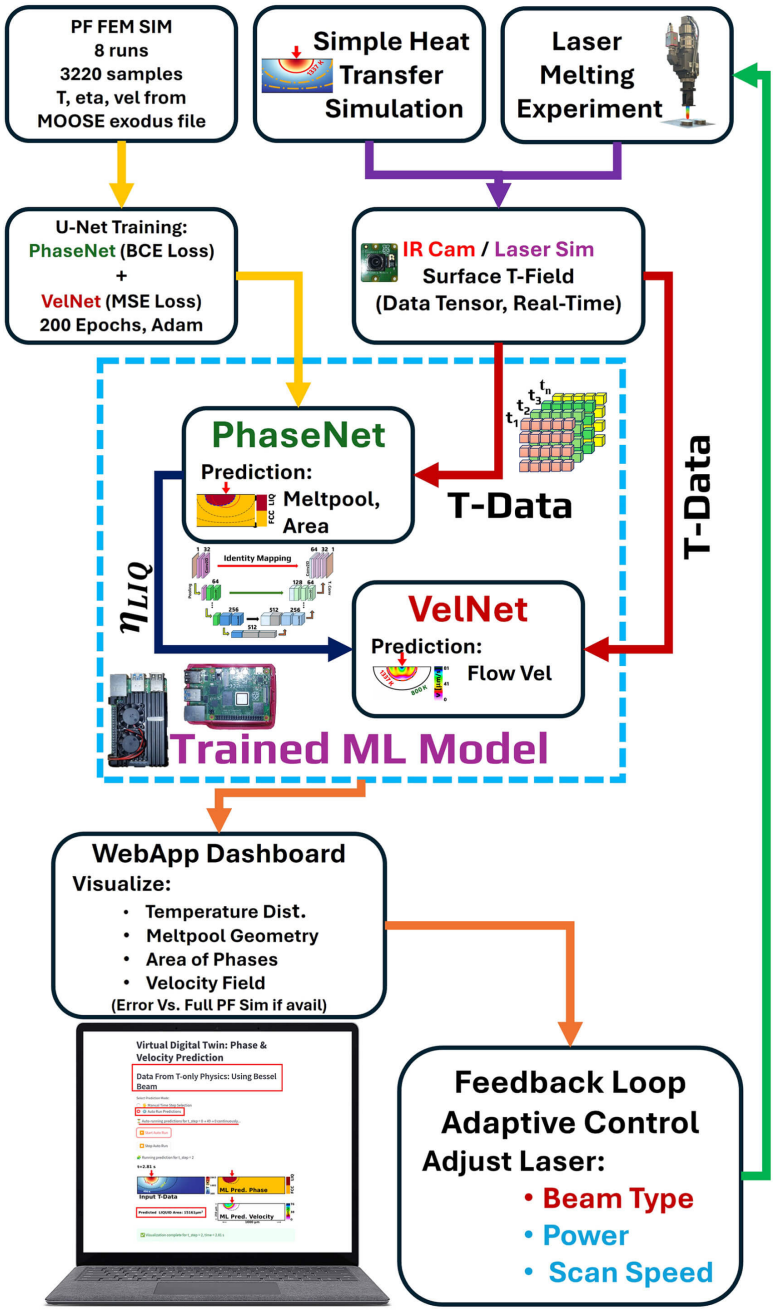


Figure 4.18 Flowchart of the Virtual Digital Twin framework for real-time melt-pool prediction and control using U-Net models via WebApp interface. Phase-field simulations provide training data for **MicroTwin** (PhaseNet), which predicts phase from temperature, and **FlowTwin** (VelNet), which predicts velocity using temperature and *MicroTwin* outputs [5].

Table 4.3 Comparison of inference time for the Virtual Digital Twin framework across different computing platforms showing sub-second prediction times for phase and velocity estimation [5].

	Inference Time
Raspberry Pi 4	≈0.265 s
Dell Precision 7920 Tower	≈0.192 s
Cloud Computing via Streamlit	≈0.397 s

This integrated framework combines physical fidelity from phase-field modeling, data efficiency from tensor representation, and predictive capability from machine learning. It establishes a consistent flow of information across stages, where laser parameters define the thermal field, the thermal field drives phase evolution, and the resulting microstructure is used for predictive modeling. As a result, the framework functions as a scalable Digital Twin for $\mathscr{L}$-$\mathscr{M}$ interaction, maintaining consistency with the underlying thermodynamic behavior.

4.4 Hierarchical determinants of $\mathscr{L}$-$\mathscr{M}$ Interaction

The $\mathscr{L}$-$\mathscr{M}$ interface evolves under the combined influence of external processing conditions and internal material response. Rather than treating all factors equally, a reduced set of dominant determinants that directly govern interface behavior. Based on the integrated framework developed in this work, these are grouped into three categories: (i) laser-side, (ii) material response, and (iii) interface-level in between. This classification emphasizes causality over description.

4.4.1 Laser-side control variables

Laser parameters define how energy is introduced into the system. Irradiance sets the magnitude of thermal input and determines meltpool size and reaction extent. Scan speed controls interaction time, governing the duration of thermally activated processes. Beam profile defines spatial distribution of energy, shaping thermal gradients and meltpool geometry. These variables act jointly to define the effective process window within which interfacial evolution occurs [4, 5].

Across the included studies, the specific laser variables differ depending on the alloy system, and intended physical response. The laser-side process window is defined using discrete combinations of laser power, irradiance, scan speed, and beam radius used to generate thermal, phase, velocity, and composition fields. A few laser-side parameter values used in the study are listed in Table 4.4.

Table 4.4 Laser power, irradiance, scan speed, and beam radius values used for the phase-field simulations and machine learning modeling **[2, 4, 5]**.

Parameter	**Values**
Laser power, P (mW)	25
Laser Irradiance, I (kW/cm^2)	0.244, 0.269, 150, 134.6
Scan speed, v (mm/s)	0.03, 200
Beam radius, r (μm)	0.12, 70, 122.5

A useful interpretation is that laser parameters define the accessible thermodynamic space. They determine the temperature-time conditions that can be reached and, consequently, which transformations are possible, without uniquely fixing the resulting microstructure.

4.4.2 Microstructure response variables

Material variables govern how the alloy system responds to the imposed thermal conditions. These variables include composition, thermodynamic stability, diffusion kinetics, and interfacial mobility. Composition defines the possible phase pathways, while the free-energy landscape determines which phases are thermodynamically favorable. In systems such as *Ti-Au* (**Article IV**) and $Cu_x(Ti\text{-}6Al\text{-}4V)_y$ (**Article II**), intermetallic formation is therefore controlled by the combined effect of chemical composition, free-energy stability, and laser-induced thermal history. However, thermodynamic stability alone is not sufficient to determine the final microstructure, because diffusion kinetics limit whether a phase can form and grow within the available thermal exposure time. This introduces an important constraint in $\mathscr{L}$-$\mathscr{M}$ interaction: thermal and chemical processes operate on different timescales. Heat transport is generally faster than mass diffusion, which creates a mismatch between the thermal front, phase front, and chemical diffusion front. This lag affects the location, extent, and morphology of interfacial reactions during laser processing [4]. Material variables therefore act as microstructure-side filters on the imposed laser input, determining which transformations can occur within the accessible processing window.

4.4.3 Numerically fingerprinting the interfacial dynamics

Interfacial evolution emerges from the coupled action of thermodynamic driving forces and diffusion kinetics, rather than purely geometric considerations. A key descriptor identified in this work is the lead-lag dynamics between thermal and phase fronts. Because phase evolution requires both thermodynamic driving force and mass transport, the phase boundary does not instantaneously follow the thermal field, resulting in a spatial and temporal offset that defines the effective interface position [4, 5]. This lag is a fundamental characteristic of non-isothermal microstructure evolution and directly influences meltpool-microstructure interaction. Its manifestation at the interface is reflected through geometric features such as curvature, thickness, and connectivity, which govern whether the morphology evolves smoothly or develops instabilities.

To quantify this behavior, the interface is characterized using geometric and image-based descriptors such as *phase area*, *interface thickness*, *shape index*, *blob structures*, and *microstructural similarity index* [1, 3]. These descriptors provide measurable representations of morphology while preserving spatial information at the interface level.

4.5 Multi-level quantification of $\mathscr{L}$-$\mathscr{M}$ Interface

The central objective of this dissertation is not only to simulate or predict microstructure evolution, but to **quantify the $\mathscr{L}$-$\mathscr{M}$ interface** in a consistent and physically grounded manner. Quantifi-

cation here refers to the ability to represent, measure, compare, and predict interface behavior across processing conditions and material systems. This requires a framework that connects thermodynamic variables, spatial morphology, and data-driven descriptors within a unified structure. The approach developed in this work defines interface quantification across four interconnected levels: (i) thermodynamic representation, (ii) field variables, (iii) geometric descriptors, and (iv) data-driven similarity measures. These levels form a hierarchy in which physical processes are progressively transformed into measurable quantities suitable for analysis and prediction.

4.5.1 Thermodynamic representation of the interface

At the most fundamental level, the interface is defined through thermodynamic fields derived from free-energy formulations. Bulk and interfacial free-energy densities govern phase stability and interface motion, while temperature and composition define the local thermodynamic state. In multiphase systems, the interface emerges as a region where competing phases evolve under a temperature-dependent free-energy landscape driven by energy gradients. This provides a physically consistent definition of the interface, but it is not directly measurable.

This thermodynamic definition is realized through continuous field variables obtained from phase-field simulations, including temperature, composition, phase fraction, and velocity. In this framework, the interface is a diffuse region, and its position is quantified through the spatial evolution of order parameters or phase fractions. This enables extraction of quantities such as meltpool boundaries, phase-front trajectories, and temporal effects including the positional lag between thermal and phase fronts.

For practical quantification, these fields are reduced to geometric and morphological descriptors such as meltpool depth and width, intermetallic layer thickness, phase fractions, and grain morphology [4, 5]. These descriptors link process conditions to microstructural outcomes and capture variations in interface geometry. In addition, local features such as curvature, grain boundaries, and spatial phase distribution distinguish microstructures with similar global characteristics but different interfacial structures. At the highest level of abstraction, the interface is encoded using data-driven descriptors that preserve spatial and structural information. These include microstructural similarity index, blob detection, (**Article I**), grayscale histogram features, and shape index (**Article III**). Unlike purely geometric measures, these descriptors capture both global agreement and local interfacial features, enabling rigorous comparison and evaluation of predictive models.

4.5.2 Tensor-based quantification and ML approaches

The tensor-based representation provides a unified structure for encoding microstructural evolution while preserving spatial, temporal, and physical correlations. The interface is implicitly embedded

within this representation through the evolving field variables. Tensor decomposition and reconstruction enable efficient handling of large datasets while retaining essential interfacial features [1]. The fidelity of this representation is evaluated using metrics such as root mean square error and microstructural similarity index, which quantify the preservation of interface morphology.

Building on this representation, machine learning models are used to predict interface evolution. Tensor-encoded data serve as inputs to predictive frameworks, such as U-Net architectures, where temperature fields are mapped to phase distribution and velocity fields [3, 5]. This establishes a direct link between thermal input and microstructural response, enabling prediction of interface dynamics under varying conditions.

The overall framework integrates multiple levels of representation into a unified pathway from thermodynamic driving forces to predictive modeling of interfacial behavior, with each level contributing a distinct role in interface quantification:

(i) Thermodynamic representation defines the driving forces for interface evolution

(ii) Field variables define its spatial and temporal evolution

(iii) Geometric descriptors define its measurable morphology

(iv) Data descriptors enable comparison and evaluation

(v) Tensor representation enables efficient storage and transformation

(vi) Machine learning enables prediction under new conditions

4.6 Major Findings

This section consolidates the key findings of the integrated framework developed in this chapter and aligns them with the scientific hypothesis defined in Chapter III. The main finding is that interface evolution can be quantified only when laser processing, thermal history, composition-dependent thermodynamics, morphology, tensor representation, and predictive learning are treated as a connected information pathway rather than as separate modeling outputs.

4.6.1 Kinematics of interface attributes

The multiphysics phase-field simulations show that $\mathscr{L}$-$\mathscr{M}$ interaction is governed by coupled thermal, chemical, and interfacial processes. The thermal field defines meltpool geometry and transformation conditions, while the free-energy landscape controls phase stability and interface motion. In both *Ti-Au* and $Cu_x(Ti\text{-}6Al\text{-}4V)_y$ systems, intermetallic formation is driven by the coupled influence of temperature and composition under non-isothermal conditions.

A key finding is the sensitivity of interface evolution to the formulation of the free-energy function. TDB-based free-energy expressions produce a gradual and physically consistent increase in driving

force (ramp-up rate 'Λ'), whereas fitted expressions exhibit a steeper response at elevated temperatures, leading to accelerated non-physical phase evolution. This difference alters transformation rates, interface propagation, and meltpool morphology. As presented in **Article V**, TDB-based formulations capture realistic evolution pace, while fitted models overestimate temporal progression. Additionally, a consistent lead-lag between thermal and phase fronts is observed, confirming that heat transfer and phase transformation operate on different timescales. This lag, arising from the disparity between thermal and chemical diffusion, directly influences interface location and growth [4, 5]. It demonstrates that interface evolution cannot be inferred from temperature fields alone.

4.6.2 Compact representation of $\mathscr{M}_{Global}$ and $\mathscr{M}_{Local}$

The tensor-based representation shows that high-dimensional microstructural data can be compressed and reconstructed while preserving essential spatial and interfacial features. Sparsification and decomposition achieve significant data reduction with minimal loss of structural information. Tucker decomposition consistently yields higher reconstruction fidelity than CP decomposition, particularly at moderate sparsity levels. These results confirm that tensor representation retains both global morphology and local interface characteristics, allowing microstructure to be treated as a structured spatio-temporal dataset rather than independent snapshots [1].

4.6.3 Portable information at manifest space

The machine learning frameworks predict microstructural evolution and meltpool behavior with high accuracy while preserving spatial fidelity. The Conv-LSTM model enables multi-generational prediction of microstructure evolution, maintaining interface morphology as verified by microstructural similarity index, blob detection, and shape-based metrics. The U-Net framework extends this capability by mapping temperature fields directly to phase distribution and velocity. A key result is that prediction is performed in physically interpretable manifest space rather than latent representations. This ensures that interface features remain measurable and comparable, linking model predictions directly to physical microstructure [3, 5].

4.6.4 $\mathscr{L}$-$\mathscr{M}$ information retention

The integration of multiphysics modeling, tensor representation, and machine learning establishes a consistent framework for both simulation and prediction of $\mathscr{L}$-$\mathscr{M}$ interaction. This framework preserves the flow of information from laser parameters to thermal fields, from thermal fields to microstructure, and from microstructure to predictive models. It demonstrates the key characteristics of a Digital Twin system: physical consistency, data efficiency, and predictive capability. The use of tensor representation ensures that multiphysics information is retained during the transition from

simulation to learning, enabling scalable and physically grounded prediction of interface behavior. Beyond predictive capability, the framework supports near real-time autonomous inference, where microstructural response is continuously estimated from temperature inputs without requiring repeated multiphysics simulations. The demonstrated sub-second inference times and deployment across embedded, workstation, and cloud platforms indicate that the system operates beyond a purely conceptual stage and approaches a functional Digital Twin implementation [5]. This positions the framework within an intermediate Technological Readiness Level (TRL), where core components are validated in a controlled computational environment and integrated into a feedback-enabled predictive pipeline. Within this setting, the framework provides a foundation for conditional automation in additive manufacturing, enabling adaptive control based on real-time inputs such as temperature, meltpool morphology, and phase evolution through continuous prediction and feedback, supported by phase-field simulations and machine learning architectures as the core building blocks for data-driven process control.

4.7 Integrated outcomes

The findings presented in this chapter demonstrate that the $\mathscr{L}$-$\mathscr{M}$ interface can be systematically represented, quantified, and predicted through an integrated framework combining thermodynamic modeling, tensor representation, multiphysics simulation, and machine learning. This directly addresses the objectives defined in Chapter II: multiphysics simulations capture the governing thermal, chemical, and interfacial processes; tensor representation provides a structured form for microstructural evolution data; and machine learning enables scalable prediction while preserving spatial and interface-level information.

At a broader level, the results show that the interface is not an isolated geometrical feature, but a dynamic outcome of coupled thermal input, material response, and local morphology. By linking these components within a consistent framework, the dissertation converts complex microstructural evolution into measurable, compressible, reconstructable, and predictive quantities. This establishes the methodological basis for treating laser-induced microstructure evolution as a physically meaningful information pathway rather than as separate simulation outputs.

CHAPTER V

CONCLUSIONS AND FUTURE OUTLOOKS

5.1 Conclusion

This dissertation addressed the problem of representing, quantifying, compressing, reconstructing, and predicting the laser-microstructure ($\mathscr{L}$-$\mathscr{M}$) interface in alloy systems. The work showed that this interface is not only a geometrical boundary between phases, but a dynamic region where thermal history, composition, free-energy landscape, diffusion, interfacial reactions, and meltpool flow jointly determine microstructural evolution.

The phase-field studies demonstrated that laser-induced interface evolution is governed by coupled thermal, chemical, and interfacial processes. In the $Cu_x(Ti\text{-}6Al\text{-}4V)_y$ and *Ti-Au* systems, the combination of finite-element heat-transfer analysis, non-isothermal phase-field modeling, and thermodynamic free-energy descriptions showed that intermetallic formation depends on local thermal exposure, composition, and diffusion kinetics. The observed mismatch between thermal and phase fronts confirmed that temperature fields alone are insufficient to describe interface motion during laser processing.

The tensor-based part of the work showed that microstructural evolution can be converted into a structured and compact representation without losing essential interfacial information. By applying sparsification, decomposition, and reconstruction, the Thermodynamic Tensor Representation enabled high-dimensional microstructural data to be treated as a portable object for storage, analysis, and prediction while preserving global morphology and local interface features.

The machine learning studies established that microstructural evolution can be predicted directly in manifest space. Conv-LSTM models enabled multi-generational prediction of evolving microstructures, while U-Net based MicroTwin and FlowTwin models connected thermal fields to phase and velocity responses in laser-processed meltpool systems. These models retained spatial interpretability and allowed prediction quality to be evaluated through interface-sensitive descriptors rather than only global error metrics.

Overall, the dissertation establishes a computational route toward Digital Twin development for laser-processed multicomponent alloys. The main contribution is the integration of thermodynamically consistent simulation, tensor-based microstructural representation, and physics-informed prediction into a single framework for describing the $\mathscr{L}$-$\mathscr{M}$ interface. The five included publications together demonstrate that microstructural evolution can be analyzed not only as a sequence of simulation images, but as a physically meaningful information pathway linking laser input, thermodynamic response, interface morphology, and predictive learning.

5.2 Future outlook

The results of this dissertation provide a foundation for extending thermodynamic tensor representation, multiphysics phase-field modeling, and physics-informed learning toward more adaptive Digital Twin frameworks. The immediate future direction is to increase the scale, transferability, and practical applicability of the developed methodology. This includes larger simulation domains, longer processing times, broader process windows, and a wider range of alloy compositions. Such extensions are important because $\mathscr{L}$-$\mathscr{M}$ interaction is controlled not only by the imposed process parameters, but also by material-side variables such as thermodynamic stability, diffusion kinetics, and composition-dependent transport behavior.

A key future direction is the development of composition-aware prediction models for multicomponent alloy processing. In such systems, the microstructural response is not determined only by laser power, scan speed, or beam shape. Even small differences in initial alloy composition may alter free-energy stability, meltpool morphology, phase evolution, and interface motion. Therefore, future models should treat composition as an active input variable rather than a fixed material descriptor. This would allow thermodynamic data, phase-field simulations, and learned mappings to be combined for rapid exploration of process-composition windows. Current ongoing work explores this direction by extending the physics-informed learning concept toward multicomponent laser processing. In this perspective, the model architecture discussed in Figure 4.17 provides a route for using existing simulation data to estimate the response at new processing conditions. The prediction problem can be interpreted as a weighted information-transfer task, where available physics-based simulations guide the response at a target laser condition. This type of approach is especially relevant for multicomponent alloys, because composition introduces an additional material-side variable that can modify the effective thermal and microstructural response.

Figure 5.1 presents preliminary results that indicate an outlook toward this future direction. The current phase-field model and its AI-surrogate are useful for predicting spatio-temporal fields and meltpool-related properties in medium-entropy alloy systems with principal elements $N < 5$. However, the direct extension of such models to high entropy alloys (HEAs) design ($N > 6$) remains challenging because the composition state space becomes significantly larger with increasing degrees of freedom, even though the temperature state space can be resolved more straightforwardly. Therefore, the present medium-entropy alloy-based model can serve as a gateway framework for developing more advanced future models for additively manufactured HEAs once the challenges associated with composition-space design are addressed. The temperature profiles show that alloy systems containing the same principal elements, but with small differences in their initial composition, can produce different thermal responses under comparable laser-processing conditions. The

peak-temperature variation and meltpool-depth comparison further indicate that composition can influence the effective thermal history and meltpool morphology. These observations support the broader conclusion of the dissertation that the $\mathscr{L}$-$\mathscr{M}$ interface is governed by both process-side variables and material-side variables.

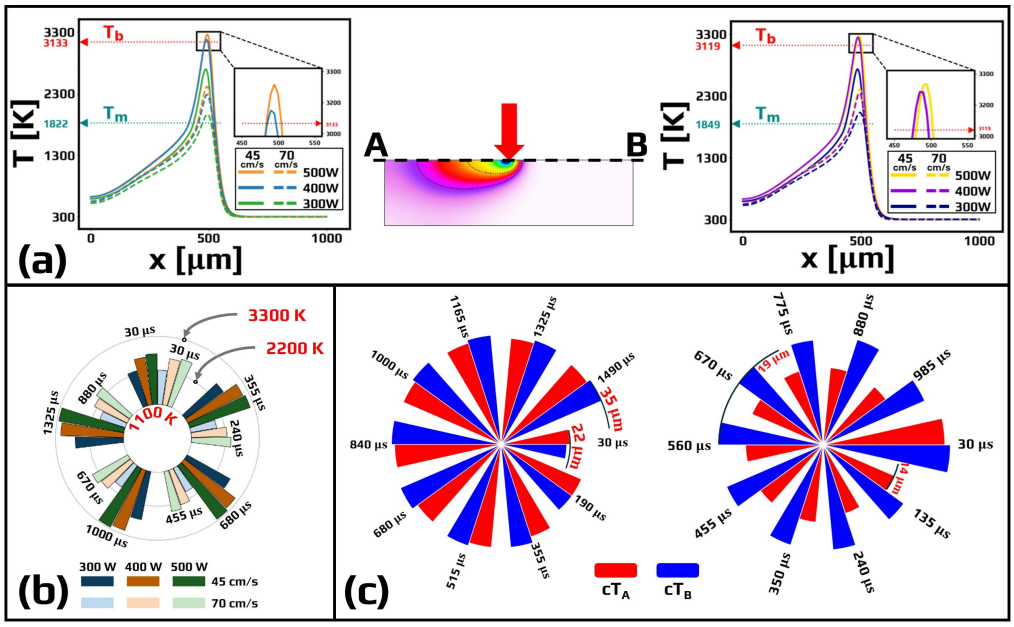


Figure 5.1 Future outlook on composition-aware thermal response and meltpool morphology prediction. An AI-surrogate of a composition-state-space-aware meltpool computation model, developed for a medium-entropy alloy-type system ($N < 5$), can serve as a gateway foundation for the future design of additively manufactured high entropy alloys ($N > 6$), where N is the number of principal alloying elements. **(a)** Temperature profiles along line AB for different laser powers and scan speeds, compared for two slightly different initial composition states of the same multicomponent alloy system. **(b)** Temporal peak-temperature variation under different laser conditions. **(c)** Meltpool-depth rose diagrams comparing the two initial compositions at constant laser power and different scan speeds. (Authors' own work)

Another important future direction is the coupling of simulation-driven models with experimental sensing and uncertainty quantification. The machine learning models developed in this dissertation are trained primarily on simulation-generated data. Although these data are physically grounded, experimental process monitoring would introduce additional information related to powder-bed variability, surface condition, and measurement noise. Integrating such data with thermodynamic tensor representations would make the Digital Twin framework more robust and closer to practical laser powder bed fusion applications. The Tensor Model can also be further developed into an adaptive data structure for active learning. Instead of storing simulation outputs only after computation, future workflows could use tensor reconstruction error, interface descriptors, and uncertainty estimates to decide where new phase-field simulations are most needed. In this way, the tensor representation would become not only a compression and reconstruction tool, but also a guide for selecting new simulations in high-dimensional process-composition space.

These future directions do not change the main contribution of the thesis, which is established through the included published articles. Rather, they show how the completed thermodynamic tensor and multiphysics learning framework can be extended as machine learning methods and Digital Twin concepts continue to evolve. A long-term perspective is the development of flexible, composition-aware, and uncertainty-aware Digital Twin tools in which thermodynamic databases, phase-field simulations, tensor representations, and learned models operate together to rapidly explore laser-processing conditions for multicomponent alloys.

REFERENCES

Constituent publications forming the scientific framework of the dissertation:

[1] U. Subedi, N. Moelans, T. Tański, A. Kunwar, Rapid portabilization of elasto-chemical evolution data for dental Ti-Cr alloy microstructure through sparsification and tensor computation, Scripta Materialia 244 (2024) 116027. doi:10.1016/j.scriptamat.2024.116027.
URL https://www.sciencedirect.com/science/article/pii/S1359646224000629

[2] H. B. Mamo, U. Subedi, T. Poloczek, M. Adamiak, A. N. S. Appiah, M. Skonieczna, P. M. Nuckowski, Y. Geng, B. Haldar, A. Kunwar, Prototyping Ti2Cu intermetallic grain growth heterogeneously in Ti6Al4V matrix through laser additive manufacturing, Materials & Design 246 (2024) 113312. doi:10.1016/j.matdes.2024.113312.
URL https://www.sciencedirect.com/science/article/pii/S0264127524006877

[3] U. Subedi, N. Moelans, T. Tański, A. Kunwar, Foretelling microstructural interface with multi-generational convolutional-LSTM framework, Engineering with Computers 41 (4) (2025) 2593–2617. doi:10.1007/s00366-025-02117-z.
URL https://link.springer.com/article/10.1007/s00366-025-02117-z

[4] U. Subedi, N. Moelans, T. Tański, A. Kunwar, A non-isothermal multi-phase field approach to model the meltpool and IMC grains interaction in Ti-Au material, Computational Materials Science 255 (2025) 113875. doi:10.1016/j.commatsci.2025.113875.
URL https://www.sciencedirect.com/science/article/pii/S0927025625002186

[5] U. Subedi, A. Bhattarai, N. Moelans, T. Tański, A. Kunwar, Spatiotemporally learning the morphological and dynamic features of Au meltpool under different heat source types with phase-field informed U-Net framework, Computational Materials Science 263 (2026) 114456. doi:10.1016/j.commatsci.2025.114456.
URL https://www.sciencedirect.com/science/article/pii/S0927025625007992

Supplementary bibliography:

[6] H. L. Wei, J. Mazumder, T. DebRoy, Evolution of solidification texture during additive manufacturing, Scientific Reports 5 (2015) 16446. doi:10.1038/srep16446.
URL https://www.nature.com/articles/srep16446

[7] J. Romano, L. Ladani, M. Sadowski, Thermal Modeling of Laser Based Additive Manufacturing Processes within Common Materials, Procedia Manufacturing 1 (2015) 238–250.

doi:10.1016/j.promfg.2015.09.012.
URL https://www.sciencedirect.com/science/article/pii/S2351978915010124

[8] B. S. Kim, N. Lee, S. Thota, T. Gemming, H. H. Cho, Effects of radiative local heating on metal solidification during selective laser melting for additive manufacturing, Applied Surface Science 496 (2019) 143594. doi:10.1016/j.apsusc.2019.143594.
URL https://www.sciencedirect.com/science/article/pii/S0169433219323918

[9] Y. Huang, M. Ansari, H. Asgari, M. H. Farshidianfar, D. Sarker, M. B. Khamesee, E. Toyserkani, Rapid prediction of real-time thermal characteristics, solidification parameters and microstructure in laser directed energy deposition (powder-fed additive manufacturing), Journal of Materials Processing Technology 274 (2019) 116286. doi:10.1016/j.jmatprotec.2019.116286.
URL https://www.sciencedirect.com/science/article/pii/S0924013619302584

[10] S. Liu, M. Lee, C. Choi, K. Shin, Effect of additive manufacturing of SUS316L using selective laser melting, Journal of Materials Research and Technology 24 (2023) 9824–9833. doi:10.1016/j.jmrt.2023.05.160.
URL https://linkinghub.elsevier.com/retrieve/pii/S2238785423011262

[11] M. Parsazadeh, S. Sharma, N. Dahotre, Towards the next generation of machine learning models in additive manufacturing: A review of process dependent material evolution, Progress in Materials Science 135 (2023) 101102. doi:10.1016/j.pmatsci.2023.101102.
URL https://www.sciencedirect.com/science/article/pii/S0079642523000348

[12] N. Moelans, B. Blanpain, P. Wollants, An introduction to phase-field modeling of microstructure evolution, Calphad 32 (2) (2008) 268–294. doi:https://doi.org/10.1016/j.calphad.2007.11.003.
URL https://www.sciencedirect.com/science/article/pii/S0364591607000880

[13] S. Yang, J. Zhong, J. Wang, L. Zhang, G. Kaptay, OpenIEC: an open-source code for interfacial energy calculation in alloys, Journal of Materials Science 54 (2019) 10297–10311. doi:10.1007/s10853-019-03639-w.
URL https://link.springer.com/article/10.1007/s10853-019-03639-w

[14] B. Mallia, P. A. Dearnley, The corrosion-wear response of Cr-Ti coatings, Wear 263 (1-6 SPEC. ISS.) (2007) 679–690. doi:10.1016/j.wear.2006.12.058.
URL https://linkinghub.elsevier.com/retrieve/pii/S0043164807003754

[15] W. F. Ho, T. Y. Chiang, S. C. Wu, H. C. Hsu, Mechanical properties and deformation behavior of cast binary Ti-Cr alloys, Journal of Alloys and Compounds 468 (1-2) (2009) 533–538.

doi:10.1016/j.jallcom.2008.01.046.
URL https://linkinghub.elsevier.com/retrieve/pii/S0925838808001011

[16] S. Wang, Z. Ma, Z. Liao, J. Song, K. Yang, W. Liu, Study on improved tribological properties by alloying copper to CP-Ti and Ti–6Al–4V alloy, Materials Science and Engineering: C 57 (2015) 123–132. doi:10.1016/j.msec.2015.07.046.
URL https://linkinghub.elsevier.com/retrieve/pii/S0928493115302265

[17] D. Xu, T. Wang, Z. Lu, Y. Wang, B. Sun, S. Wang, Q. Fu, Z. Bi, S. Geng, Ti-6Al-4V-5Cu synthesized for antibacterial effect in vitro and in vivo via contact sterilization, Journal of Materials Science & Technology 90 (2021) 133–142. doi:10.1016/j.jmst.2021.03.007.
URL https://linkinghub.elsevier.com/retrieve/pii/S1005030221002863

[18] U. Tariq, R. Joy, S.-H. Wu, M. A. Mahmood, A. W. Malik, F. Liou, A state-of-the-art digital factory integrating digital twin for laser additive and subtractive manufacturing processes, Rapid Prototyping Journal 29 (10) (2023) 2061–2097. doi:10.1108/RPJ-03-2023-0113.
URL https://doi.org/10.1108/RPJ-03-2023-0113

[19] X. Gong, K. Chou, Phase-Field Modeling of Microstructure Evolution in Electron Beam Additive Manufacturing, JOM 67 (2015) 1176–1182. doi:10.1007/s11837-015-1352-5.
URL http://link.springer.com/10.1007/s11837-015-1352-5

[20] D. Liu, Y. Wang, Mesoscale multi-physics simulation of rapid solidification of Ti-6Al-4V alloy, Additive Manufacturing 25 (2019) 551–562. doi:10.1016/j.addma.2018.12.005.
URL https://linkinghub.elsevier.com/retrieve/pii/S2214860417306139

[21] S. Sahoo, K. Chou, Phase-field simulation of microstructure evolution of Ti–6Al–4V in electron beam additive manufacturing process, Additive Manufacturing 9 (2016) 14–24. doi:10.1016/j.addma.2015.12.005.
URL https://linkinghub.elsevier.com/retrieve/pii/S2214860415300051

[22] Y. Yang, O. Ragnvaldsen, Y. Bai, M. Yi, B. X. Xu, 3D non-isothermal phase-field simulation of microstructure evolution during selective laser sintering, npj Computational Materials 5 (1) (2019) 81. doi:10.1038/s41524-019-0219-7.
URL https://www.nature.com/articles/s41524-019-0219-7

[23] N. Nohira, W.-T. Chiu, M. Tahara, H. Hosoda, Microstructural changes and mechanical property response to aging heat treatment in hypereutectoid Ti-Au-Mo biomedical alloys, Materials Science and Engineering: A 912 (2024) 146956. doi:10.1016/j.msea.2024.146956.
URL https://www.sciencedirect.com/science/article/pii/S0921509324008876

[24] E. Svanidze, T. Besara, M. Fevsi Ozaydin, C. S. Tiwary, J. K. Wang, S. Radhakrishnan,

S. Mani, Y. Xin, K. Han, H. Liang, T. Siegrist, P. M. Ajayan, E. Morosan, High hardness in the biocompatible intermetallic compound b-Ti3Au, Science Advances 2 (7) (jul 2016). doi:10.1126/sciadv.1600319.
URL https://www.science.org/doi/10.1126/sciadv.1600319

[25] C. Y. Tan, C. Wen, H. Q. Ang, Influence of laser parameters on the microstructures and surface properties in laser surface modification of biomedical magnesium alloys, Journal of Magnesium and Alloys 12 (2024) 72–97. doi:10.1016/j.jma.2023.12.008.
URL https://www.sciencedirect.com/science/article/pii/S2213956724000331

[26] D. Wang, J. Lv, Z. Liu, L. Liu, Y. Wei, C. Chang, W. Zhou, Y. Zhang, C. Han, Interface Optimization, Microstructural Characterization, and Mechanical Performance of CuCrZr/GH4169 Multi-Material Structures Manufactured via LPBF-LDED Integrated Additive Manufacturing, Materials 18 (2025) 2206. doi:10.3390/ma18102206.
URL https://www.mdpi.com/1996-1944/18/10/2206

[27] D. Gu, Laser Additive Manufacturing (AM): Classification, Processing Philosophy, and Metallurgical Mechanisms, in: Laser Additive Manufacturing of High-Performance Materials, Springer Berlin Heidelberg, Berlin, Heidelberg, 2015, pp. 15–71. doi:10.1007/978-3-662-46089-4_2.
URL https://link.springer.com/10.1007/978-3-662-46089-4_2

[28] Y. A. Coutinho, N. Vervliet, L. D. Lathauwer, N. Moelans, Combining thermodynamics with tensor completion techniques to enable multicomponent microstructure prediction, npj Computational Materials 6 (2020) 2. doi:10.1038/s41524-019-0268-y.
URL https://www.nature.com/articles/s41524-019-0268-y

[29] R. Darabi, E. Azinpour, A. Reis, J. C. de Sa, Multi-scale Multi-physics Phase-field coupled Thermo-mechanical approach for modeling of powder bed fusion process, Applied Mathematical Modelling 122 (2023) 572–597. doi:10.1016/j.apm.2023.06.021.
URL https://linkinghub.elsevier.com/retrieve/pii/S0307904X23002767

[30] C. Hu, S. Martin, R. Dingreville, Accelerating phase-field predictions via recurrent neural networks learning the microstructure evolution in latent space, Computer Methods in Applied Mechanics and Engineering 397 (2022) 115128. doi:10.1016/j.cma.2022.115128.
URL https://linkinghub.elsevier.com/retrieve/pii/S0045782522003097

[31] A. A. Kazemzadeh Farizhandi, M. Mamivand, Spatiotemporal prediction of microstructure evolution with predictive recurrent neural network, Computational Materials Science 223 (2023) 112110. doi:10.1016/j.commatsci.2023.112110.

URL https://linkinghub.elsevier.com/retrieve/pii/S0927025623001040

[32] I. Steinbach, F. Pezzolla, B. Nestler, M. Seeßelberg, R. Prieler, G. Schmitz, J. Rezende, A phase field concept for multiphase systems, Physica D: Nonlinear Phenomena 94 (1996) 135–147. doi:10.1016/0167-2789(95)00298-7.
URL https://www.sciencedirect.com/science/article/pii/0167278995002987

[33] N. Moelans, B. Blanpain, P. Wollants, An introduction to phase-field modeling of microstructure evolution, Calphad: Computer Coupling of Phase Diagrams and Thermochemistry 32 (2) (2008) 268–294. doi:10.1016/j.calphad.2007.11.003.
URL https://linkinghub.elsevier.com/retrieve/pii/S0364591607000880

[34] B. Nestler, A. Choudhury, Phase-field modeling of multi-component systems, Current Opinion in Solid State and Materials Science 15 (2011) 93–105. doi:10.1016/j.cossms.2011.01.003.
URL https://www.sciencedirect.com/science/article/abs/pii/S1359028611000040

[35] R. Qin, E. Wallach, A phase-field model coupled with a thermodynamic database, Acta Materialia 51 (2003) 6199–6210. doi:10.1016/S1359-6454(03)00443-9.
URL https://www.sciencedirect.com/science/article/pii/S1359645403004439

[36] S. Kavousi, A. Gates, L. Jin, M. A. Zaeem, A temperature-dependent atomistic-informed phase-field model to study dendritic growth, Journal of Crystal Growth 579 (2022) 126461. doi:10.1016/j.jcrysgro.2021.126461.
URL https://www.sciencedirect.com/science/article/pii/S002202482100436X

[37] A. Kunwar, J. Hektor, S. Nomoto, Y. A. Coutinho, N. Moelans, Combining multi-phase field simulation with neural network analysis to unravel thermomigration accelerated growth behavior of Cu6Sn5 IMC at cold side Cu–Sn interface, International Journal of Mechanical Sciences 184 (2020) 105843. doi:10.1016/j.ijmecsci.2020.105843.
URL https://linkinghub.elsevier.com/retrieve/pii/S0020740320314466

[38] O. Bialas, A. N. Appiah, M. Wala, A. Kunwar, A. Woźniak, P. M. Nuckowski, W. Simka, P. Råback, M. Adamiak, Laser assisted fabrication of mechanochemically robust Ti3Au intermetallic at Au-Ti interface, Engineering Science and Technology, an International Journal 42 (2023) 101413. doi:10.1016/j.jestch.2023.101413.
URL https://linkinghub.elsevier.com/retrieve/pii/S2215098623000903

[39] S. Wang, Z. Chen, R. Chen, Z. Wu, Y. Jia, W. Zhang, Y. Wang, W. Liu, Y. Zhao, R. Shi, et al., Superior strength-ductility synergy in additively manufactured CoCrFeNi high-entropy alloys with multi-scale hierarchical microstructure, Journal of Alloys and Compounds 1006 (2024)

176268. doi:10.1016/j.jallcom.2024.176268.
URL https://www.sciencedirect.com/science/article/pii/S092583882402855X

[40] O. Bialas, A. Kunwar, A. Taratuta, M. Skonieczna, K. Matus, M. Adamiak, Surface Engineering of Ti13Zr13Nb Biomaterial Alloy with Gold Via Laser Melting for Enhanced Biocompatibility and Functional Performance, Metallurgical and Materials Transactions A 56 (2025) 2235–2251. doi:10.1007/s11661-025-07763-y.
URL https://link.springer.com/article/10.1007/s11661-025-07763-y

[41] A. Kunwar, E. Yousefi, X. Zuo, Y. Sun, D. Seveno, M. Guo, N. Moelans, Multi-phase field simulation of Al3Ni2 intermetallic growth at liquid Al/solid Ni interface using MD computed interfacial energies, International Journal of Mechanical Sciences 215 (2022) 106930. doi:10.1016/j.ijmecsci.2021.106930.
URL https://www.sciencedirect.com/science/article/pii/S0020740321006408https://linkinghub.elsevier.com/retrieve/pii/S0020740321006408

[42] Z. Chafia, J. Yvonnet, J. Bleyer, S. Vincent, S. E. Ouafa, Massively parallel phase field fracture simulations on supercomputers: towards multi-billion degree-of-freedom computations, Advanced Modeling and Simulation in Engineering Sciences 11 (2024) 25. doi:10.1186/s40323-024-00280-4.
URL https://link.springer.com/article/10.1186/s40323-024-00280-4

[43] H. Razavi, N. Moelans, Physics-informed GCN-LSTM framework for long-term forecasting of 2D and 3D microstructure evolution, npj Computational Materials (4 2026). doi:10.1038/s41524-026-01999-x.
URL https://www.nature.com/articles/s41524-026-01999-x

[44] X. Chen, Y. Chen, N. Saunier, L. Sun, Scalable low-rank tensor learning for spatiotemporal traffic data imputation, Transportation Research Part C: Emerging Technologies 129 (2021) 103226. doi:10.1016/j.trc.2021.103226.
URL https://www.sciencedirect.com/science/article/pii/S0968090X21002400

[45] Y. chen Liu, S. yu Yen, S. hsiang Chu, S. kang Lin, M.-H. Tsai, Mechanical and thermodynamic data-driven design of Al-Co-Cr-Fe-Ni multi-principal element alloys, Materials Today Communications 26 (2021) 102096. doi:10.1016/j.mtcomm.2021.102096.
URL https://www.sciencedirect.com/science/article/pii/S235249282100088X

[46] K. Hareharen, T. Panneerselvam, R. R. Mohan, Improving the performance of machine learning model predicting phase and crystal structure of high entropy alloys by the synthetic minority oversampling technique, Journal of Alloys and Compounds 991 (2024) 174494.

doi:10.1016/j.jallcom.2024.174494.
URL https://www.sciencedirect.com/science/article/pii/S0925838824010818

[47] Z. Li, M. Greenwood, A. Phillion, A phase field methodology for simulating the microstructure evolution during laser powder bed fusion in-situ alloying process, IOP Conference Series: Materials Science and Engineering 1281 (1) (2023) 012017. doi:10.1088/1757-899X/1281/1/012017.
URL https://iopscience.iop.org/article/10.1088/1757-899X/1281/1/012017

[48] N. Moelans, A quantitative and thermodynamically consistent phase-field interpolation function for multi-phase systems, Acta Materialia 59 (2011) 1077–1086. doi:10.1016/j.actamat.2010.10.038.
URL https://linkinghub.elsevier.com/retrieve/pii/S1359645410007019

[49] D. Gaston, C. Newman, G. Hansen, D. Lebrun-Grandié, MOOSE: A parallel computational framework for coupled systems of nonlinear equations, Nuclear Engineering and Design 239 (10) (2009) 1768–1778. doi:10.1016/j.nucengdes.2009.05.021.
URL https://linkinghub.elsevier.com/retrieve/pii/S0029549309002635

[50] M. R. Tonks, D. Gaston, P. C. Millett, D. Andrs, P. Talbot, An object-oriented finite element framework for multiphysics phase field simulations, Computational Materials Science 51 (1) (2012) 20–29. doi:10.1016/j.commatsci.2011.07.028.
URL https://linkinghub.elsevier.com/retrieve/pii/S0927025611004204

[51] W. H. Xiong, W. Liu, M. M. Dai, J. Q. Liu, X. G. Lu, Assessments of molar volumes of Co-, Ni- and Ti- related bcc and fcc phases, Calphad: Computer Coupling of Phase Diagrams and Thermochemistry 66 (2019) 101629. doi:10.1016/j.calphad.2019.101629.
URL https://linkinghub.elsevier.com/retrieve/pii/S0364591619300896

[52] N. Vervliet, O. Debals, L. Sorber, L. De Lathauwer, Breaking the Curse of Dimensionality Using Decompositions of Incomplete Tensors: Tensor-based scientific computing in big data analysis, IEEE Signal Processing Magazine 31 (5) (2014) 71–79. doi:10.1109/MSP.2014.2329429.
URL https://ieeexplore.ieee.org/document/6879619

APPENDIX A: PUBLICATIONS

ARTICLE I

Rapid portabilization of elasto-chemical evolution data for dental Ti-Cr alloy microstructure through sparsification and tensor computation

Scripta Materialia 244 (2024) 116027

Contents lists available at ScienceDirect

Scripta Materialia

journal homepage: www.journals.elsevier.com/scripta-materialia

Rapid portabilization of elasto-chemical evolution data for dental Ti-Cr alloy microstructure through sparsification and tensor computation

Upadesh Subedi [a,b,c,*], Nele Moelans [c], Tomasz Tański [a], Anil Kunwar [b]

[a] Department of Engineering Materials and Biomaterials, Faculty of Mechanical Engineering, Silesian University of Technology, Konarskiego 18A, 44-100 Gliwice, Poland
[b] Scientific and Didactic Laboratory of Nanotechnology and Material Technologies, Faculty of Mechanical Engineering, Silesian University of Technology, Towarowa 7A, 44-100 Gliwice, Poland
[c] Department of Materials Engineering, KU Leuven, Kasteelpark Arenberg 44 Bus 2450, 3001 Leuven, Belgium

ARTICLE INFO

Dataset link: https://github.com/subediupadesh/Microstructure_Tensor_ReGen

Keywords:
Phase field method
Eigen strain
Ti-Cr alloy
Tensor inpainting
Microstructural similarity

ABSTRACT

Tailoring the microstructural design of a metastable two-phase Ti-Cr dental implant alloy with the optimal quantity of Cr-rich LAVES structure requires an integration of computation with informatics. This research introduces a stepwise process for generating alloy microstructure data using the phase field method, followed by sparsification and tensor computation techniques to reconstruct a microstructural informatics database for Ti-Cr alloy. This results in a significant 28-fold reduction in data size. Characterized by inpainting accuracies of 94.38% (Tucker decomposition) and 90.38% (Canonical Polyadic), the Tucker method is declared as the superior one in preserving microstructural elastic deformation information. The findings suggest that tensor computation methods present a robust strategy for accurately reconstructing complex microstructures, offering valuable insights for the digital manufacturing of Ti-Cr dental implant alloy.

Titanium-based alloys, known for their nearly ideal metallic biomaterial characteristics, play a crucial role in contemporary dental implant applications. Extensive studies highlight the exceptional performance of 3D printed Titanium implants, showcasing excellence in biocompatibility [1,2], corrosion resistance [3,4], stability [5], a favorable strength-to-weight ratio [6], resistance to wear and fatigue [7], and hydrophilicity [8], establishing them as the optimal choice for maxillofacial [9] and mandible reconstruction [10].

In this context, the Titanium-Chromium (Ti-Cr) binary alloy emerges as a compelling option for dental implants [11]. Its attributes, such as improved mechanical performance [12], resistance to high temperature, oxidation, and excellent biocompatibility [13], position it favorably compared to the potentially toxic Ti-6Al-4V implant material [14]. Furthermore, Ti-Cr, a titanium alloy considered to be bio-inert in nature [11,15], exhibits considerable strength and resistance to mechano-chemical wear [16] and corrosion within the human body [17]. By subjecting the Ti-Cr alloy to heat treatment during 3D printing, its microstructure can be precisely tailored, offering advantages over conventional methods [13]. Mechanical properties such as bending strength, capability of elastic recoverability [18], and micro-hardness [16] underscore the alloy's performance, with higher Cr content enhancing its properties [19,20]. Studies reveal a spinodal decomposition in the Ti-Cr binary alloy system [21,22], leading to Ti-rich (α) and Cr-rich (β) phases, providing opportunities for tailored microstructure design in dental implants through 3D printing.

Building upon this foundation, we present a groundbreaking approach: designing a microstructural informatics database of the Ti-Cr phase through the tensor computation method. Our work capitalizes on a high-dimensional dense microstructural-evolution tensor, reconstructed from a sparsely populated compositional tensor of the Ti-Cr alloy system undergoing phase separation. This innovative method could facilitate on-the-fly design and development of microstructural evolution during manufacturing, including but not limited to the 3D printing process.

The overall computational modeling and data compression technique, potentially beneficial for digital manufacturing, is schematically depicted in Fig. 1. Fig. 1**a** illustrates the simulated phase separation of the Ti-Cr alloy system using the physics-based Phase Field (PF) method. This simulation generates microstructural data (X_μ) to serve as microstructure (μ) informatics in the tensor computation system (Fig. 1**b**). For example, the graph in Fig. 1**a** obtained from the PF simulation quantitatively reveals the individual areas of the Ti-rich HCP region

* Corresponding author at: Faculty of Mechanical Engineering, Silesian University of Technology, Konarskiego 18A, 44-100 Gliwice, Poland.
E-mail address: upadesh.subedi@polsl.pl (U. Subedi).
URLs: https://www.researchgate.net/profile/Upadesh-Subedi, https://www.linkedin.com/profile/view?id=upadesh-s-0b321a15b (U. Subedi).

https://doi.org/10.1016/j.scriptamat.2024.116027
Received 6 January 2024; Accepted 4 February 2024
Available online 14 February 2024
1359-6462/© 2024 The Author(s). Published by Elsevier Ltd on behalf of Acta Materialia Inc. This is an open access article under the CC BY license (http://creativecommons.org/licenses/by/4.0/).

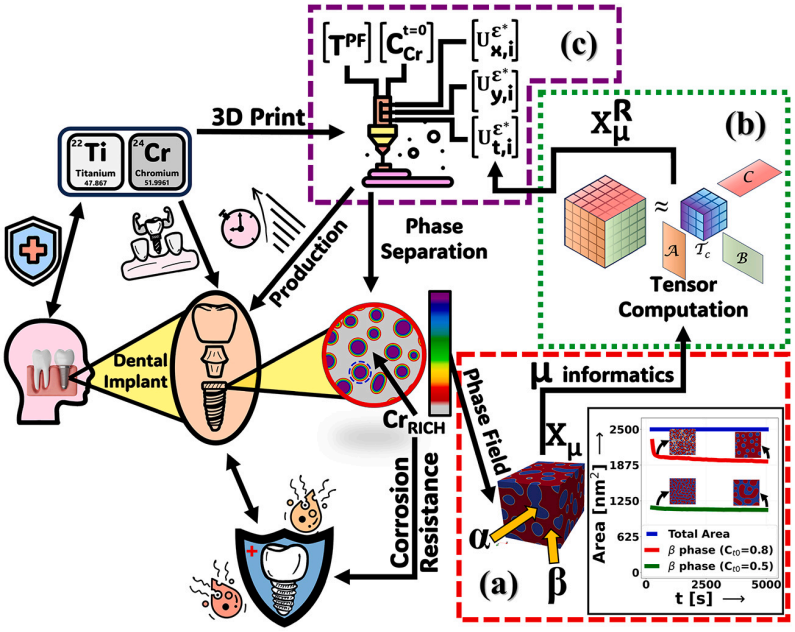


Fig. 1. The presented workflow delineates the 3D printing process for Titanium-Chromium dental implants, highlighting its proficiency in swiftly producing a biocompatible, mechanically robust, and corrosion-resistant alloy. **(a)** Phase-field modeling (**PF**) revealing phase separation during printing, leading to the formation of a corrosion-resistant Cr-rich (β) phase. Microstructure informatics (X_μ) obtained from PF simulation guide Tensor Computation. The graph in the inset of **(a)** presents the temporal evolution of mathematically integrated area of relatively more corrosion resistant LAVES (Cr-rich) microstructure within the metastable two phase alloy at 700.15 K. With two distinct initial Cr compositional conditions for simulation, denoted as $c_{t0=0.8}$ (red colored line) and $c_{t0=0.5}$ (green colored line), leading to varying growth rates in microstructural area proportions: 0.7744 and 0.436 respectively at the end of the simulation. **(b)** Illustration of Tucker tensor decomposition as a computational method, involving factor matrices $\mathcal{A}$, $\mathcal{B}$, $\mathcal{C}$, and core tensor $\mathcal{T}_c$, facilitating microstructure sparsification, decomposition, and reconstruction (X^R_μ). **(c)** 3D printing of Ti-Cr dental implants incorporating microstructure-informed tensor modes $[U^{\epsilon^*}_{X,i}], [U^{\epsilon^*}_{Y,i}], [U^{\epsilon^*}_{t,i}]$, alongside PF simulation characteristics of phase separation temperature (T^{PF}) and Chromium-rich phase design ($C^{t=0}_{Cr}$). (For interpretation of the colors in the figure(s), the reader is referred to the web version of this article.)

and Cr-rich LAVES region in a domain of 2500 nm^2 at 700.15 K. Two phase field simulations with different initial Cr compositions, $c_{t_0=0.8}$ and $c_{t_0=0.5}$ resulted in area proportion of 0.7744 and 0.436 respectively, making the tailored design of Cr-rich (β) phase for dental implant possible. As the LAVES phase offers better corrosion resistance, its area proportion within the alloy is a determinant of the overall usability in dental applications. The methodology involves storing high-dimensional microstructural evolution informatics as sparse tensors, subsequently reconstructing them into the original dense form during 3D printing using the tensor decomposition-reconstruction method. The mapping of tensor components and dispatching it to the 3D printer controller can be achieved by encoding the mode of tensor with microstructural morphology evolution in the spatial direction and data of lattice mismatch (ϵ^*) between α and β crystalline phases as $[U^{\epsilon^*}_{X,i}], [U^{\epsilon^*}_{Y,i}], [U^{\epsilon^*}_{t,i}]$ represented by Fig. 1**c**. The representation of microstructural evolution data in tensor format in our approach results in a substantial decrease in the memory requirement for storing the oversized PF exodus. Our study has shown that the file size is reduced from 14.6 GB to only 0.5 GB, showcasing a remarkable 28-fold reduction in data size and enhancing portability. Furthermore, by incorporating elastic heterogeneity into the phase separation process, our model successfully replicates the real-life scenario of a dental implant alloy undergoing elastic deformation. This phenomenon is effectively captured through tensor reconstruction methods, adding a valuable layer of realism to the 3D printing of dental implant materials.

The phase separation in the Ti-Cr system, governed by the Cahn-Hilliard Equation (1) and studied via PF method, served as input dataset for tensor decomposition methods. We employed two types of tensor decomposition techniques, namely **(i)** CP (Canonical Polyadic) and **(ii)** Tucker, to break down high-dimensional microstructural evolution exodus result of PF simulation into factor matrices and core tensors.

$$\frac{\partial c}{\partial t} = \nabla . M \nabla \left(\frac{\partial f_{chem}(c) + f_{el}(c)}{\partial c} - \kappa \nabla^2 c \right) \tag{1}$$

Here, c represents the mole fraction of Chromium (Cr), M is the mobility (1.4326×10^{-29} m^5/Js), and κ the gradient energy coefficient (1.2357×10^{-10} J/m). The chemical and elastic energy of the system are represented by $f_{chem}(c)$ and $f_{el}(c)$ respectively. Chemical energy $f_{chem}(c)$ (J/mol) is calculated using system's Gibbs free energy (G) and molar volume (V_{mol}) of Chromium provided in Equation (2) whereas elastic energy is given by the Equation (3) [23]. Fig. 2**a** illustrates the free energy of the system, fitted as the function of Chromium's composition at 700.15 K, obtained from the thermodynamic database (TDB) [24]. In a binary Ti-Cr alloy it is evident from Fig. 2**b** that the two metastable phases namely HCP (Ti-rich α) and LAVES (Cr-rich β) coexists at this temperature.

$$f_{chem}(c) = \frac{\alpha(\epsilon c - c_{eq})^2 + \beta(\epsilon c - c_{eq}) + \gamma(\epsilon c - c_{eq})^6 + \delta}{V_{mol}} \tag{2}$$

$$f_{el}(c) = \frac{1}{2} \epsilon^E_{ij} C^\rho_{ijkl} \epsilon^E_{kl} \tag{3}$$

In the above equation, ϵ_{ab} represents the elastic strain. A symmetry 9 stiffness tensor C^ρ_{ijkl} is used to represent the material property of a region ρ. In matrix form, this tensor would look like:

$$C^\rho_{ijkl} = \begin{bmatrix} C_{11} & C_{12} & C_{13} & 0 & 0 & 0 \\ C_{21} & C_{22} & C_{23} & 0 & 0 & 0 \\ C_{31} & C_{32} & C_{33} & 0 & 0 & 0 \\ 0 & 0 & 0 & C_{44} & 0 & 0 \\ 0 & 0 & 0 & 0 & C_{55} & 0 \\ 0 & 0 & 0 & 0 & 0 & C_{66} \end{bmatrix} \tag{4}$$

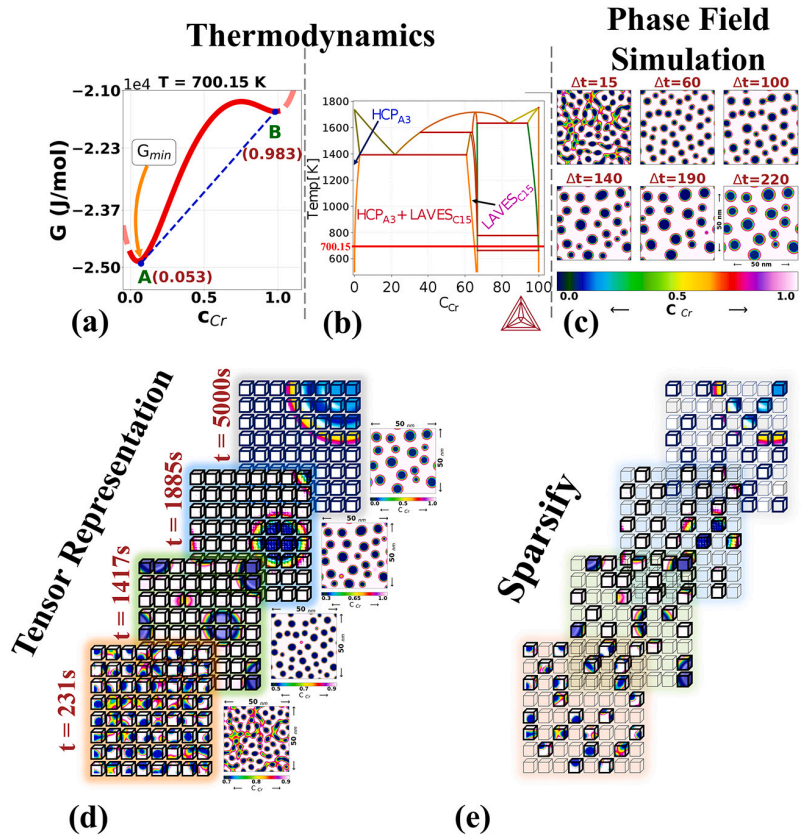


Fig. 2. (a) Gibbs free energy curve at 700.15K for Ti-Cr binary alloy system, revealing global (A) and local (B) minima at Cr-composition 0.053 and 0.983 with values of -2.48631×10^4 J/mol and -2.147797×10^4 J/mol. **(b)** Ti-Cr phase diagram obtained from Thermocalc [25] exhibits dual-phase region of Ti-rich HCP_{A3} + Cr-rich $LAVES_{C15}$, suggesting phase separation. **(c)** PF simulation of Ti-Cr alloy phase separation performed in MOOSE Framework [26] with each subplot representing distinct time steps. The dark blue color signifies the Ti-rich HCP phase. The colorbar at the bottom reflects the compositional perspective of Cr-rich Laves phases, ranging from 0 (absence) to 1 (complete presence). **(d)** Schematic of PF simulation result represented in multi-dimensional array making a dense tensor with temporal dimension presented as the depth of tensor. **(e)** Schematic of sparse tensor, highlighting eliminated elements (0 values) in spatio-temporal dimensions.

The 3D visualization [27] of Young's Modulus for Ti and Cr rich regions is shown in Fig. 3**a** and 3**c** with the variation in its value of 140 to 230 GPa for α region and 280 to 440 GPa for β region. Under the plane stress condition used for PF simulation, the 2D visualization [28] of Young's Modulus is presented in Fig. 3**b** and 3**d** in the $x-y$ plane. Since Cr-rich region has greater Young's modulus, its area fraction in the total microstructure if larger can enhance the overall strength of the alloy. As evidenced earlier PF simulations can be run to investigate the relative area proportions of HCP (α) and LAVES (β) metastable phases.

Here in α region, $C^{\alpha}_{11} = C^{\alpha}_{22} = 196$ GPa, $C^{\alpha}_{12} = C^{\alpha}_{21} = 83$ GPa, $C^{\alpha}_{13} = C^{\alpha}_{31} = 50$ GPa, $C^{\alpha}_{33} = 251$ GPa, $C^{\alpha}_{44} = C^{\alpha}_{55} = 52$ GPa and $C^{\alpha}_{66} = 56$ GPa. Similarly for β region, $C^{\beta}_{11} = C^{\beta}_{22} = C^{\beta}_{33} = 499$ GPa, $C^{\beta}_{12} = C^{\beta}_{13} = C^{\beta}_{21} = C^{\beta}_{31} = C^{\beta}_{23} = C^{\beta}_{32} = 139$ GPa and $C^{\beta}_{44} = C^{\beta}_{55} = C^{\beta}_{66} = 102$ GPa [29].

The presence of lattice mismatch [30] between the metastable two phase regions results in production of eigen strains (ϵ^*). The total strain ($\epsilon = \frac{1}{2}\left[\nabla u + (\nabla u)^T\right]$) can be expressed as a function of mechanical displacement (u). The following partial differential equation [31,32] represents the strain-induced mechanical deformation in the metastable two phase ($\alpha + \beta$) microstructures:

$$\rho \frac{\partial^2 \vec{u}}{\partial t^2} - \nabla . \sigma_c = \vec{b} \tag{5}$$

Where, b is the body force vector and σ_c is Cauchy stress.

At steady state, $\rho \frac{\partial^2 \vec{u}}{\partial t^2} = 0$ and the above equation can be rewritten as $\nabla . \sigma_c + \vec{b} = 0$. Piola-Kirchhoff stress for the mechanical system is provided by the following equation [33]:

$$\sigma_{ij} = C^{\rho}_{ijkl} . \epsilon_{kl} \tag{6}$$

As per the Khachaturyan theory [34], elastic strain (ϵ^{el}_{kl}) can be defined as the disparity between the overall strain (ϵ^{T}_{kl}) and the eigenstrain, as expressed in Equation (7). The origin of this eigenstrain arises from the incongruity between the α and β regions.

$$\epsilon^{el}_{kl} = \epsilon^{T}_{kl} - \epsilon^* \tag{7}$$

The coupled set of partial differential equations - Eq. (1) and steady state Eq. (5) are solved using finite element method (FEM) in MOOSE Framework [26,35,36]. A value of 0.1 was assigned as the eigenstrain to the α region, while β region is depicted with $\epsilon^* = 0$.

Two PF simulations were preformed, one devoid of elastic effect and other incorporating elasticity. The details about the PF simulation setup are presented in **Appendix A** of supplementary section.

To incorporate the composition dependent elasticity interpolating function into PF simulation via Cahn-Hilliard equation, we introduced the following function to interpolate C^{ρ}_{ijkl} along the interface of α and β.

$$h_{el} = \frac{1}{1 + e^{-10(2c-1)}} \tag{8}$$

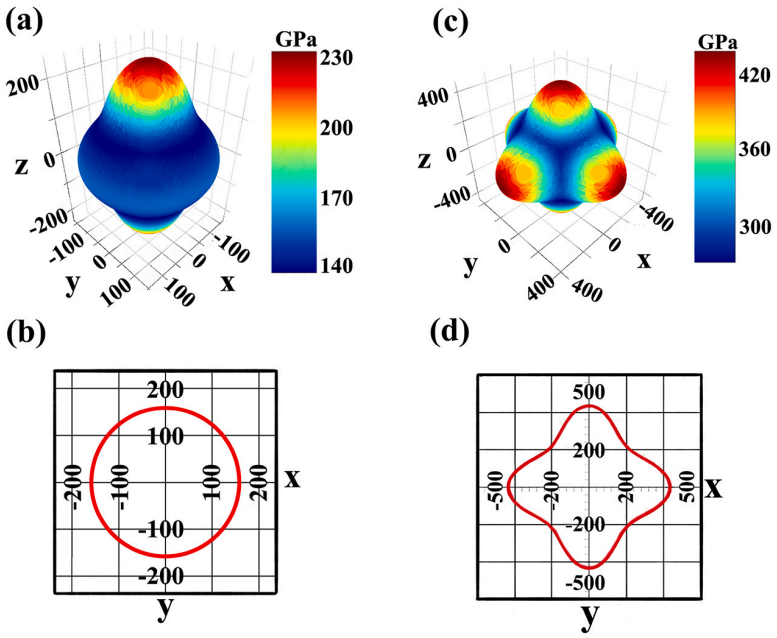


Fig. 3. Three-dimensional representations (**(a)** and **(c)**) depict directionally dependent Young's Modulus in elastically heterogeneous Ti-Cr alloy phases, revealing variations from 140 GPa to 230 GPa in Ti-rich and 280 GPa to 440 GPa in Cr-rich regions. Complementary two-dimensional schematics (**(b)** and **(d)**) in the $x-y$ plane illustrate Young's Modulus under plane stress conditions. This knowledge of LAVES phase's larger modulus as compared to the HCP phase could be used in the tailored design of metastable two phase Ti-Cr dental implant alloy with enhanced mechanical strength.

For $c < 0.5$ (Ti-rich), $h_{el} \approx 0$, $C^{\rho}_{ijkl} \approx C^{\alpha}_{ijkl}$, where as for $c > 0.5$ (Cr-rich), $h_{el} \approx 1$ and $C^{\rho}_{ijkl} \approx C^{\beta}_{ijkl}$, where:

$$C_{ijkl} = C^{\alpha}_{ijkl}(1-h) + C^{\beta}_{ijkl}h \tag{9}$$

The diffused interface incorporates h_{el}, ensuring a smooth transition of the stiffness tensor. This c-dependent h_{el} effectively tracks and interpolates elasticity tensor values in computational domains thereby enabling the mathematical distinction between α and β regions.

The originally generated datasets from phase field simulations Fig. 2**c** (401 × 401 FEM nodes, $\Delta t = 315$) were converted into a tensor of 50,652,315 elements as depicted in Fig. 2**d**. This tensorial representation ($\mathcal{T}$) efficiently stores high-dimensional microstructural data, enhancing operational ease and organized access during calculations. However, the curse of tensorial dimensionality poses several challenges [37]. Tensor decomposition help in addressing the challenges associated with high dimensional data representation. In this study, the tensor formed from the phase field generated dataset was first sparsified in the proportion of 10% (illustrated in Fig. 2**e**), 15% and 20%. Then, the sparse tensor was decomposed via CP and Tucker methods to be subsequently reconstructed (Fig. 3**c**) using tensor-inpainting technique [38]. The Conjugate Gradient Method (Algorithm **1** in **Appendix B**) was utilized in the tensor reconstruction procedure.

The results of two tensor decomposition-reconstruction techniques on three variants of sparse microstructural tensors were analyzed using four statistical techniques namely: **(i)** Root Mean Squared Error (RMSE), **(ii)** Microstructural Similarity Index μ_{SIM}, **(iii)** Blob Detection, and **(iv)** Shape Index confirming that tensor reconstructed microstructure images are statistically identical. The detailed explanation and formulation for these four quantification measures is presented in **Appendix C**. The model corresponding to 10% sparsification had the lowest RMSE in CP (RMSE = 0.017) and Tucker (RMS = 0.011). In context of microstructural similarity, as illustrated in Figure **C.1** (**Appendix C**), the same 10% sparsity model outperformed other ones. While the CP procedure yielded a μ_{SIM} of 90.4%, the Tucker method produced result having μ_{SIM} as high as 93.0%. For statistical evaluation in blob detection method via Determinant of Hessian (DoH), Tucker produced the better results. For example, in 10% sparsity, Tucker method was characterized by a deviation as low as 0.04 whereas CP had a variation of more than 0.06. The shape index evaluation (Figure **C.3**), the local microstructure curvature comparison between original phase field generated data and tensor reconstructed data has been accomplished. Both CP and Tucker reconstructed microstructures resemble to an acceptable degree with the original data.

It is to be noted that Fig. 4**a** presents a snapshot of microstructural evolution in the absence of elastic effects, showcasing undistorted microstructure in both α and β regions. On the other hand, Fig. 4**b** highlights the microstructural deformation induced by eigen strain in the α region (highlighted with a blue dotted circle emphasizing the spatial coordinate distortion). Fig. 4**c** demonstrates the successful tensor decomposition-reconstruction using Tucker method on a sparsely populated tensor, preserving both compositional data and structural deformation information caused by elastic effects. The tensor mode ($[U^{\epsilon^*}_{X,i}], [U^{\epsilon^*}_{Y,i}], [U^{\epsilon^*}_{t,i}]$) datafile related to this subplot is available at [39]. Fig. 4**d** depicts the Von Mises stress observed in the microstructure due to the elastic effect leading to the deformation (dotted blue circles in Fig. 4**b** and 4**c** highlights the deformed microstructure blobs). The magnitude of displacement in the microstructure resulting from this stress is depicted in Fig. 4**e**. The spider chart in Fig. 4**f** and 4**g** illustrates the microstructural similarity index (μ_{SIM}) values for reconstruction via Tucker and CP decomposition, with the sparse input tensor ($\mathcal{T}^{T}_{10\%}$) achieving highest μ_{SIM} value of 94.38% and 90.38% respectively. From these investigations, we infer that Tucker decomposition based reconstruction for model with 10% sparsity resembles the most original data

In conclusion, our study utilized tensor computation techniques to explore the phase separation of Ti-Cr binary dental implant alloys, yielding valuable insights. Employing the phase field method, we generated a spatio-temporal microstructural dataset, which was represented as a dense tensor. From this dataset, three sparse tensor categories were derived with sparsity levels of 10%, 15%, and 20%. The tensor decomposition via CP and Tucker methods, followed by reconstruction using the tensor inpainting technique with the conjugate gradient method, enabled a comprehensive analysis. The quantifier μ_{SIM}

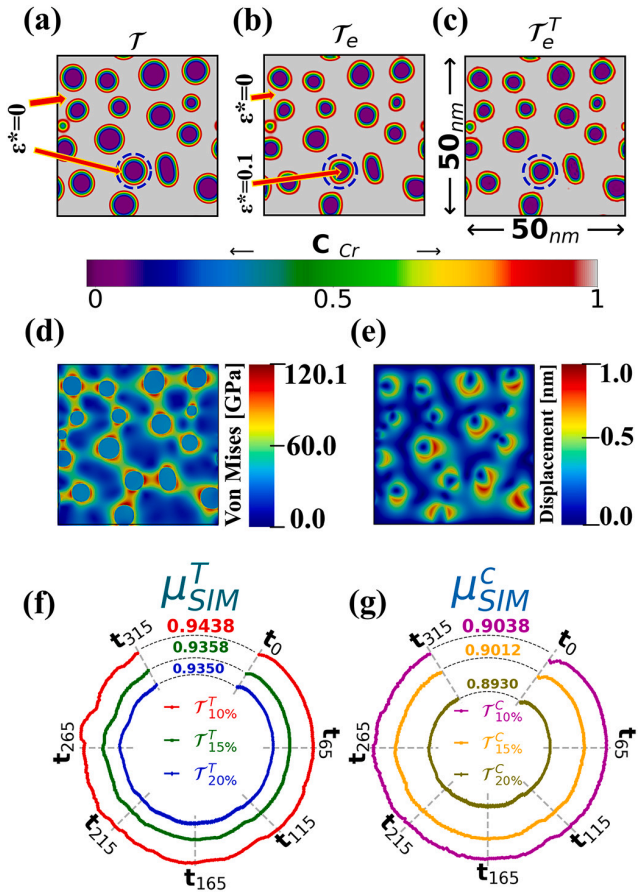


Fig. 4. Figure **(a)** presents a microstructural snapshot at a random time step, unaffected by elastic effects, showcasing undistorted shapes. In **(b)**, microstructure deformation arises from region-specific elastic strain, with $\epsilon^* = 0.1$ (α region) and $\epsilon^* = 0$ (β region), resulting in noticeable shape distortion. **(c)** illustrates the reconstructed microstructural snapshot through Tucker decomposition with 10% sparsity, preserving both compositional data and structural deformation information effectively. **(d)** reveals the Von Mises stress induced by eigen strain in the α region, transforming circular microstructural blobs (in **a**) into oval shapes (**b** and **c**), with stress magnitude ranging from 0 (blue) to 120.1 GPa (red). Microstructural deformation varies from 0 to 1 nm in **(e)**. The spider chart in **(f)** depicts μ_{SIM} values for Tucker decomposition, with the 10% sparse tensor ($\mathcal{T}^T_{10\%}$) achieving the highest accuracy at 0.9438, followed by 15% ($\mathcal{T}^T_{15\%}$) and 20% ($\mathcal{T}^T_{20\%}$) sparse tensors with commendable average μ_{SIM} values of 0.9358 and 0.9350, respectively. In **(g)**, the μ_{SIM} index for CP decomposition-reconstruction method across three sparse input tensors demonstrates that Tucker decomposition, particularly with highly sparse tensors, excels in microstructure reconstruction, with the 10% sparse tensor achieving the highest accuracy at 0.9038, followed by the 15% and 20% sparse tensors with respectable average μ_{SIM} values of 0.9012 and 0.8930, respectively.

demonstrated that 10% sparsity exhibited superior efficiency in tensor decomposition-reconstruction compared to 15% and 20%. Notably, Tucker decomposition consistently outperformed CP for the microstructural reconstruction of Ti-Cr dental implant material, with even the best-case scenario for CP falling short of the worst-case scenario for Tucker. Furthermore, the root mean square error (RMSE) consistently favored Tucker, aligning with microstructural similarity patterns. Importantly, the reconstructed microstructure revealed that information about elastic deformation is totally preserved during the entire procedure of sparsification, decomposition and reconstruction. Consequently, we assert that tensor computation methods offer a robust and accurate approach for reconstructing complex microstructural morphologies and shapes resulting from anisotropic elastic loading. Since the phase field computed microstructural information has now been successfully represented in the form of efficient and lightweight tensors, the tailored design of the Ti-Cr alloy could be accomplished in future with sufficient ease. Complete information related to elastic properties and structural morphologies of metastable two phase alloy can be supplied to a 3D printer supported with infrastructures of digital manufacturing.

These insights are crucial as control parameters in the digital manufacturing of Ti-Cr dental implants alloy.

CRediT authorship contribution statement

Upadesh Subedi: Conceptualization, Data curation, Formal analysis, Investigation, Methodology, Software, Validation, Visualization, Writing – original draft. **Nele Moelans:** Conceptualization, Methodology, Validation, Writing – review & editing. **Tomasz Tański:** Supervision, Validation, Visualization, Writing – review & editing. **Anil Kunwar:** Data curation, Funding acquisition, Methodology, Project administration, Supervision, Validation, Writing – review & editing.

Declaration of competing interest

The authors declare that they have no known competing financial interests or personal relationships that could have appeared to influence the work reported in this paper.

Data availability

All the codes used are available at https://github.com/subediupadesh/Microstructure_Tensor_ReGen.

Acknowledgement

This work was supported by the National Science Centre, Poland (UMO-2021/42/E/ST5/00339). The resources and services used in this work were provided by the VSC (Flemish Supercomputer Center), funded by the Research Foundation - Flanders (FWO) and the Flemish Government.

Appendix. Supplementary material

The supplementary information for this article is presented in a single PDF file, divided into three appendices. **Appendix A** provides a description of the computational hardware utilized for conducting the Phase Field Simulation. **Appendix B** outlines the two types of Tensor Decomposition Techniques (CP and Tucker decomposition) along with the algorithm for the Conjugate Gradient Method employed in this study. This appendix includes 1 Algorithm and 1 figure (Fig **B.1**). **Appendix C** offers detailed information pertaining to Microstructure Quantification Metrics, including μ_{SIM}, RMSE, Blobs detection, and Shape Index and three figures (Fig **C.1**, Fig **C.2**, Fig **C.3**).

Supplementary material related to this article can be found online at https://doi.org/10.1016/j.scriptamat.2024.116027.

References

[1] J. Tedesco, B.E. Lee, A.Y. Lin, D.M. Binkley, K.H. Delaney, J.M. Kwiecien, K. Grandfield, Osseointegration of a 3D printed stemmed titanium dental implant: a pilot study, Int. J. Dent. 2017 (2017) 1–11, https://doi.org/10.1155/2017/5920714, https://www.hindawi.com/journals/ijd/2017/5920714/.

[2] M. Abdel-Hady Gepreel, M. Niinomi, Biocompatibility of Ti-alloys for long-term implantation, J. Mech. Behav. Biomed. Mater. 20 (2013) 407–415, https://doi.org/10.1016/j.jmbbm.2012.11.014, https://linkinghub.elsevier.com/retrieve/pii/S1751616112003268.

[3] P. Bocchetta, L.-Y. Chen, J.D.C. Tardelli, A.C. dos Reis, F. Almeraya-Calderón, P. Leo, Passive layers and corrosion resistance of biomedical Ti-6Al-4V and β-Ti alloys, Coatings 11 (5) (2021) 487, https://doi.org/10.3390/coatings11050487, https://www.mdpi.com/2079-6412/11/5/487.

[4] X. Zhao, M. Niinomi, M. Nakai, J. Hieda, T. Ishimoto, T. Nakano, Optimization of Cr content of metastable β-type Ti–Cr alloys with changeable Young's modulus for spinal fixation applications, Acta Biomater. 8 (6) (2012) 2392–2400, https://doi.org/10.1016/j.actbio.2012.02.010, https://linkinghub.elsevier.com/retrieve/pii/S1742706112000633.
[5] L. Li, J. Lee, H.B. Amara, J.B. Lee, K.S. Lee, S.W. Shin, Y.M. Lee, B. Kim, P. Kim, K.T. Koo, Comparison of 3D-printed dental implants with threaded implants for osseointegration: an experimental pilot study, Materials 13 (21) (2020) 1–10, https://doi.org/10.3390/ma13214815, https://www.mdpi.com/1996-1944/13/21/4815.
[6] R.P. Verma, Titanium based biomaterial for bone implants: a mini review, Mater. Today Proc. 26 (2020) 3148–3151, https://doi.org/10.1016/j.matpr.2020.02.649, https://linkinghub.elsevier.com/retrieve/pii/S2214785320314048.
[7] J. Yu, Z. Zhao, L. Li, Corrosion fatigue resistances of surgical implant stainless steels and titanium alloy, Corros. Sci. 35 (1–4) (1993) 587–597, https://doi.org/10.1016/0010-938X(93)90193-K, https://linkinghub.elsevier.com/retrieve/pii/0010938X9390193K.
[8] J.H. Kim, M.Y. Kim, J.C. Knowles, S. Choi, H. Kang, S. hyun Park, S.M. Park, H.W. Kim, J.T. Park, J.H. Lee, H.H. Lee, Mechanophysical and biological properties of a 3D-printed titanium alloy for dental applications, Dent. Mater. 36 (7) (2020) 945–958, https://doi.org/10.1016/j.dental.2020.04.027, https://linkinghub.elsevier.com/retrieve/pii/S0109564120301366.
[9] U.L. Lee, S. Yun, H. Lee, H.L. Cao, S.H. Woo, Y.H. Jeong, T.G. Jung, C.M. Kim, P.H. Choung, Osseointegration of 3D-printed titanium implants with surface and structure modifications, Dent. Mater. 38 (10) (2022) 1648–1660, https://doi.org/10.1016/j.dental.2022.08.003, https://linkinghub.elsevier.com/retrieve/pii/S0109564122002433.
[10] J.H. Park, M. Odkhuu, S. Cho, J. Li, B.Y. Park, J.W. Kim, 3D-printed titanium implant with pre-mounted dental implants for mandible reconstruction: a case report, Maxillofac. Plast. Reconstr. Surg. 42 (1) (2020) 28, https://doi.org/10.1186/s40902-020-00272-5, https://jkamprs.springeropen.com/articles/10.1186/s40902-020-00272-5.
[11] X. Liu, S. Chen, J.K. Tsoi, J.P. Matinlinna, Binary titanium alloys as dental implant materials-a review, Regen. Biomater. 4 (5) (2017) 315–323, https://doi.org/10.1093/rb/rbx027, http://academic.oup.com/rb/article/4/5/315/4210443/Binary-titanium-alloys-as-dental-implant.
[12] W.F. Ho, T.Y. Chiang, S.C. Wu, H.C. Hsu, Evaluation of low-fusing porcelain bonded to dental cast Ti-Cr alloys, J. Alloys Compd. 474 (1–2) (2009) 505–509, https://doi.org/10.1016/j.jallcom.2008.06.152, https://linkinghub.elsevier.com/retrieve/pii/S0925838808010931.
[13] J. Thomas, J.E. Mogonye, S.A. Mantri, D. Choudhuri, R. Banerjee, T.W. Scharf, Additive manufacturing of compositionally graded laser deposited titanium-chromium alloys, Addit. Manuf. 33 (2020) 101132, https://doi.org/10.1016/j.addma.2020.101132, https://linkinghub.elsevier.com/retrieve/pii/S2214860419320779.
[14] C.N. Elias, J.H. Lima, R. Valiev, M.A. Meyers, Biomedical applications of titanium and its alloys, JOM 60 (3) (2008) 46–49, https://doi.org/10.1007/s11837-008-0031-1, http://link.springer.com/10.1007/s11837-008-0031-1.
[15] Nonalloyed Titanium as a Bioinert Metal—A Review, J. Prosthet. Dent. 96 (1) (2006) 12, https://doi.org/10.1016/j.prosdent.2006.02.020, https://linkinghub.elsevier.com/retrieve/pii/S002239130600076X.
[16] H.C. Hsu, S.C. Wu, T.Y. Chiang, W.F. Ho, Structure and grindability of dental Ti-Cr alloys, J. Alloys Compd. 476 (1–2) (2009) 817–825, https://doi.org/10.1016/j.jallcom.2008.09.116, https://linkinghub.elsevier.com/retrieve/pii/S0925838808015879.
[17] H.C. Hsu, S.C. Wu, C.F. Wang, W.F. Ho, Electrochemical behavior of Ti-Cr alloys in artificial saliva, J. Alloys Compd. 487 (1–2) (2009) 439–444, https://doi.org/10.1016/j.jallcom.2009.07.172, https://linkinghub.elsevier.com/retrieve/pii/S0925838809015175.
[18] W.F. Ho, T.Y. Chiang, S.C. Wu, H.C. Hsu, Mechanical properties and deformation behavior of cast binary Ti-Cr alloys, J. Alloys Compd. 468 (1–2) (2009) 533–538, https://doi.org/10.1016/j.jallcom.2008.01.046, https://linkinghub.elsevier.com/retrieve/pii/S0925838808001011.
[19] B. Mallia, P.A. Dearnley, The corrosion-wear response of Cr-Ti coatings, Wear 263 (1-6 SPEC. ISS.) (2007) 679–690, https://doi.org/10.1016/j.wear.2006.12.058, https://linkinghub.elsevier.com/retrieve/pii/S0043164807003754.
[20] S. Takemoto, M. Hattori, M. Yoshinari, E. Kawada, K. Asami, Y. Oda, Corrosion mechanism of Ti-Cr alloys in solution containing fluoride, Dent. Mater. 25 (4) (2009) 467–472, https://doi.org/10.1016/j.dental.2008.09.005, https://linkinghub.elsevier.com/retrieve/pii/S0109564108002479.
[21] A.M. Mebed, T. Miyazaki, Computer simulation and experimental investigation of the spinodal decomposition in the β Ti-Cr binary alloy system, Metall. Trans. A 29 (3) (1998) 739–749, https://doi.org/10.1007/s11661-998-0264-1, https://link.springer.com/10.1007/s11661-998-0264-1.
[22] Phase Evolution in Laser-Deposited Titanium-Chromium Alloys, Metall. Trans. A, Phys. Metall. Mater. Sci. 33 (7) (2002) 2129–2138, https://doi.org/10.1007/s11661-002-0044-2, https://link.springer.com/10.1007/s11661-002-0044-2.
[23] X. Zuo, N. Moelans, Phase-field study of elastic effects on precipitate evolution in (Al)0.05CrFeNi, Int. J. Mech. Sci. 247 (2023) 108163, https://doi.org/10.1016/j.ijmecsci.2023.108163, https://linkinghub.elsevier.com/retrieve/pii/S0020740323000656.
[24] W. Li, B. Tang, Y.-W. Cui, R. Hu, H. Chang, J. Li, L. Zhou, Assessment of diffusion mobility for the bcc phase of the Ti–Al–Cr system, Calphad 35 (3) (2011) 384–390, https://doi.org/10.1016/j.calphad.2011.05.006, https://linkinghub.elsevier.com/retrieve/pii/S0364591611000502.
[25] J.-O. Andersson, T. Helander, L. Höglund, P. Shi, B. Sundman, Thermo-Calc & DICTRA, computational tools for materials science, Calphad 26 (2) (2002) 273–312, https://doi.org/10.1016/S0364-5916(02)00037-8, https://linkinghub.elsevier.com/retrieve/pii/S0364591602000378.
[26] D. Gaston, C. Newman, G. Hansen, D. Lebrun-Grandié, MOOSE: a parallel computational framework for coupled systems of nonlinear equations, Nucl. Eng. Des. 239 (10) (2009) 1768–1778, https://doi.org/10.1016/j.nucengdes.2009.05.021, https://linkinghub.elsevier.com/retrieve/pii/S0029549309002635.
[27] M. Friak, D. Lago, N. Koutna, D. Holec, T. Rebok, M. Sob, Multi-phase ELASTic Aggregates (MELASA) software tool for modeling anisotropic elastic properties of lamellar composites, Comput. Phys. Commun. 247 (2020) 106863, https://doi.org/10.1016/j.cpc.2019.106863, https://linkinghub.elsevier.com/retrieve/pii/S0010465519302504.
[28] R. Gaillac, P. Pullumbi, F.-X. Coudert, ELATE: an open-source online application for analysis and visualization of elastic tensors, J. Phys. Condens. Matter 28 (27) (2016) 275201, https://doi.org/10.1088/0953-8984/28/27/275201, https://iopscience.iop.org/article/10.1088/0953-8984/28/27/275201.
[29] A. Jain, S.P. Ong, G. Hautier, W. Chen, W.D. Richards, S. Dacek, S. Cholia, D. Gunter, D. Skinner, G. Ceder, K.A. Persson, Commentary: the materials project: a materials genome approach to accelerating materials innovation, APL Mater. 1 (1) (2013), https://doi.org/10.1063/1.4812323, https://pubs.aip.org/apm/article/1/1/011002/119685/Commentary-The-Materials-Project-A-materials.
[30] A. Durga, P. Wollants, N. Moelans, Phase-field study of IMC growth in Sn–Cu/Cu solder joints including elastoplastic effects, Acta Mater. 188 (2020) 241–258, https://doi.org/10.1016/j.actamat.2020.01.052, https://linkinghub.elsevier.com/retrieve/pii/S135964542030077X.
[31] S. Shang, A. Kunwar, J. Yao, Y. Wang, H. Ma, Y. Wang, Effect of the TiO2 nanoparticles on the growth behavior of intermetallics in Sn/Cu solder joints, Met. Mater. Int. 25 (2) (2019) 499–507, https://doi.org/10.1007/s12540-018-0189-1, http://link.springer.com/10.1007/s12540-018-0189-1.
[32] K. Chockalingam, M.R. Tonks, J.D. Hales, D.R. Gaston, P.C. Millett, L. Zhang, Crystal plasticity with Jacobian-Free Newton–Krylov, Comput. Mech. 51 (5) (2013) 617–627, https://doi.org/10.1007/s00466-012-0741-7, http://link.springer.com/10.1007/s00466-012-0741-7.
[33] L. Zhao, P. Chakraborty, M. Tonks, I. Szlufarska, On the plastic driving force of grain boundary migration: a fully coupled phase field and crystal plasticity model, Comput. Mater. Sci. 128 (2017) 320–330, https://doi.org/10.1016/j.commatsci.2016.11.044, https://linkinghub.elsevier.com/retrieve/pii/S092702561630605X.
[34] A.G. Khachaturyan, S. Semenovskaya, T. Tsakalakos, Elastic strain energy of inhomogeneous solids, Phys. Rev. B 52 (22) (1995) 15909–15919, https://doi.org/10.1103/PhysRevB.52.15909, https://link.aps.org/doi/10.1103/PhysRevB.52.15909.
[35] M.R. Tonks, D. Gaston, P.C. Millett, D. Andrs, P. Talbot, An object-oriented finite element framework for multiphysics phase field simulations, Comput. Mater. Sci. 51 (1) (2012) 20–29, https://doi.org/10.1016/j.commatsci.2011.07.028, https://linkinghub.elsevier.com/retrieve/pii/S0927025611004204.
[36] A.D. Lindsay, D.R. Gaston, C.J. Permann, J.M. Miller, D. Andrš, A.E. Slaughter, F. Kong, J. Hansel, R.W. Carlsen, C. Icenhour, L. Harbour, G.L. Giudicelli, R.H. Stogner, P. German, J. Badger, S. Biswas, L. Chapuis, C. Green, J. Hales, T. Hu, W. Jiang, Y.S. Jung, C. Matthews, Y. Miao, A. Novak, J.W. Peterson, Z.M. Prince, A. Rovinelli, S. Schunert, D. Schwen, B.W. Spencer, S. Veeraraghavan, A. Recuero, D. Yushu, Y. Wang, A. Wilkins, C. Wong, 2.0 - MOOSE: enabling massively parallel multiphysics simulation, SoftwareX 20 (2022) 101202, https://doi.org/10.1016/j.softx.2022.101202.
[37] N. Vervliet, O. Debals, L. Sorber, L. De Lathauwer, Breaking the curse of dimensionality using decompositions of incomplete tensors: tensor-based scientific computing in big data analysis, IEEE Signal Process. Mag. 31 (5) (2014) 71–79, https://doi.org/10.1109/MSP.2014.2329429, https://ieeexplore.ieee.org/document/6879619.
[38] X. Chen, Fluid inpainting, https://medium.com/@xinyu.chen/inpainting-fluid-dynamics-with-tensor-decomposition-numpy-d84065fead4d, 2022.
[39] U. Subedi, Tensor decomposition reconstruction, https://github.com/subediupadesh/Microstructure_Tensor_ReGen/tree/main/Figure_data_folder, 2023.

ARTICLE II

Prototyping Ti_2Cu intermetallic grain growth heterogeneously in Ti6Al4V matrix through laser additive manufacturing

Materials & Design 246 (2024) 113312

Contents lists available at ScienceDirect

Materials & Design

journal homepage: www.elsevier.com/locate/matdes

Prototyping Ti_2Cu intermetallic grain growth heterogeneously in Ti6Al4V matrix through laser additive manufacturing

Hana Beyene Mamo [a], Upadesh Subedi [a], Tomasz Poloczek [a], Marcin Adamiak [a], Augustine Nana Sekyi Appiah [a], Magdalena Skonieczna [b], Paweł M. Nuckowski [a], Yaoxiang Geng [c], Barun Haldar [d], Anil Kunwar [a,*]

[a] Faculty of Mechanical Engineering, Silesian University of Technology, Konarskiego 18A, 44-100 Gliwice, Poland
[b] Department of Systems Biology and Engineering, Silesian University of Technology, 16 Akademicka Street, 44-100 Gliwice, Poland
[c] School of Materials Science and Engineering, Jiangsu University of Science and Technology, 212100 Zhenjiang, China
[d] Mechanical Engineering Department, College of Engineering, Imam Mohammad Ibn Saud Islamic University, 11432 Riyadh, Saudi Arabia

ARTICLE INFO

Dataset link: https://github.com/abeyenem/Experimental-Data

Dataset link: https://github.com/anilkunwar/effective_material_properties

Dataset link: https://github.com/subediupadesh/Ti2Cu_IMC_evolution

Keywords:
Ti6Al4V alloy
Super-Gaussian heat source
Intermetalic compound
Finite element method
Interdiffusion
Antibacterial application

ABSTRACT

The Ti_2Cu intermetallics compound possessing an ability to release Cu^{2+} ions has promising antibacterial properties. This research integrates experimental and computational techniques to delve into the interfacial intermetallic (IMC) formation within the Ti6Al4V/Cu system. Heat transfer analysis is performed to numerically outline the thermal history within the microstructure during laser surface alloying (power = 1000 W and scan speed = 200 mm/s), while the phase field method is employed to describe the Ti_2Cu IMC grain growth in the Ti6Al4V matrix. As the IMC and the matrix phases respectively have free energy minima of -68.52 and -61.35 kJ/mol at $T_{average}$ = 1250.0 K, the growth of Ti_2Cu IMC grains at the Ti6Al4V matrix located around the depth of 5 μm from the top surface is thermodynamically favorable. Laser processing can cause the nucleation of IMC precipitates of irregular sizes and curvature profiles, in which case the curvature driven effects between the adjacent grains can additionally affect their growth kinetics. Furthermore, microbiological assays underscore the superior antibacterial efficacy of the Ti6Al4V+Ti_2Cu heterostructures as compared to the control (Ti6Al4V) counterpart.

1. Introduction

Titanium alloys, particularly Ti6Al4V, have become outstanding biomedical materials due to their unique properties suitable for medical devices and implants [1–3]. Ti6Al4V exhibits remarkable strength [4], corrosion resistance [5,6], and biocompatibility [7], making it an ideal choice for orthopedic implants, cardiovascular implants, dental implants, and other medical devices. The exceptional strength-to-weight ratio of Ti6Al4V guarantees structural integrity, concurrently fortified by its corrosion-resistant attributes, safeguarding against degradation within the challenging physiological milieu of the human body [8,9]. Furthermore, the biocompatibility of Ti6Al4V facilitates osseointegration, promoting the integration of the implant with surrounding bone tissue [10]. These attributes and the ability to be easily shaped and fabricated contribute to the widespread adoption of Ti6Al4V in various biomedical applications, enhancing patient outcomes and the longevity of implants [11,12].

However, despite stringent aseptic measures during replacement surgeries, titanium alloy implants remain highly susceptible to bacterial colonization due to several factors. According to Marta and other researchers, contamination from surgical procedures is the leading cause of bacterial colonization in orthopedic implants [13]. Mirjam M. and others also reported that Bacterial colonization occurred within 30 min after dental implant placement. Numerous studies have also shown that a bloodstream bacterium affects cardiovascular implants [14]. Once bacteria establish a colony on the implant and form a protective slimy biofilm, they become resistant to medications and the body's immune system, ultimately fostering recurrent infections. This resistance often necessitates implant removal, causing patient discomfort and compro-

* Corresponding author.
E-mail address: anil.kunwar@polsl.pl (A. Kunwar).

https://doi.org/10.1016/j.matdes.2024.113312
Received 27 May 2024; Received in revised form 10 August 2024; Accepted 11 September 2024
Available online 14 September 2024
0264-1275/© 2024 The Author(s). Published by Elsevier Ltd. This is an open access article under the CC BY license (http://creativecommons.org/licenses/by/4.0/).

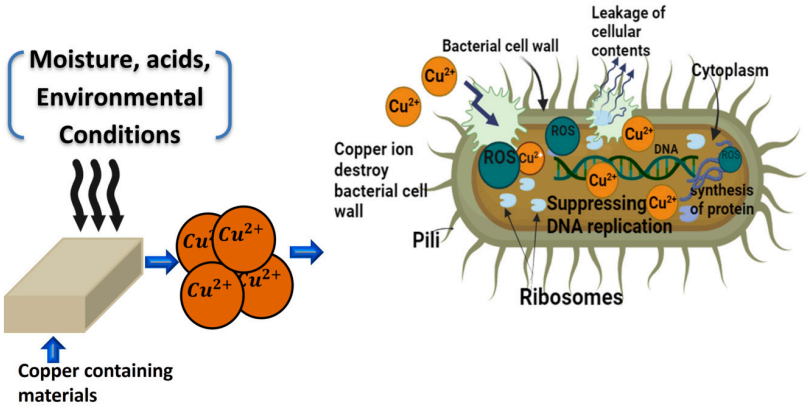


Fig. 1. The significant antibacterial effectiveness of liberated Cu^{2+} ions stems from various mechanisms: Firstly, Cu^{2+} ions interfere with the integrity of bacterial cell membranes, causing leakage of cellular contents and eventual bacterial death. Secondly, these ions penetrate bacterial cells, disrupting crucial cellular processes such as respiration and DNA replication, which impairs bacterial viability. Thirdly, Cu^{2+} ions promote the production of reactive oxygen species (ROS) within bacterial cells, inducing oxidative stress and further contributing to bacterial demise. Lastly, Cu^{2+} ions possess the capability to disrupt bacterial biofilms, preventing bacterial colonization and persistence on surfaces.

mising the structural integrity of implants, hindering the process of osseointegration, and, in severe cases, leading to implant failure [15,16].

In the pursuit of augmenting the antibacterial attributes of Ti6Al4V alloys, researchers have delved into the incorporation of antimicrobial agents like silver (Ag), copper (Cu), and zinc (Zn) [17,18]. Notably, copper integration has emerged promising due to its effectiveness against diverse bacterial strains [19]. Significantly, this integration does not undermine the alloy's mechanical properties, biocompatibility, or corrosion resistance [20]. Investigations have revealed that titanium alloys infused with copper exhibit superior wear resistance, heightened hardness, enhanced cell viability, and elevated corrosion resistance when contrasted with copper-free counterparts [21,22].

Including copper in titanium alloys creates a copper-enriched phase termed Ti_2Cu, which releases copper ions (Cu^{2+}) when exposed to moisture. These liberated Cu^{2+} showcase significant antibacterial effectiveness, as elucidated by various mechanisms illustrated in Fig. 1. However, conventional alloying methods such as powder metallurgy and casting pose challenges in achieving precise alloy compositions and uniform microstructures [23,24]. Laser surface alloying (LSA) is a promising technique to overcome these challenges by allowing precise control and localized incorporation of copper into the titanium alloy [25,26].

Despite significant advancements in laser surface alloying (LSA) techniques aimed at modifying Ti6Al4V alloys with copper (Cu) to bolster their antibacterial properties, a conspicuous research gap remains regarding the precise understanding of temperature dynamics throughout the alloying process. Existing state-of-the-art experiments need more critical temperature data for a comprehensive analysis of the thermal evolution involved in the formation and growth of Ti_2Cu intermetallic compounds (IMCs) within the alloy matrix. To address this gap, this research introduces an innovative laser manufacturing pathway to incorporate copper elements into Ti6Al4V alloys, enhancing their antibacterial performance. Advanced techniques, including Finite Element Analysis (FEA), were employed to overcome challenges in temperature measurement during LSA of Ti6Al4V with Cu. The computational approach leverages thermodynamic principles to accurately simulate temperature profiles, providing crucial insights into thermal dynamics. Subsequently, investigations into microstructural evolution, particularly the formation and growth of Ti_2Cu IMCs, were conducted. This involved integrating phase-field modeling to simulate the microstructural evolution and distribution of Ti_2Cu IMCs during laser processing.

Furthermore, microstructural characterization techniques such as X-ray Diffraction (XRD), Scanning Electron Microscopy (SEM), and Energy Dispersive Spectroscopy (EDS) were employed to analyze the resulting material structure and composition. Additionally, a microbiological study was conducted to evaluate the antibacterial efficacy of the Ti-Al-V-Cu alloys against relevant pathogens. By integrating experimental observations with computational predictions, this study elucidates the intricate relationship between processing conditions, thermodynamics, and microstructural evolution, laying the groundwork for optimized laser surface alloying processes and enhanced material performance in biomedical applications.

Table 1
Chemical composition of base material, (Ti6Al4V).

Element	Al	Ti	V
Wt%	5.66	92.21	2.13
At%	9.63	88.45	1.92

2. Methodology

2.1. Experimental methods

The current study utilized commercially sourced titanium alloys (Ti6Al4V) as a substrate. Employing Energy Dispersive X-ray Analysis (EDS), a meticulous elemental analysis verified the presence of three alloying elements within the substrate, as outlined in Table 1. Copper powders, procured with a density of no less than 10.59 g/cm^3 were acquired from NMD New Materials Development GmbH and utilized as the alloying agent. The structural characteristics of the powder particles was assessed using a Zeiss Evo MA 15 series electron microscope for scanning (SEM). Fig. 2**(c)** illustrates the morphological traits of the Copper (Cu) powder. The copper (Cu) powder particles exhibit a dendritic structural pattern (Fig. 2**(d)**). Analyzing particle size via a laser-assisted size analyzer, the ANALYSETTE 22 from Fritsch based in New Jersey, USA, provided statistical D10, D50, and D90 values of 7.30 μm, 18.56 μm, and 34.81 μm, respectively, as depicted in Fig. 2**(b)**). The degree of particle uniformity, a.k.a. as the dimensionless size span (s), is mathematically computed as $s = (D90 - D10)/D50 = 1.5$. This value denotes a notable level of uniformity, presenting a favorable attribute crucial for the efficacy of the laser alloying process. The TruDisk 3302, a Ytterbium-doped Yttrium Aluminum Garnet (Yb: YAG) disk laser system capable of delivering continuous wave (CW) output power up to 3.3 kilowatts (KW), was employed for the alloying process as shown in Fig. 3**(a)**. The focused laser spot diameter was approximately 245 μm, maintaining a consistent distance of 20 mm above the substrate for precise laser beam placement. To prevent oxidation of molten pools, a controlled in-

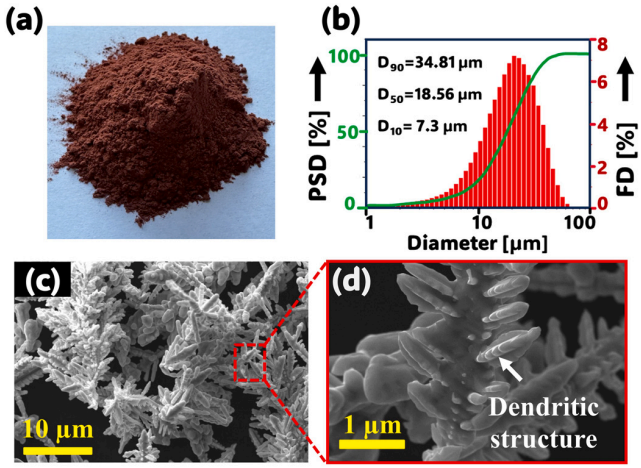


Fig. 2. Cu powder: (a) Raw Cu powder (b) powder particle size distribution plot showing statistical derivations and computed particle span. (c) SEM image of pure copper powder (d) magnification of dendrite.

ert argon (Ar) shielding environment was established. Key parameters governing the laser surface alloying process were comprehensively detailed in Table 2. Notably, a laser scan speed of 200 mm/s was specified, and a laser power of 1000 watts was utilized to alloy the Cu elements onto the titanium alloy substrate. Other essential parameters encompassed an initial room temperature and a shielding gas flow rate of 118 mm/min. Following the preparation of metal powder slurry using a 4 wt percent polyvinyl alcohol solution (PVA), the application of copper materials onto the base material was carried out.

The metallographic specimen was sectioned transversely across the alloyed layer for microstructural analysis and embedded in Bakelite powder using a precision mounting press for support during grinding

Table 2
Process parameters during laser processing and material properties of experimental samples.

Properties	Values
scan speed	200 mm/s
shielding gas flow	118 mm/min
laser power	1000 W
Melting Point of Cu	1358 K
Melting Point of Ti6Al4V	1923 K
absorptance of powder bed	5.0×10^7 m^{-1}
initial porosity ($\phi_{t=0}$)	0.45

and polishing. The grinding process involved the use of the Tergamin-30 grinding-polishing machine (Struers, Willich, Germany) and silicon carbide (SiC) grinding paper with grit sizes of 600 and 1200. The specimen was first ground with 600 grit SiC paper for 2 minutes, followed by 1200 grit SiC paper for an additional 2 minutes. This systematic grinding removed surface irregularities and created a smooth, flat surface. Following grinding the specimen underwent a polishing process using the Tergamin-30 grinding-polishing machine. Appropriate polishing cloths and diamond suspension or colloidal silica were utilized to remove fine scratches and achieve a mirror-like finish, essential for detailed microstructural analysis. To enhance adhesion and eliminate surface impurities, a chemical etching process was employed using a reagent composed of 5 ml of Nitric Acid (HNO_3), 1.0 ml of Hydrofluoric Acid (HF), and 95 ml of purified water. This solution was applied to the mechanically polished surface for a brief etching duration of 1 minute. After etching, the specimen was thoroughly rinsed with purified water to remove any residual etchant and dried using warm air to prevent oxidation or contamination.

Microstructural analysis was conducted utilizing an optical microscope (OM, Zeiss, Oberkochen, Germany) first. A comprehensive X-ray investigation was conducted on the copper powder, the surface of Ti6Al4V, and the Ti6Al4V-Cu alloy at a subsurface depth of 0.15 mm.

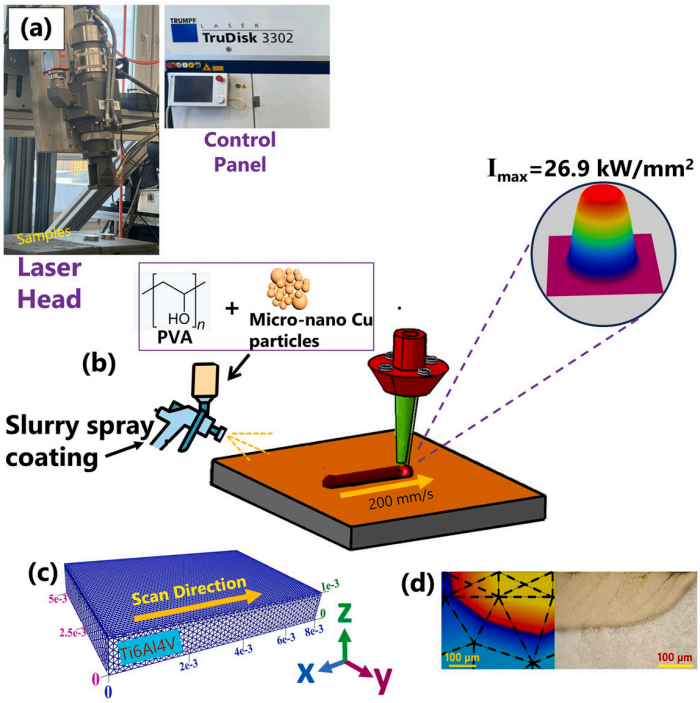


Fig. 3. (a) Laser surface alloying system **(b)** Visualization of flat top [33] **(c)** The computational mesh consists of two layers: the lower Ti6Al4V substrate (thickness = 0.925 mm) and the upper Cu powder bed (thickness = 75 µm). **(d)** computational-experimental cross-section.

Phase analysis was conducted using an X'pert Pro X-ray diffractometer (Panalytical, Almelo, Netherlands) equipped with a cobalt lamp X-ray source. The X-ray diffraction measurements were performed under a voltage of 40 kV and a current of 30 mA, following the Bragg-Brentano geometry. The resulting diffractograms were meticulously analyzed using the X'pert High Score Plus software (version 3.0e) in conjunction with the Inorganic Crystal Structure Database (ICSD) from Fiz (Karlsruhe, Germany). Chemical composition analysis was conducted on specific regions of the transversely sectioned surface. The distribution of Ti-Cu intermetallic phases within the cross-section was determined using an SEM EVO MA10 (Zeiss, Oberkochen, Germany) equipped with an EDS spectrum analyzer.

In a microbiological study, Gram-negative bacterial strain, *Escherichia coli* ATCC25922, was cultured overnight. The bacterial concentration was adjusted to 1×1.0^4 CFU/ml. A 100 μl aliquot of this suspension was inoculated into each flat-bottomed 12-well non-pyrogenic cell culture plate (Biologix Europe) containing 2 ml of sterile Lysogeny broth (LB). The specimens under investigation were then placed into the LB and incubated overnight at 37 °C without shaking. The LIVE/DEAD™ *Bac*Light™ Bacterial Viability Kit (Life Technologies, Thermo Fisher Scientific) was employed to assess bacterial viability [27,28]. The LIVE/DEAD *Bac*Light™ kit uses SYTO™ 9 stain to label live bacteria in green and propidium iodide to label dead bacteria in red. Imaging and analysis were performed using an Olympus FluoView FV1000 scanning confocal microscope. Images were captured at 400x magnification, focusing primarily on detecting green and red fluorescent signals. Fluorescent images were collected with the Olympus FV1000 confocal fluorescent microscope. ImageJ software (Fiji, NIH) was utilized for image analysis, which involved converting grayscale images to binary and counting the number of pixels corresponding to the stained bacteria signal relative to the background. Further analysis using Matlab R2022a involved calculating the ratio of the positive signal (white from stained bacteria cells) to the background.

The collected bacteria were stained using *Bac*Light™ kit in accordance with the protocol of LIVE/DEAD flow cytometry concerning the microscopy and quantitative assays [29–32]. The Thermo Scientific Varioskan LUX Multimode Microplate Reader measured the signals of live bacteria, with green-fluorescent SYTO™ 9 and red-fluorescent propidium iodide used to distinguish live and dead cells. Absorption/emission wavelengths were 485/498 nm for live cells and 535/617 nm for dead cells.

2.2. Numerical methods

2.2.1. Thermal history determination using finite element analysis

Comprehending the transient temperature distribution at the interface of Ti6Al4V and Cu-powder during laser processing holds paramount importance for orchestrating the kinetics of interdiffusion and the formation of interfacial phases. The Spatial and temporal variations in temperature profoundly influence microstructural evolution, thereby determining the ultimate properties of the alloyed surface. Finite Element Analysis is a potent tool for simulating the dynamic heat transfer process during laser irradiation, furnishing a nuanced comprehension of the temperature dynamics at the interface over time.

The focal point of numerical scrutiny lies within the Ti6Al4V/Cu-powder interface. The dimensions of the computational domain for this physical model encompass an 8.0 mm × 5.0 mm × 1.0 mm domain, as depicted in Fig. 3**(c)**. Cu powder bed layer with an effective thickness of 75 μm is spread on top of the 0.925 mm thick Ti6Al4V substrate. Though Cu powder is composed of discrete particles, the FEA sub-mesh for the powder bed is conceptualized as a continuum layer comprising Cu spheres embedded within an air matrix. For an example, the effective property (density or thermal conductivity) of the pre-sintered powder bed layer will be computed as the weighted sum of the property of powder and property of air. The T-dependent porosity (ϕ) of Cu-powder bed starts to decrease drastically when temperature starts to increase beyond sintering temperature (T_s), and becomes zero when the melting temperature (T_m) is reached. At two-phase regime (mushy region) and liquid regime, the porosity of Cu powder bed can be assumed to be equal to zero i.e. $\phi = 0$.

During the laser surface alloying process of the Ti6Al4V sample with Cu elements, a fraction of the sample may undergo melting, leading to the presence of both solid and liquid phases within the computational domain. The method utilizing apparent or effective heat capacity to simulate melting in the Ti6Al4V/Cu sample was used. This method was selected for its efficacy in concurrently capturing the intricate thermal dynamics inherent in laser-induced surface alloying processes. The enthalpy of the j^{th} material layer (whether it be the Cu powder bed or the Ti6Al4V substrate) at a specific temperature (T) is defined by the subsequent expression [34].

$$H_j(T) = \int_0^T \rho_i \left(C_{p,i} + L_j \frac{\partial f_j}{\partial T} \right) dT \tag{1}$$

In Eq. (1), the symbols ρ_i and $C_{p,i}$ represent the density and specific heat capacity, respectively, of the i^{th} phase (solid or liquid) within the j^{th} layer. L_j denotes the latent heat of fusion of the j^{th} layer, whereas the fraction of liquid in the material layer j is denoted as f_j. While the enthalpy determination for ternary Ti6Al4V alloys is straight forward, it will be necessary to simplify the process for computing the enthalpy of Cu-powder bed. Since, the height and profile of two-phase regions in a H-T curve for a given phase mainly dominates the accuracy of the finite element analysis, it is possible to use the porosity value of two-phase regime for the entire temperature ranges of enthalpy computation for powder bed. At two phase regime, the T-dependent enthalpy of bulk Cu is equal to that of Cu-powder bed. The thermodynamic CALPHAD (Calculation of Phase Diagrams) information for the Ti6Al4V alloy is acquired from the work of Lindahl et al. [35] whereas that for Cu is obtained from Demin et al. [36]. Enthalpies of Cu and the Ti6Al4V phase are computed using opencalphad software as a temperature function. The resulting H(T) values for Cu and Ti6Al4V are illustrated in Fig. 4**(c)**. Melting points of the respective metal/alloy are delineated along the lines exhibiting abrupt vertical shifts in the enthalpy curves (1358 K for Cu and 1923 K for Ti6Al4V). The latent heats of fusion (L_f) are quantified by the overall increment in enthalpy magnitude corresponding to these transitions within the H-T curve's melting regime.

The laser beam (with a power of 1000 W and a scanning speed of 200 mm/s) is directed onto the upper surface of the computational domain, comprising the Cu-powder/Ti6Al4V material system. Initially, the material system is at a temperature of 298 K, with the Cu powder portion (of the top bed) and the Ti6Al4V base in a solid phase state. Upon laser exposure (spot diameter: 245 μm), Cu powder primarily captures thermal flux, initiating heat transfer.

Given the laser heat source (Q_{laser}) influence on the computational domain (Fig. 5**(a)**), the partial differential equation (PDE) for describing the heat transfer process is given as follows [34]

$$\rho_i \overline{C_i} \left(\frac{\partial T}{\partial t} + \vec{u}.\nabla T \right) = k_{th,i} \nabla^2 T + Q_{laser} \tag{2}$$

The transient term is the first term inside the bracket in the left-hand side of equation (2), expressed as the partial derivative of temperature (T) w.r.t. time (t). The convection component, which is only significant at the meltpool regime, is the second term enclosed in the same bracket. $\vec{u}$ in the convection term is the flow velocity, and its variation in the meltpool is described by the incompressible Navier-Stokes equations (refer Appendix A.1). On the other hand, the first term at the right hand side of the equation is the conduction term which is the primary mode of heat transfer throughout the whole domain. The material properties, namely apparent heat capacity ($\overline{C_i}$), density (ρ_i) and thermal conductivity ($k_{th,i}$) are dependent not only on the structure, composition of the 4 phases (powder Cu(s) + air, continuous Cu(l), Ti6Al4V(s) and Ti6Al4V(l)) constituting the computational domain but also on temperature. Though it will be later known that the substrate Ti6Al4V will always remain solid(s) throughout the entire simulation duration, the

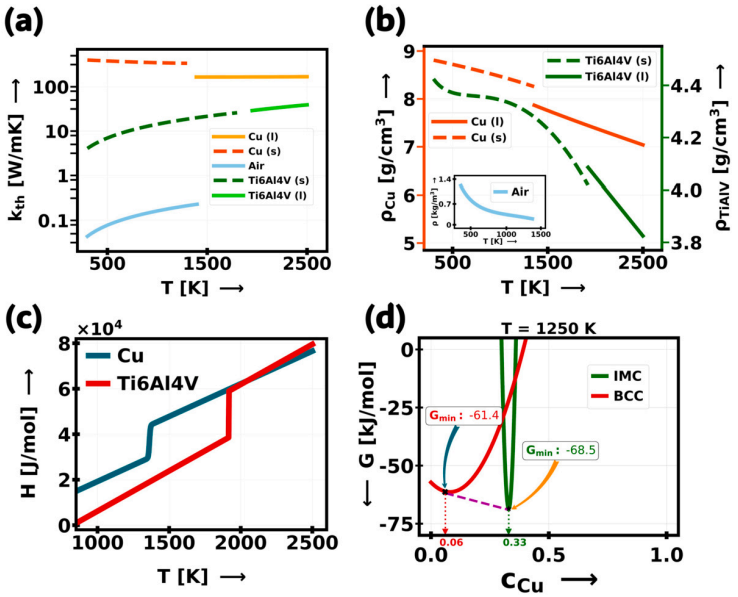


Fig. 4. (a) Thermal conductivity (k_{th}) as a function of temperature (T) across various materials and phases. **(b)** T-dependent density (ρ) of phases. **(c)** Enthalpies of Copper and Ti6Al4V are expressed as a function of temperature. **(d)** Parabolically fitted Gibbs free energy of IMC and BCC phases at 1250 K.

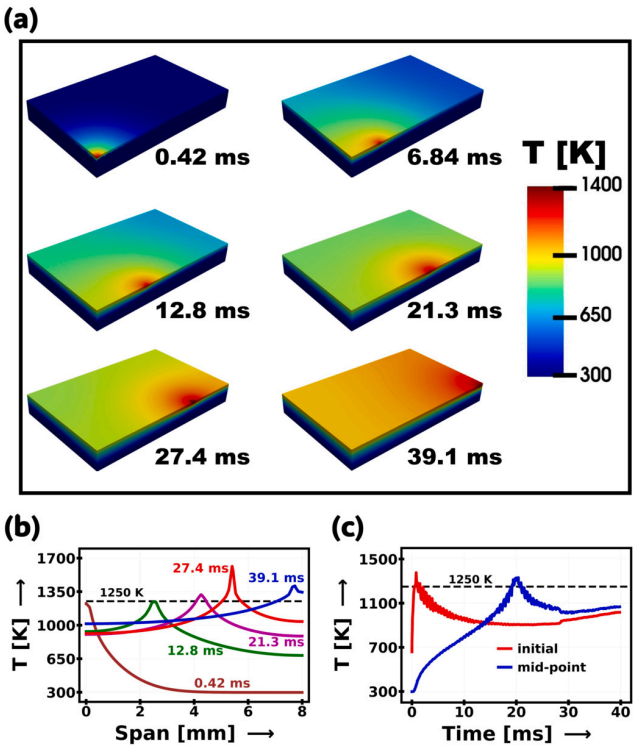


Fig. 5. The transient thermal distribution profiles **(a)** for the 3D computational domain, and **(b)** along the scanning direction (line at which the center of the beam spot passes) at t = 0.42, 6.84, 12.8, 21.3, 27.4 and 39.1 ms. The thermal cycle illustrations in **(c)** are the temporal evolution of temperature field for the starting (initial) point and mid-point of the domain located at the scanning path. The peaks of the curves are when these points are intersected by the center point of the beam during its journey.

initial model set up will take the material properties of the substrate at both solid (s) and liquid (l) states. As Eq. (2) is primarily concerned in the computation of thermal history, and not on microstructure evolution; the formation of intermetallic phase is ignored at this stage and the material properties at the interface are interpolated as the average values of the properties for the top layer and the substrate.

Apparent heat capacity, expressed as $\overline{C_i} = \frac{\partial H_j/\partial t}{\partial T/\partial t}$, is computed using the H-T curves for top and substrate layers. The thermal conductivity ($k_{th,Ti6Al4V(j)}$) and the density $\rho_{Ti6Al4V(j)}$ of jth state (j = liquid or solid) continuum Ti6Al4V substrate can be expressed solely as the functions of temperature as provided in Appendix A.2 (Table A1, A2) and Figs. 4**(a)** and 4**(b)** respectively. However, the powder bed on the top, has been approximated as an equivalent continuum material consisting of spherical Cu particles in the matrix of gaseous air [37]. As mentioned earlier, the proportion of gaseous air within the powder bed is quantified by ϕ. For the powder bed consisting initially of Cu powder, T_s = 1173.0 K and T_m = 1358.0 K. For T ≤ 1173.0 K, porosity is assumed to maintain its constant initial value of 0.45, and ϕ will start decreasing when T exceeds the sintering temperature. That is, sintering between Cu powder particles will result in decrease of porosity. When the powder melts, the liquid state is assumed to have zero porosity i.e. ϕ = 0 at T ≥ 1358.0 K. For numerical depiction of the different cases of thermal conductivity property in the powder bed region, the thermal conductivity of continuum solid Cu(s) is denoted as k_{th}^{bulk}, that of continuum liquid phase Cu(l) as k_{th}^{liquid} and finally that of continuum gaseous air as k_{th}^{air}. The T-dependence of k_{th}^{bulk}, k_{th}^{liquid} and k_{th}^{air} are presented in Appendix A.1 (Table A1) and Figs. 4**(a)**. Eventually, the thermal conductivity of powder Cu, k_{th}^{powder} can be defined by Eq. (3):

$$k_{th}^{powder} = (1-\phi)k_{th}^{bulk} + \phi k_{th}^{air} \tag{3}$$

So, the effective thermal conductivity of top layer that incorporates the conductivities of pre-sintered powder, sintered powder and molten Cu will be holistically represented by the case Eq. (4):

$$k_{\text{th,top}} = \begin{cases} k_{\text{th}}^{\text{powder}} & ; T \le T_s \\ \left(k_{\text{th}}^{\text{bulk}} - k_{\text{th}}^{\text{powder}}\right)\left(\frac{T-T_s}{T_m-T_s}\right) + k_{\text{th}}^{\text{powder}} & ; T_s \le T \le T_m \\ k_{\text{th}}^{\text{liquid}} & ; T_m \le T \end{cases} \tag{4}$$

The densities for the powder bed layer in the computational domain are quantified in the similar way. ρ^{bulk} of Cu(s), ρ^{liquid} of Cu(l) and ρ^{air} of

gaseous air are presented in Appendix 2 (Table A2) and Fig. 4**(b)**. The powder's equivalent density is given by Eq. (5). The overall density of top layer is then expressed by Eq. (6)

$$\rho^{powder} = (1-\phi)\rho^{bulk} + \phi\rho^{air} \tag{5}$$

$$\rho_{\text{top}} = \begin{cases} \rho_{\text{powder}} & ; T \le T_s \\ \left(\frac{\rho^{\text{bulk}} - \rho^{\text{powder}}}{T_m - T_s}\right)(T - T_s) + \rho^{\text{powder}} & ; T_s \le T \le T_m \\ \rho_{\text{liquid}} & ; T \ge T_m \end{cases} \tag{6}$$

The heat source type for the experimental TruDisk 3302 laser is flat top. Therefore, irradiation intensity (I_{flat}) of the source term Q_{laser} in Eq. (2) can be expressed by the following super-Gaussian function [38]:

$$I = \frac{A^{1/k} P k \lambda}{\pi r_o^2 \Gamma(1/k)} \exp\left[-C\left(\frac{r}{r_0}\right)^{2k}\right] \tag{7}$$

$$\Gamma(\mathbf{1/k}) = \int_0^\infty t^{\frac{1}{k}-1} e^{-t} dt \tag{8}$$

where P represents the laser power, λ denotes the efficiency, k is super-Gaussian order, $\Gamma(1/k)$ represents the gamma function of 1/k expressed by Eq. (8) and r_0 stands for the equivalent beam radius. With P = 1000 W, $k = 3$ (for flat top $k > 0$), $\lambda = 0.9$, $r_0 = 122.5$ μm and C = 2.0, the distribution of intensity appears as shown in Fig. 1(b). The peak value of intensity (I_{peak}) for the flat top heat source beam is 26.94 kW/mm^2. The initial position of the beam center is defined by the radial displacement of point (x, y) relative to the center (x(t), y_0) of a itinerant beam. The velocity of laser scanning, denoted as (V_s), is characterized by its definition $V_s = \frac{\partial x}{dt} = \frac{x(t)-x_0}{t}$. The behavior of fluid motion within the molten pool is elucidated through the incompressible Navier-Stokes equations.

The outcomes derived from finite element analysis at a designated power of 1000 W, as depicted in Fig. 5**(a)**, offer an intricate scrutiny of the spatiotemporal evolution of temperature within the computational framework. Upon reaching a simulation conclusion at $t = 39.1$ ms, the focal point of the laser has traversed the entirety of the Cu-Ti6Al4V computational domain, propelled by a scanning velocity (Vs) of 200 mm/s. Under these conditions of power and scanning velocity, the apex temperature attains 1250 Kelvin. Despite a protracted duration of $t = 39.1$ ms for total laser surface alloying, the pivotal interface within the computational realm, subject to 1000 W and 200 mm/s parameters, remains below the respective melting thresholds of Ti6Al4V and Cu. Fig. 5(b) depicts the spatial distribution of temperatures across the upper surface of the domain along the x-axis, synchronized with the lateral movement of the laser from left to right, showcasing distinct temperature profiles captured at five discrete time intervals.

Fig. 5**(c)** delineates the trajectory of temperature variations throughout the Laser Surface Alloying process. This graphical representation elucidates the thermal cycle at specific junctures within the interface, emphasizing the initial and intermediate stages. Initially, a discernible surge in temperature underscores the rapid absorption of energy from the laser, culminating in the fusion of the titanium alloy and copper constituents.

2.2.2. Phase field modeling of heterostructure formation

As highlighted in the previous section, the temperature at the interface between the powder bed and the substrate can reach temperature larger than 1250.0 K (refer Fig. 5(c)) at some point of time during application of laser irradiation. At such elevated temperature values, interdiffusion mechanism is very significant to cause the diffusion based transport of elements Ti, Al, Cu and V in the multiphase system. The diffusion of Cu elements from top layer (Cu-rich zone) into the substrate transforms the latter into a quaternary Ti-Al-V-Cu system. The non-uniform and unsteady nature of temperature profile along the substrate geometry (refer Geometrical Figure of FEA) is significant enough to cause heterogeneity in the distribution of Cu elements within the substrate. Larger proportion of Cu species is present near the top surface due to lower radial distance from the moving beam spot, and Cu concentration decreases with the increase in depth of the substrate. Owing to this reality, the computational domain of interest for the phase field modeling is the substrate microstructure at the vicinity of the initial powder bed. Due to sintering induced densification, the overall thickness of the initial powder bed will shrink and the distance between the surface and interface will decrease. For phase field modeling, the microstructural domain of the bulk substrate Ti-Al-V-Cu alloy that is effectively at a location well within 5 μm from the original interface is considered. Within this domain of the multicomponent Ti-Al-V-Cu substrate, some sub-regions consisting of relatively larger proportion of Cu are associated with the nucleation of Ti_xCu_y intermetallics. As will be revealed later from SEM micrographs in Sec. 3, the dominant intermetallic is Ti_2Cu. As these intermetallics are found as discrete phases in the bulk of substrate, they will be termed as primary Ti_2Cu phases. The broader regions of multicomponent Ti-Al-V-Cu substrate that have not so much high concentration of Cu remain as Ti-Al-V-Cu alloy.

A simplified phase field model is designed by neglecting the role of Al and V in the diffusion based properties of Ti-Al-V-Cu alloy. That is the model will portray the behavior of a binary Ti-Cu system. While titanium-rich phase exhibits a hexagonal closed-packed (HCP) structure below 1155 K, it transforms to a body-centered cubic (BCC) phase at elevated temperatures [39]. At 1250 K, Ti-rich phase will have a BCC crystal structure. In this study, two simulations (Case I and Case II) are carried out in a computational domain of 500 $nm \times 500$ nm which consists of two phases namely (Ti-rich) BCC and 4 Ti_2Cu IMC grains. Initially, for Case I and Case II, the area of BCC phase is designed to be 2.1×10^5 nm^2 and 2.08×10^5 nm^2 respectively. Whereas the combined area of all IMC grains (G_1, G_2, G_3 and G_4) sums up to 0.4×10^5 nm^2 and 0.42×10^5 nm^2 for the first and second cases. To track the spatio-temporal evolution of individual phases, we assign each phase and grains with a special kind of non-conserved phase field variable called order parameter (η_i) whose value is taken as 1 inside the phase i and 0 outside the phase. In the binary Ti-Cu system, a single conserved composition variable "c" (molar fraction of Cu, c^{Cu}) can represent the whole computational domain's compositional information. For the two distinct phases, the local mole fraction of Cu is given by c_{bcc} and c_{imc} for BCC and IMC phases respectively. Fig. 6 illustrates the considered computational domain of 2-Phase 5-order-parameter system.

A multiphase system needs a thermodynamically accurate function that can swiftly interpolate the material properties and their characteristics among the distinct phases across their interface. For this purpose we employ the function $h_i(\eta)$ introduced by Moelans [40]. Based on the grains representing each phase, this interpolation function is divided into two expressions, for the phase with single grain i.e. BCC phase the function is defined as Expression (9), whereas for the IMC phase with 4 grains, the interpolation function is given by Equation (10) [41].

$$h_i = \frac{\eta_i^2}{\sum_{k=1}^{N} \eta_k^2} \tag{9}$$

$$h_i = \frac{\sum_{j=1}^{4} \eta_{i,j}^2}{\sum_{k=1}^{N} \eta_k^2} \tag{10}$$

The current model is a 2 phase 5 order parameter system, and so N = 5 in the above equations. Another simplification made in this model is the assumption of equivalent isothermal condition for description of input material properties. An unsteady temperature profile generated by laser heating means that the T-dependent material properties have to evolve with time, and non-uniform thermal distribution causes these properties to differ along top and bottom locations of the microstructural domain. Moreover, the Cu species diffusing from the top layer can start from a location at a very high initial temperature, and during their journey into the microstructural domain can face situation of reduced

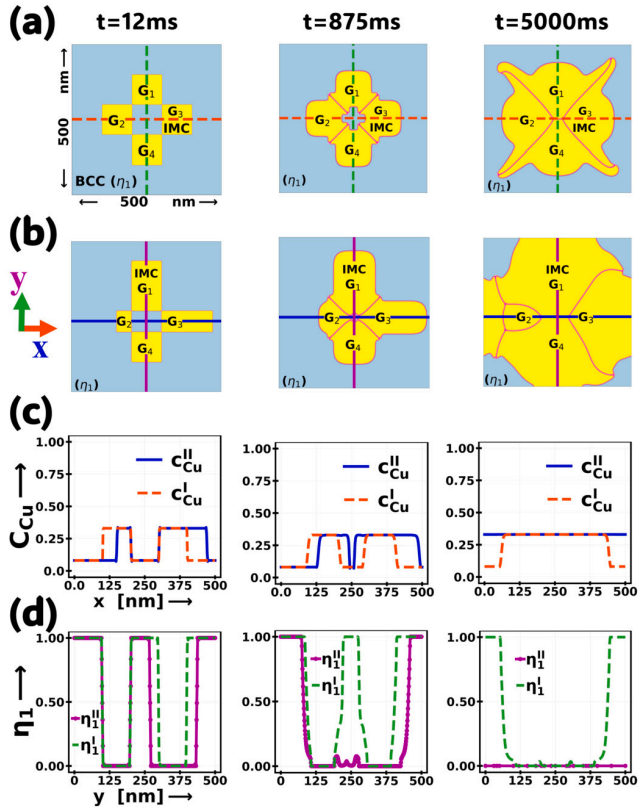


Fig. 6. The illustration depicts the evolution of compositionally heterogeneous structures i.e. IMC grains and BCC phase within a computational domain measuring 500 *nm* × 500 *nm* for two distinct cases, showcasing the progression at time intervals of t = 12 ms, t = 875 ms, and t = 5000 ms. The model comprises a 2-phase 5-order-parameters system, with the BCC phase denoted by η_1 in a light blue-colored region, and four IMC grains labeled as G_1, G_2, G_3, and G_4 depicted in yellow. **(a)** Demonstrates the phase evolution in Case I, where uniform IMC grain area is evident at three time points of the simulation. The growth of IMC grains follows a symmetrical pattern, expanding equally in all directions. **(b)** In Case II, characterized by non-uniform initial grain area, the growth of IMC grains exhibits a non-linear trajectory. Larger grains grow faster and larger compared to smaller ones. Due to periodic boundary conditions along the x-direction, grain G_3 appears on the left side at time t = 5000 ms. **(c)** The plot illustrates the evolution of global composition (c) along the horizontal marked lines for Case I (orange dotted line) and Case II (blue solid line). Notably, the composition within the BCC phase is minimal, while inside the IMC, it increases to 0.33 for both cases. **(d)** The graph presents the values for the non-conserved order parameter (η_1) associated with the BCC phase along the vertical midpoint of the computational domain, indicated by the green dotted line and solid magenta line in **(a)** and **(b)** respectively. It is observed that for both cases at t = 12 ms, η_1 initiates with a value of 1 within the light-blue region, subsequently dropping to 0, indicating a phase shift from BCC to IMC, coinciding with the emergence of IMC grain G_4. The BCC phase reappears at the midpoint, elevating the magnitude of η_1 back to 1. The value then decreases within grain G_1, before rising back to 1 near the top end of the computational domain. Due to the evolving phase, at t = 875 ms, the BCC phase in the middle of the domain is consumed by IMC grains, as evidenced by the magenta line dropping to zero and the thinning of the dotted green line at y = 250 nm. Similarly, at t = 5000 ms, a complete disappearance of the magenta and dotted green lines to zero at y = 250 nm is observed.

temperature. These challenges can be simplified by assuming equivalent isothermal condition, and a constant temperature of 1250.0 K (depicted in thermal history image of Fig. T-t) has been selected in the phase field model. As illustrated in Fig. T-span, this constant temperature of 1250. K is not only located midway between the peak temperature and minimum temperature for red curve but also is intersected by the majority of the curves during the mid-journey of the laser.

Table 3
Coefficients of composition-dependent Gibbs free energy at 1250 K.

Coeff / Phases	BCC	IMC
A_i (J/mol)	634492.7	76756681.3
B_i (J/mol)	138293.9	175805.5
C_i (J/mol)	-53822.5	-68421.6

Table 4
The input parameters and material characteristics employed in the phase field simulation.

Parameters	Values
V_m (cm^3/mol)	7.11 [45]
δ (nm)	10
σ (J/m^2)	0.5
m (J/m^3)	2×10^{-8}
κ (J/m)	5×10^{-9}
M_{IMC} (m^5/Js)	2×10^{-16}
M_{BCC} (m^5/Js)	2×10^{-18}
M_{gb} (m^5/Js)	2×10^{-14}

The spatio-temporal morphological changes that occur in the microstructure are primarily driven by the free energies of the system, and for modeling microstructural evolution we have considered the two major energies: bulk chemical free energy (F_{chem}) and interfacial energy (F_{int}) expressed as Equation (11)

$$F_{total} = F_{chem} + F_{int} = \int_V (f_{chem} + f_{int})dV \tag{11}$$

The bulk free energy density (f_{chem}) and interfacial free energy density (f_{int}) are further expressed in Equation (12) and (14) respectively.

$$f_{chem} = \sum_i h_i f^i_{chem} = \sum_i \frac{G^i_m}{V_m} \tag{12}$$

In the above equation, bulk chemical free energy of i^{th} phase is denoted as (f^i_{chem}). The molar volume V_m provided in Table 4 is assumed to be equal in both phases. The term G^i_m represents the molar Gibbs free energy of phase i at T = 1250.0 K, fitted from the thermodynamic database (TDB) file [42]. For the Ti_2Cu IMC, a parabolic composition dependence is assumed here to achieve a higher order differentiability of free energy function. The composition dependent Gibbs free energy function for phase i is expressed in Equation (13).

$$G_i = A_i(c - c^i_{eq})^2 + B_i(c - c^i_{eq}) + C_i \tag{13}$$

where the coefficients A^i, B^i, and C^i, for BCC and IMC phases are tabulated in Table 3, and Fig. 4**d** illustrates the parabolic fitted Gibbs free energy for two phases, red curve representing BCC phase with minimum free energy value of -61.358 kJ/mol and green curve for IMC phase with the overall lowest free energy value of -68.522 kJ/mol at a temperature of 1250 K.

The composition at which the IMC phase reaches equilibrium with the BCC phase (IMC/BCC) is given by the projection of tangent point (green dotted line with arrow at composition axis) to the green curve (IMC) drawn from the red curve (BCC), whereas for the equilibrium composition c_{eq} for BCC phase to be in equilibrium with IMC phase is given by the projection of tangent point at red (BCC) curve drawn from the green (IMC) curve as denoted by dotted red line with arrow pointing at the composition axis in the Fig. 4**d**. These equilibrium compositional points are calculated using a open-source equilibrium point finder WebApp [43].

The interfacial free energy density f_{int} can be expressed mathematically as follows:

$$f_{int} = m f_{barrier} + \frac{\kappa}{2}\sum_i (\nabla \eta_i)^2 \tag{14}$$

Now, let's discuss about the quantities associated with f_{int}. Quantified in Table 4, the diffused interface width ($\delta[m]$) and the interface energy $\sigma[J/m^2]$ are related to model parameters "m" and "k" by following expressions:

$$m = 6 \times \frac{\sigma}{\delta} \tag{15}$$

$$\kappa = \frac{3}{4} \times \delta\sigma \tag{16}$$

The term $f_{barrier}$ in Equation (14) is given by the Expression (17), which is a fourth order Landau polynomial of the phase field variable [41].

$$f_{barrier} = \sum_i \left(\frac{(\eta_i)^4}{4} - \frac{(\eta_i)^2}{2} \right) + \gamma \sum_i \sum_{j \neq i} \eta_i^2 \eta_j^2 + \frac{1}{4} \tag{17}$$

The spatio-temporal evolution of conserved variable ("c") occurs with a gradient in composition field which is expressed in Equation (18).

$$\frac{\partial c}{\partial t} = \nabla . \left(\sum h_i M_i \right) \nabla \left(\frac{\partial f_{bulk}}{\partial c^i} \right) \tag{18}$$

where, M_i denotes the Cahn-Hilliard mobility of phase "i", contingent upon the diffusivity of phase D_i, thermodynamic factors, and grain boundary mobility M_{gb}, as delineated below.

$$M_i = \frac{D_i}{A_i} + \sum_{j \neq i} h_j M_{gb} \tag{19}$$

In this work, M_{gb} is taken 100 times the bulk phase mobility of IMC [44].

The evolution of phases along with all the IMC grains dictated by the diffusion mechanics is given by the following Alan-Cahn type Expression (20).

$$\frac{\partial \eta_i}{\partial t} = -L\left(\eta_1, ..., \eta_N\right) \left(\frac{\partial f_{bulk}}{\partial \eta_i} - \nabla \cdot \frac{\partial f_{int}}{\partial \nabla \eta_i} \right) \tag{20}$$

where $L(\eta_1, ..., \eta_N) = L_i$ is further defined in Equation (21).

$$L_i = \frac{\sum_{i=1}^{N} \sum_{j>1}^{N} L_{ij} \eta_i^2 \eta_j^2}{\sum_{i=1}^{N} \sum_{j>1}^{N} \eta_i^2 \eta_j^2} \tag{21}$$

the term L_{ij} is the interfacial mobility, for the current study of Ti-Cu binary system it is approximated as Equation (22).

$$L_{ij} = \frac{4m}{3\kappa} \times \frac{M_i + M_j}{2 \times (c^i_{i,eq,j} - c^j_{j,eq,i})(c^i_{i,eq,j} - c^j_{j,eq,i})} \tag{22}$$

Where M_i and M_j are the mobilities of i^{th} and j^{th} phases respectively, from Fig. 4**d** the quantity $(c^i_{i,eq,j} - c^j_{j,eq,i})$ is obtained as 0.27.

3. Discussions

The study reveals the dynamic evolution of IMC and BCC phases within a 500 *nm* × 500 *nm* computational domain under two distinct scenarios (Case I and Case II). The growth of Ti_2Cu IMC grains in the Ti6Al4V matrix phase is attributed to the lower Gibbs free energy of the IMC phase (-68.522 kJ/mol) compared to BCC (-61.358 kJ/mol) illustrated in Fig. 4**d**. In Case I, equality of individual IMC grain area at t = 0 is evident, showcasing symmetrical growth, whereas in Case II, characterized by non-identical initial individual grain area, the growth trajectory exhibits non-linearity, with larger grains expanding faster as depicted in Fig. 7. The total area of IMC phase (combined areas of G_1, G_2, G_3 and G_4) is nearly same for both cases at t = 0. For Case I, each individual grain is a square of area 0.1E+05 nm^2 initially (length of 100 *nm*). However, for Case II, the individual grains have different areas and aspect ratios initially. The G_4 of both cases have identical profile initially. The G_2 of Case II is a rectangle of smaller area (50 *nm* × 70 *nm*) than the square G_2 of Case I. While G_1 (100 *nm* × 165 *nm*), and G_3 (170 *nm* × 70 *nm*) of Case II are rectangles, the corresponding grains in Case I are squares. While the lengths of these both rectangles (Case II) are longer than the length of square grains of Case I, the breadth of rectangular G_1 is identical to that of the length of square G_1. The breadth of rectangular G_3 is smaller than that of square G_3. These initial morphologies of nucleated grains will have a significant impact on the kinetics of evolution. In context of Case II, besides the driving force related to the chemical free energy of different phases, the curvature driven growth [47–50] associated with the grain shape will promote the overall growth gain the area at the expense of the relatively narrower and smaller G_2 grain. Since G_1 being longer than G_4, the former will have the largest area at t = 5000 ms. The length of G_3 is larger initially, its initial area is quite large and the periodic boundary condition ensures that it also grows horizontally at the expense of shorter and narrower G_1 grain. However its vertical growth is in a good competition with the growing G_1 and G_4 grains. The grain growth rate (V) due to grain or phase boundary curvature is $V = -M_{ij}.\sigma\tau$. The net curvature between two adjacent grains or phase is expressed as $\tau = \frac{1}{r_1} - \frac{1}{r_2}$. In context of Case I, the identical grain nuclei will offer resistance to the growth of adjacent IMC grains as they have the same curvature based driving force, and the net curvature driving force between adjacent IMC grains is zero. Still the curvature based driving force between grains and matrix phase is non-zero. The identical grains (Case I) can only grow at the expense of BCC matrix phase. Hence the presence of additional curvature based driving force between two non-identical grains helps in the attainment of larger overall area of IMC phase in context of Case II. Despite comparable initial IMC phase areas, Case II exhibits a visibly greater rate of IMC phase growth, reaching a total area twice that of Case I by the end of the simulation (t = 5000 ms) as shown in Fig. 7**a**. While the total area of Ti_2Cu IMC phase in context of Case I is 1.2E+05 nm^2, it is already around 2.08E+05 nm^2 for Case II. During the laser processing, the non-uniform and transient thermal profile can result in the nucleation and growth of randomly sized and shaped IMC grains. These grains will then grow into patterned grains as shown in Fig. 9(d). With the analysis of equivalent grain radius Fig. 7**b** [46], we observed that the growth of IMC grain is a non-linear process primarily guided by the driving free energy and surrounding grains. The grain G_2 of Case I (initial equivalent radius of around 55 nm) grows continually at the expense of matrix BCC phase and attains the value of 95.75 nm at t = 5000 ms. However, the G_2 of Case I expands initially from 33.37 nm equivalent radius to a value of 64.33 nm at t = 3750 nm. However, the curvature driven effect when it is entirely surrounded by G_1, G_3 and G_4 leaves its equivalent radius to a value of 54.52 nm at t = 5000 ms. As Case II represents the more realistic condition of laser processed samples, the presence of irregularly shaped microstructure of IMC grains of Fig. 9(d) is anticipated in the experimental samples consisting of Ti6Al4V + Ti_2Cu heterostructures.

The optical micrographs presented in Fig. 8**a** to Fig. 8**d** illustrate significant microstructural changes across the fusion zone, heat-affected region, and matrix resulting from the laser surface alloying. In Fig. 8**a** the micrographs reveal the fusion zone where the titanium alloy surface has undergone laser-induced alloying with Cu, showcasing refined microstructures and the formation of new phases due to the complex interactions among the laser beam, titanium alloy, and the introduced copper. Adjacent to this zone, the heat-affected region is visible, where thermal transformations have occurred without direct melting. The microstructural characteristics at the fusion boundary, shown in Fig. 8**b** highlight marked differences between the fusion zone and the matrix. Notably, fine-grained structures are observed, particularly in the lower

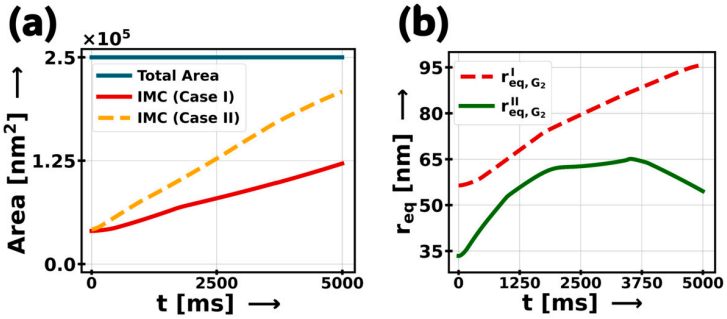


Fig. 7. Plots illustrating the temporal evolution of IMC grain areas and equivalent grain radius for two simulation cases. **(a)** Visualization of IMC grain growth in Case I (equal initial grain size) and Case II (non-uniform grain size at beginning), although the total initial IMC phase area for both cases are near equal (≈ 0.41 × 10^5 nm^2), the rate of IMC Phase growth for non-uniform grain is visibly greater and by the end of t = 5000 ms, the total IMC area for Case II sums to 2.08 × 10^5 nm^2 where as for Case I it is limited to just 1.21 × 10^5 nm^2. **(b)** A non-linear growth pattern of IMC grain (G_3) shown in an equivalent radius form [46]. For Case I, the grain continuous to grow until the end of the simulation whereas for Case II, grain G_2 grows for a while and gets squeezed by neighboring grains subsequent decreasing the area and equivalent radius in the later half of the simulation.

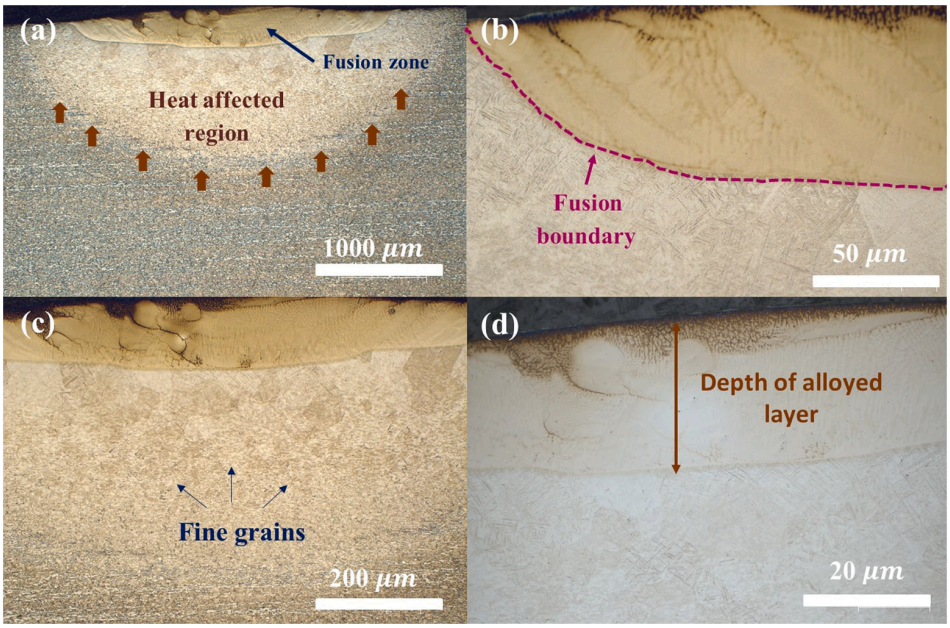


Fig. 8. Optical micrographs of the Ti6Al4V-Cu alloy, showcasing microstructural changes at different magnifications. **(a)** Overview of the fusion zone and heat-affected region at low magnification, highlighting the area of laser-induced alloying **(b)** Detailed view of the fusion boundary and the transition into the matrix **(c)** The refined microstructures **(d)** Depth of alloying.

sections of the fused areas Fig. 8**c** indicating rapid cooling and swift solidification following the laser treatment. The presence of these refined grains underscores the successful execution of the alloying process, evidencing the effective dispersion of copper within the Ti6Al4V matrix. The depth of the alloyed layer indicates the extent of modification achieved (Fig. 8**d**).

Fig. 9**(a)** presents the X-ray diffraction (XRD) analysis of the laser surface alloyed (LSAed) sample, substrate (Ti6Al4V), and Cu powder. Notably, three distinct peaks were detected at 2θ values of 50.861°, 59.451°, and 89.052°, corresponding to the (111), (002), and (022) planes of copper, as illustrated in Fig. 9**a(i)**. This observation confirms the crystalline nature of the resulting particles as cubic nanostructured copper powder. Such findings are consistent with the research of Jinping et al. [51] and Sun et al. [52] who identified similar diffraction peaks, affirming the cubic crystalline structure of copper nanoparticles. The exceptional properties of Copper Nano powder, including outstanding conductivity, catalytic behavior, excellent compatibility, and antibacterial characteristics [53,54] make it a promising material for various applications. Fig. 9**a(ii)** and Fig. 9**a(iii)** depict the XRD patterns of Ti6Al4V and Ti-Al-V-Cu alloys, respectively, revealing predominantly the presence of the Ti-α phase in both cases and a minor diffraction peak of Ti-β. Moreover, Fig. 9**a(iii)** shows the emergence of new peaks. This new peak indicates the formation of new intermetallic compound (Ti_2Cu phases) due to the super saturation of copper within the Ti-matrix during the laser surface alloying process. Furthermore, some of the new peaks in Fig. 9**a(iii)** exhibit broadening compared to Ti6Al4V sample, which may be indicative of changes in crystal structure or fine grain size resulting from the laser surface alloying process.

Laser transitions are observed in the image from the scanning electron microscope (Fig. 9**c**), causing the Cu element to melt together with the Ti6Al4V material in varying proportions. This results in a laminar structure, indicated by the gray color lamellar formation, which suggests the presence of the Ti_2Cu intermetallic compound (IMC). The elemental variations across this area are shown in Fig. 10. A laminar structure in the Ti6Al4V-Cu alloy aligns with findings from other studies, such as Z. Sun et al. [55], who observed similar lamellar structures in tita-

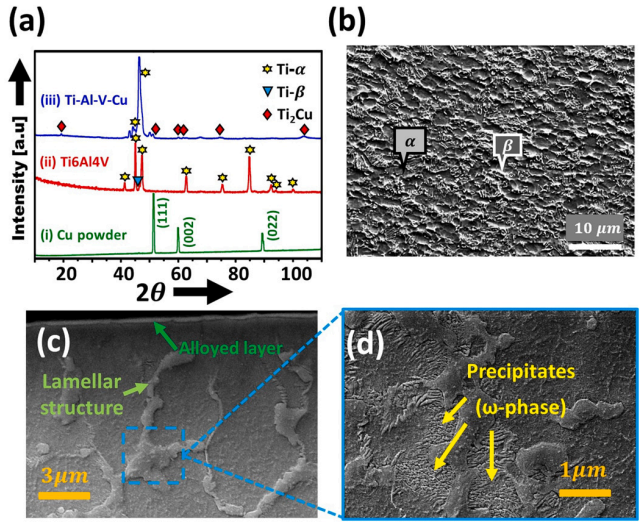


Fig. 9. Results of microstructural characterization: **(a)** X-ray diffraction profile of: (i) Cu powder, (ii) Ti6Al4V, (iii) Ti-Al-V-Cu; **(b)** The SEM micrograph of Ti6Al4V alloy prior to laser alloying is shown; dark and light regions are α and β-phases respectively **(c)**; The image in **(d)** is the magnified view of the highlighted region of **(c)**.

nium alloys subjected to surface alloying. Specifically, they noted the formation of a lamellar structure in the microstructural evolution of Ti6Al4V/Inconel625 gradient coating alloy. Additionally, Fig. 9**d** highlights the presence of ω-phase precipitates finely dispersed within the β-phase, with a distinct correlation to the β-phase orientation. The finer dimensions of the ω-phase are notable, as revealed by Energy Dispersive Spectroscopy (EDS) spectra of the brighter phase which indicate an elemental composition of approximately 65.62 at.% Ti, 5.71 at.% Al, 1.79 at.% V, and 26.89 at.% Cu.

The confocal microscopy allowed multidimensional imaging of bacterial cells. The images revealed live bacteria stained green with SYTO9 and dead bacteria stained red. Analysis of these images showed a distribution of stained bacteria, with the results expressed as the cumulative signal from the green and red channels as shown in Fig. 11**(a)** and 11**(b)**. The analysis of the LIVE/DEAD® assay results, visualized via microscopic images (Fig. 11**(c)** and 11**(d)**, demonstrated distinct signals for live (green) and dead (red) bacterial cells. Quantitative data from the Varioskan LUX microplate reader indicated the signals of viable bacteria, plotted in corresponding charts. The data provided insights into the extent of bacterial colonization and viability on the tested materials.

4. Conclusions

The study integrates experimental and computational techniques to understand the interfacial intermetallic formation within the Ti6Al4V-Cu system. A laminar structure was observed in scanning electron microscope images, indicating Ti_2Cu intermetallic compound formation. X-ray diffraction analysis confirms new intermetallic compound formation, validating laser surface alloying's effectiveness in enhancing antibacterial properties.

The outcomes derived from FEA under an identified power of 1000 W and scanning velocity of 200 mm/s offer an exhaustive exploration of the spatiotemporal temperature progression within the computational domain. Despite an extended duration of laser surface alloying, the interface point subjected to specific parameters remains below the melting points of Ti6Al4V and Cu. This underscores the effectiveness of the laser surface alloying process in controlling temperature evolution and preventing excessive melting. Overall, the thermal history determination using finite element analysis offers valuable insights into the thermal dynamics and microstructural evolution during the alloying process, contributing to a broad comprehension of the laser surface alloying process and its impact on material properties.

The phase field model provides insights into the temperature distribution, interdiffusion mechanisms, and the transformation of the substrate into a quaternary Ti-Al-V-Cu system. It also reveals the nucleation

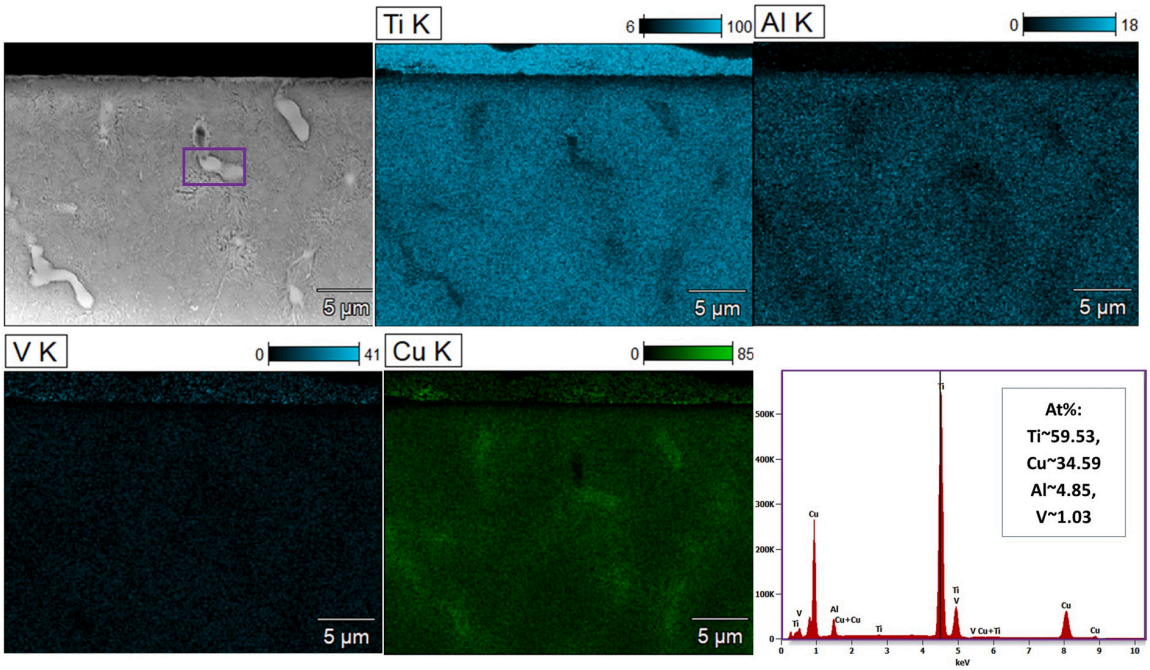


Fig. 10. Energy-dispersive X-ray spectroscopy (EDS) analysis performed on the lamellar structure. The annotated region with purple colored rectangle in the top left image shows the portion of the microstructure that has been probed by the instrument for the quantitative compositional analysis presented at the bottom left image. The four remaining images exhibit the EDX mapping for the elements Ti, Al, V and Cu in the total microstructural region of image at top left.

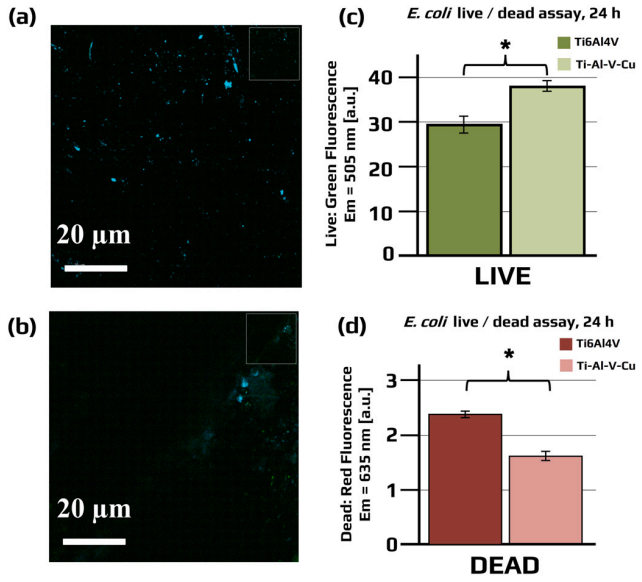


Fig. 11. Positive indications of viable stained *E. coli* (appearing as blue signals) were observed following 24 hours of incubation on the specimens. Fluorescence microscopy shows live cells (SYTO 9, green) on **(a)** Ti6Al4V and **(b)** Ti-Al-V-Cu samples. The bar charts show the quantified signals of **(c)** live and **(d)** dead bacteria. The superior antibacterial performance of the Ti-Al-V-Cu alloy can be attributed to the presence of the Cu element.

of intermetallic compounds, particularly the primary Ti_2Cu phases, within the substrate. The model's simplifications, such as neglecting the role of Al and V in the diffusion-based properties and assuming equivalent isothermal conditions, contribute to a comprehensive understanding of the evolution of primary Ti_2Cu intermetallic. Additionally, the model's findings shed light on the growth behavior of intermetallic grains and their preferential growth driven by the driving free energy and surrounding grains. Overall, the phase field model provides profound insights into the intricate interdiffusion mechanisms and dynamics of the Ti-Cu system throughout laser surface alloying.

The microbiological study revealed that Ti-Al-V-Cu exhibited greater inhibition of bacteria compared to that of control (Ti6Al4V). The study on developing an advanced biomedical material through laser additive manufacturing focuses explicitly on the growth of Ti_2Cu intermetallic grains within a Ti6Al4V matrix. This material shows promise for use in biomedical implants due to its enhanced antibacterial properties, attributed to copper integration into the titanium alloy. The study uses experimental techniques and computational methods to understand the temperature dynamics and microstructural evolution during the alloying process. The resulting material demonstrates superior antibacterial efficacy against bacterial strains like E. coli. This research contributes to biomaterials by providing a method to create implants with improved antibacterial performance, which is critical for reducing the risk of implant-related infections.

CRediT authorship contribution statement

Hana Beyene Mamo: Writing – original draft, Visualization, Validation, Software, Methodology, Investigation. **Upadesh Subedi:** Writing – review & editing, Visualization, Validation, Software, Methodology, Investigation. **Tomasz Poloczek:** Writing – review & editing, Validation, Investigation. **Marcin Adamiak:** Writing – review & editing, Supervision, Methodology, Conceptualization. **Augustine Nana Sekyi Appiah:** Writing – review & editing, Investigation. **Magdalena Skonieczna:** Writing – review & editing, Investigation. **Paweł M. Nuckowski:** Writing – review & editing, Investigation. **Yaoxiang Geng:** Writing – review & editing, Supervision, Methodology, Funding acquisition. **Barun Haldar:** Writing – review & editing, Supervision, Methodology. **Anil Kunwar:** Writing – review & editing, Supervision, Software, Project administration, Methodology, Investigation, Funding acquisition, Data curation, Conceptualization.

Declaration of competing interest

The authors declare that they have no known competing financial interests or personal relationships that could have appeared to influence the work reported in this paper.

Data availability

As outlined in the Methodology section (Section 2), the data in this study are categorized based on either the experimental methods (Sec. 2.1) or numerical methods (Sec. 2.2). The data related to the experimental work are available at https://github.com/abeyenem/Experimental-Data. The remaining data belong to the finite element method-based numerical approaches of Sec. 2.2.1 (Thermal history analysis) and Sec. 2.2.2 (Phase field modeling). The codes and data related to finite element analyis for thermal history determination are available at https://github.com/anilkunwar/effective_material_properties. The data and codes associated with phase field simulations can be accessed at https://github.com/subediupadesh/Ti2Cu_IMC_evolution.

Acknowledgement

This work was supported by the National Science Centre, Poland (UMO-2021/42/E/ST5/00339) and the National Natural Science Foundation of China (Grant Number: 52001140).

Appendix A

A.1. Theory of fluid flow in meltpool

During laser processing, only a limited volume fraction of the Cu powder region bed undergoes melting (T > 1358 K) at a given time. Within this melt pool zone, the fluid flow is characterized by the following incompressible Navier-Stokes equations:

$$\nabla.\vec{u} = 0 \tag{A1}$$

$$\rho_i \frac{\partial \vec{u}}{\partial t} + \rho(\vec{u}.\nabla)\vec{u} = \nabla.[-pI + \nu_i(\nabla\vec{u} + (\nabla\vec{u})^T)] + F_i \tag{A2}$$

Eqs. (A1) and (A2) are respectively the continuity and momentum equations. Velocity ($\vec{u}$) and pressure (p) are the velocity and pressure variable. In the present study only portions of the upper region consisting of Cu powder bed can reach the molten state whereas the Ti6Al4V substrate remains well within the solid state. While the viscosity (ν_i) is assumed to decrease exponentially with temperature in liquid state, it is considered to be an asymptotic viscosity in the mushy zone. At 1358.8 K and 1358.9 K, the portion of powder bed which is in mushy zone has been assigned viscosity values of 0.83 and 0.44 Pa s respectively. However, at 1360 K, the liquid viscosity has already been given a highly reduced value of 2.45 mPa s. The viscosity values for the liquid Cu at 1400 K is 2.2 mPa s. The density of liquid Cu ($\rho_{(Cu,l)}$), and its temperature dependence is provided through Table A1 of Sec. A.2. The densities of solid phases are also considered in the Navier-Stokes equation. However, the assumption of very large viscosity values in solid phases render the velocity in these phases to have zero magnitudes at all directions. The term F_i in the right hand side of Eq. (A2) is the body force corresponding to Boussinesq approximation for natural convection. The maximum magnitude of velocity obtained for the meltpool in the current numerical simulation is 2.23 µm/s. In the finite element analysis, the continuity and momentum equations have been coupled with the energy equation. The fluid flow inside the meltpool is responsible for convection heat transfer.

Table A1
The coefficients in the polynomial terms for the thermal conductivity expression (Eq. (A3)) are presented along with their units. The thermal conductivities of Solid Ti6Al4V ($k_{th}^{base,solid}$) and Liquid Ti6Al4V ($k_{th}^{base,liquid}$) are assigned to the substrate in the numerical model. The powder bed on the top is represented via the composite functions of thermal conductivities of Solid Cu (k_{th}^{bulk}), Liquid Cu (k_{th}^{liquid}) and Air (k_{th}^{air}).

k_ψ (Units)	Solid		Liquid		Air
	Cu	Ti6Al4V	Cu	Ti6Al4V	
A_ψ (W/mK^2)	-1.064 $\times 10^{-1}$	1.46 $\times 10^{-2}$	-1.6 $\times 10^{-4}$	1.83 $\times 10^{-2}$	1.71 $\times 10^{-4}$
B_ψ (W/mK^3)	4.0 $\times 10^{-5}$	–	2.51 $\times 10^{-6}$	–	–
C_ψ (W/mK)	405.76	−0.32	165.58	−6.66	-7.448 $\times 10^{-3}$
T_{ref} (K)	250.0	0.0	1358.0	0.0	0.0

Table A2
The density expression's polynomial coefficients (Eq. (A4)) are outlined alongside their respective units. Within the numerical model, the substrate is attributed the densities of solid Ti6Al4V ($\rho^{base,solid}$) and liquid Ti6Al4V ($\rho^{base,liquid}$). Meanwhile, the powder bed above is delineated by the densities of solid Cu (ρ^{bulk}), liquid Cu (ρ^{liquid}), and air (ρ^{air}).

ρ_χ (Units)	Solid		Liquid		Air
	Cu	Ti6Al4V	Cu	Ti6Al4V	
A_χ (kg/m^{3}K^2)	-4.28 $\times 10^{-1}$	1.152	-7.96 $\times 10^{-1}$	-0.452	3.16 $\times 10^{-3}$
B_χ (kg/m^{3}K^3)	-6.12 $\times 10^{-8}$	-4.1197 $\times 10^{-4}$	8.69 $\times 10^{-5}$	–	-7.65 $\times 10^{-7}$
C_χ (kg/m^{3}K^4)	-2.77 $\times 10^{-8}$	–	-2.38 $\times 10^{-8}$	–	–
D_χ (kg/m^3)	–	-4.25 $\times 10^2$	–	–	-1.94
E_χ (K^{-1})	–	1.0	–	–	1.0
F_χ (kg/m^3)	8810	6542.63	7890	4955	11.4
T_{ref} (K)	300.0	0.0	1330.0	0.0	0.0

A.2. Fitting of temperature dependent ρ and k_{th}

The variability of density and thermal conductivity during laser processing underscores the importance of comprehending their temperature-dependent variations for precise modeling and prediction of material behavior. Employing polynomial equations enables capturing the non-linear relations between temperature and material properties.

$$k_\psi = A_\psi \cdot (T - T_{\text{ref}}) + B_\psi \cdot (T - T_{\text{ref}})^2 + C_\psi \tag{A3}$$

$$\rho_\chi = A_\chi \cdot (T - T_{\text{ref}}) + B_\chi \cdot (T - T_{\text{ref}})^2 + C \cdot (T_\chi - T_{\text{ref}})^3 + D_\chi \cdot \ln(E_\chi \cdot (T - T_{\text{ref}})) + F_\chi \tag{A4}$$

eqs (A3) and (A4) represent polynomial equations governing thermal conductivity (k) and density (ρ) respectively, utilizing temperature (T) as the independent variable. These equations are structured to capture the nonlinear relationships between temperature and material properties, incorporating coefficients whose values are detailed in Tables A1 and A2, along with reference temperatures (T_{ref}). For solid copper Cu and Ti6Al4V, the reference temperature (T_{ref}) for thermal conductivity spans from 250K to 1358K, with a distinct range for Ti6Al4V extending from 1400K to 1800K. Conversely, for liquid phases, the reference temperatures for Cu and Ti6Al4V shift to 1358K and 1330K respectively, with Ti6Al4V's liquid phase extending from 1950K to 2700K. Regarding density, the reference temperature (T_{ref}) for solid Cu ranges from 250K to 1358K, whereas for liquid Cu, it stands at 1330K. For solid Ti6Al4V, the reference temperature spans from 298K to 1923K, while for its liquid phase, it ranges from 1923K to 2500K. These delineations provide crucial insights into the temperature-dependent behavior of the thermal conductivity and density of the materials under investigation.

References

[1] M. Kaur, K. Singh, Review on titanium and titanium based alloys as biomaterials for orthopaedic applications, Mater. Sci. Eng. C 102 (2019) 844–862, https://doi.org/10.1016/j.msec.2019.04.064.

[2] J. Ju, R. Zan, Z. Shen, C. Wang, P. Peng, J. Wang, B. Sun, B. Xiao, Q. Li, S. Liu, T. Yang, Remarkable bioactivity, bio-tribological, antibacterial, and anti-corrosion properties in a Ti-6Al-4V-xCu alloy by laser powder bed fusion for superior biomedical implant applications, Chem. Eng. J. 471 (2023) 144656, https://doi.org/10.1016/j.cej.2023.144656.

[3] A. Hariharan, P. Goldberg, F. Schell, U. Hempel, F. Striggow, M. Hantusch, M. Medina-Sánchez, A.F. Lasagni, A. Gebert, Single- and multiscale laser patterning of 3d printed biomedical titanium alloy: toward an enhanced adhesion and early differentiation of human bone marrow stromal cells, Adv. Funct. Mater. 34 (8) (2024) 2310607, https://doi.org/10.1002/adfm.202310607.

[4] H. Wang, Q. Chao, X. Cui, Z. Chen, A. Breen, M. Cabral, N. Haghdadi, Q. Huang, R. Niu, H. Chen, B. Lim, S. Primig, M. Brandt, W. Xu, S. Ringer, X. Liao, Introducing c phase in additively manufactured ti-6al-4v: a new oxygen-stabilized face-centred cubic solid solution with improved mechanical properties, Mater. Today 61 (2022) 11–21, https://doi.org/10.1016/j.mattod.2022.10.026.

[5] E. Almanza, M. Pérez, N. Rodríguez, L. Murr, Corrosion resistance of ti-6al-4v and astm f75 alloys processed by electron beam melting, J. Mater. Res. Technol. 6 (3) (2017) 251–257, https://doi.org/10.1016/j.jmrt.2017.05.003.

[6] P. Goldberg, A. Hariharan, F. Schell, M. Hantusch, M.O. Cichocka, N. Pérez, A. Voß, L. Giebeler, V. Hoffmann, C. Zwahr, A.F. Lasagni, A. Gebert, Fine-tuning effect of direct laser interference patterning on the surface states and the corrosion behavior of a biomedical additively manufactured beta ti alloy, Corros. Sci. 219 (2023) 111230, https://doi.org/10.1016/j.corsci.2023.111230.

[7] A. Sidambe, Biocompatibility of advanced manufactured titanium implants—a review, Materials 7 (12) (2014) 8168–8188, https://doi.org/10.3390/ma7128168.

[8] P. Jiang, Y. Zhang, R. Hu, B. Shi, L. Zhang, Q. Huang, Y. Yang, P. Tang, C. Lin, Advanced surface engineering of titanium materials for biomedical applications: from static modification to dynamic responsive regulation, Bioact. Mater. 27 (2023) 15–57, https://doi.org/10.1016/j.bioactmat.2023.03.006.

[9] M. Sarraf, E. Rezvani Ghomi, S. Alipour, S. Ramakrishna, N. Liana Sukiman, A state-of-the-art review of the fabrication and characteristics of titanium and its alloys for biomedical applications, Bio-Des. Manuf. 5 (2) (2022) 371–395, https://doi.org/10.1007/s42242-021-00170-3.

[10] O.G. Bodelón, C. Clemente, M.A. Alobera, S. Aguado-Henche, M.L. Escudero, M.C.G. Alonso, Osseointegration of TI6Al4V dental implants modified by thermal oxidation in osteoporotic rabbits, Int. J. Implant Dent. 2 (1) (2016) 18, https://doi.org/10.1186/s40729-016-0051-5.

[11] G. Dinda, L. Song, J. Mazumder, Fabrication of Ti-6Al-4V scaffolds by direct metal deposition, Metall. Mater. Trans. A 39 (12) (2008) 2914–2922, https://doi.org/10.1007/s11661-008-9634-y.

[12] D. Wang, W. Dou, Y. Yang, Research on selective laser melting of Ti6Al4V: surface morphologies, optimized processing zone, and ductility improvement mechanism, Metals 8 (7) (2018) 471, https://doi.org/10.3390/met8070471.

[13] M. Ribeiro, F.J. Monteiro, M.P. Ferraz, Infection of orthopedic implants with emphasis on bacterial adhesion process and techniques used in studying bacterial-

material interactions, Biomatter 2 (4) (2012) 176–194, https://doi.org/10.4161/biom.22905.
[14] C. Moerke, M. Kloss, K. Wulf, S. Illner, S. Kischkel, M. Sombetzki, N. Grabow, E. Reisinger, A. Öner, H. Ince, Evaluation of a murine model for testing antimicrobial implant materials in the blood circulation system, Biomedicines 9 (10) (2021) 1464, https://doi.org/10.3390/biomedicines9101464.
[15] K. Kasperkiewicz, R. Major, A. Sypien, M. Kot, M. Dyner, Ł. Major, A. Byrski, M. Kopernik, J.M. Lackner, Antibacterial optimization of highly deformed titanium alloys for spinal implants, Molecules 26 (11) (2021) 3145, https://doi.org/10.3390/molecules26113145.
[16] P. Mahmoudi, M.R. Akbarpour, H.B. Lakeh, F. Jing, M.R. Hadidi, B. Akhavan, Antibacterial Ti–Cu implants: a critical review on mechanisms of action, Mater. Today Bio 17 (2022) 100447, https://doi.org/10.1016/j.mtbio.2022.100447.
[17] S. Prabhu, E.K. Poulose, Silver nanoparticles: mechanism of antimicrobial action, synthesis, medical applications, and toxicity effects, Int. Nano Lett. 2 (1) (2012) 32, https://doi.org/10.1186/2228-5326-2-32.
[18] F.N.S. Raja, T. Worthington, R.A. Martin, The antimicrobial efficacy of copper, cobalt, zinc and silver nanoparticles: alone and in combination, Biomed. Mater. 18 (4) (2023) 045003, https://doi.org/10.1088/1748-605X/acd03f.
[19] C. Amaning Danquah, P.A.B. Minkah, I. Osei Duah Junior, K.B. Amankwah, S.O. Somuah, Antimicrobial compounds from microorganisms, Antibiotics 11 (3) (2022) 285, https://doi.org/10.3390/antibiotics11030285.
[20] D. Sun, D. Xu, C. Yang, J. Chen, M.B. Shahzad, Z. Sun, J. Zhao, T. Gu, K. Yang, G. Wang, Inhibition of Staphylococcus aureus biofilm by a copper-bearing 317L-Cu stainless steel and its corrosion resistance, Mater. Sci. Eng. C 69 (2016) 744–750, https://doi.org/10.1016/j.msec.2016.07.050.
[21] S. Wang, Z. Ma, Z. Liao, J. Song, K. Yang, W. Liu, Study on improved tribological properties by alloying copper to CP-Ti and Ti–6Al–4V alloy, Mater. Sci. Eng. C 57 (2015) 123–132, https://doi.org/10.1016/j.msec.2015.07.046.
[22] D. Xu, T. Wang, Z. Lu, Y. Wang, B. Sun, S. Wang, Q. Fu, Z. Bi, S. Geng, Ti-6Al-4V-5Cu synthesized for antibacterial effect in vitro and in vivo via contact sterilization, J. Mater. Sci. Technol. 90 (2021) 133–142, https://doi.org/10.1016/j.jmst.2021.03.007.
[23] Y. Alshammari, F. Yang, L. Bolzoni, Low-cost powder metallurgy Ti-Cu alloys as a potential antibacterial material, J. Mech. Behav. Biomed. Mater. 95 (2019) 232–239, https://doi.org/10.1016/j.jmbbm.2019.04.004.
[24] M. Kikuchi, Y. Takada, S. Kiyosue, M. Yoda, M. Woldu, Z. Cai, O. Okuno, T. Okabe, Mechanical properties and microstructures of cast Ti–Cu alloys, Dent. Mater. 19 (3) (2003) 174–181, https://doi.org/10.1016/S0109-5641(02)00027-1.
[25] R. Filip, Alloying of surface layer of the Ti-6Al-4V titanium alloy through laser treatment, J. Achiev. Mater. Manuf. Eng. 15 (1) (2006) 174–180.
[26] U. Tariq, R. Joy, S.-H. Wu, M.A. Mahmood, A.W. Malik, F. Liou, A state-of-the-art digital factory integrating digital twin for laser additive and subtractive manufacturing processes, Rapid Prototyping J. 29 (10) (2023) 2061–2097, https://doi.org/10.1108/RPJ-03-2023-0113.
[27] J. Honselmann genannt Humme, K. Dubrowska, B. Grygorcewicz, M. Gliźniewicz, O. Paszkiewicz, A. Głowacka, D. Musik, G. Story, R. Rakoczy, A. Augustyniak, Optimised stress – intensification of pyocyanin production with zinc oxide nanoparticles, Microb. Cell Fact. 23 (1) (2024) 215, https://doi.org/10.1186/s12934-024-02486-y.
[28] J. Lee, N. Menon, C.T. Lim, Dissecting gut-microbial community interactions using a gut microbiome-on-a-chip, Adv. Sci. 11 (20) (2024) 2302113, https://doi.org/10.1002/advs.202302113.
[29] M. Berney, F. Hammes, F. Bosshard, H.-U. Weilenmann, T. Egli, Assessment and interpretation of bacterial viability by using the live/dead baclight kit in combination with flow cytometry, Appl. Environ. Microbiol. 73 (10) (2007) 3283–3290, https://doi.org/10.1128/AEM.02750-06.
[30] L. Boulos, M. Prévost, B. Barbeau, J. Coallier, R. Desjardins, Live/dead® baclight™: application of a new rapid staining method for direct enumeration of viable and total bacteria in drinking water, J. Microbiol. Methods 37 (1) (1999) 77–86, https://doi.org/10.1016/S0167-7012(99)00048-2.
[31] M.A.E. Auty, G.E. Gardiner, S.J. McBrearty, E.O. O'Sullivan, D.M. Mulvihill, J.K. Collins, G.F. Fitzgerald, C. Stanton, R.P. Ross, Direct in situ viability assessment of bacteria in probiotic dairy products using viability staining in conjunction with confocal scanning laser microscopy, Appl. Environ. Microbiol. 67 (1) (2001) 420–425, https://doi.org/10.1128/AEM.67.1.420-425.2001.
[32] P. Teixeira, B. Fernandes, A.M. Silva, N. Dias, J. Azeredo, Evaluation by flow cytometry of escherichia coli viability in lettuce after disinfection, Antibiotics 9 (1) (2020), https://doi.org/10.3390/antibiotics9010014.
[33] U. Subedi, 3d laser visualization, https://github.com/subediupadesh/laser_heat_source. (Accessed 2 November 2024), 2024.
[34] A. Kunwar, L. An, J. Liu, S. Shang, P. Råback, H. Ma, X. Song, A data-driven framework to predict the morphology of interfacial Cu6Sn5 IMC in SAC/Cu system during laser soldering, J. Mater. Sci. Technol. 50 (2020) 115–127, https://doi.org/10.1016/j.jmst.2019.12.036.
[35] B. Lindahl, X.L. Liu, Z.-K. Liu, M. Selleby, A thermodynamic re-assessment of Al–V toward an assessment of the ternary Al–Ti–V system, Calphad 51 (2015) 75–88, https://doi.org/10.1016/j.calphad.2015.07.002.
[36] M.M. Demin, O.N. Koroleva, A.A. Aleksashkina, V.I. Mazhukin, Molecular-dynamic modeling of thermophysical properties of phonon subsystem of copper in wide temperature range, Math. Montisnigri 47 (2020) 137–151, https://doi.org/10.20948/mathmontis-2020-47-12.
[37] Z. Luo, Y. Zhao, A survey of finite element analysis of temperature and thermal stress fields in powder bed fusion additive manufacturing, Addit. Manuf. 21 (2018) 318–332, https://doi.org/10.1016/j.addma.2018.03.022.
[38] W. Jiazhu, T. Liu, H. Chen, F. Li, H. Wei, Y. Zhang, Simulation of laser attenuation and heat transport during direct metal deposition considering beam profile, J. Mater. Process. Technol. 270 (2019) 92–105, https://doi.org/10.1016/j.jmatprotec.2019.02.021.
[39] M.R. Akbarpour, H.M. Mirabad, A. Hemmati, H.S. Kim, Processing and microstructure of ti-cu binary alloys: a comprehensive review, Prog. Mater. Sci. 127 (2022) 100933, https://doi.org/10.1016/j.pmatsci.2022.100933.
[40] N. Moelans, A quantitative and thermodynamically consistent phase-field interpolation function for multi-phase systems, Acta Mater. 59 (3) (2011) 1077–1086, https://doi.org/10.1016/j.actamat.2010.10.038.
[41] A. Kunwar, J. Hektor, S. Nomoto, Y.A. Coutinho, N. Moelans, Combining multi-phase field simulation with neural network analysis to unravel thermomigration accelerated growth behavior of cu6sn5 imc at cold side cu–sn interface, Int. J. Mech. Sci. 184 (2020) 105843, https://doi.org/10.1016/j.ijmecsci.2020.105843.
[42] H. Bo, L.I. Duarte, W.J. Zhu, L.B. Liu, H.S. Liu, Z.P. Jin, C. Leinenbach, Experimental study and thermodynamic assessment of the Cu-Fe-Ti system, Calphad 40 (2013) 24–33, https://doi.org/10.1016/j.calphad.2012.12.001.
[43] U. Subedi, Equilibrium composition calculator, https://github.com/subediupadesh/Ti2Cu_IMC_evolution. (Accessed 2 April 2024), 2024.
[44] J. Hektor, M. Ristinmaa, H. Hallberg, S.A. Hall, S. Iyengar, Coupled diffusion-deformation multiphase field model for elastoplastic materials applied to the growth of cu6sn5, Acta Mater. 108 (2016) 98–109, https://doi.org/10.1016/j.actamat.2016.02.016.
[45] C.N. Singman, Atomic volume and allotropy of the elements, J. Chem. Educ. 61 (2) (1984) 137, https://doi.org/10.1021/ed061p137.
[46] V. Yadav, N. Moelans, Investigation on the existence of a 'Hillert regime' in normal grain growth, Scr. Mater. 142 (2018) 148–152, https://doi.org/10.1016/j.scriptamat.2017.08.036.
[47] S.G. Kim, D.I. Kim, W.T. Kim, Y.B. Park, Computer simulations of two-dimensional and three-dimensional ideal grain growth, Phys. Rev. E 74 (2006) 061605, https://doi.org/10.1103/PhysRevE.74.061605.
[48] B. Radhakrishnan, T. Zacharia, Simulation of curvature-driven grain growth by using a modified Monte Carlo algorithm, Metall. Mater. Trans. A 26 (1) (1995) 167–180, https://doi.org/10.1007/BF02669802.
[49] S. Shahandeh, M. Militzer, Grain boundary curvature and grain growth kinetics with particle pinning, Philos. Mag. 93 (24) (2013) 3231–3247, https://doi.org/10.1080/14786435.2013.805277.
[50] Y.J. Lan, D.Z. Li, Y.Y. Li, A mesoscale cellular automaton model for curvature-driven grain growth, Metall. Mater. Trans. B 37 (1) (2006) 119–129, https://doi.org/10.1007/s11663-006-0091-y.
[51] J. Liu, K. Sun, L. Zeng, J. Wang, X. Xiao, J. Liu, C. Guo, Y. Ding, Microstructure and properties of copper–graphite composites fabricated by spark plasma sintering based on two-step mixing, Metals 10 (11) (2020) 1506, https://doi.org/10.3390/met10111506.
[52] F. Sun, P. Liu, X. Chen, H. Zhou, P. Guan, B. Zhu, Mechanical properties of high-strength Cu–Cr–Zr alloy fabricated by selective laser melting, Materials 13 (21) (2020) 5028, https://doi.org/10.3390/ma13215028.
[53] M.L. Ermini, V. Voliani, Antimicrobial nano-agents: the copper age, ACS Nano 15 (4) (2021) 6008–6029, https://doi.org/10.1021/acsnano.0c10756.
[54] S. Wahyudi, S. Soepriyanto, M.Z. Mubarok, Sutarno, Synthesis and applications of copper nanopowder a review, IOP Conf. Ser., Mater. Sci. Eng. 395 (2018) 012014, https://doi.org/10.1088/1757-899X/395/1/012014.
[55] Z. Sun, X. Ji, W. Zhang, L. Chang, G. Xie, H. Chang, L. Zhou, Microstructure evolution and high temperature resistance of Ti6Al4V/Inconel625 gradient coating fabricated by laser melting deposition, Mater. Des. 191 (2020) 108644, https://doi.org/10.1016/j.matdes.2020.108644.

ARTICLE III

Foretelling microstructural interface with multi-generational convolutional-LSTM framework

Engineering with Computers
https://doi.org/10.1007/s00366-025-02117-z

ORIGINAL ARTICLE

Foretelling microstructural interface with multi-generational convolutional-LSTM framework

Upadesh Subedi[1,2] · **Nele Moelans**[3] · **Tomasz Tánski**[1] · **Anil Kunwar**[2]

Received: 19 September 2023 / Accepted: 25 January 2025
© The Author(s), under exclusive licence to Springer-Verlag London Ltd., part of Springer Nature 2025

Abstract
Predicting multi-generational microstructural evolution in the manifest space using convolutional-LSTM neural network models is a promising approach towards computational reducibility. Two predictive models were trained, analyzed, and compared using data generated from varying the driving force in phase-field simulations of phase decomposition in a binary alloy system. The four consecutive predicted generations exhibited microstructural similarity indices (μ_{SIM}) of 0.994, 0.987, 0.980, and 0.967, respectively, compared to the ground truth computational results. By utilizing blobs, μ_{SIM}, and shape index features, we validated that the predicted images retain microstructural information down to the interfacial level. The time-aware data-driven model was applied to rapidly forecast structural changes in Pd–Rh and Cu–Mn engineering alloys.

Keywords Conv-LSTM · Shape Index · Double-well potential · Phase field modeling · Microstructural similarity · Multi generational prediction

1 Introduction

The microstructural evolution of any material fundamentally dictates its physical and mechanical properties observed at the macro-level. Therefore, the spatio-temporal study of microstructure stands as a paramount requirement for comprehending the design and development of new materials [1]. Understanding a material's morphological transformations can directly facilitate the discovery of concealed microstructural imperfections, which, in sensitive cases, can lead to possible catastrophic failures [2–7]. In such scenarios, the phase-field method takes the forefront in mesoscale microstructural studies, enabling the simulation of phenomena such as grain growth [8], crack propagation [9, 10], spinodal decomposition [11], and coarsening [12]. Surpassing traditional methods in material design and discovery, the new era of Industry 4.0 is currently witnessing an upswing, thanks to state-of-the-art in-silico data-driven approaches. In this fast-paced and rapidly evolving technological landscape, leveraging big data informatics to decipher complex microstructural evolution is imperative to stay ahead of innovations in materials [13–15].

The phase-field method is undeniably a robust, multifaceted, and versatile technique for microstructural simulation16, 17. However, it consumes an astronomical amount of computational resources to solve the system of nonlinear coupled partial differential equations (PDEs). This presents a significant barrier in achieving computational reducibility. At every next time step of microstructural evolution, phase-field simulation requires solving complex PDEs with intricate physics and geometry, posing challenges in computation and convergence criteria.

1.1 Background

A sound understanding and proficiency in microstructural evolution are critical for materials utilized in essential infrastructures, such as nuclear reactors, space launch systems, high-performance locomotives, and life-saving devices like artificial pacemakers or stents in blood vessels. Even minor

✉ Upadesh Subedi
upadesh.subedi@polsl.pl

[1] Department of Engineering Materials and Biomaterials, Faculty of Mechanical Engineering, Silesian University of Technology, Konarskiego 18A, 44-100 Gliwice, Poland

[2] Scientific and Didactic Laboratory of Nanotechnology and Material Technologies, Faculty of Mechanical Engineering, Silesian University of Technology, Towarowa 7A, 44-100 Gliwice, Poland

[3] Department of Materials Engineering, KU Leuven, Kasteelpark Arenberg 44 Bus 2450, 3001 Leuven, Belgium

Published online: 28 February 2025

microstructural imperfections in these devices can lead to significant property damage or loss of human life. Therefore, a scientifically robust and physics-backed approach to spatio-temporal prediction of microstructure is necessary. Proper and accurate inference of microstructural evolution enables the timely detection of critical failure points in high-impact mechanical systems within infrastructure. Phenomena such as the corrosion of alloys in molten salt reactors [18], high-temperature crack growth in turbine blades [19], or mechanical strength deterioration in biomedical implants due to phase transformation [20, 21] can all be assessed and mitigated early with the aid of physics-informed microstructure predictive models.

1.2 Existing studies

Numerous researchers have proposed various methods and models to analyze microstructural patterns and their temporal transformations. However, the majority of these approaches lack either adequate situational awareness or a robust foundation of physics-informed guidance. Furthermore, almost none of the studies have primarily focused on anticipating interface-focused microstructure evolution.

Recently, Machine Learning (ML) models, particularly Artificial Neural Networks (ANNs), have emerged as leading tools in predictive modeling22. Time-aware neural networks such as Recurrent Neural Networks (RNNs), Long Short-Term Memory (LSTM), and Gated Recurrent Units (GRU) have shown promising results in predicting microstructural evolution to some extent [23, 24]. However, most of these studies that solely rely on standalone vanilla neural network algorithms are insufficient in predicting quantifiable microstructural evolution. Additionally, they often lack a thermodynamically consistent calculation of driving force (free energy).

Hu et al. [25] employed simple RNN, GRU, and vanilla LSTM models as microstructural predictive tools in their work. Nevertheless, inferring quantitative parameters from their model proved challenging as the predictions primarily reside in a 'latent space'. Predictions based on latent space offer computational ease, but the transformation of high-dimensional spatial data into a reduced form results in the loss of essential spatial information present in the microstructure. Consequently, any correlations between neighboring spatial coordinates of microstructures are lost as they are diminished and flattened into an array of numbers.

Furthermore, it is important to note that the predictions made within these latent spaces are not readily understandable to end-users and require additional computational steps to convert them into human-interpretable 2D image vectors. Moreover, the lack of quantification measures in these works exacerbates the challenge of dimensionality. The robustness of any machine learning model is determined by the quantification metrics for its predicted results; a higher numerical resemblance of predicted results to that of the ground truth indicates a reliable and better-performing model. A work by Farizhandi et al. [26] uses PredRNN to predict microstructure changes in the FeCrCo system, but their study lacks a comprehensive analysis of generational prediction behavior across different model architectures, and the limited range of quantification techniques employed further undermines its reliability. Ahmad et al. [27], in their study, cleverly compressed microstructural data to enhance computational efficiency, representing the spatial information of microstructures in their nascent form using auto-encoders and ConvLSTM. However, their work lacks error quantification at the interface level of the predicted microstructure. In the phase-field method, interface informatics play a crucial role, as the method itself is a numerical approach to simulate and track the microstructural evolution of phase boundaries and interfaces over time. Quantifying microstructural morphology at interfaces provides valuable insights into understanding the sensitivity of the phase-field model and its key parameters controlling microstructural evolution.

1.3 Computer-learned interface pattern: the solution

To address the challenges related to prediction, quantification, and model application, we propose a spatio-temporal multi-generational prediction toolkit for microstructures, employing Convolutional LSTM. This toolkit aims to proficiently decode the spatio-temporal progression of microstructural interfaces by intricately combining two cutting-edge machine learning models: Convolutional layers and LSTM neural networks. By integrating these tools, our toolkit strives to achieve computational reducibility in the analysis of microstructural evolution.

Conv-LSTM offers a two-fold solution to the major challenges faced in contemporary microstructural prediction methods. Firstly, it eliminates the need for dimensional reduction detours by enabling the direct implementation of high-dimensional spatial microstructural data into the model, thereby providing a more comprehensive representation of microstructure within the prediction process. Secondly, and perhaps most importantly, Conv-LSTM facilitates the prediction of microstructural images in manifest spaces, rather than latent spaces, enabling direct quantitative analysis of predicted microstructures. Additionally, by leveraging one of the key features of Conv-LSTM, its ability to incorporate multi-dimensional, multi-channel input, we can expedite predictions across multiple future time steps, making it a multi-generational prediction tool.

In Sect. 3, it is explained in detail about how we employed specialized algorithms to track, detect, and differentiate interfacial patterns in microstructures, quantifying the comparison between the model-predicted and simulation-generated results.

2 Method

To prognosticate the spatio-temporal microstructural evolution in a generic binary (A–B) alloy system, driven by Gibbs Free energy (ranging from -10^4 J/mol), we synergistically combined two state-of-the-art, Artificial Intelligence Algorithms: Convolutional Neural Networks (CNNs) and Long Short Term Memory (LSTM) neural networks. The integration of these two algorithms resulted in our functional prediction model, Conv-LSTM.

Our study challenges the practice of converting high-resolution two-dimensional simulation results into a non-user-friendly latent space for dimensional reduction and microstructure prediction. We argue that such transformations are unproductive and cumbersome, leading to information loss. The transformation process diminishes resolution by reducing the information present in high-dimensional microstructure data. Moreover, since prediction also occurs within the latent space, hindering user understandability, it undermines and discards the very essence of spatial data. Lastly, the retrieval of predicted outcomes from a low-dimensional latent space shaped back as a user-understandable image vector becomes a daunting task, necessitating secondary models.

Harnessing the capabilities of Convolutional Layers, we efficiently address the inefficiencies associated with conventional approaches involving latent spaces. These layers enable the processing of two-dimensional microstructural image vectors through various vector manipulation techniques such as resizing, pooling, and normalization, before passing the microstructural data to the LSTM neural network. The integration of the LSTM network on top of Convolutional Layers eliminates the need for dimensional transformation through latent space, allowing direct time-aware prediction of microstructural evolution in high-dimensional image format. This novel approach not only enhances the accuracy and usability of the results but also ensures the preservation of spatial information and the co-relationship between adjacent microstructural patterns.

Additionally, it is essential to highlight that the significant advantage of utilizing Conv-LSTM extends beyond generational microstructural prediction in high-definition image format. One of the greatest benefits lies in the ability to leverage a wide range of image quantification techniques derived from computer vision research. These techniques allow us to visually and quantitatively assess the machine-predicted microstructural progression. In our study, we have considered these image quantification tools, including the Microstructural Similarity Index (μ_{SIM}), gray image histogram for pixel intensity, microstructural blob detection, and shape curvature index. By incorporating such quantification methods, we establish our work as a benchmark model for robust microstructural prediction, providing a comprehensive and rigorous analysis of multi-generational predicted results.

2.1 Phase field simulation and spatio-temporal dataset

Multiple phase field simulations were conducted for a generic (A_i–B_i) binary alloy system undergoing phase decomposition driven by the driving force. Efforts were made to ensure that its free energies (G_i) fall within the range applicable to real engineering alloys.

The Cahn–Hilliard Eq. (1) was solved using the finite element method within the MOOSE framework [28–31] to simulate the decomposition of the alloy system. The simulations were carried out on a 15 nm × 15 nm 2D mesh using QUAD4 elements.

$$\frac{\partial c}{\partial t} = \nabla \cdot M \nabla \left(\frac{\partial g(c)}{\partial c} - \kappa \nabla^2 c \right) \tag{1}$$

Here, 'c' represents the mole fraction of one of the elements in the binary alloy system, 'M' denotes the mobility of the same element with units of m^5/Js, and 'κ' stands for the gradient energy coefficient with units of J/m. The key term in the Cahn–Hilliard equation is 'g(c)', which represents the free energy density of the system. Free energy plays a crucial role in driving the phase separation process by promoting the growth of compositional fluctuations during phase decomposition. The numerical value of free energy density can be calculated using two quantities : (i) the system's Gibbs free energy (G), and (ii) the molar volume (V_{mol}) of the focused element, as shown in Eq. (2).

$$g(c) = \frac{G}{V_{mol}} \tag{2}$$

In a binary alloy system, phase decomposition is governed by the minimization of Gibbs free energy, leading the system to evolve through compositional fluctuations to reach equilibrium at the lowest state of free energy. The Gibbs free energy curve for the phase decomposition of a binary alloy exhibits a characteristic double-well structure with two minima, each representing one of the two distinct coexisting phases. These minima correspond to the compositions of the separated phases in a stable equilibrium state, minimizing the free energy of the entire system. Various expressions for double-well free energy can be found in the literature

[32–41] to model phase decomposition or spinodal decomposition. We introduce the following machine learning descriptors generating double-well function summarizing all of these variants to create a large set of microstructural evolution data and subsequently train the machine learning model.

$$G = \alpha(\epsilon c - c_{eq})^2 + \beta(\epsilon c - c_{eq}) + \gamma(\epsilon c - c_{eq})^4 + \delta \quad (3)$$

While quantitative polynomial equations of different orders [42] could be used to generalize the double-well free energy expressions, this study confines itself to a 4th order Eq. (3) due to its established proximity with known thermodynamic free energy models such as Ginzburg–Landau and Flory–Huggins potentials [40, 43, 44]. This expression for the driving force (G [J/mol]) comprises six different coefficients (α, β, γ, δ, ϵ, and c_{eq}) that influence the shape and structure of the free energy curve. The flexibility of this polynomial allows for a wide variance in the Gibbs free energy landscape, which is crucial for generating a diverse dataset for training the neural network model.

In this expression, the coefficients α, β, γ, and δ share the same unit as Gibbs free energy, i.e., J/mol, while ϵ and c_{eq} are unitless parameters. The numerical range for each of these features (coefficients) is provided in Table 1, and these variations are purposefully made to ensure a diverse training dataset obtained from microstructure phase-field simulations. The impact of variations in these six coefficients and parameters on the Gibbs free energy landscape is discussed in detail in Appendix A. To ensure that G attains realistic values, the coefficient δ is approximated to have a magnitude closer to the global minima of the Au–Pt alloy system at 1525.15 K. In addition to varying the Gibbs free energy attributes, features corresponding to fluctuations in the model were implemented via the initial seed number of nuclei, as shown in Fig. 1b.

Table 1 Coefficients of free energy expression (3) used as features for creation of variable phase field simulations so as to create diverse range of training data

Features	Minimum value*	Maximum value*	Unit
α	−8.9128e4	−4.3879e4	(J/mol)
β	−2.0e3	3.0e3	(J/mol)
γ	1.15e5	7.0e5	(J/mol)
δ	−5.736e3	−4.604e3	(J/mol)
ϵ	1.2	1.9	–
c_{eq}	0.5	0.7476	–

* The minimum and maximum values of these variables are statistically assigned around the central values based upon the CALPHAD information of the global minima for free energy curve of standard Au–Pt binary alloy at 1525.15 K

Using the expression for thermodynamically consistent and physically realistic Gibbs free energy, we conducted simulations with different landscapes of the driving force. The mobility (M) and gradient energy coefficient (κ) were held constant at 2.329×10^{-31} m^5/Js and 7.965×10^{-8} J/m for all simulations. In Sect. 3.3, we will discuss how the kinetics of the reaction can be virtually varied by sequencing images in model training. Leveraging this concept of virtually varying kinetic parameters, we performed phase-field simulations while keeping mobility constant. Figure 1a illustrates the Gibbs free energy curve for one of the simulations conducted at a temperature of 1525.15 K. The simulation results were visualized using ParaView, a visualization toolkit [45]. The composition tensor at every mesh coordinate for each time step was extracted into a CSV file. These composition tensors were then used to create image-vector frames (Fs) measuring 401×401 pixels. For computational efficiency, all image vectors were reshaped to 64×64 pixels, as shown in Fig. 1b.

To train the neural network model, we constructed a large set of video samples (VS) by grouping 20 frames of image vectors into a 3D image tensor, where each successive image vector was δ frames apart. Each video sequence consisted of exactly 20 frames. To curate the training-validation dataset, a dedicated algorithm was developed to generate video sequences from image-vector frames obtained from six phase-field simulations, as depicted in Fig. 1c. In total, 1196 image-vector frames were generated from the six simulations, and 3625 different video sequences were constructed using the algorithm.

This process ensured that our dataset contained a diverse set of microstructural evolution scenarios, enabling the Conv-LSTM model to learn and predict the temporal progression of microstructural features effectively. The generated video sequences not only captured a broad range of phase decomposition phenomena but also provided the necessary data for training and validating the predictive model, as outlined in Sect. 3.3. For the training, validation, and testing purposes, 80% of the video data sequences were used for model training, while 10% of the dataset was reserved for validation and the remaining 10% for testing the trained model. The separation of data into these subsets was done to ensure a robust evaluation of the model's performance across unseen data, thereby assessing its generalizability and accuracy in predicting microstructural evolution.

2.2 CNN and LSTM models

Neural networks are complex systems of mathematical and statistical computational steps designed to approximate functions using data points. Convolutional Neural Networks (CNNs) represent a groundbreaking advancement in

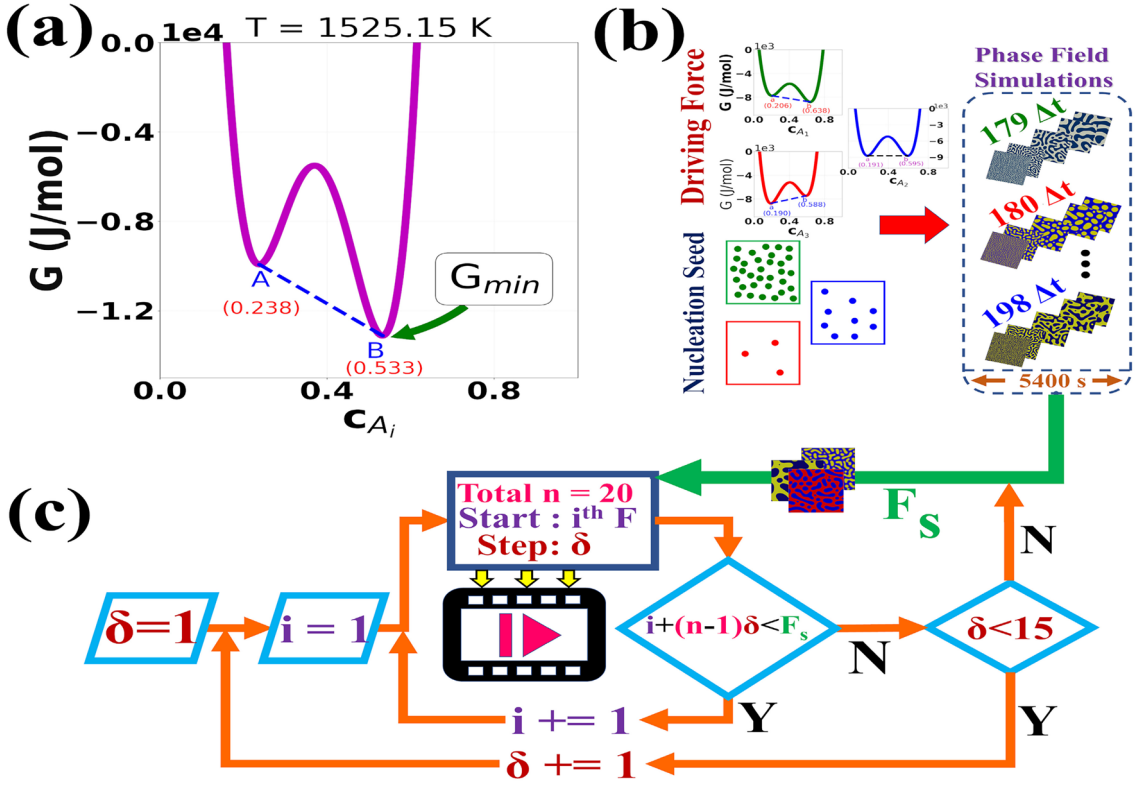


Fig. 1 Illustration of the phase decomposition in a generic A–B binary alloy system governed by the Gibbs Free Energy driving force. **a** The thermodynamically consistent driving force curve fitting was performed at a temperature of 1525.15 K using composition-based TDB files [46] for one of the simulations in the *pycalphad* 47 Python library. The curve exhibits two local minima, denoted as compositions A (0.238) and B (0.533), with the global minimum at B, having a value of -1.31×10^4 J/mol. **b** A schematic diagram of the Phase Field simulations conducted in the MOOSE Framework [30]. Simulations varied in driving force and nucleation seed and ran for 5400 s each. The adaptive time iteration for convergence resulted in different time steps (Δt) for each simulation. Image vector data was extracted from each simulation using ParaView, treating each time step Δt simulation result as Image Vectors (Fs). **c** Image vectors (Fs) were used to create a large set of video sequences through a custom-developed algorithm. Each video sequence consists of 20 image frames (n), curated by changing the starting frame (i^{th}F) and the step to the next frame (δ). Increasing the step size can be considered equivalent to increasing kinetics, making the reaction faster. Step sizes ranging from 1 to 15 were considered for the study

machine learning, initially introduced by LeCun et al. [48] in 1995. CNNs are specifically designed to handle high-dimensional data, such as images or video frames, without requiring feature reduction techniques like latent spaces or principal component analysis. In this study, we utilized CNNs to effectively process phase-field simulation-generated image-vector frames, allowing us to directly train the LSTM model.

Figure 2a illustrates the architecture of a three-layered convolutional network used in our approach. The network begins with a 5×5 kernel, progresses to a 3×3 kernel in the middle layer, and concludes with a 1×1 kernel in the final layer. Each convolutional layer applies its kernel across the entire image to extract spatial features, such as blobs, voids, or edges, which are then passed to the subsequent layer.

The choice of kernel sizes is crucial for the network's performance. A larger kernel size, such as 5×5, is adept at capturing global features and patterns in high-dimensional data but increases computational time due to a higher number of associated parameters and may degrade spatial resolution in deeper layers. To balance feature extraction and computational efficiency, a medium-sized kernel (3×3) was used in the second layer. This kernel size captures important spatial details while maintaining reasonable computational demands and minimizing the risk of overfitting by limiting the number of parameters. The final layer employs a 1×1 kernel, which reduces the depth of the image channels, optimizing computational efficiency and memory usage.

Following the convolutional layers, the Long Short Term Memory (LSTM) network is applied to capture temporal dependencies and predict future microstructural states. LSTM networks, introduced by Hochreiter et al. [49], represents a significant advancement over the traditional Recurrent Neural Network (RNN). LSTMs were specifically developed to address the challenges associated with long-term dependencies in sequential data, such as the vanishing and

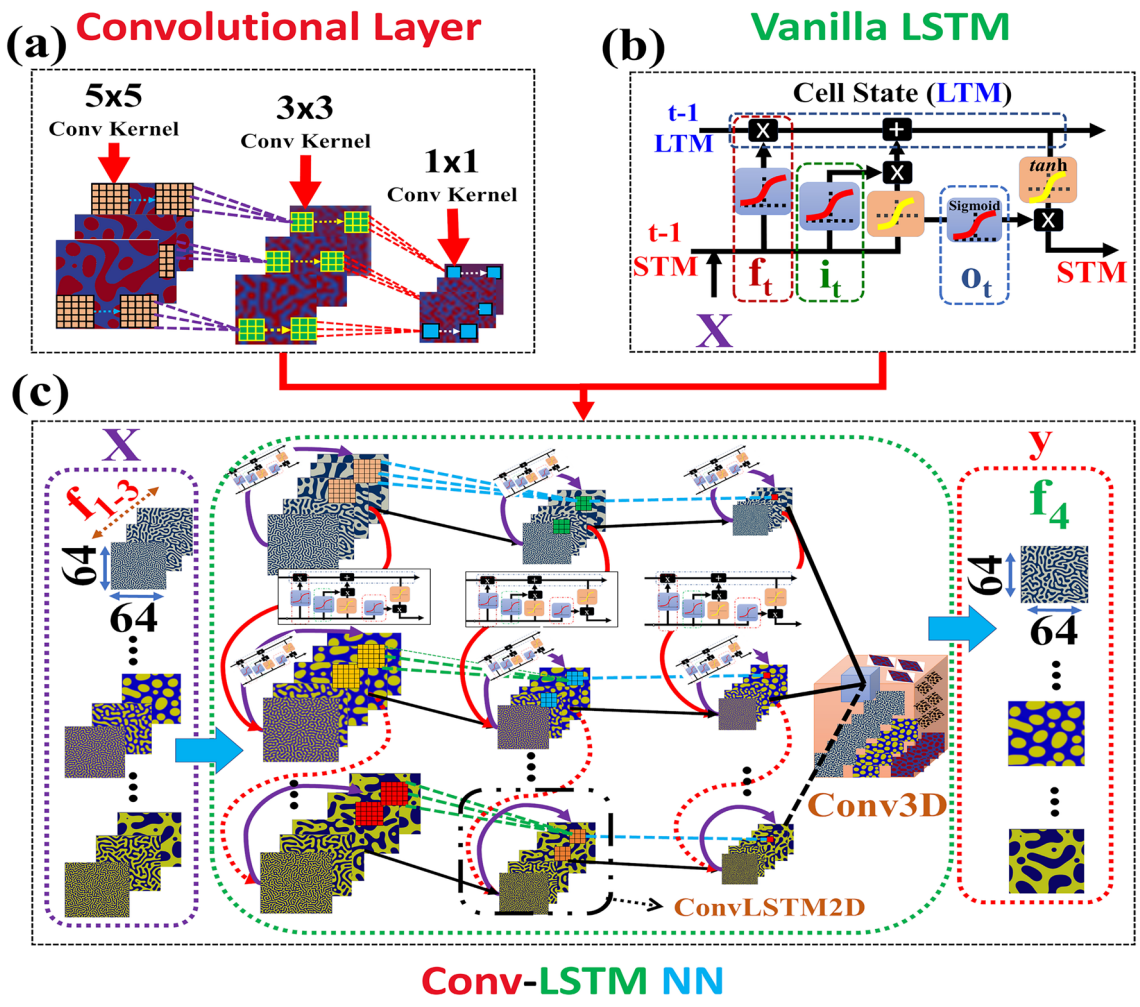


Fig. 2 Illustration of the components of the Convolutional LSTM Neural Network. **a** Three convolutional layers with kernels of sizes 5×5, 3×3, and 1×1, respectively, process frames from Video Samples (VS). These layers analyze microstructures by convolving kernels around each pixel of the frame and pass condensed information from one layer to the next for further analysis. **b** A schematic diagram of a vanilla LSTM Neural Network capable of intercepting Long-Term Memory (LTM) or Cell State and Short-Term Memory (STM) from the previous time period $(t-1)$. It combines STM and Input (I/P) at time t, analyzing them through three gates: forget gate (f_t), input gate (i_t), and output gate (o_t). These gates control the amount of information retained and passed to the next time step in the form of LTM or STM using mathematical expressions defined in Eq. (4). **c** A complex model architecture featuring intertwined layers of Convolutional and LSTM networks, forming a unique ConvLSTM Neural Network structure. This work's model architecture takes three frames (f_{1-3}) of size 64×64 pixels from VS as input and predicts the fourth frame (f_4) in succession with the same pixel dimensions. The model can handle batches of VS simultaneously, predicting corresponding batches of the next frame, creating a 3D layer of convolved predictions

exploding gradient problems that commonly affect standard RNNs [50]. LSTMs have since become a cornerstone in time series forecasting [51] and various other applications, including speech recognition and natural language processing [52].

At the heart of the LSTM architecture is the cell state or memory cell, which serves as a conduit for information flow across time steps in the sequence. Information flow in a cell state is regulated by a series of mechanisms referred as "gates." The input gate determines the proportion of new input to be passed to the cell state, while the forget gate acts as a filter for information from the previous state. The output gate controls the information to carry from the current cell state to the final state. This stepwise calculation, filtering, and passing of information from the previous cell state to the next is the essence of LSTM.

Figure 2b illustrates the structure of a vanilla LSTM network and its gated mechanisms. The numerical expressions governing each gate in the network are represented in Eq. (4) [50], where f_t, i_t, c_t, o_t, and h_t denote the input gate, forget gate, cell state, output gate, and final state, respectively, at time step t. The weights and biases of individual gates and

states are represented by W and B with subscripts indicating the gate and time step. Sigmoid (σ) and tanh functions are employed as activation functions within these gates, as indicated in Fig. 2b with red and yellow curves representing different gates.

A LSTM layer commences with the forget gate f_t (depicted as a red dotted rectangular box in Fig. 2b). The sigmoid function is applied to the current input X_t and the Short-Term Memory from the previous time step STM_{t-1}, yielding a value between 0 and 1. This value is then used to pointwise multiply with the Long-Term Memory (LTM_{t-1}) to determine how much information from LTM should be discarded. Subsequently, LTM is updated by adding a portion of the potential long-term memory generated from the input gate (represented by the green dotted rectangle in Fig. 2b). This update occurs in several steps: first, two operations are performed using X_t and STM_{t-1}, where information is extracted via the tanh function and a percentage value is determined with the sigmoid function. In the second step, the outcomes of these two operations are multiplied together, resulting in the amount of information added to LTM. The final stage of the LSTM network involves updating the short-term memory unit, where a sigmoid function is applied at the output gate (blue dotted box in Fig. 2b) to X_t and STM_{t-1}, and this result is then multiplied by the outcome of the tanh function on LTM_t. The superscript α in Eq. (4) indicates that these expressions are for the Vanilla LSTM network, and $\circ$ represents the pointwise product.

$$\begin{aligned} f_t^\alpha &= \sigma\left(W_f^\alpha\left[STM_{t-1}^\alpha, X_t^\alpha\right] + b_f^\alpha\right) \\ i_t^\alpha &= \left[\sigma\left(W_i^\alpha\left[STM_{t-1}^\alpha, X_t^\alpha\right] + b_i^\alpha\right)\right) \\ &\quad \circ\left(tanh\left(W_i^\alpha\left[STM_{t-1}^\alpha, X_t^\alpha\right] + b_i^\alpha\right)\right] \\ LTM_t^\alpha &= f_t^\alpha \circ LTM_{t-1}^\alpha + i_t^\alpha \\ o_t^\alpha &= \sigma\left(W_o^\alpha\left[STM_{t-1}^\alpha, X_t^\alpha\right] + b_o^\alpha\right) \\ STM_t^\alpha &= o_t^\alpha \circ tanh LTM_t \end{aligned} \tag{4}$$

2.3 ConvLSTM NN

As discussed in Sect. 2.2, Convolutional Neural Networks (CNNs) and vanilla Long Short Term Memory (LSTM) networks are among the most powerful machine learning tools available, each serving distinct purposes when used individually. CNNs are commonly employed for image data processing tasks such as image classification and disease detection from medical images [53, 54]. However, they lack the inherent capability to handle temporal information in image data. In contrast, LSTM networks are designed for predicting time-dependent phenomena, such as time series forecasting and voice assistance. Despite this, vanilla LSTMs can only process data as one-dimensional vectors, which necessitates the flattening of any spatial information within input image-vectors before training.

To combine the strengths of these two algorithms, Shi et al. [55] introduced a fusion of Convolutional layers with LSTM neural networks, resulting in the Convolutional-LSTM (ConvLSTM) Neural Network. The equations used to describe this hybrid ConvLSTM network are provided in Eq. (5). In this equation, X_t, C_t, and H_t represent the inputs, cell output (Long-Term Memory), and hidden states (Short-Term Memory) at time t, while i_t, f_t, and o_t denote the input, forget, and output gates, respectively. The symbol $\odot$ represents the convolutional operator, and $\circ$ signifies element-wise multiplication. Weights and biases for operations in each state and gate are denoted by W and b, with lowercase subscripts indicating the respective state or gate. The superscript β in Eq. (5) specifically denotes the Convolutional-LSTM network.

In simpler terms, it can be stated that with the advent of modern algorithms like transformers [56, 57], a plain vanilla LSTM model has become somewhat outdated. Studies that employ RNNs or standalone LSTMs [25], using latent space feature reduction for phase-field prediction, also face the limitation of not being able to process high-dimensional spatial image-vector data as input into the network. In this work, we address this significant issue by implementing the ConvLSTM NN and successfully predict the evolution of microstructures by training the model with spatial information of microstructures at different time steps in the form of image-vectors generated from phase field simulations.

$$\begin{aligned} f_t^\beta &= \sigma\left(W_{xf}^\beta \odot X_t^\beta + W_{hf}^\beta \odot H_{t-1}^\beta + W_{cf}^\beta \circ C_{t-1}^\beta + b_f^\beta\right) \\ i_t^\beta &= \sigma\left(W_{xi}^\beta \odot X_t^\beta + W_{hi}^\beta \odot H_{t-1}^\beta + W_{ci}^\beta \circ C_{t-1}^\beta + b_i^\beta\right) \\ C_t^\beta &= f_t^\beta \circ C_{t-1}^\beta + i_t^\beta \circ \tanh\left(W_{xc}^\beta \odot X_t^\beta + W_{hc}^\beta \odot H_{t-1}^\beta + b_c^\beta\right) \\ o_t^\beta &= \sigma\left(W_{xo}^\beta \odot X_t^\beta + W_{ho}^\beta \odot H_{t-1}^\beta + W_{co}^\beta \circ C_t^\beta + b_o^\beta\right) \\ H_t^\beta &= o_t^\beta \circ \tanh\left(C_t^\beta\right) \end{aligned} \tag{5}$$

A neural network model's architecture can vary according to the specific use case and application field. In this work, we designed the ConvLSTM NN architecture using the built-in Keras [58] ConvLSTM2D module [59, 60]. We developed two distinct model architectures for the ConvLSTM NN and trained both on the same dataset.

The first model, denoted as (1I/P-O/P), takes a single input frame and predicts the subsequent frame. In contrast, the second model, denoted as (3I/P-O/P), processes three successive frames as input and predicts the fourth frame. For a more detailed discussion of these two model architectures, refer to Sect. 2.4.

For both model architectures, the model hyperparameters are nearly identical except for the input layer.

The loss function is one of the most crucial parameters in the training of a neural network model, and its selection primarily depends on the type of prediction being made. In our case, dealing with a binary alloy system with two phases: c_A -rich and c_B-rich regions where c_A and c_B are the two components of the alloy. The phases can be represented by a single composition variable, c_A, since c_B can be expressed as $1 - c_A$. The range of this composition variable (c_A) varies from 0 to 1, where a value of 1 indicates a phase rich in c_A and a value of 0 indicates a phase poor in c_A. Inside the bulk region of the microstructure, after phase separation, the phase is either rich in composition c_A (i.e., $c_A = 1$) or c_B (i.e., $c_A = 0$). However, in the interface region, there is a compositional gradient from c_A to c_B (i.e., from $c_A = 1$ to $c_A = 0$) and vice versa. Leveraging this fact, we employed the Negative Log Loss function, also known as the Binary Cross Entropy Loss function, in our model. This function measures the performance of the model by outputting probability values between 0 and 1, which aligns with the range of the compositional variable in our system. The expression for the Negative Log Loss function is given in Eq. (6) [61]

$$logloss = -\frac{1}{N}\sum_{i=1}^{N}\left[y_{t,i}.\log(y_{p,i} + (1 - y_{t,i}).\log(1 - y_{p,i})\right] \quad (6)$$

where, $y_{t,i}$ and $y_{p,i}$ are the ground truth and prediction values, respectively.

Since the prediction task involves identifying phase separation in a binary alloy system with a single compositional variable varying from 0 to 1, the nature of the prediction aligns well with a binary classification problem, which is effectively handled by the log loss function. Additionally, the log loss function allows the model to output probabilities that represent the likelihood of the phase being rich or poor in c_A. This probabilistic interpretation is useful for capturing uncertainty and the interfacial region during phase separation.

2.4 Two architectures study

The final step before commencing neural network training is to categorize the training data into features and labels. Training features serve as the inputs to the neural network, while labels are used to verify the predicted results. Our training data consists of video sequences composed of image frames, and the goal is to predict each subsequent frame. Consequently, we treat each following frame as a label, while the preceding frame(s) serve as features. To achieve this, we created two different model architectures, denoted as A_1: 1I/P-O/P and A_2: 3I/P-O/P.

The distinction between these two architectures lies in the number of frames used as features during the training process. In A_1, each individual frame (f_t) in a video sequence is input into the model to predict the adjacent frame (f_{t+1}). In contrast, A_2 uses three consecutive frames from a video sequence (f_t, f_{t+1}, f_{t+2}) as features to predict the fourth frame (f_{t+3}), as depicted in Fig. 4. Both models were trained for 25 epochs with a batch size of 15 on a Dell Precision 7920 Tower equipped with 24 cores, 64 GB RAM, and an Intel Xeon(R) Gold 5220R CPU @ 2.20 GHz × 48. Each model took slightly over an hour to complete a single iteration, with the entire training process spanning approximately 28 h. It is worth noting that the A_2 architecture required more training time due to the larger input feature size. The choice of hyperparameters, including epoch size and batch number, was made to balance training time, processor performance, and training progress. The prediction performance of these two model architectures is discussed comprehensively in Sect. 3.

3 Results and discussion

3.1 Quantification of microstructure prediction

Quantifying machine-learned predictions essentially involves comparing the prediction results with the corresponding Ground Truth (GT). In this work, we expanded our approach from the default neural network metrics of accuracy and loss to include advanced image analysis techniques. One widely used method for image quality assessment is the Human Visual System (HVS). Although numerically quantifying visual perception is challenging, the HVS can provide a somewhat robust evaluation for distinguishing between visual stimuli [62]. However, since HVS is inherently based on individual perception, which varies according to biology and vision dynamics, this method can be subjective, inconvenient, and non-standard [63].

To overcome the limitations of HVS, we employed state-of-the-art, mathematically consistent error quantification methods, including the Microstructural Similarity Index (MSIM) [64], Blobs Detection, Shape Index [65], and Root Mean Squared Error (RMSE). These quantification tools were implemented using Python libraries such as *OpenCV* [66], *scikit-image* [67], *sewar* [68], and *pydom* [69]. Visualization of the quantitative analysis was performed with *Matplotlib* [70], which provided a means to observe and analyze deviations between the predicted results and the ground truth. This approach offers an objective method for quantifying physics-based neural network predictions, as opposed to the subjective nature of HVS. By employing these advanced metrics, our work establishes a new standard benchmark for future research. It represents one of the first state-of-the-art

multi-model machine learning algorithms designed to predict spatio-temporal microstructural evolution as an image-tensor using physics-based phase-field simulations.

3.2 Best predictive model selection

Two NN models, A_1 and A_2 as discussed in Sect. 2.4, were trained on the same Video Sequence dataset. These models differ in architecture: A_1 uses one frame as input to predict the subsequent frame, while A_2 uses three frames as input to predict the fourth frame. It is expected that these architectural differences will lead to variations in the predictions made by the two models. To numerically and scientifically quantify the predictions from these two NN models, we employed two image quality assessment methods and used a rigorous threshold measure to select the model for further analysis. The goal of this threshold measurement is to understand the differences in inferred microstructural evolution between the one-to-one prediction model (A_1) and the many-to-one prediction model (A_2). The Root Mean Squared Error (RMSE), a widely used error metric known for its simplicity in calculation and ease of interpretation, serves as the initial method for comparing these two NN models. The RMSE value between the predicted image frame and the ground truth (GT) image frame quantifies how far the pixel values in the predicted frame are from the corresponding pixel values in the GT frame. In Eq. (7), $f_{(i,j)}$ and $f'_{(i,j)}$ represent the pixel values at spatial coordinates i and j for the GT frame and predicted frame, respectively, where both frames have the same pixel dimensions of $N \times M$.

$$RMSE = \sqrt{\frac{1}{MN}\sum_{i=0}^{M-1}\sum_{j=0}^{N-1}\left[f_{(i,j)} - f'_{(i,j)}\right]^2} \tag{7}$$

For testing purpose a randomly selected 137 video samples from testing dataset was taken, which were used to evaluate both neural network (NN) model architectures. Root Mean Square Error (RMSE) was calculated for each video sequence, and the resulting RMSE values were plotted against the video sequence numbers, as shown in Fig. 3a for model architecture A_1 and Fig. 3b for model architecture A_2. The average RMSE values across all 137 video sequences in Prediction Generation Zero (GEN-0) and Prediction Generation One (GEN-1) were 0.1 and 0.34, respectively, for architecture A_1, while for architecture A_2, they were 0.06 and 0.09. It is important to note that in this context, GEN-0 prediction refers to predictions made by the NN model using input solely from the phase field simulation, whereas GEN-1 predictions incorporate inputs derived from GEN-0 predictions as well. For a more detailed discussion on generational prediction, refer to Sect. 3.3.

The second metric used as a quantifier is the Microstructural Similarity Index (μ_{SIM}). μ_{SIM} assesses image quality by comparing similarities in terms of luminance, contrast,

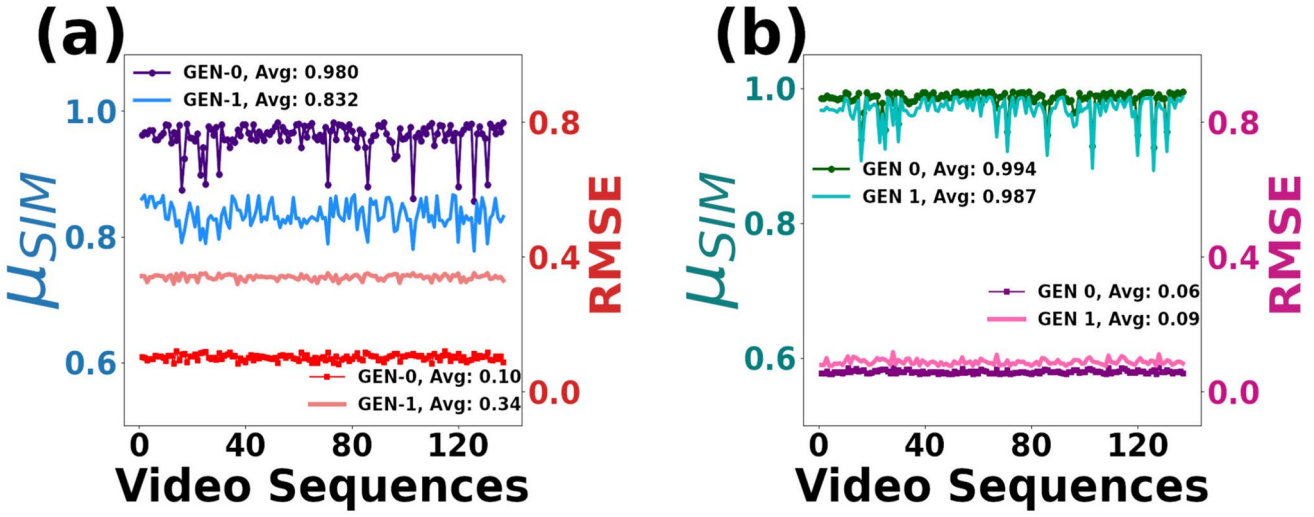


Fig. 3 Prediction result quantification for selection of best model among two purposed model architectures. **a** Microstructural similarity index along with root mean squared error comparison of Model architecture A_1 for two successive generations (GEN-0, GEN-1) of predictions, The Left Y-axis represents μ_{SIM} index with a blue shade color of graph and Right Y-axis represents RMSE value with red shade of color. The average μ_{SIM} and RMSE value for GEN-0 prediction for A_1 is 0.98 and 0.1 respectively, as we approach to GEN-1, MSIM plummets to 0.812 where as RMSE rockets up to 0.34. **b** Result of μ_{SIM} and RMSE same successive generation for Model architecture A_2. It is observed in prediction result of A_2 that the drop and rise of μ_{SIM} and RMSE is not that significant in two generations as compared to A_1 indicating the robustness of A_2 architecture. For both models the predictions were performed for exact same 137 validation video-sequences as represented by X-axis in both plots

and pixel structure between two images. The mathematical expression to calculate μ_{SIM} is presented in Eq. (8), originally formulated by Wang et al. [63] as the Structural Similarity Index (SSIM) to quantify similarities between two image frames. In this study, we adapted Wang et al.'s similarity index for the specific purpose of microstructural quantification, thus naming it the Microstructural Similarity Index (μ_{SIM}) [71]. In the equation, f_t represents the ground truth microstructural image frame, and f'_t denotes the predicted microstructure frame at time 't'.

$$\mu_{SIM}(f_t, f'_t) = \frac{(2\mu_{f_t}\mu_{f'_t} + \alpha_{f_t})(2\sigma_{f_t f'_t} + \alpha_{f'_t})}{(\mu_{f_t}^2 + \mu_{f'_t}^2 + \alpha_{f_t})(\mu_{f_t}^2 + \mu_{f'_t}^2 + \alpha_{f'_t})} \tag{8}$$

The symbols μ_{f_t}, $\mu_{f'_t}$, $\sigma_{f_t}^2$, and $\sigma_{f'_t}^2$ represent the pixel sample mean intensities and variances of frames f_t and f'_t, respectively, while $\sigma_{f_t f'_t}$ denotes the covariance between the two image frames. The terms α_{f_t} and $\alpha_{f'_t}$ are constants introduced to prevent division by zero errors. One crucial condition for obtaining an accurate MSIM index is that both frames, f_t and f'_t, must have equal pixel sizes of $N \times M$.

Similar to RMSE, we also calculated the MSIM for the predictions of both models on the 137 validation video sequences. The MSIM values for each video sequence are plotted in Fig. 3a, b, categorized into two generations: GEN-0 and GEN-1, for the two NN model architectures A_1 and A_2. It is observed that the MSIM index decreases while the RMSE value increases with each generational step. Between the two architectures, A_1 and A_2, the latter, which takes three frames as input, appears to perform better. The drop in MSIM and the increase in RMSE values in model architecture A_1 upon reaching GEN-1 are more significant than those in architecture A_2, suggesting that the second architecture is more robust and reliable for generational prediction.

Based on the analysis of the results from the two metrics, RMSE and MSIM, we decided to select model architecture A_2 as our best model and proceed further with this model for the further investigation.

3.3 Multi-generational prediction with μ_{SIM}

One of the key aspects of any machine learning or predictive model is to assess and quantify how accurately its predictions hold over successive time steps. In this work, which deals with inferring microstructure evolution, we have assessed generational prediction and quantified the evolution of microstructure in successive generations of prediction using various image correlation metrics. These metrics include the structural similarity index [63, 71, 72], the ratio of blob detection [73], and the root mean squared error (RMSE) between predicted and ground truth images.

As illustrated in Fig. 4a, the first row of the figure shows the model taking three frames (f_1, f_2, f_3) of image data generated from the simulation results of the Phase Field Model produced by the MOOSE Framework, which is driven by the physics of phase decomposition. The prediction result (f'_4) from the model is considered as the generation zero (GEN-0) prediction with no cross-breeding, where every input (parent) to the model is a physics-backed simulation result. For the next generation (GEN-1) prediction, we use two frames (f_2, f_3) from the simulation results and one frame from the machine-predicted zeroth generation result (f'_4) as the parent image frames (input image frames) to the model. By using the prediction of the previous generation as the parent for the next generation, we cross-breed between machine learning and physics-based results, transitioning from purely physics-based inference to physics-informed machine learning methods. In this way, the first-generation prediction result (f'_5) inherits the characteristics of its parent frames (f_2, f_3, and f'_4). Similarly, for the second-generation result (f'_6), we use one frame from the simulation result (f_3), one from GEN-0 (f'_4), and one from GEN-1 (f'_5) as input parents to the model, which predicts the result as GEN-2 inference (f'_6). At each generation, we progress along a path of computational reducibility by transitioning more toward machine-predicted microstructural evolution. On the third generation, GEN-3, we complete the transition and fully intake three image frames as parent frames from each prediction result of each generation: GEN-0: f'_4, GEN-1: f'_5, and GEN-2: f'_6. The third and final generation results in frame f'_7, which is the culmination of predictions built upon previous predictions.

It can be observed that the structural similarity index drops by a certain fraction in every successive generation from GEN-0 to GEN-3. This is because each subsequent predicted generation inherits certain microstructural characteristics from its parent generation, including the differences between ground truth and the model's prediction, thus differing slightly more from the ground truth with each generation.

The approach of using three frames as features to predict the next frame allows us to address kinetics. As the model is trained on a large number of video sample sequences comprising different simulation parameters, as discussed in Sect. 2.1, our model architecture A_2 is capable of predicting successive next frames by intelligently learning the time step difference Δt between the three input image frames. To address the variable kinetics of the reaction, we strategically curated training video sequences with different frame steps δ ranging from 1 to 15. In every video sequence, δ plays a crucial role in determining each subsequent frame of the image to incorporate. By varying δ within the range of 1 to 15, we were able to virtually speed up the phase field simulation's kinetic parameters.

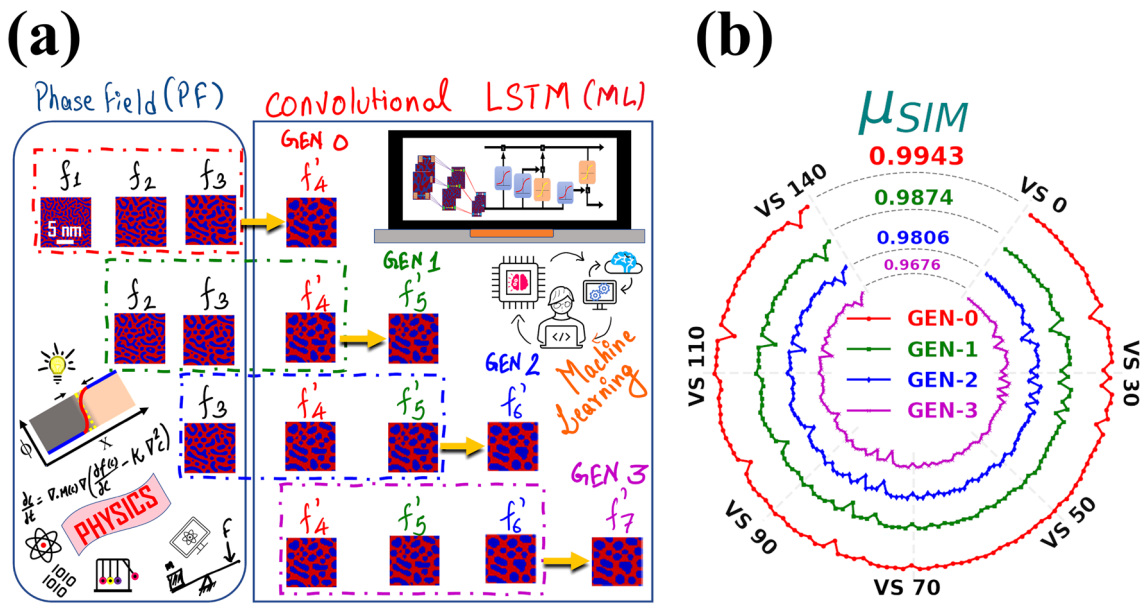


Fig. 4 **a** A flow diagram visualizing multi-generational microstructural prediction for architecture A_2. The first red colored dotted box-row represents generation zero (GEN 0) prediction where 3 input frames (f_1, f_2, f_3) are supplied to the trained model, to predict fourth frame f_4', at this generation all input frames (15 nm × 15 nm each) are generated from phase field simulation. On reaching generation one (GEN 1), i.e. second row green dotted box, two frames (f_2, f_3) are taken from phase field result in combination with frame (f_4') of GEN 0, to predict fifth frame (f_5'). Moving on to generation two (GEN 2) i.e. blue colored dotted box on third row, we take one frame (f_3) given by simulation alongside two predicted frames (f_4', f_5') from GEN 0 and GEN 1 as input, this results in prediction of sixth frame (f_6'). At every generation, input to the trained model is shifting from physics informed phase field generated microstructural image-frames towards previous image-frames predicted by the model itself on previous generation. And lastly, at generation three (GEN 3) the magenta colored dotted box at fourth row, we completely shift model's input from phase field simulated frames to generational predicted frames (f_4', f_5', f_6'). The outcome of GEN 3 i.e. seventh frame (f_7') is purely a result of nested machine learning framework, hence making it a prediction based on predictions. At this step we are fully in the territory of Convolitional LSTM region (right rectangular box of Machine Learning) leaving the physics backed region (left rectangular box of Physics) of Phase Field. **b** Radial line graph of Microstructural Similarity Index (MSIM) of microstructural evolution in four successive multi-generational prediction among validation video sequences. It is observed that MSIM value drops on every next generation starting from GEN-0 with average value of 0.9942 to GEN-3 with 0.9672. This drop in structural similarity index can be considered as a consequence of children generation inheriting prediction inaccuracies from the parent generation

We further investigated the accuracy and robustness of the selected NN model architecture A_2 through an in-depth analysis of the Microstructural Similarity Index (μ_{SIM}). Individual assessments of the μ_{SIM} index for all four generational predictions were conducted using the validation video samples, and a comparative radial line graph was plotted, as shown in Fig. 4b.

It is observed that the similarity index is highest for the zeroth generation prediction (GEN-0), with an average μ_{SIM} value of 0.9942 across 137 video samples. A visible pattern emerges in the graph, indicating that the μ_{SIM} index drops slightly from 0.9942 in GEN-0 to 0.9874 in GEN-1, further to 0.9806 in GEN-2, and finally to 0.9672 in GEN-3. We have concluded that this gradual decrease in the μ_{SIM} index value in every successive generation is due to the inheritance of microstructural prediction features from one generation to another. These inherited features can contribute either constructively or detrimentally, depending on the specific prediction being made. As our NN model utilizes prior generational prediction results as input for subsequent generation predictions, it establishes a parent–child relational dynamic with feature inheritance between each generational prediction.

Since, after GEN-3, the model's predictions become independent of the input frames generated from the phase field simulations and rely solely on the results of previous predictions, this phase is referred to as the 'prediction-based prediction' zone. Our analysis shows that the model achieves a microstructural similarity index of 90% or higher for up to the 10th generation of prediction as illustrated in Fig. 12. This corresponds to an estimated computational time of 273.25 s. Beyond the 10th generation, however, the model's accuracy, measured by the microstructural similarity index, falls below the 90% threshold. Therefore, we do not recommend using the results beyond this point for actual decision-making processes in failure analysis.

3.4 Microstructural blobs detection

We further applied a priori algorithm to detect microstructural blobs present on the alloy surface. Blobs refer to patterns or regions in a microstructure surface with different compositional properties compared to their surroundings. Numerically quantifying the blobs present on the surface can serve as a valuable tool for studying imperfections on the alloy surface. This approach can be used to detect cracks in the bulk phase, precipitates in the matrix phase, or voids in a grain boundary.

The detection of differences in patterns or blobs occurs when there is a sudden change in pixel intensity (i.e., crossing an edge) while convolving a kernel within an image. For blob detection, we applied the Laplacian of Gaussian (LoG) Kernel to both the ground truth (GT) image frame and the predicted frame. LoG has a well-established history of being used to detect patterns and blobs in highly sensitive scientific fields such as medical imaging [74–76]. The expression for LoG calculation is represented by Eq. (9) [77, 78], where M and N are positional image coordinates with certain pixel intensities and a specified spatial constant S_σ. Another pattern-detecting algorithm is the Difference of Gaussian (DoG), also represented in Eq. (9). DoG is primarily an approximation of the scale-normalized LoG itself [79], where $S_{\sigma 1}$ and $S_{\sigma 2}$ represent the standard deviations of two Gaussian functions selected by the user to capture global and local microstructural details in an image. Figure 5a displays the application of the LoG and DoG algorithms to a randomly selected frame from one video sample.

Moreover, our study primarily focused on using the Laplacian of Gaussian Kernel to analyze the rate of blobs detected in different frames of predicted images compared to the ground truth image frame.

$$(LoG) : \nabla^2 G(M,N) = \frac{1}{\pi S_\sigma^4}\left(1 - \frac{M^2+N^2}{2S_\sigma^2}\right)\exp\left(-\frac{M^2+N^2}{2S_\sigma^2}\right)$$
$$DoG = LoG(M,N,S_{\sigma 1}) - LoG(M,N,S_{\sigma 2}) \tag{9}$$

We began by implementing the Laplacian of Gaussian (LoG) Kernel [80] on image-frames from ten randomly selected validation video samples using the *Scikit-Image* library [67]. Similarly, for the same selected video frames, we conducted predictions for four generations of microstructural evolution and subsequently applied the LoG Kernel to them. We chose the ratio of blobs detected in the Phase Field-generated image-frames compared to that in the NN-predicted image-frames as the metric to assess the robustness of our model. An ideal prediction model would yield predicted image frames with an equal number of blobs as in the ground truth (GT) image-frames, resulting in a ratio of blob detection equal to 1. This information allows us to further analyze our model's performance in generational microstructure prediction.

The lower section of Fig. 5 displays the ratio of blobs detected in ten video samples, each containing 17 frames (a total of 170 frames), for four generations of microstructure prediction. In Fig. 5b, it can be observed that GEN-0 exhibits the least deviation (±0.032) from the mean (0.98), while the standard deviation continues to increase with each successive generation. Figure 5c corresponds to GEN-1, Fig. 5d to GEN-2, and, finally, the most significant deviation in the blobs detection ratio can be observed in the final generation of the study, GEN-3, as shown in Fig. 5e. The increasing deviation in blobs detection over the four generations suggests that certain generational traits are being carried over in each generation, and a threshold deviation could be established, above which we may consider discontinuing generational prediction. In this case, even though the fourth generation (GEN-3) has the highest deviation (±0.065) compared to previous generations, the value itself is not particularly significant, making generational analysis an interesting consideration.

3.5 Histogram of gray pixels

A histogram is a visualization tool used to represent the frequency of occurrence in a particular subject of study. It can serve as a quantification measure by comparing the histogram graphs between different subjects. A histogram of gray pixels refers to the distribution of pixel intensity values in a grayscale image frame. By definition, grayscale image pixel values range between various shades of gray, with a maximum value of 255 for white and a minimum of 0 for black. Therefore, a histogram of a grayscale image provides information about the number of occurrences of specific pixel values in that image. We plotted the histogram chart to compare the generational predictions of microstructural evolution with the ground truth image frame, as shown in Fig. 6a.

In the histogram graph, we can observe that the microstructural evolution data exhibits a bimodal distribution. There are two separate peaks skewed towards opposite ends of the pixel values (0 and 255), corresponding to two different phases. It can also be inferred that among the four prediction generations, GEN-0 (red line) provides the most accurate representation of the ground truth, with the highest frequency of pixel values at the opposite ends. This is followed by GEN-1 (green line), GEN-2 (blue line), and finally GEN-3 (magenta line). This observation aligns with our previous quantification measures of μ_{SIM} and blob detection ratio.

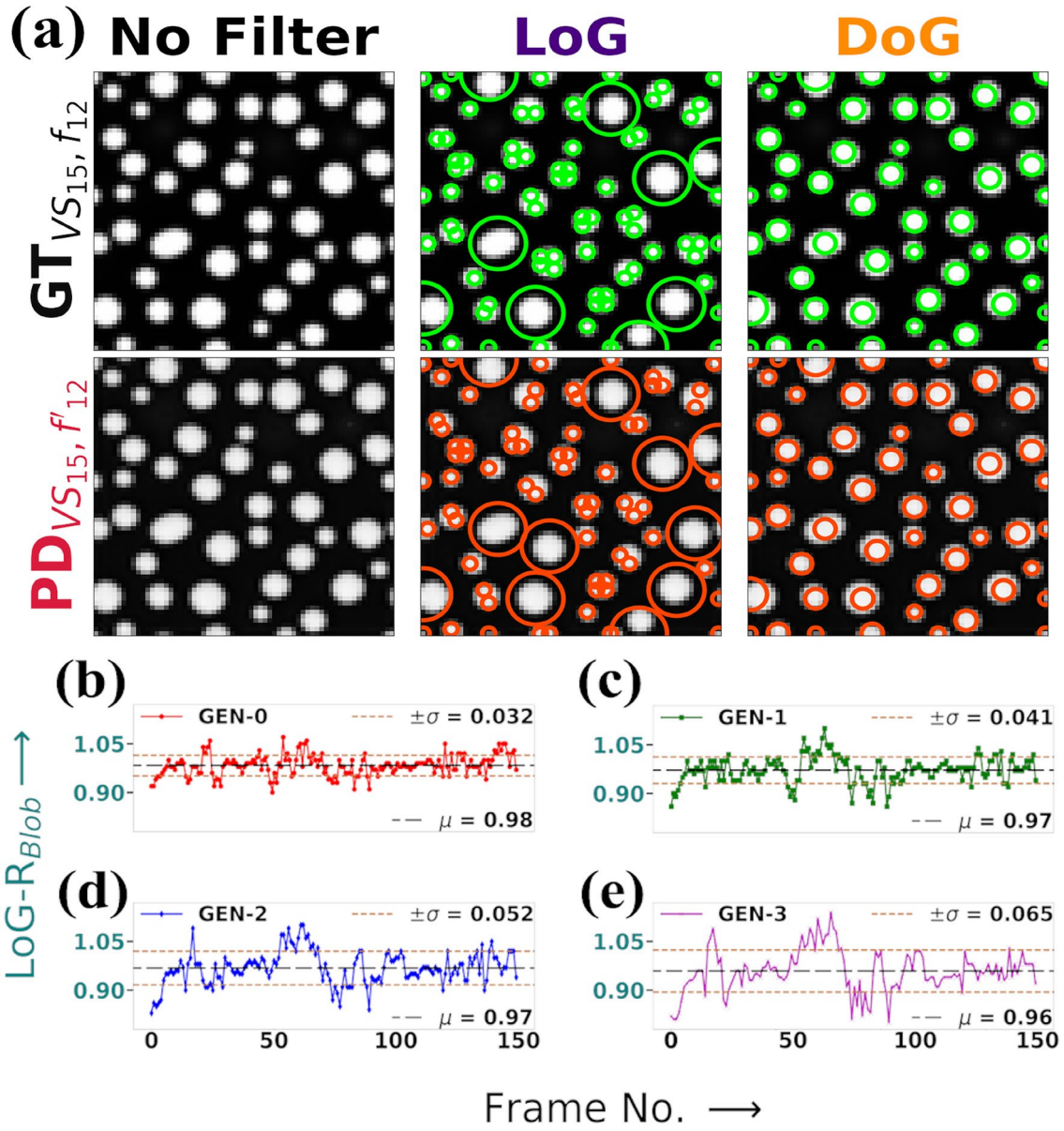


Fig. 5 Graphical comparison between microstructural blobs present in neural network predicted, and phase field simulation generated image-frame alongside the quantitative study of multi-generational blobs detection ratio in ground truth to predicted microstructure. **a** the first row consists of ground truth frame 12 (f_{12}) of video sequence 1 (VS_1) with no filter, Laplacian of Gaussian (LoG) filter and Difference of Gaussian (DoG) filter applied on each individual columns, while second row represents same filters applied along each column for predicted frame 12 (f'_{12}) of video sequence 1 (VS_1). **b** Ratio of blobs detected in image frames of GEN-0 predictions to GT image frames. GEN-0 shows the least deviation (standard deviation of 0.032) in detecting blobs in comparison to that of blobs present in simulation result where as the deviation in detection is found to increase on every successive generational prediction **c** GEN-1 with deviation of 0.041 **d** GEN-2 with deviation of 0.052 and on reaching GEN-3 **e** the final generation considered for this study it is observed to have the maximum deviation of 0.065 from the mean blobs detected. For all four generations, image frames are taken from 10 randomly sampled validation video sequences

It is worth noting that there are relatively few cases of extreme pixel values (0 or 255, black or white) compared to the frequency of pixel values near black (between 25 and 50) and near white (between 200 and 240). This suggests that the microstructure is in a transitional phase of decomposition, where it has yet to fully separate into two opposite phases. Histogram analysis can also assist in determining whether the decomposition reaction is complete or ongoing by observing the peak frequency of pixel intensity values.

Figure 6b, c present a sample case study for pixel intensity comparison at specific pixel coordinates between two image frames, one from the ground truth and the other from GEN-0

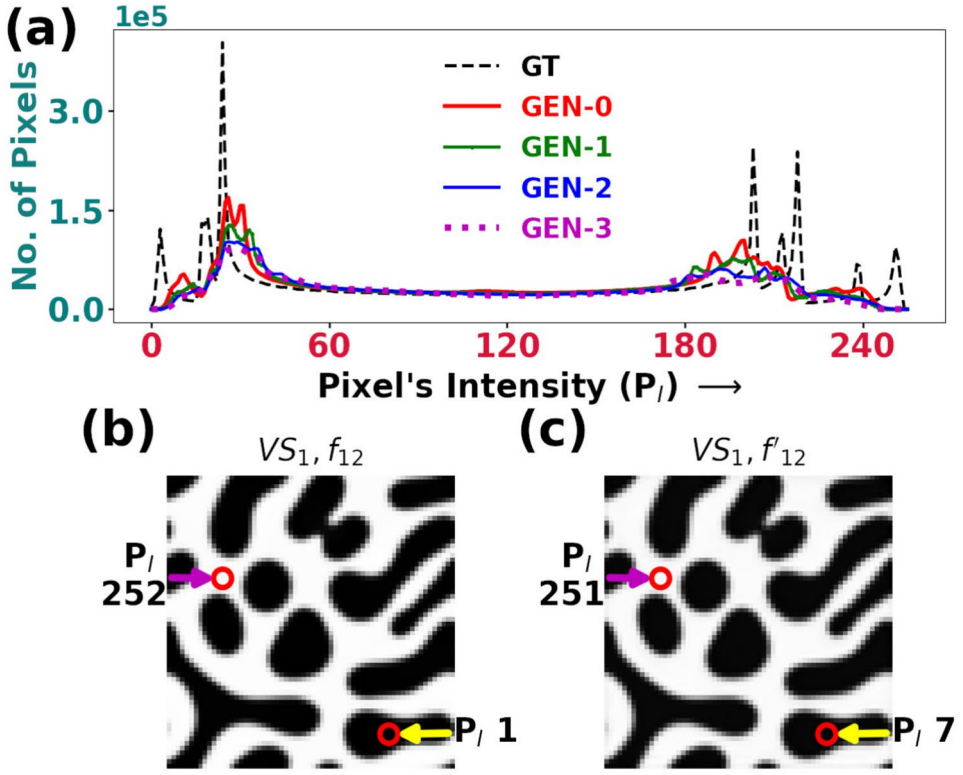


Fig. 6 **a** Histogram plot between Ground Truth (black line) image frame of all validation video-sequences and four generational predictions GEN-0: red, GEN-1: green, GEN-2: blue and GEN-3: magenta. Histogram curve flattens out as generation progresses in time indicating predictions will be of lower intensity and diffused image-frame. **b** A ground truth image frame from validation video-sample no 1, frame no 12. Image pixel intensities at two random coordinate points with opposite shades of gray are found to be P_i: 252 (near white region) and P_i: 1 (near black region). **c** GEN-0 predicted image-frame for exactly same video-sequence and frame number with pixel intensities of P_i: 251 (near white region) and P_i: 7 (near black region) calculated at the exact same coordinate point to that of ground truth image frame

prediction. It is evident that GEN-0 prediction maintains a well-coordinated result of pixel intensities when compared between two different positions with opposite intensities.

3.6 Shape index (σ_t)

In the context of surface shape classification, a combination of Mean Curvature (H) and Gaussian Curvature (K) is used to categorize a point on the image surface into distinct shapes such as Elliptical, Hyperbolic, Parabolic, or Planar. This classification is based on the principal curvatures k_1 and k_2, where $K = k_1 k_2$ and $H = \frac{k_1+k_2}{2}$ [81]. Since our study focuses on analyzing the interfacial region where the phase transitions from one to another, we require an index that can intuitively describe the region where phase transformation occurs, specifically the diffused interface region. This index should account for the interfaces and boundaries of local curvature within the microstructure. For such an analysis, a single value, dimensionless number that fulfills the quantification criteria is the Shape Index (σ_t) as proposed by Koenderink et al. [65]. They decoupled the shape from the magnitude of curvedness, making the surface curvature invariant to changes in scale. The Shape Index provides a continuous measure of the shape of a surface at a point, ranging from -1 to $+1$. The expression for calculating the Shape Index is given in Eq. (10) [82].

$$\sigma_t = \frac{2}{\pi} \arctan \frac{k_2 + k_1}{k_2 - k_1}; \quad (k1 \geq k2) \tag{10}$$

where k_1 and k_2 are the maximum and minimum principal curvatures, calculated as the eigenvalues of the Hessian matrix.

In this work, we have employed the Shape Index to identify and locate curvatures in the microstructure by analyzing distinctive interfacial characteristics. A positive Shape Index value corresponds to regions with a convex shape, whereas a negative Shape Index indicates a concave shape. A Shape Index value of zero ($\sigma_\mu = 0$) signifies the presence of an edge or a transition between different shapes. Since an interface represents a change in metastable phase curvature or a transition from one phase to another, a Shape Index value of zero serves as a reference point for correlating the interface between the predicted microstructure and the ground truth frame. The calculation of the Hessian matrix and the subsequent Shape Index value is performed using the open-source Python library Scikit-Image. [67].

Figure 7 illustrates the curvature features and interface regions detected using the shape index target $\sigma_t = 0$. Interface detection is performed for both the ground truth and predicted frames of the same microstructural frame. The magenta dots surrounding the microstructure's interface denote points that deviate by no more than 0.3 from the targeted value of 0.

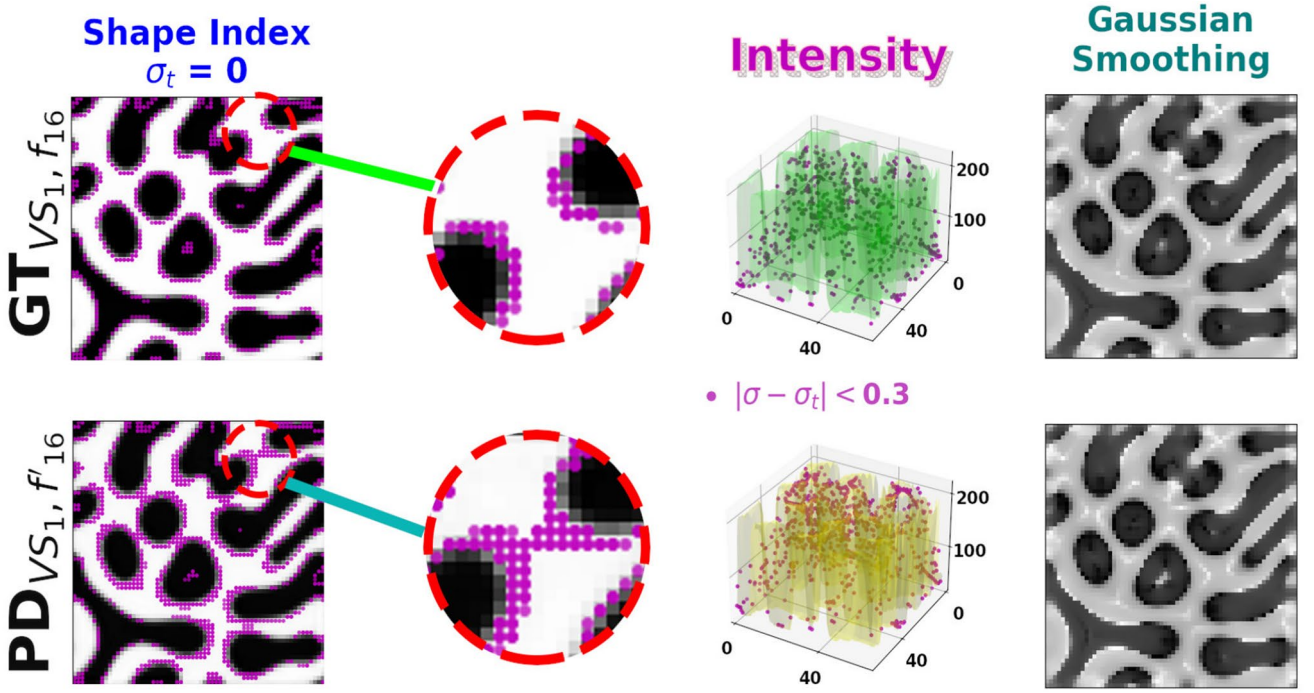


Fig. 7 Shape index could be potentially utilized as a tool for interface informatics. Microstructural interface detected in ground truth and predicted image for a randomly selected microstructural frame of a video sequence using the shape index with target value of $\sigma_t = 0$. The difference detected in the magnified part of GT and PD suggest the predicted microstructural image frame doesn't have a clearly defined interface compared to the ground truth and therefore there might be phase growth corresponding to darker region in future time step. The magenta dots in the shape index diagram suggests that these regions are the ones which deviate from the targeted shape index value of 0 no more than 0.3 suggesting that the interfacial region is of smaller width that shown by the magenta dots. The value of 0.3 as cutoff deviation is chosen for visualization purpose as the dots becomes finer and difficult to visualize for deviation near to zero value. The 3D intensity graph represents the microstructural pixel intensity ranging from 0 to 255 in a three dimensional framework with interface denoted by magenta dots in it. Gaussian smoothing performed for detection of interface via shape index to attenuate the image noise present in microstructure frame, this smoothing technique also helps in finding the sharp change in interface by showing these regions in contrasting colors such as white in dark background

The magnified section inside the dotted circle provides a closer look at the difference between the interfaces detected in the ground truth and predicted frames. It is evident that, in the predicted frame, the interface appears larger, suggesting potential phase growth in that region in future time steps. The 3D graph in the center displays the intensity of microstructural pixels in a three-dimensional framework, with magenta dots marking the interface regions within this 3D space. On the rightmost column, the microstructural images for both the ground truth and predicted frames are shown after passing through a Gaussian smoothing kernel. Gaussian smoothing is applied to reduce and attenuate noise present in the microstructural image data before determining the shape index. The Gaussian smoothing of the microstructural image frame, used for detecting interfaces with a shape index value of zero, visually provides information related to interfacial changes. In the figure, a bright spot within the dark phase at the center of the microstructure is highlighted by the magenta dots in the shape index diagram.

4 Interface in microstructures of Pd–Rh and Cu–Mn alloys

We employed the trained model to rapidly forecast microstructural changes in two distinct engineering alloy systems: Pd–Rh and Cu–Mn. Phase field simulations were conducted for both alloy systems using the MOOSE Framework. The values of the driving force ($G_{min_{Cu-Mn}}$ and $G_{min_{Pd-Rh}}$) were determined from thermodynamic data based on CALPHAD at temperatures of 586.15 and 1196.0 K, respectively. These temperatures were chosen with reference to phase stability decomposition studies conducted by Saha et al. [83] and Garcia et al. [84].

The landscape of the Gibbs free energy curve for both the Pd–Rh and Cu–Mn alloy systems is dictated by the coefficients of Eq. (3), as shown in Fig. 8a for the Cu–Mn alloy system and Fig. 8b for the Pd–Rh system. The values of the six coefficients corresponding to Eq. (3) for the Cu–Mn and Pd–Rh systems are presented in Table 2.

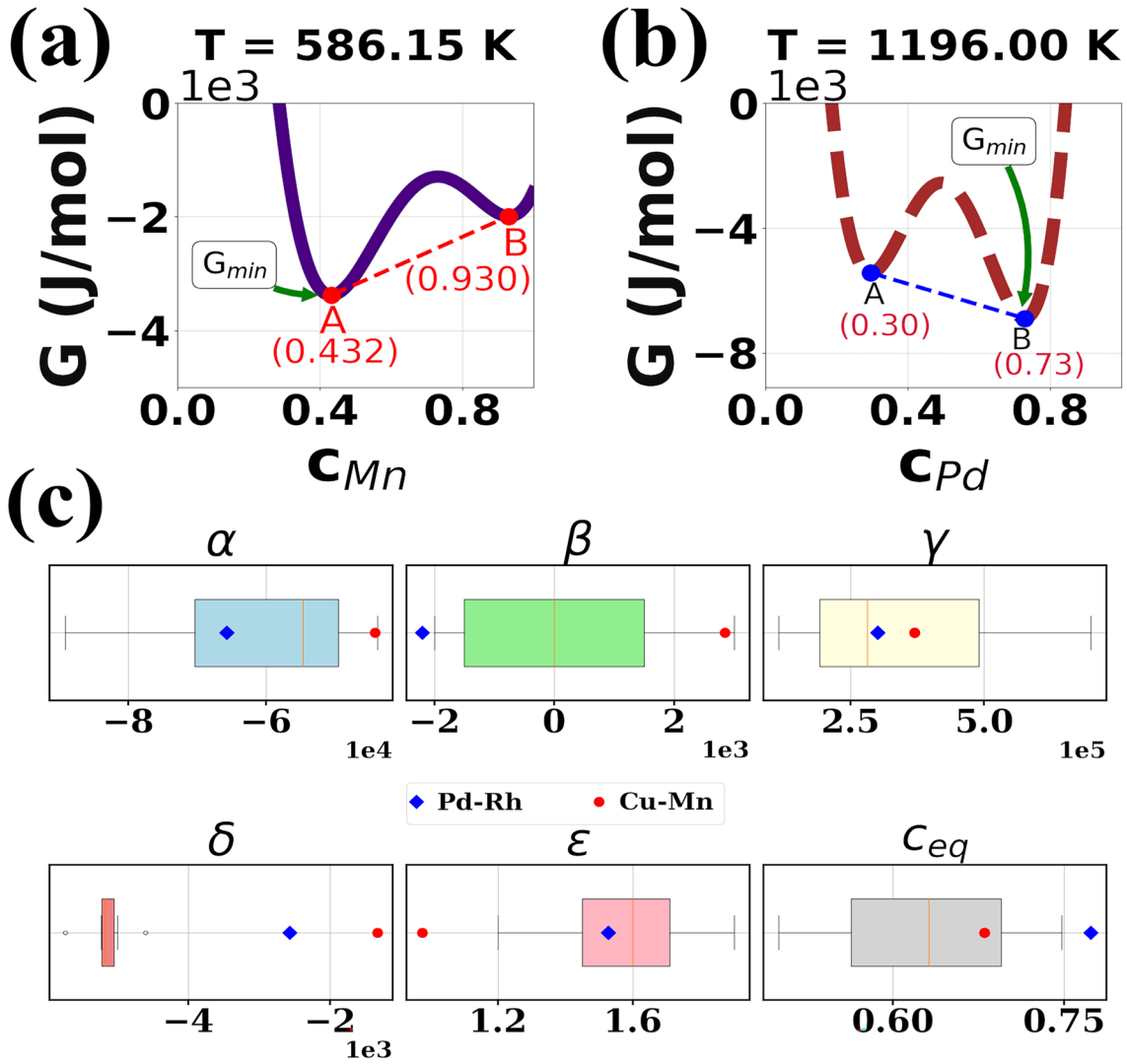


Fig. 8 **a** The landscape of double well curve representing Gibbs free energy for Cu–Mn binary alloy system at 586.15 K with x axis denoting composition of *Mn*. The two points A (c_{Mn} =0.432), and B (c_{Mn} =0.930) denotes two minima points in free energy curve, where global minima of free energy lies at the composition c_{Mn} = 0.432 with a value of G_{min} = −3.378*e*3 J/mol. Similarly, **b** represents the free energy curve for Pd–Rh alloy system at 1163 K with two points A (c_{Pd} =0.30) and B (c_{Pd} =0.73) representing two wells of double well curve with a global minima of free energy G_{min} = −6.893*e*3 J/mol at composition c_{Pd} = 0.73. **c** Box plot visualizing the variation in values of six different coefficients used in Eq. (3) to create the training data for the model along with the values of same coefficients for Pd–Rh system (represented in blue diamond shape) and Cu–Mn system (represented in red dot)

Table 2 The values of coefficients (features) for Cu–Mn and Pd–Rh binary alloy system that subsequently create the phase field generated input in the prediction model

Alloy	α (J/mol)	β (J/mol)	γ (J/mol)	δ (J/mol)	ϵ	c_{eq}	G_{min} (J/mol)
Cu–Mn	−4.4232e4	2.8438e3	3.6976e5	−1.339e3	0.9743	0.68	−3.378e3
Pd-Rh	−6.5701e4	−2.2055e3	3.0077e5	−2.568e3	1.527	0.7733	−6.893e3

It is to be noted that the magnitudes of these variables were determined from the CALPHAD information. For binary Cu–Mn alloy α, β, γ and c_{eq} are well within the features range ascribed in training data whereas, δ and ϵ clearly outside the training data range. Similarly, for Pd–Rh system β, δ and c_{eq} fall outside the range of training values whereas α, γ and ϵ are within the range

By leveraging the four microstructural analysis tools discussed in Sect. 3, we can quantify the errors at the interface level of the predicted microstructure in these two engineering alloy systems. The Microstructural Similarity Index (μ_{SIM}) measures differences in contrast, luminance, and structure at an interfacial resolution to assess the predicted microstructure in comparison to the ground truth image frame.

Blobs detection is utilized to identify regions in the microstructure where there are notable changes in background contrast, indicating an edge or interface of a microstructural phase. Additionally, the Shape Index is employed to detect the entire region of interfaces present in the microstructure by targeting a shape index value of $_{\sigma_t}$ to 0.

Similarly, the histogram of pixel intensity graph can provide insights into prediction accuracy, interfacial width, and the clear separation of phases in the microstructure.

4.1 How similar are the learned microstructures?

To quantify our model's predictions in real engineering alloy systems, we initially analyzed four consecutive generations of microstructural evolution predictions using the μ_{SIM} index. The calculation of the Microstructural Similarity Index (μ_{SIM}) was performed for a randomly sampled set of 100 video sequences generated using our proprietary algorithm, as discussed in Sect. 2.1, for both alloy systems.

Figure 9a displays a linear graph plotting the μ_{SIM} values for four generations of predictions in the Cu–Mn alloy system. The graph illustrates that for the first prediction generation (GEN-0), the μ_{SIM} value is the highest at 0.917, but it gradually decreases to 0.871, 0.829, and 0.792 in the subsequent three generations. In contrast, for the Pd–Rh system, as shown in Fig. 9b, the μ_{SIM} value for the first generation is higher at 0.976, and the microstructural similarity index does not decrease as rapidly for the next

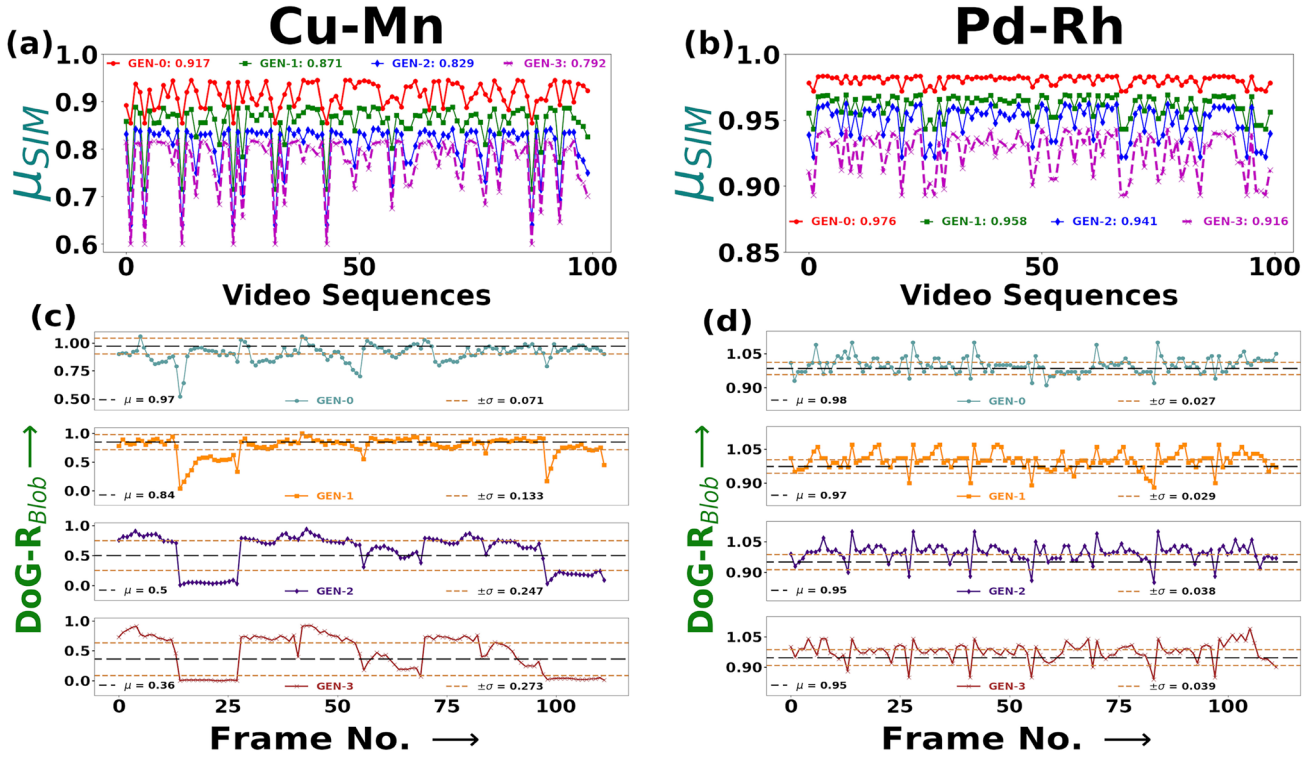


Fig. 9 **a** Microstructural similarity index (μ_{SIM}) plotted for randomly samped 100 video sequences in four generations of predicted microstructure for Cu–Mn binary alloy system. The consecutive μ_{SIM} values for four generations are 0.917, 0.871, 0.829 and 0.792 represented by red, green, blue and magenta lines respectively. **b** Linear plot of μ_{SIM} in generational prediction result of Pd–Rh alloy system for randomly selected 100 video sequences, the four generation of prediction are represented by red, gree, blue and magenta colored lines with μ_{SIM} values of 0.976, 0.958, 0.941 and 0.916 respectively. **c** The ratio of blobs detected in predicted frame of microstructure to that of ground truth frame for four consecutive generation of predictions made by the model for Cu–Mn alloy system using difference of gaussian kernel. The teal colored line represents first generation of prediction and has the least amount of blobs detection deviation where as the yellow, purple and brown colored graph corresponds to second, third and fourth prediction generation with increasing value of deviation for number of blobs detected. **d** Ratio of blobs detected by the difference of gaussian kernel for Pd–Rh alloy system in four consecutive microstructure prediction generation. Although deviation in blobs detected from ground truth frame to that of predicted frame increases from 0.027 to 0.039 from first generation to fourth generation, the change in deviation is quite less significant compared to that in Cu–Mn alloy system

three generations, with values of 0.958, 0.941, and 0.916, respectively.

In the preliminary stage of quantifying microstructural evolution predictions in real engineering alloys, our machine learning model appears to predict the Pd–Rh alloy system with greater accuracy than the Cu–Mn system.

4.2 Locating the edges

Upon further investigation of blobs detected in the microstructural surface for predicted frames and ground truth image frames in a randomly sampled set of 140 microstructural images, using the technique discussed in Sect. 3.4, some interesting findings emerged. For the Cu–Mn alloy system, the number of blobs detected in the predicted microstructure image matches that of the simulation-generated frame in the first generation, with a mean ratio exceeding 0.97 and a deviation of 0.071. However, the mean ratio drops to 0.84 in the second generation and plummets further to 0.5 and 0.36 in the third and fourth generations, as illustrated in Fig. 9c. This suggests that the model provides fairly accurate predictions up to the second prediction generation for the Cu–Mn alloy system.

In contrast, for the Pd–Rh alloy system, the results are significantly different. The ratio of blobs detected in multiple prediction generations for Pd–Rh remains consistently high, with a mean value for blobs detected in the microstructural surface in all four consecutive generations exceeding 0.95 and a maximum deviation of 0.039 observed at the end of the fourth generation. This further supports the finding that the model predicts remarkably well for the Pd-Rh alloy system compared to the Cu–Mn system.

Several factors may contribute to our model's superior performance in the Pd–Rh alloy system compared to the Cu–Mn system. One such factor is the value of the driving force (G_{min}), which is significantly higher for Pd–Rh (−6893.89 J/mol) compared to Cu–Mn (3378.08 J/mol). This suggests that the model performs better for alloy systems with G_{min} values in the range of 10e4.

Additionally, the model's performance can be correlated with the landscape of the Gibbs free energy curve for both alloy systems, as shown in Fig. 9a, b. For an alloy system where phase separation occurs near the equal composition region of the constituent elements, the model appears to predict microstructural evolution more accurately.

4.3 Spatially positioning the region of microstructural transition: ingenuity of Shape Index

As discussed in Sect. 3.6, the shape index can be employed to detect microstructural interfaces by targeting a shape index value equal to zero. The shape index also assists in quantifying differences in microstructural patterns and changes occurring at phase boundaries. For both the Pd–Rh alloy and Cu–Mn system, we randomly selected a single frame of microstructure from the set of video sequences and compared the results of interface detection in predicted and ground truth frames.

Figure 10a illustrates the microstructural interface detected for the Pd–Rh system. In the zoomed area, it is evident that there is a certain region in the predicted frame detected as the microstructure interface, indicating the potential development and growth of a phase boundary in future time steps.

Similarly, in Fig. 10b, the interface detected for the Cu–Mn alloy system is shown. The magnified portion highlights that the predicted frame still contains a small dark region acting as a phase interface, while this region is absent in the ground truth. Using the shape index, we can not only compare and quantify the phase interface between predicted and simulation-generated microstructural frames but also detect regions where interfaces may develop in future time steps.

4.4 Detecting errors of prediction

The third and final quantification measure used to assess the model's performance in two engineering alloy systems (Pd–Rh and Cu–Mn) is the histogram of pixel intensity. Figure 10c presents a twin-plot of the histogram of pixel intensity in randomly selected 100 video frames for both alloy systems.

It is noticeable that for both the Cu–Mn system and Pd–Rh system, the histogram curve for the ground truth microstructural frame peaks at the two extremes of intensity values, near 0 and near 255, represented by the green and black solid lines, respectively. However, when examining the histogram of the first generational predicted frame for the Cu–Mn system, it becomes evident that the curve deviates away from the extremes and toward the center for GEN-0 and GEN-3, represented by the teal colored solid line and yellow dashed line. This deviation may be attributed to the poor prediction of the bulk microstructure phase along with wider interfacial region predictions.

Since the microstructural interface represents the region where there is a change in pixel intensity, transitioning from white to gray or gray to white microstructural patterns, a histogram curve with a high number of pixels in the middle pixel intensity region suggests the presence of a wider interface with less distinct bulk phases. In contrast, for the Pd–Rh alloy system, the first (red solid line) and fourth (magenta dotted line) generational predictions closely align with the ground truth microstructural image, as they do not deviate towards the middle range of pixel intensity and remain near the extreme values. This further validates the model's

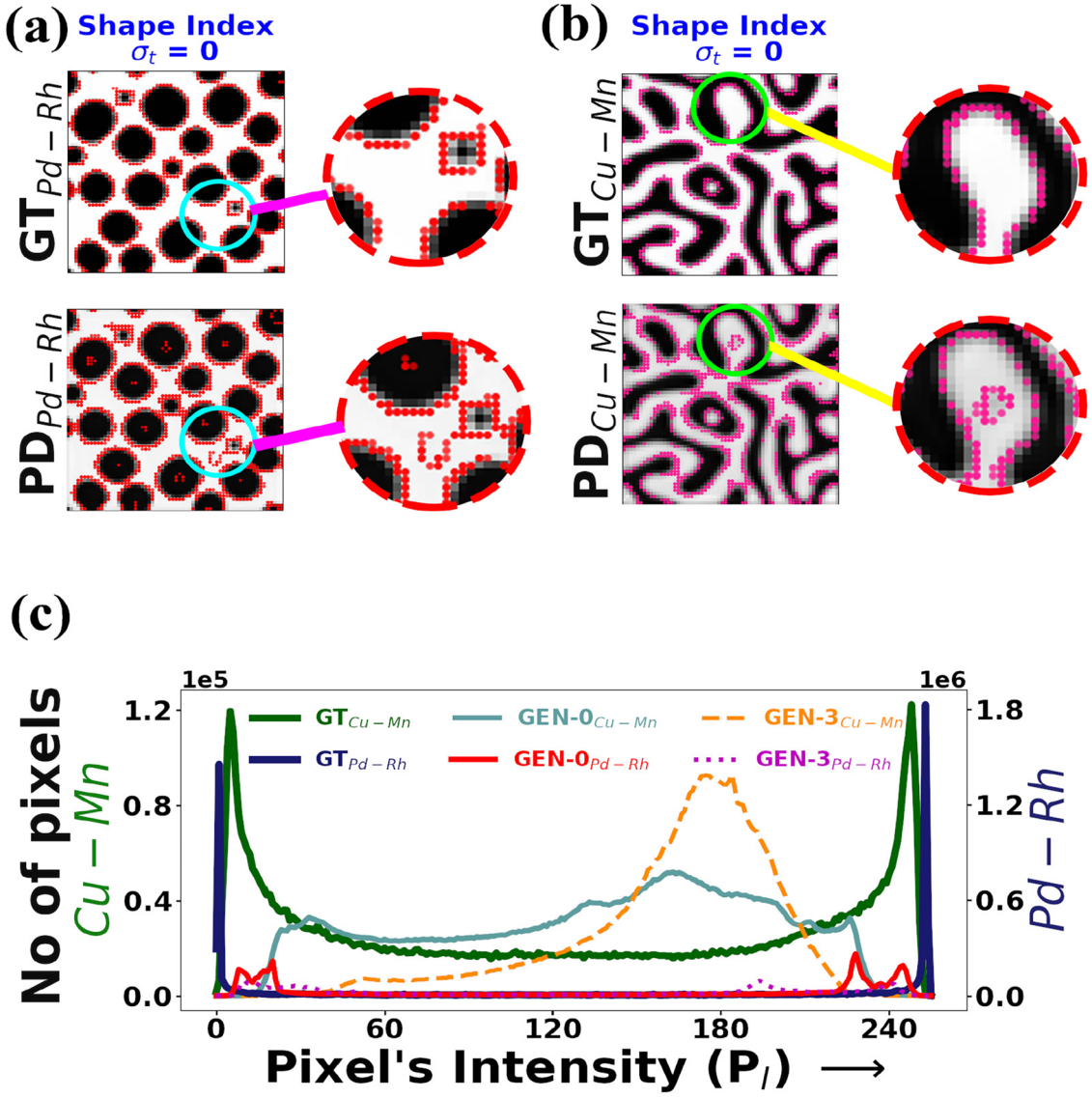


Fig. 10 **a** Detection and comparison of microstructural phase-interface in Pd–Rh engineering alloy system between ground truth image and model predicted image of a randomly selected microstructural frame by the application of shape index analysis. The magnified part denoting the difference in interface detected in ground truth and predicted frame where, a small extra interfacial region is highlighted in predicted frame by the shape index. Shape index value ranges from − 1 to 1 with two extreme denoting either concave or convex microstructural pattern, where as shape index of value 0 denotes the interface or edge in the pattern, hence setting the target of shape index $\sigma_t = 0$ we are able to detect the microstructural interface in the image frame. **b** Similar analysis of interfacial region detected for Cu–Mn alloy system with a highlight showing an interface in predicted frame which is absent in ground truth meaning the predicted result is lagging behind. **c** A twin plot representing the histogram of pixel intensity for predicted and ground truth microstructural frames in two real alloy system. The left y-axis represents Cu–Mn alloy system with a green colored solid line for ground truth frame's pixel histogram which lies mostly at the extreme values of intensity 0 and 255 (0 for black region, 255 for white). The first and fourth generation prediction result is represented by teal solid line and yellow dashed line which deviates from the extreme intensity value meaning the prediction result has wider interface with not so distinct phase separation. Meanwhile the right y-axis represents Pd–Rh alloy system with purple solid line for ground truth microstructural frames that rises at the two extremities of 0 and 255. The major difference between Cu–Mn and Pd–Rh system lies in the generational prediction result as the first and fourth generation denoted by red solid line and magenta dotted line also mimics the ground truth result by rising near the extremities meaning the interface width is shorter and there is clear phase separation in this system

superior performance for the Pd–Rh alloy system compared to the Cu–Mn system.

5 Conclusion

In conclusion, this research work establishes a benchmark model for predicting multi-generational microstructural evolution using state-of-the-art Conv-LSTM neural networks. By capturing spatio-temporal dependencies with remarkable accuracy, the proposed neural network architecture demonstrates its robustness and computational efficiency in predicting microstructural changes in binary alloy systems undergoing phase decomposition. Transitioning from finite element analysis to data-driven machine models for inferring microstructural behavior, this study successfully achieves the objective of computational reducibility, yielding high microstructural similarity indices. It offers a comprehensive insight into the prediction capabilities of the trained model through various quantification techniques, including μ_{SIM}, blob detection ratio, histogram-based pixel intensity comparisons, and shape index differences.

The significance of this research work lies in its contribution to the field of spatio-temporal behavior prediction of microstructures, where accurate inferences are of utmost importance for engineering applications. Notably, the model not only performs well on the testing dataset but also accurately predicts the microstructural evolution and interfacial changes in real engineering alloys, specifically in the Pd–Rh and Cu–Mn systems. A comparison between these two binary alloy systems reveals a superior performance of the model in predicting the Pd–Rh alloy system, with driving force differences playing a major role in dictating model accuracy.

These findings demonstrate the potential applications of these tools in high-risk scenarios to enable early action in preventing hazards and accidents by predicting material deterioration at the microstructural level. The combination of quantitative evaluation metrics with Conv-LSTM model predictions also paves the way for future research to uncover previously undiscovered material behaviors, facilitating the design and optimization of advanced materials. This work opens up new possibilities in the integration of machine learning models with image analysis techniques, providing insights into dynamic and intricate microstructural evolution behavior. Furthermore, it advances the field of materials science and engineering by enabling accurate and efficient predictions of multiple generations of microstructural patterns.

Subsequent progress and further enhancements of the current predictive model are possible and can be achieved by implementing changes in the training dataset, such as increasing pixel resolution and the number of input microstructural image frames. Expanding the range of driving force parameters, considering a wider range of materials, and incorporating various microstructural evolution phenomena in the training set will enhance the model's predictive capabilities in terms of applicability and generalizability.

In summary, the approach presented in this paper for predicting multi-generational microstructural evolution through Conv-LSTM neural networks, coupled with quantification and evaluation metrics, provides a valuable framework for advancing the understanding of material behavior, design, and optimization across a wide range of engineering applications.

Table 3 Values of six coefficients taken as initial reference

α (J/mol)	β (J/mol)	γ (J/mol)	δ (J/mol)	ϵ	c_{eq}
−5.5e4	0	2.75e5	−0.5e3	1.5	0.65

Appendix: Parametrization of driving force G

To visualize the effects of coefficient changes on the landscape of Gibbs free energy, as governed by Eq. (3), we initially selected a random set of parametric values as a reference, as presented in Table 3. In Eq. (3), 'c' represents the composition of an element in the alloy system, while all other variables are coefficients with specific meanings that determine certain characteristics of the Gibbs free energy curve. In the following sections, we individually varied each of these coefficients and visualized their effects.

Effects of change in α

The coefficient α determines the amplitude of the double-well structure in the Gibbs free energy curve. To create minima at two points and promote phase separation, a negative value of α is necessary. This separation leads to the formation of distinct phases. As illustrated in Fig. 11a, a higher α value of $-5.5e4$ J/mol causes the red curve to dip more than the green curve.

Variation in β

The β parameter is associated with the slope of the free energy curve, influencing the stability of separated phases. When $\beta = 0$, both separated phases are equally preferred, resulting in a symmetrical curve. However, a non-zero β value favors one of the phases, making the free energy curve asymmetrical. Figure 1a illustrates that at composition ($c = 0.533$), the concave region of the curve is more prominent than at composition ($c = 0.238$). Consequently, the free energy is lowest at this composition, indicating a

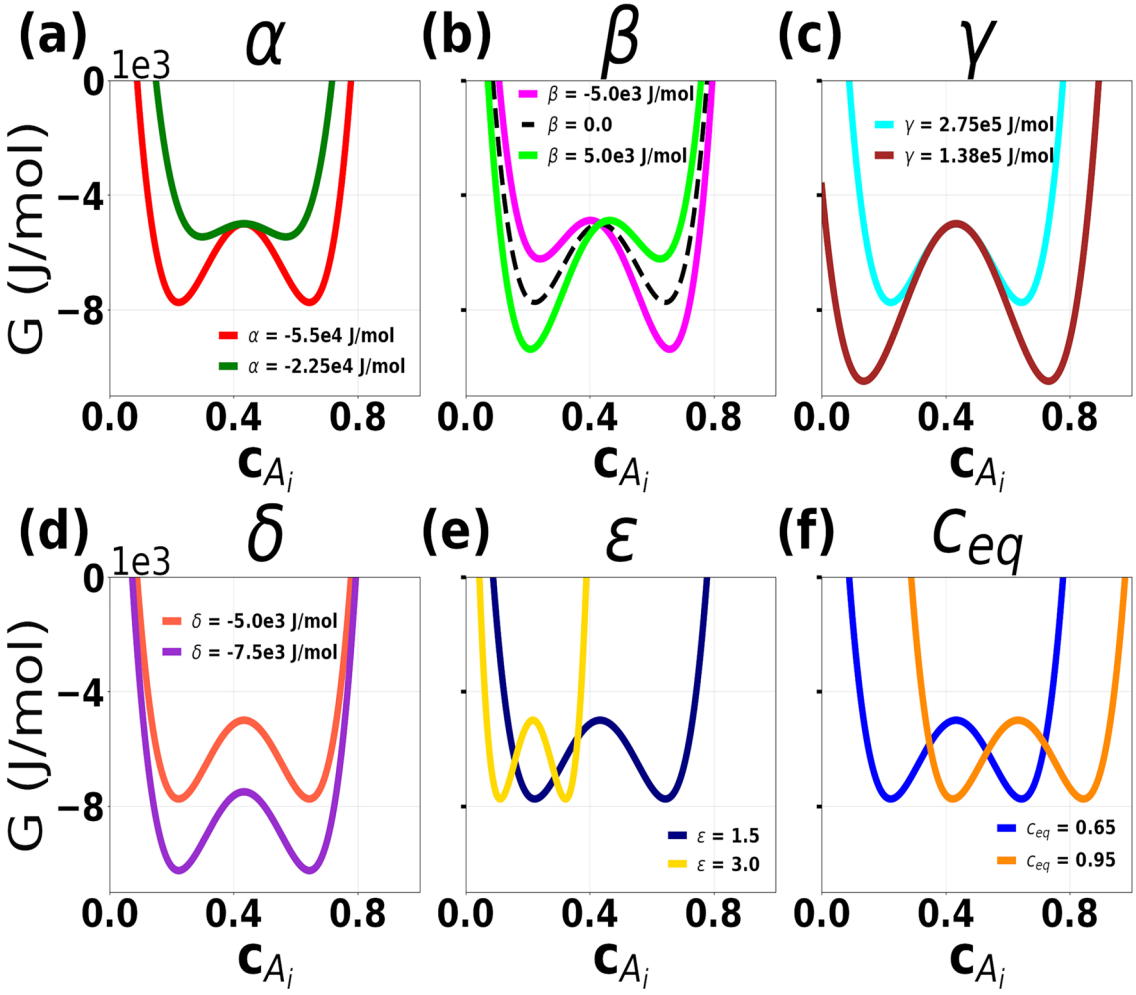


Fig. 11 Gibbs free energy landscape fluctuation with the variation of parameters: **a** α, **b** β, **c** γ, **d** δ, **e** ϵ, and **f** c_{eq}

non-zero β value ($\beta = -0.4e4$ J/mol) and a preference for the phase at ($c = 0.533$). In Fig. 11b, the three different curves representing variations in the driving force also have different β values. The green curve has a positive β value of $5.0e3$ J/mol, the magenta curve has a negative β value ($-5.0e3$ J/mol), while the dotted black curve is completely symmetric, with a slope of 0, indicating $\beta = 0$. This type of expression is used in [35]. In summary, the β coefficient in Eq. (3) can significantly affect the shape of a free energy curve.

Changing γ

The coefficient γ introduces a higher-order interaction between the two components of a binary alloy. Similar to α, it is associated with the quadratic term of the expression, affecting the depth of the double-well structure, as shown in Fig. 11c. For a binary alloy system to undergo phase separation through phase decomposition, it is necessary for γ to have an opposite sign to that of α. In a thermodynamically and physically valid Gibbs free energy of a system, the value of α must always be negative, making γ positive. A positive γ value facilitates phase separation, while an opposite value hinders the separation process, reducing the double-well shape to an inverted parabola.

Role of δ

The term δ is independent of composition but plays a major role in accounting for external factors related to the enthalpy and entropy of the system. It represents a global energy offset that does not alter the shape of the energy function or affect the relative stability or nature of the double-wells. However, variations in δ cause the entire curve to shift vertically, uniformly impacting the overall energy level of the system. This effect is illustrated in Fig. 11d, where the magnitude of δ determines the vertical position of the free energy curve.

Parameter ϵ

The unit-less term ϵ in the equation is associated with the characteristic range of the composition, its value determines the width of double-well curvature. As shown in Fig. 11e a larger value of ϵ (yellow curve with $\epsilon = 3$) means the phase decomposition is observed in narrower compositional range whereas for a smaller value (dark blue curve with $\epsilon = 1.5$) the decomposition occurs over a broader compositional range. For a realistic phenomenon with non-negative compositional values, ϵ should always be greater than zero.

c_{eq} in G

The c_{eq} parameter is used as a reference or origin point for the energy function, the difference between the composition c and c_{eq} affects the double-well and energy landscape's position, it shifts the horizontal position of the curve without changing the shape and symmetry of the free energy landscape as shown in Fig. 11f.

Superposed effect

Collectively, all the coefficients and parameters of free energy expression defines the curvature, slope, polynomial behavior and global energy offset of the system, as a whole they determine the characteristic nature of the landscape of energy function and drive the phase separation process.

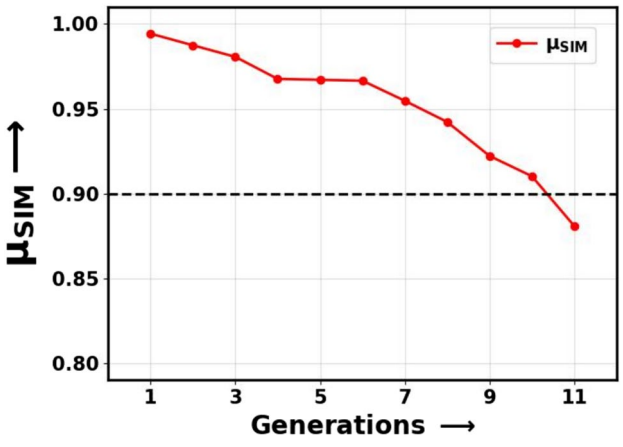


Fig. 12 Microstructural similarity index (μ_{SIM}) of predicted consecutive 10 generations for model architecture A2 with 3 frames as input to the model. It is observed that the prediction similarity index is above 90% for the 10 consecutive generations and only after the 10th generation the prediction similarity index (accuracy) drops the 90% bench-mark

Appendix: Prediction accuracy beyond GEN-3

After Generation 3, the model's predictions become completely independent of the input frames supplied from the phase field simulations, relying solely on the results of previous predictions, thus entering the 'prediction-based prediction' zone. Our analysis reveals that for model architecture A2 with 3 frames as input maintains a microstructural similarity index of 90% or higher up to the 10th generation, as shown in Fig. 12, with an estimated computational time of 273.25 s. However, after the 10th generation, the accuracy of the model, measured by the microstructural similarity index, falls below the 90% mark. Consequently, we do not recommend using predictions beyond this generation for critical decision-making processes in any kind of failure analysis.

Acknowledgements This work was supported by the National Science Centre, Poland (UMO-2021/42/E/ST5/00339) and the HORIZON EUROPE European Research Council (101123107-μTWIN).

Data Availability The data and codes for this work are available at https://github.com/subediupadesh/Micro-Interface-ConvLSTM.

Declarations

Conflict of interest The authors declare that they have no conflict of interest.

References

1. Moelans N, Blanpain B, Wollants P (2008) An introduction to phase-field modeling of microstructure evolution. CALPHAD: Comput Coupl Phase Diagr Thermochem 32(2):268–294. https://doi.org/10.1016/j.calphad.2007.11.003
2. Prawoto Y, Ikeda M, Manville SK, Nishikawa A (2008) Design and failure modes of automotive suspension springs. Eng Fail Anal 15(8):1155–1174. https://doi.org/10.1016/j.engfailanal.2007.11.003
3. Dallago M, Winiarski B, Zanini F, Carmignato S, Benedetti M (2019) On the effect of geometrical imperfections and defects on the fatigue strength of cellular lattice structures additively manufactured via Selective Laser Melting. Int J Fatigue 124:348–360. https://doi.org/10.1016/j.ijfatigue.2019.03.019
4. Li F, Li J, Huang T, Kou H, Zhou L (2017) Compression fatigue behavior and failure mechanism of porous titanium for biomedical applications. J Mech Behav Biomed Mater 65:814–823. https://doi.org/10.1016/j.jmbbm.2016.09.035
5. Aksakal B, Yildirim OS, Gul H (2004) Metallurgical failure analysis of various implant materials used in orthopedic applications. J Fail Anal Prev 4(3):17–23. https://doi.org/10.1007/s11668-996-0007-9
6. Moghadasi K, Mohd Isa MS, Ariffin MA, Mohdjamil MZ, Raja S, Wu B, Yamani M, Bin Muhamad MR, Yusof F, Jamaludin MF, AbKarim MS, Abdul Razak B, Yusoff N (2022) A review on biomedical implant materials and the effect of friction stir based techniques on their mechanical and tribological properties. J Market Res 17:1054–1121. https://doi.org/10.1016/j.jmrt.2022.01.050

7. Mohammadi A, Edalati P, Arita M, Bae JW, Kim HS, Edalati K (2022) Microstructure and defect effects on strength and hydrogen embrittlement of high-entropy alloy CrMnFeCoNi processed by high-pressure torsion. Mater Sci Eng A 844:143179. https://doi.org/10.1016/j.msea.2022.143179
8. Krill CE, Chen LQ (2002) Computer simulation of 3-D grain growth using a phase-field model. Acta Mater 50(12):3057–3073. https://doi.org/10.1016/s1359-6454(02)00084-8
9. Spatschek R, Brener E, Karma A (2011) Phase field modeling of crack propagation. Phil Mag 91(1):75–95. https://doi.org/10.1080/14786431003773015
10. Lo YS, Borden MJ, Ravi-Chandar K, Landis CM (2019) A phase-field model for fatigue crack growth. J Mech Phys Solids 132:103684. https://doi.org/10.1016/j.jmps.2019.103684
11. Lowengrub JS, Ratz A, Voigt A (2009) Phase-field modeling of the dynamics of multicomponent vesicles: spinodal decomposition, coarsening, budding, and fission. Phys Rev E Stat Nonlinear Soft Matter Phys 79(3):031926. https://doi.org/10.1103/PhysRevE.79.031926
12. Yang M, Wang L, Yan W (2021) Phase-field modeling of grain evolutions in additive manufacturing from nucleation, growth, to coarsening. NPJ Comput Mater 7(1):56. https://doi.org/10.1038/s41524-021-00524-6
13. Subedi U, Coutinho YA, Malla PB, Gyanwali K, Kunwar A (2022) Automatic featurization aided data-driven method for estimating the presence of intermetallic phase in multi-principal element alloys. Metals 12(6):964. https://doi.org/10.3390/met12060964
14. Subedi U, Poudel S, Gyanwali K, Amorim Coutinho Y, Matula G, Kunwar A (2022) State-of-the-art review on the aspects of martensitic alloys studied via machine learning. Metals 12(11):1884. https://doi.org/10.3390/met12111884
15. Poudel S, et al (2024) AlloyManufacturingNet for discovery and design of hardness-elongation synergy in multi-principal element alloys. Eng Appl Artif Intell 132:107902. https://doi.org/10.1016/j.engappai.2024.107902
16. Mamo HB, et al (2024) Prototyping Ti2Cu intermetallic grain growth heterogeneously in Ti6Al4V matrix through laser additive manufacturing. Mater Des 246:113312. https://doi.org/10.1016/j.matdes.2024.113312
17. Poudel S, et al (2024) Unraveling elastochemical effects in microstructural evolution of Al–Cu–Ni system through DFT-informed multi-phase field simulations. Int J Solids Struct 300:112894. https://doi.org/10.1016/j.ijsolstr.2024.112894
18. Vivek Bhave C, Zheng G, Sridharan K, Schwen D, Tonks MR (2023) An electrochemical mesoscale tool for modeling the corrosion of structural alloys by molten salt. J Nucl Mater 574:154147. https://doi.org/10.1016/j.jnucmat.2022.154147
19. Yang H, Bao R, Zhang J, Peng L, Fei B (2011) Creep-fatigue crack growth behaviour of a nickel-based powder metallurgy superalloy under high temperature. Eng Fail Anal 18(3):1058–1066. https://doi.org/10.1016/j.engfailanal.2010.12.025
20. Chevalier J, Gremillard L, Deville S (2007) Low-temperature degradation of zirconia and implications for biomedical implants. Annu Rev Mater Res 37(1):1–32. https://doi.org/10.1146/annurev.matsci.37.052506.084250
21. Challa VSA, Nune KC, Gong N, Misra RDK (2020) The significant impact of mechanically-induced phase transformation on cellular functionality of biomedical austenitic stainless steel. J Mech Behav Biomed Mater 108:103815. https://doi.org/10.1016/j.jmbbm.2020.103815
22. Poudel, S., et al., PiezoTensorNet: Crystallography informed multi-scale hierarchical machine learning model for rapid piezoelectric performance finetuning Applied Energy 361, 122901 (2024) https://doi.org/10.1016/j.apenergy.2024.122901
23. Oca Zapiain D, Stewart JA, Dingreville R (2021) Accelerating phase-field-based microstructure evolution predictions via surrogate models trained by machine learning methods. NPJ Comput Mater 7(1):3. https://doi.org/10.1038/s41524-020-00471-8
24. Yang K, Cao Y, Zhang Y, Fan S, Tang M, Aberg D, Sadigh B, Zhou F (2021) Self-supervised learning and prediction of microstructure evolution with convolutional recurrent neural networks. Patterns 2(5):100243. https://doi.org/10.1016/j.patter.2021.100243
25. Hu C, Martin S, Dingreville R (2022) Accelerating phase-field predictions via recurrent neural networks learning the microstructure evolution in latent space. Comput Methods Appl Mech Eng 397:115128. https://doi.org/10.1016/j.cma.2022.115128
26. Kazemzadeh Farizhandi AA, Mamivand M (2023) Spatiotemporal prediction of microstructure evolution with predictive recurrent neural network. Comput Mater Sci 223:112110. https://doi.org/10.1016/j.commatsci.2023.112110
27. Ahmad O, Kumar N, Mukherjee R, Bhowmick S (2023) Accelerating microstructure modelling via machine learning: a new method combining Autoencoder and ConvLSTM. arXiv:2305.00938
28. Gaston D, Newman C, Hansen G, Lebrun-Grandié D (2009) MOOSE: a parallel computational framework for coupled systems of nonlinear equations. Nucl Eng Des 239(10):1768–1778. https://doi.org/10.1016/j.nucengdes.2009.05.021
29. Tonks MR, Gaston D, Millett PC, Andrs D, Talbot P (2012) An object-oriented finite element framework for multiphysics phase field simulations. Comput Mater Sci 51(1):20–29. https://doi.org/10.1016/j.commatsci.2011.07.028
30. ...Lindsay AD, Gaston DR, Permann CJ, Miller JM, Andrš D, Slaughter AE, Kong F, Hansel J, Carlsen RW, Icenhour C, Harbour L, Giudicelli GL, Stogner RH, German P, Badger J, Biswas S, Chapuis L, Green C, Hales J, Hu T, Jiang W, Jung YS, Matthews C, Miao Y, Novak A, Peterson JW, Prince ZM, Rovinelli A, Schunert S, Schwen D, Spencer BW, Veeraraghavan S, Recuero A, Yushu D, Wang Y, Wilkins A, Wong C (2022) 2.0—moose: Enabling massively parallel multiphysics simulation. SoftwareX 20:101202. https://doi.org/10.1016/j.softx.2022.101202
31. Aagesen LK, Gao Y, Schwen D, Ahmed K (2018) Grand-potential-based phase-field model for multiple phases, grains, and chemical components. Phys Rev E 98(2). https://doi.org/10.1103/PhysRevE.98.023309
32. Iquebal AS, Wu P, Sarfraz A, Ankit K (2023) Emulating the evolution of phase separating microstructures using low-dimensional tensor decomposition and nonlinear regression. MRS Bull. https://doi.org/10.1557/s43577-022-00443-x
33. Iwamatsu M (2008) Direct numerical simulation of homogeneous nucleation and growth in a phase-field model using cell dynamics method. J Chem Phys. https://doi.org/10.1063/1.2883652
34. Wu P, Iquebal AS, Ankit K (2023) Emulating microstructural evolution during spinodal decomposition using a tensor decomposed convolutional and recurrent neural network. Comput Mater Sci 224:112187. https://doi.org/10.1016/j.commatsci.2023.112187
35. Zhang L, Tonks MR, Gaston D, Peterson JW, Andrs D, Millett PC, Biner BS (2013) A quantitative comparison between and elements for solving the Cahn–Hilliard equation. J Comput Phys 236:74–80. https://doi.org/10.1016/j.jcp.2012.12.001
36. Nolte DD (2019) Introduction to modern dynamics. Oxford University Press. https://doi.org/10.1093/oso/9780198844624.001.0001
37. Yang X, Ju L (2017) Linear and unconditionally energy stable schemes for the binary fluid-surfactant phase field model. Comput Methods Appl Mech Eng 318:1005–1029. https://doi.org/10.1016/j.cma.2017.02.011
38. Yang X, Xiao J (2019) On linear and unconditionally energy stable algorithms for variable mobility Cahn–Hilliard type equation with

logarithmic Flory–Huggins potential. Commun Comput Phys. https://doi.org/10.4208/cicp.OA-2017-0259
39. Binder K (2007) Double-well thermodynamic potentials and spinodal curves: how real are they? Philos Mag Lett 87(11):799–811. https://doi.org/10.1080/09500830701496560
40. Wang X, Kou J, Cai J (2020) Stabilized energy factorization approach for Allen–Cahn equation with logarithmic Flory–Huggins potential. J Sci Comput 82(2):25. https://doi.org/10.1007/s10915-020-01127-x
41. Hussain MM, Ma H, Huang M, Gao Z, Cao J, Wang C, Dong C, Wang Y, Kunwar A (2020) Fabrication of cerium myristate coating for a mechanochemically robust modifier-free superwettability system to enhance the corrosion resistance on 316L steel by one-step electrodeposition. Surf Coat Technol 398:125970. https://doi.org/10.1016/j.surfcoat.2020.125970
42. Kunwar A, Tonks MR, Shang S, Song X, Wang Y, Ma H (2017) Quantitative polynomial free energy based phase field model for void motion and evolution in Sn under thermal gradient. In: 2017 18th International Conference on Electronic Packaging Technology (ICEPT), pp. 1502–1507. IEEE. https://doi.org/10.1109/ICEPT.2017.8046720 . http://ieeexplore.ieee.org/document/8046720/
43. Bandyopadhyay AK, Ray PC, Gopalan V (2006) Dynamical systems analysis for polarization in ferroelectrics. J Appl Phys. https://doi.org/10.1063/1.2388124
44. Shin W, Lee J, Chang K (2020) The effects of inhomogeneous elasticity and dislocation on thermodynamics and the kinetics of the spinodal decomposition of a Fe–Cr system: a phase-field study. Metals 10(9):1209. https://doi.org/10.3390/met10091209
45. Ahrens J, Geveci B, Law C (2005) ParaView: An End-User Tool for Large Data Visualization ParaViewWeb View project. In: Los Alamos National Laboratory, vol 836. Elesvier. https://datascience.dsscale.org/wp-content/uploads/2016/06/ParaView.pdf
46. Singhal SP, Herman H, Hirvonen JK (1978) Spinodal decomposition in amorphous Au-implanted Pt. Appl Phys Lett 32(1):25–26. https://doi.org/10.1063/1.89819
47. Otis R, Liu Z-K (2017) pycalphad: CALPHAD-based computational thermodynamics in Python. J Open Res Softw 5(1):1. https://doi.org/10.5334/jors.140
48. Lecun Y, Bengio Y (1995) In: Arbib MA (ed) Convolutional networks for images, speech and time series. The MIT Press, pp 255–258
49. Hochreiter S, Schmidhuber J (1997) Long short-term memory. Neural Comput 9:1735–1780. https://doi.org/10.1162/neco.1997.9.8.1735
50. Olah C (2015) Understanding LSTM Networks. http://colah.github.io/posts/2015-08-Understanding-LSTMs/
51. Elsworth S, Guttel S (2020) Time series forecasting using lstm networks: a symbolic approach. arXiv:2003.05672
52. Bird JJ, Faria DR, Ekart A, Premebida C, Ayrosa PPS (2020) Lstm and gpt-2 synthetic speech transfer learning for speaker recognition to overcome data scarcity. arXiv:2007.00659
53. Singh SP, Wang L, Gupta S, Gulyas B, Padmanabhan P (2021) Shallow 3D CNN for detecting acute brain hemorrhage from medical imaging sensors. IEEE Sens J 21(13):14290–14299. https://doi.org/10.1109/JSEN.2020.3023471
54. Li Q, Cai W, Wang X, Zhou Y, Feng DD, Chen M (2014) Medical image classification with convolutional neural network. In: 2014 13th international conference on control automation robotics and vision, ICARCV 2014, pp 844–848. IEEE. https://doi.org/10.1109/ICARCV.2014.7064414 . http://ieeexplore.ieee.org/document/7064414/
55. Shi X, Chen Z, Wang H, Yeung DY, Wong WK, Woo WC (2015) Convolutional lstm network: a machine learning approach for precipitation nowcasting. In: Advances in neural information processing systems, pp 802–810. arXiv:1506.04214
56. Vaswani A, Shazeer N, Parmar N, Uszkoreit J, Jones L, Gomez AN, Kaiser Ł, Polosukhin I (2017) Attention is all you need. In: Advances in neural information processing systems, pp 5999–6009. arXiv:1706.03762
57. Radford A, Narasimhan K, Salimans T, Sutskever I (2018) Improving language understanding by generative pre-training. Homol Homot Appl 9:399–438
58. Chollet F, et al (2015) Keras. GitHub. https://github.com/fchollet/keras
59. Keras: ConvLSTM2D layer (2022). https://keras.io/api/layers/recurrent_layers/conv_lstm2d/
60. Amogh J (2021) Keras: next-frame video prediction with convolutional LSTMs. https://keras.io/examples/vision/conv_lstm/ https://github.com/keras-team/keras-io/blob/master/examples/vision/conv_lstm.py
61. Kunwar A, Malla PB, Sun J, Qu L, Ma H (2021) Convolutional neural network model for synchrotron radiation imaging datasets to automatically detect interfacial microstructure: An in situ process monitoring tool during solar PV ribbon fabrication. Sol Energy 224:230–244. https://doi.org/10.1016/j.solener.2021.06.006
62. Um K, Hu X, Wang B, Thuerey N (2021) Spot the difference: accuracy of numerical simulations via the human visual system. ACM Trans Appl Percept 18:1–15. https://doi.org/10.1145/3449064
63. Wang Z, Bovik AC, Sheikh HR, Simoncelli EP (2004) Image quality assessment: from error visibility to structural similarity. IEEE Trans Image Process 13:600–612. https://doi.org/10.1109/TIP.2003.819861
64. Silva EA, Panetta K, Agaian SS (2007) Quantifying image similarity using measure of enhancement by entropy. 6579:219–230. https://doi.org/10.1117/12.720087
65. Koenderink JJ, Doorn AJ (1992) Surface shape and curvature scales. Image Vis Comput 10(8):557–564. https://doi.org/10.1016/0262-8856(92)90076-F
66. Bradski G (2000) The OpenCV Library. Dr. Dobb's Journal of Software Tools
67. Walt S, Schönberger JL, Nunez-Iglesias J, Boulogne F, Warner JD, Yager N, Gouillart E, Yu T (2014) scikit-image: image processing in python. PeerJ 2:453. https://doi.org/10.7717/peerj.453
68. Khalel A (2018) Sewar. https://github.com/andrewekhalel/sewar
69. Kumar J, Chen F, Doermann D (2019) Sharpness estimation for document and scene images. https://github.com/umang-singhal/pydom
70. Hunter JD (2007) Matplotlib: a 2D graphics environment. Comput Sci Eng 9(3):90–95. https://doi.org/10.1109/MCSE.2007.55
71. Subedi U, Moelans N, Tański T, Kunwar A (2024) Rapid portabilization of elasto-chemical evolution data for dental Ti–Cr alloy microstructure through sparsification and tensor computation. Scripta Mater 244:116027. https://doi.org/10.1016/j.scriptamat.2024.116027
72. Brunet D, Vrscay ER, Wang Z (2012) On the mathematical properties of the structural similarity index. IEEE Trans Image Process 21:1488–1499. https://doi.org/10.1109/TIP.2011.2173206
73. Walt S, Schonberger JL, Nunez-Iglesias J, Boulogne F, Warner JD, Yager N, Gouillart E, Yu T (2014) scikit-image: image processing in Python. PeerJ 2:453. https://doi.org/10.7717/peerj.453
74. Catarious DM, Baydush AH, Floyd CE (2006) Characterization of difference of Gaussian filters in the detection of mammographic regions. Med Phys 33(11):4104–4114. https://doi.org/10.1118/1.2358326
75. Zhao F, DeSilva CJS (2002) Use of the Laplacian of Gaussian operator in prostate ultrasound image processing 2:812–815. https://doi.org/10.1109/iembs.1998.745557
76. Fotin SV, Yankelevitz DF, Henschke CI, Reeves AP (2019) A multiscale Laplacian of Gaussian (LoG) filtering approach to

pulmonary nodule detection from whole-lung CT scans. arXiv:1907.08328
77. Kong H, Akakin HC, Sarma SE (2013) A generalized Laplacian of gaussian filter for blob detection and its applications. IEEE Trans Cybern 43(6):1719–1733. https://doi.org/10.1109/TSMCB.2012.2228639
78. Sotak GE, Boyer KL (1989) The Laplacian-of-Gaussian kernel: a formal analysis and design procedure for fast, accurate convolution and full-frame output. Comput Vis Graph Image Process 48(2):147–189. https://doi.org/10.1016/S0734-189X(89)80036-2
79. Lindeberg T (2015) Image matching using generalized scale-space interest points. J Math Imaging Vis 52(1):3–36. https://doi.org/10.1007/s10851-014-0541-0
80. Gunn SR (1999) On the discrete representation of the Laplacian of Gaussian. Pattern Recogn 32(8):1463–1472. https://doi.org/10.1016/S0031-3203(98)00163-0
81. Besl PJ, Jain RC (1986) Invariant surface characteristics for 3D object recognition in range images. Comput Vis Graph Image Process 33(1):33–80. https://doi.org/10.1016/0734-189X(86)90220-3
82. Cantzler H, Fisher RB. Comparison of HK and SC curvature description methods. In: Proceedings third international conference on 3-D digital imaging and modeling, pp 285–291. IEEE Computer Society. https://doi.org/10.1109/IM.2001.924458. http://ieeexplore.ieee.org/document/924458/
83. Saha T, Mookerjee A (1997) A phase-stability study of PdRh alloys. J Phys Condens Matter 9(10):2179–2186. https://doi.org/10.1088/0953-8984/9/10/007
84. Sigala-Garcia DA, Lopez-Hirata VM, Saucedo-Munoz ML, Dorantes-Rosales HJ, Villegas-Cardenas JD (2022) Phase-field simulation of spinodal decomposition in Mn–Cu alloys. Metals 12(7):1220. https://doi.org/10.3390/met12071220

Publisher's Note Springer Nature remains neutral with regard to jurisdictional claims in published maps and institutional affiliations.

Springer Nature or its licensor (e.g. a society or other partner) holds exclusive rights to this article under a publishing agreement with the author(s) or other rightsholder(s); author self-archiving of the accepted manuscript version of this article is solely governed by the terms of such publishing agreement and applicable law.

ARTICLE IV

A non-isothermal multi-phase field approach to model the meltpool and IMC grains interaction in Ti-Au material

Computational Materials Science 255 (2025) 113875

Contents lists available at ScienceDirect

Computational Materials Science

journal homepage: www.elsevier.com/locate/commatsci

Full length article

A non-isothermal multi-phase field approach to model the meltpool and IMC grains interaction in Ti-Au material

Upadesh Subedi [a,b,c,*], Nele Moelans [c], Tomasz Tański [a], Anil Kunwar [b]

[a] Department of Engineering Materials and Biomaterials, Faculty of Mechanical Engineering, Silesian University of Technology, 44-100 Gliwice, Poland
[b] Scientific and Didactic Laboratory of Nanotechnology and Material Technologies, Faculty of Mechanical Engineering, Silesian University of Technology, 44-100 Gliwice, Poland
[c] Department of Materials Engineering, KU Leuven, Kasteelpark Arenberg 44 Bus 2450, 3001 Leuven, Belgium

ARTICLE INFO

Dataset link: https://github.com/subediupadesh/MultiPhysics_MultiPhaseField_LaserProcessing

Keywords:
Interdiffusion
Laser irradiance
Non-isothermal model
Meltpool-IMC interaction
Lewis number

ABSTRACT

This study introduces a combined phase-field multi-physics approach to simulate laser-induced phase transformations and microstructural evolution in the Ti-Au alloy system, which is crucial for advancing additive manufacturing processes. By varying laser parameters, such as irradiance and scan speed, we used simulations to quantify phase areas and free energy dynamics, revealing intricate interplays between heat flow and chemical diffusion. The simulations show that under maximum heat flux conditions (150 kW/cm^2 at 4 nm/ms), meltpool depth reached 180 nm, surpassing the 158 nm depth observed at 134.6 kW/cm^2. Moreover, the growth of Ti_3Au intermetallic compound (IMC) formed due to the interfacial reaction was studied. IMC layer thickness peaked at 364 nm under higher irradiance, marking a 25% increase over lower irradiance conditions. Analysis of Lewis Number revealed that meltpool diffusion occurs more slowly than heat transfer.

1. Introduction

Titanium alloys has been ubiquitously used as one of the key materials in modern manufacturing processes. Mainly due to their heightened superior qualities such as high-strength-to-weight ratio [1], lightweight, corrosion resistance [2], enhanced mechanical properties [3] and bio-compatibility [4,5]. One of them which has gained significant research attraction is titanium-gold (Ti–Au), which is considered to have a huge potential in medical sector as bio-implant material [6]. The inert nature of gold alloyed with superior mechanical properties of titanium gives result into an unique combination of strength, non-toxicity, corrosion-resistance, high radiopacity as well as showcasing the shape memory effect [7]. In addition, the improved integration of alloy with bone tissue makes it highly suitable for bodily implant resulting in faster and reliable osseointegration [8,9].

In recent study, Svanidze et al. [10] reported that an intermetallic compound (IMC) of Titanium-Gold (Ti_3Au) exhibits an exceptional hardness nearly the four times as that of pure Ti or steel alloys. Similarly, Lukose et al. [11] found that Ti_3Au thin film not only shows high hardness but also an excellent bio-compatibility with viability level greater than 95% suggesting it as the future of thin film coating capable of expanding lifetime of bodily implants. In another work by Kocabas et al. [12], the intermetallics Ti_3Au showed a remarkable enhancement of energy absorption in thin-walled tubes under different impact loading.

With such incredible physical and mechanical properties, the practical application of the intermetallics Ti_3Au comes to the challenge of manufacturing it with purity. A few methods have been used to produce Ti_3Au intermetallics samples on small quantities for purely research purposes such as, Svanidze et al. used arc melting method with several remelting cycles. Similarly, magnetron sputtering with a Nano PVD deposition has been used to create Ti_3Au on a Ti_6Al_4V substrate [11,13,14] on a nanoscale. In a study by Bialas et al. [6], the development of Ti_3Au was carried out by electrochemical coating of titanium on a gold layer with additional heat deposition from laser to induce the intermetallics at the Ti–Au interface.

The advancement in complex yet miniaturized product development has lead to a chain reaction in innovation of advanced manufacturing techniques such as nano-structure fabrication producing nanoparticles, nano-wires and nano-tubes along with the 3D nano-structures [15]. With an advancement in nano-scale technologies following the empirical Moore's law [16], the effect of miniaturization in transistors on an integrated circuit has created a cascade effect on all the aspects of modern product-development ecosystem making them smaller, lighter compact and highly energy efficient [17]. As the product gets

* Corresponding author.
Linkedin: upadesh-s-0b321a15b (U. Subedi).
E-mail address: upadesh.subedi@polsl.pl (U. Subedi).

https://doi.org/10.1016/j.commatsci.2025.113875
Received 17 February 2025; Received in revised form 27 March 2025; Accepted 28 March 2025
0927-0256/© 2025 Elsevier B.V. All rights are reserved, including those for text and data mining, AI training, and similar technologies.

smaller and compact the need of cutting-edge advanced manufacturing techniques that can operate in nano-scale with high precision and accuracy becomes evident. With an extreme control over the processing parameters and nano-scale localized energy deposition, laser technology has evolved as one of the primary method of nano-material processing. Previously, lasers were preferred choice for a top-down approach of material processing for material removal and machining using methods such as ion beam, ion etching, laser ablation while the nano-fabrication was carried out with bottom-up approach to obtain nano-structures via deposition atoms and molecules with vapor deposition techniques [18–20]. But lately, with the technological advancement of nano-scale ultra fast lasers, the pulsed laser deposition, laser chemical vapor deposition and nano-additive manufacturing has become possible to fabricate nano-structures of high dimensional accuracy [21–23]. The ultra-fast lasers enables nano-scale energy deposition minimizing thermal effects on surrounding materials and preserves the nano-structure's integrity [24]. This approach of precise control over the temperature fields and heating mechanism enables the nucleation and growth of nanostructures with a high spatial accuracy [25]. The latest nano-manufacturing techniques such as: multiphoton polymerization, multiphoton photoreduction, nano-welding, nano-forming has further shaped the way of fabricating 3D nanostructures with high spatial resolution aiding to the application of laser in nano-scale additive manufacturing [26]. Deep ultra-violet laser source are used to produce 90 nm–130 nm lines in lithography whereas, femto second pulsed laser has been used for nano-resolution fabrication with ablation threshold setting to that of Gaussian beam profile. These ultra-fast lasers have been used to create nano-features such as pits, voids, strips, ripples, lines in the nano-scale well below 100 nm in dimensions [15,27]. With the development of lasers that can accurately and precisely deposit heat at nano-scale the use of such technology becomes evident in additive manufacturing of nano-materials with nano-structures. From the laser deposition of nano-particles to supply the localized thermal energy at nano-scale enhancing the growth of nano-structures, the application of latest ultrafast laser devices are going to play a major role in nano-additive manufacturing.

As the additive manufacturing (AM) technologies have started to replace the mainstream manufacturing methods and prototype development, the different aspects of AM methods can be employed in sectors requiring rapid, agile and reliable product [28–30]. Additionally, the real world application of Ti–Au alloys in multi-disciplinary industrial area such as aerospace, automotive, energy, medical, marine, and chemical processing is broadening. [3,31–38]. With multiple AM techniques as Selective Laser Melting (SLM) [39], Selective Laser Sintering (SLA) [40], and Directed Energy Deposition (DED) [41] the window of possibilities are wide open where one can perform rapid prototyping to the development of industrial standard highly customized and complex geometries in within hours. In addition to these versatile technologies, utilizing the latest machine learning data-driven models and toolkits [42–46] the spatial evolution of microstrucurtres, their physical and mechanical properties can be predicted and pre-calculated, offering an unprecedented control over the complex design and material properties to level of the microstructural growth.

As described by Nohrira et al. [7], with specific heat treatment of Ti–Au binary system, it can produce the Ti_3Au intermetallics with desired mechanical properties. And by utilizing a focused energy beam, a precise, repeatable and high control over the microstructure along with the mechanical properties can be attained via the additive manufacturing technologies [47,48]. With this insight we extend the horizon of growth evolution of Ti_3Au intermetallics grains with the computational study of application of laser heat source in this work. With a detailed analysis of laser processing parameter's effect on microstructure evolution, our work primarily focus on effects of two variables: laser scan speeds and laser irradiation on IMC grain growth. Similarly, we explore the laser-meltpool characteristics, temperature-composition dependent free-energy driving the phase transitions, thermal history of the system, and further proceed to quantify the lead–lag dynamics between chemical diffusion and heat transfer in-terms of a dimensionless scalar value called Lewis number [49].

In order to track the growth evolution of microstructure and phase transitions due to the influence of laser irradiation in the computational domain, Phase Field (PF) diffused interface model is employed with multiple physics coupled tightly. A number of PF models and techniques exists in literature such as entropy functional [50], free energy functional [51,52], and grand potential functional [53] for microstructure evolution study. Our model consists of phase-field variables evolving spatio-temporally described by a set of partial differential equations dictating the changes in system's phases. And the driving force for these changes depends upon the free-energy functional, temperature and composition [54] of individual phases.

Since, PF method serves as an excellent computational tool tracking the microstructure evolution, it has gained significant attention in modeling additive manufacturing processes. Phase field modeling of such process involving the melting, solidification and grain growth can be established by coupling the heat transfer and fluid flow physics with it. Gong et al. [55] studied solidification and dendrite growth during the electron beam additive manufacturing (EBAM) of Ti–6Al–4V alloy. Although their work claims to show grain growth comparable to experimental results, their model lacks several essential parameters for accurately representing the phenomenon. Their binary approximation of a ternary system and the absence of fluid-flow coupling to the phase-field model, assuming a flow-less melt pool regime, are significant limitations. Additionally, their assumption of a uniform temperature within individual phases makes it a constant temperature model. The composition dependence of free energy is restricted to two constant composition values for solid and liquid phases, using a double-well approximation. Liu et al. [52] combined the phase-field method with the lattice Boltzmann method to simulate dendrite growth, heat transfer, and fluid flow during the additive manufacturing process involving Ti–6Al–4V alloy. Despite claiming a tight coupling of the two methods, their model lacks composition-temperature dependence of the free energies of the individual phases. For the phase field simulation, two fixed temperatures are considered: 1878 K for the solid phase and 1928 K for the liquid phase. They further assume constant material properties throughout the non-isothermal process, and employ a pseudo-binary approach for modeling a ternary alloy system. A similar approach for simulating microstructural evolution during the EBAM process of Ti–6Al–4V alloy is found in the work by Sahoo et al. [56] work. Their model also uses a binary approximation of a ternary alloy system and lacks fluid-flow coupling. The constant values for thermophysical properties reduce the model's reliability, as thermodynamic processes such as solidification and phase transition depend on material properties that fluctuate with temperature. Darabi et al. [57] presented a multi-scale, multi-physics model of powder bed fusion of Inconel-625. Their model includes the coupling of elasticity with the phase-field method but the coupling of thermal history with the phase-field lacks continuous temperature dependence of free energy. They have used two fixed temperatures for the molten and solidified phases each, without consideration of flow within the melt pool. Similarly, their work assumes constant material properties (such as: thermal conductivity, density, specific heat capacity) within a phase, ignoring the temperature dependence of material properties. The assumption of powder alloy as a single-component system further overlooks interdiffusion effects and, the formation and growth of intermetallics. Yang et al. [50] simulated microstructure evolution during the selective laser sintering (SLS) process using phase-field modeling for stainless steel (316L) powder. Their model does not consider the role of steel alloy's phase composition regarding its influencing the evolution pattern. In reality the phase field model for a binary or multi-component alloy should be different to that of pure metal [58]. The alloy model is infact the significant expansion of pure material model as the former must account for the composition dependence of the alloy phase not only at the bulk but also at the

interface. In phase field modeling of laser processed alloys, the free energy term should account for both composition and temperature. Our present model meticulously blends the compositional and thermal field to describe the microstructure evolution, thereby becoming novel work by accounting for the material phase composition in laser processed non-isothermal condition.

The formation of intermetallics at the Ti–Au interface occurs via the following exothermic thermo-chemical reaction:

$$3\mathrm{Ti} + \mathrm{Au} \xrightarrow{\mathrm{T}} \mathrm{Ti_3Au},\ \ \Delta H_f^{Ti_3Au}(\mathrm{T})$$

where, $\Delta H_f^{Ti_3Au}(\mathrm{T})$ is the enthalpy of formation for Ti_3Au intermetallic from the constituent species Ti and Au at temperature T. During laser processing it is known that the interface experiences temperature fluctuations and so it is necessary to consider the $\Delta H_f^{Ti_3Au}$ for reactions at different temperatures as following [59,60]:

$$\Delta H_f^{Ti_3Au}(298\ \mathrm{K}) = -31.39\ \mathrm{kJ/mol}$$
$$\Delta H_f^{Ti_3Au}(750\ \mathrm{K}) = -17.91\ \mathrm{kJ/mol}$$
$$\Delta H_f^{Ti_3Au}(1000\ \mathrm{K}) = -10.46\ \mathrm{kJ/mol}$$

In all these three temperatures, Ti_3Au formation is thermodynamically stable and this interfacial reaction can proceed along the Ti–Au interface. However, the stability of Ti_3Au is guaranteed only below 1350 K (critical temperature) [59,60]. Through the thermochemical reaction at the interface in a temperature range between 300 K to 1350 K, the Ti_3Au intermetallic nucleates and grows subsequently. After reaching the critical nucleation radius the intermetallic starts to grow as grains. Our present work describes such growth of the grains (product of interfacial reactions) under non-isothermal conditions where we present a multi-phase, multi-physics phase-field model of laser processing for the Ti–Au binary alloy system. Our model fully couples phase-field equations with heat transfer and fluid flow physics, offering a unique perspective on the dynamics of phase transition. We specifically address the dynamic nature of the melt pool and Ti_3Au intermetallic growth at the interface, considering interdiffusion effects. This study advances previous models by incorporating temperature-composition-dependent free energy functionals for individual phases and temperature-dependent material properties. We provide a comprehensive study and quantification of dynamic microstructure evolution and phase transition during laser treatment for a set of key laser processing parameters (irradiance and scanning speed). Detailed analyses include the evolution of phase areas, melt pool depth and width, intermetallic grain thickness, and phase stability between the melt pool and heat-affected zone.

Additionally, we introduce a novel approach to measure the difference between isotherm front and chemical diffusion by defining their values in units of time, termed "*Positional Time Lag* (δt_{pos})". This phenomenon arises because the heat flow front travels faster than the melt pool phase front [61]. We further quantify this using the non-dimensional Lewis Number, which provides a ratio of thermal flow to chemical diffusion [49]. Our work incorporates these quantities to study the effects of laser processing parameters on the relative propagation of heat transfer and chemical diffusion fronts. We employ the Finite Element Method (FEM) for discretization and conducted our simulations using the open-source FEM solver MOOSE Framework [62–64], which utilizes the PJFNK (Preconditioned Jacobian-Free Newton Krylov) solver for iteratively solving coupled non-linear partial differential equations. Our study leverages the MOOSE framework and the Phase Field method to simulate interdiffusion effects in multi-phase, multicomponent systems. We utilize the KKS model [58] to ensure chemical potential equilibrium at phase boundaries, leading to improved effectiveness, particularly in multicomponent systems.

2. Multi-physics multi-phase field formulation

Laser processing in the additive manufacturing process is inherently unsteady and transient [65]. Designing an accurate computational model to replicate the intricate events during laser treatment requires solving coupled partial differential equations governing a set of multi-physics. In our study, we developed a multi-physics model that couples phase-field, heat transfer and fluid flow equations to describe the behavior of phase-field variables, heat deposition and distribution, and flow dynamics inside the meltpool. In a multi-phase Au–Ti system, the phase-field variables of interest are composition (a conserved quantity) and order-parameters (non-conserved quantities) that evolves within the domain, driven by the system's free energy. The following sections discuss the individual physical phenomena, the coupled equations, and the temperature-dependent material properties associated with each phase.

2.1. Phase field equations

In a system initially consisting of three phases: Ti-rich HCP (Hexagonal Closed Packed) at the bottom, Au-rich FCC (Face Centered Cubic) solid at the top, and 4 IMC grains at the interface, the introduction of a laser at the top immediately adds a fourth phase, Au-rich LIQUID, as illustrated in Fig. 1**b**. A computational model with dimensions of 1300 nm × 500 nm in the x–z direction was designed for non-isothermal phase-field modeling. The initial area of each phases taken into consideration are, HCP: 1.3×10^5 nm^2, FCC: 3.4×10^5 nm^2, LIQUID: 1×10^4 nm^2. and IMC grains combined: 1.6×10^5 nm^2.

The binary Au–Ti phase diagram in Fig. 2**a** is constructed using the pyCalphad software [66] and is based on the thermodynamic database by Luo et al. [67]. In accordance to this diagram the phase structures that are relevant in the alloy during the laser manufacturing are: FCC-A1, HCP-A3, TI_3Au IMC and LIQUID. In this binary alloy, the composition of a single element is sufficient to describe the conserved phase-field variable, as the molar fractions of Au and Ti in a phase sum to 1. Here, we take the molar fraction of 'Au' (c^{Au}) as 'c' to represent the composition of the phase, with c_{HCP}, c_{IMC}, c_{LIQ} and c_{FCC} denoting the molar fraction of Au in HCP, IMC, LIQUID and FCC phases respectively. For the non-conserved variables representing HCP, FCC, LIQUID and 4 grains of IMC phases we defined a total of 7 order-parameters. These order parameters are denoted as η_i, where the value is set to 1 if they are inside their corresponding phase and 0 if outside. In this study, we define the 7 order-parameters as follows: η_1 for HCP phase, η_2, η_3, η_4 and η_5 for four grains of IMC phase, η_6 for LIQUID phase, and η_7 for FCC phase. The schematics of our computational domain showcasing the 4 phases and 7 order-parameter system is shown in Fig. 1**b**.

In a multi-phase system undergoing laser-induced phase transitions, there is constant interaction between distinct phases at the interface. This necessitates the use of an interpolation function to accurately interpolate the temperature-dependent material properties and characteristics between the co-existing phases. We have employed a thermodynamically consistent function ($h_i(\eta)$) introduced by Moelans [68] for the purpose. The corresponding interpolation function for phases with a single grain (HCP, FCC, and LIQUID), and for the multiple grains of IMC phase is given by Eq. (1) [54,69].

$$h_i = \begin{cases} \dfrac{\eta_i^2}{\sum_{k=1}^{N} \eta_k^2} & ;\ \text{HCP, FCC, LIQUID} \\ \dfrac{\sum_{j=1}^{p} \eta_{i,j}^2}{\sum_{k=1}^{N} \eta_k^2} & ;\ \text{IMC} \end{cases} \tag{1}$$

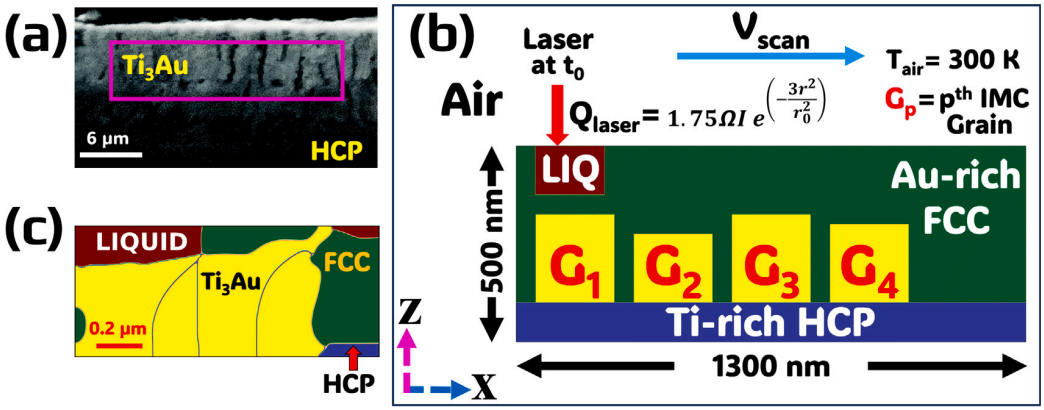


Fig. 1. **(a)** Experimental microstructural image depicting Ti_3Au intermetallics (highlighted within magenta rectangle) formed in the aftermath of laser treatment for an Au-coated Ti film [6]. Captured post-cooling, the highlighted region showcases the formation of Ti_3Au intermetallic phase at the expense of Au-rich FCC and Ti-rich HCP phases. The dark region at the bottom of the image represents HCP region (rich in Titanium). **(b)** Schematic representation of simulation setup for laser-induced heat treatment in a multiphase Ti–Au domain (1300 nm × 500 nm) comprising of four distinct phases: Ti-rich HCP, Ti_3Au IMC, Au-rich FCC, and LIQUID. A Gaussian laser heat source (depicted by the red arrow) is dynamically applied to the top layer, initially positioned at a horizontal distance of 125 nm from the left. The scanning speed of the laser is denoted as v_{scan}, and G_p signifies the pth IMC grain. **(c)** Snapshot, taken at 355.78 ms into simulation, provides a glimpse of ongoing laser treatment (I: 150 kW/cm^2; v_{scan}: 4 nm/ms) with beam already crossing the right end. Noteworthy in this image is the discernible growth of IMC grains, manifesting in irregular and distinct shapes. This observation aligns with our previous experimental findings [6], underscoring the accuracy and relevance of the simulation in capturing the dynamic evolution of IMC grains during the laser processing.

In the above equations, N represents the total order parameters, and i denotes the distinct phases. The order-parameters for HCP, FCC, and LIQUID is given by the variable η_i, while for IMC grains, it is expressed as $\eta_{i,j}$. When an external source of heat is applied to the computational domain, morphological changes in the microstructure become evident caused by the system's free energy driving the transformations. To numerically model the physical behavior of the microstructure, we incorporate the total free energy of the system as (F_{total}) in our model. This is achieved by combining the bulk free energy (F_{bulk}) and interfacial free energy (F_{int}) as follows:

$$F_{total} = F_{bulk} + F_{int} = \int_V (f_{bulk} + f_{int}) dV \tag{2}$$

In Eq. (2), the bulk and interfacial energies are expressed in terms of free energy densities, i.e., energy per unit molar volume. The first term, bulk free energy density (f_{bulk}) incorporates the heat plus chemical diffusional aspects and is expressed in Eq. (3).

$$f_{bulk} = \sum_i h_i f^i_{bulk} = \sum_i \frac{G_i(c,T)}{V_m} \tag{3}$$

where terms h_i and f^i_{bulk} represent the interpolation function and the chemical bulk free energy density of phase 'i', respectively. The molar volume V_m is assumed to be the same for all phases, taken as 10.21 cm^3/mol (the V_m of Au) [70]. The notation $G_i(c, T)$ denotes the composition-temperature dependent molar Gibbs free energy of phase 'i'. Due to thermal fluctuations induced by the laser within the computational domain, the molar Gibbs free energy of the system must accurately reflect thermodynamic changes associated with a variable temperature field. This necessitates considering both the thermal alterations (T) and the composition (c) to be incorporated in the free energy expressions as presented in Eq. (4) represented by a higher-order polynomial function. The 3D visualization of free energy function for individual phases is shown in Fig. 2**e** with composition and temperature represented on x and y axis respectively whereas, color indicating the value of free energy as a third dimension.

$$G_i = F_i \left[A_i (c_i - c^i_{eq})^m + B_i (T - T^i_{eq})^n + C_i c_i T + D_i \right] \tag{4}$$

where T represents the temperature and c_i denotes the composition of phase 'i'. The coefficients F_i, A_i, B_i, C_i, D_i, a_i, b_i, c^i_{eq}, T^i_{eq}, m and n are fitted from the thermodynamical database (.TDB file) [71]. The values and units of these coefficients are presented in Table 1. It is to be noted that this equation incorporates the effect of both chemical diffusion and thermal diffusion (mass transfer due to ∇T) in the multi-phase system. The cross-effect of T-variable on the spatial distribution of composition is briefly outlined later in Section 3.

Table 1
Tabulated coefficients of composition-temperature dependent Gibbs Free Energy, expressed through higher-order polynomial functions across distinct phases.

Coeff \ Phases	HCP	IMC	LIQ	FCC
F_i	1000	1000	11	19
A_i(J/mol)	655	2328	30013	208000
B_i(J/mol K^n)	9E−6	2E−5	1E−3	1E−3
C_i(J/mol K)	0	0	−0.75	−0.75
D_i(J/mol)	−6.9	−12.6	−21	−5.8
c^i_{eq}	0.1	0.2	0.5	0.6
T^i_{eq}	1100	859	1939	593
m	2	2	4	6
n	2	2	2	2

The interfacial free energy density (f_{int}) in Eq. (2) is mathematically expressed in Eq. (5).

$$f_{int} = m f_{barrier} + \frac{\kappa}{2} \sum_i (\nabla \eta_i)^2 \tag{5}$$

Here, the model parameter term m and κ are associated with the diffused interface width (δ) and interfacial energy σ[J/m^2] as described in the following Eqs. (6) and (7).

$$m = 6 \times \frac{\sigma}{\delta} \tag{6}$$

$$\kappa = \frac{3}{4} \times \delta\sigma \tag{7}$$

In this work, we take the values of δ and σ as 10 nm and 0.5 J/m^2 respectively [72]. The $f_{barrier}$ term of Eq. (5) is a Landau polynomial of the phase field variable in 4th order which is expressed as Eq. (8).

$$f_{barrier} = \sum_i \left(\frac{(\eta_i)^4}{4} - \frac{(\eta_i)^2}{2} \right) + \gamma \sum_i \sum_{j \neq i} \eta_i^2 \eta_j^2 + \frac{1}{4} \tag{8}$$

The phase-field simulation of laser-induced microstructural transformation can be simply understood as a mathematical system monitoring the spatio-temporal changes of conserved (c) and non-conserved (η) variables. For the conserved variable (c), its progression is tracked by Eq. (9).

$$\frac{\partial c}{\partial t} = \nabla . \left(\sum h_i M_i(T) \right) \nabla \left(\frac{\partial f_{bulk}}{\partial c_i} \right) - \vec{u} \cdot \nabla c_i \tag{9}$$

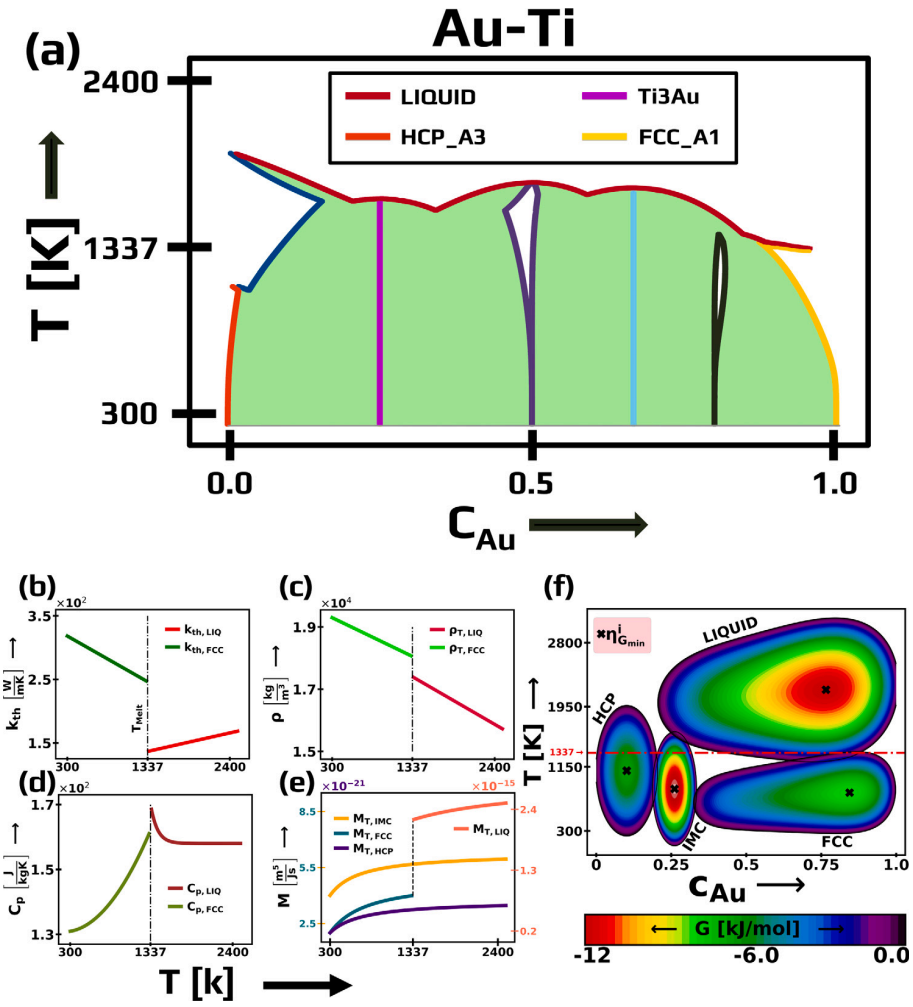


Fig. 2. The binary Au–Ti phase diagram in **(a)** highlights the FCC-A1, HCP-A3, Ti_3Au IMC and LIQUID phases, whose free energy values are presented in **(f)**. The graphs **(b)**, **(c)**, **(d)** and **(e)** respectively quantify the T-dependent thermal conductivities, densities, specific heat capacities and mobilities of the phases.

where, $M_i(T)$ is the temperature-dependent mobility of the ith phase. Its value increases exponentially with the rise in temperature (Fig. 2**d**), directly influencing the phase growth kinetics. The symbol $\vec{u}$ vector denotes the velocity of molten alloy in the LIQUID phase. The Cahn–Hilliard phase mobility $M_i(T)$ is related to the bulk chemical diffusion coefficient $D_i(T)$, thermodynamic factor A_i and grain boundary mobility (M_{gb}) as follows:

$$M_i(T) = \frac{D_i(T)}{A_i} + \sum_{j \neq i} h_j M_{gb} \tag{10}$$

Chemical diffusivity of species from higher to lower concentrations over space and time within the computational domain, influenced by the temperature and composition gradients governs the evolution of phases. In this work the two species Au and Ti are assumed to have the same diffusion coefficient for a given phase η. So, the diffusivity of the elements in a given phase 'i' is denoted by the symbol D_i. The thermodynamic factor is a second-order partial derivative of bulk free energy density with respect to the composition, given as $A_i = \frac{\partial^2 f_{bulk}(T)}{\partial (c_i)^2}$ [68]. The term M_{gb} is interconnected with the grain-boundary diffusivity (D_{gb}), phase-specific thermodynamic factors, and the width of the grain boundary channel (δ_{gb}) between two adjacent grains. The expression for M_{gb} is given in Eq. (11) [73].

$$M_{gb} = 3\frac{D_{gb}\delta_{gb}}{(h_i A_i + h_j A_j)\delta} \tag{11}$$

Here, the value of δ_{gb} is taken as 0.5 nm. For the model's simplicity, we have considered M_{gb} to be one hundred times the value of IMC bulk phase's mobility [74].

The spatio-temporal evolution of the non-conserved phase-field variable (order-parameters) dictating the phase morphology is expressed in Eq. (12) [54].

$$\frac{\partial \eta_i}{\partial t} = -L\left(\eta_1, \ldots, \eta_N\right)\left(\frac{\partial f_{bulk}}{\partial \eta_i} - \nabla \cdot \frac{\partial f_{int}}{\partial \nabla \eta_i}\right) \tag{12}$$

where, $L(\eta_1, \ldots, \eta_N) = L_i$ is defined in Eq. (13).

$$L_i = \frac{\sum_{i=1}^{N}\sum_{j>1}^{N} L_{ij}\eta_i^2\eta_j^2}{\sum_{i=1}^{N}\sum_{j>1}^{N} \eta_i^2\eta_j^2} \tag{13}$$

here, L_{ij} is the interfacial mobility which is assumed to be diffusion-controlled growth meaning that the growth is limited by the bulk diffusion which is approximated as Eq. (14).

$$L_{ij} = \frac{4m}{3\kappa} \times \frac{1}{\Omega_{ij}} \tag{14}$$

The term Ω_{ij} is a Cahn–Hilliard mobility dependent quantity which is approximated as:

$$\frac{1}{\Omega_{ij}} = \begin{cases} \frac{max(M_i(T), M_j(T))}{\tau} & i : \text{LIQUID}; j : \text{SOLID} \\ \frac{M_i(T)+M_j(T)}{2\tau} & i : \text{SOLID}_A; j : \text{SOLID}_B \end{cases} \quad (15)$$

where M_i and M_j are the temperature-dependent mobilities of phases i and j respectively. For the LIQUID–SOLID interface the largest mobility among the interacting phases is taken into consideration. Whereas for the SOLID–SOLID interface an arithmetic mean of mobilities between interacting phases is taken as presented in above case equation. (The SOLID phase in our case represents IMC or HCP or FCC phases).

In Eq. (15), the parameter τ, quantifies how the equilibrium compositions of three interacting phases (HCP, IMC, and FCC or LIQ) project onto the composition axis at a given temperature, based on the common tangent construction in Gibbs free energy diagrams. Mathematically, τ is the temperature-averaged product of the absolute lengths of two projection segments along the composition axis (c_{Au}), as given in Eq. (16) [54,72]. These segments correspond to the equilibrium compositions at the points where the common tangents between HCP & IMC and IMC & FCC (or IMC & LIQ) phases touch the Gibbs free energy curves.

$$\tau = \frac{1}{N}\sum_{q=1}^{N}\left(c_{j,eq,i}^{T_q} - c_{i,eq,j}^{T_q}\right)\left(c_{k,eq,j}^{T_q} - c_{j,eq,k}^{T_q}\right) \quad (16)$$

where, 'i' & 'j' and 'j' & 'k' are the interacting phases, T_q represents a specific temperature point at which the equilibrium compositions of the three phases are considered. In this study the magnitude of τ is calculated to be 0.1693. The calculation is further explained in Appendix A at two sample temperature points of 700 K and 1500 K in Fig. A.1**(a)** and **(b)** respectively.

2.2. Energy equation

In a non-isothermal system with laser source depositing the thermal energy dictating phase changes, the distribution of heat across the domain is given by Expression (17).

$$\rho_i Cp_i\left(\frac{\partial T}{\partial t} + \vec{u}\cdot\nabla T\right) = k_{th,i}\nabla^2 T + Q_{laser} \quad (17)$$

where temperature and time are represented by 'T' and 't', ρ_i denotes the density of the ith phase. Cp_i and $k_{th,i}$ are the specific heat capacities and thermal conductivities of respective phases, $\vec{u}$ is the flow velocity inside the meltpool. Similarly, Q_{laser} is the heat deposited by the laser following a Gaussian beam profile whose mathematical expression is presented in Eq. (18). The temperature dependence of material properties (ρ_i, Cp_i, $k_{th,i}$) are discussed in Section 2.4.

$$Q_{laser} = 1.75\,\Omega I \exp\left(-\frac{3r^2}{r_0^2}\right) \quad (18)$$

here 'I' is the laser irradiance (150 kW/cm^2 and 134.6 kW/cm^2), similarly, $\Omega = 6.67 \times \alpha_{Au}$ with the absorption coefficient (α_{Au}) of Au taken as 8.5×10^7 m^{-1} [6,75] and a nano-scale laser beam radius r_0 as 120 nm [76]. With the advancement in laser technologies, laser beam with nano-scale precision are being used in practical application such as nano-machining, nano-structuring, nano-ablation, hybrid additive and subtractive processing, crystallization [76–78]. Here, we have chosen a gaussian beam profile with radius in nano-scale for simplicity of the model describing the phase transition driven by thermal excitation.

2.3. Continuity and momentum equations

For the study of fluid flow inside the meltpool regime, the following sets of Incompressible Navier–Stokes equations in Laplace form (MOOSE Framework's Navier–Stokes Module [79]) are coupled with the phase-field and heat transfer physics. The conservation of mass is given by the continuity equation expressed in Eq. (19). Whereas the conservation of momentum is defined by Eq. (20) [80].

$$\nabla.\vec{u} = 0 \quad (19)$$

$$\rho_i\frac{\partial u}{\partial t} + \rho_i(\vec{u}.\nabla)\vec{u} = -\nabla p + \mu_i\nabla^2\vec{u} + F_{boussinesq} \quad (20)$$

where, $\vec{u}$ is the flow velocity, ρ_i and μ_i are the density and viscosity of phase 'i'. $F_{boussinesq}$ is given by Eq. (21) for LIQUID phase.

$$F_{boussinesq} = -\rho_i g\left[1 - \alpha_i(T - T_0)\right] \quad (21)$$

here Boussinesq effect is observed in only LIQUID phase which is also associated with the convection heat transfer of Eq. (17), so $\rho_i = \rho_{LIQ}$ in Eq. (21), where α_i is a constant with value −1.44 [6]. As our study primarily focuses on phase transition and IMC grain growth under non-isothermal conditions, we simplify the phase-field model by considering negligible effects of surface tension in meltpool phase.

2.4. Bulk and interfacial material properties

In this section, the material properties associated with individual phases is presented. During the simulation, the LIQUID and FCC phases go through the highest possible temperature fluctuation as a result of direct contact of laser beam at the top surface of the computational domain. Hence, temperature dependent material properties: density, specific heat, thermal conductivity are considered for these two phases whereas for the IMC and HCP phases these properties are taken as a fixed values. The expressions describing the temperature-dependent and constant material properties are presented in Table 2. Whereas the graphs illustrating the thermal conductivity, density, and specific heat for the FCC and LIQUID phases are shown in Fig. 2**(b)**, **(c)** and **(d)**, respectively. The temperature dependence of the mobilities for all four phases is considered and expressed as an Arrhenius-type equation presented in Table 2, and are plotted in Fig. 2**(e)**. The mobility values in our simulations are derived from diffusivities by ensuring a reasonable difference in diffusion coefficients between the LIQUID and SOLID phases, typically spanning 4 to 8 orders of magnitude [54,72,81]. The diffusivity data of LIQUID and SOLID phases are found to be largely scattered in the literatures [54,72,81,82]. In our case, we selected the range of diffusivities of four phases at Au melting temperature (1337 K) observing the temperature and trend established in [54,82]. Our values are selected based on the observation of mobilities used in alloys of both types: low and high melting temperatures. In the Table 'R' is the universal gas constant with value 8.31 J/mol K. Similarly, the expression for viscosity of Au-rich LIQUID phase is given by the following expression [83]:

$$\mu_{LIQ} = \exp\left(-0.1990 + \frac{2669}{T}\right) \quad (22)$$

To introduce mushy zone effect, the following Expression (23) is taken into account for viscosity (μ_{adj}) at the LIQUID–FCC boundary region:

$$\mu_{adj} = \psi \times \mu_{LIQ} \times \left[h_{LIQ} \times h_{FCC}\right] \quad (23)$$

where 'ψ' is a constant with value 10 taken for this study. h_{LIQ} and h_{FCC} are the interpolating function for LIQUID phase and FCC phase respectively.

2.5. Initial and boundary conditions

The computational domain is set with an initial temperature of 300 K, at normal atmospheric pressure. The initial condition for seven order parameters ($\eta_1, \eta_2, \ldots, \eta_7$) is shown in Fig. 1**(b)**. The initial compositions of various phases are assigned randomly to numerical values somewhat near to their equilibrium values and during the simulation, the free

Table 2
Temperature dependent material properties.

Properties	Phases (i)	Expression	Reference
ρ_i (kg/m^3)	LIQ	$19325.28 - 1.44T + 0T^2$	Bialas et. al. [6]
	FCC	$19674.6 - 1.2T + 0T^2$	
	IMC	8202.9	Jain et. al [84]
	HCP	4504.7	
$k_{th,i}$ (W/m K)	LIQ	$100 + 2.73 \times 10^{-2}T + 0T^2$	
	FCC	$338.9 - 6.93 \times 10^{-2}T + 0T^2$	Bialas et. al. [6]
	IMC	91.585	
	HCP	16.07	Powell et. al. [85]
Cp_i (J/kg K)	LIQ	$158 + 2.08 \times 10^7 \exp(1.14 \times 10^{-2}T)$	Khvan et. al. [86]
	FCC	$132 - 1.1 \times 10^{-2}T + 2.5 \times 10^{-5}T^2$	
	IMC	428.77	Bialas et. al. [6]
	HCP	528.049	Chase et. al. [87]
M_i (m^5/J s)	LIQ	$2.90 \times 10^{-15} \exp(-3043/RT)$	
	FCC	$4.88 \times 10^{-21} \exp(-2221/RT)$	
	IMC	$6.28 \times 10^{-21} \exp(-1123/RT)$	
	HCP	$3.72 \times 10^{-21} \exp(-1550/RT)$	

energy equation will finally ensure that the equilibrium condition is reached. The initial velocity of LIQUID phase η_6 is taken to be 0.

Dirichlet boundary condition is applied at the bottom surface of the domain. In other three sides, the domain is exposed to the ambient air with convection and radiative heat transfer with coefficients λ_{conv} and λ_{rad} expressed in Eq. (24).

$$k_{th}\frac{\partial T}{\partial n} = \lambda_{tot}(T - T_{air}) \tag{24}$$

where, $\lambda_{tot} = \lambda_{conv} + \lambda_{rad}$. The convection heat transfer coefficient λ_{conv} of air is taken as 15 W/m^{2}K and the radiation heat transfer coefficient λ_{rad} is expressed as $\lambda_{rad} = \epsilon\theta(T + T_{air})(T^2 + T_{air}^2)$ [88]. The emissivity ϵ of surface is taken as 0.3 and Stefan–Boltzmann constant θ = 5.67 × 10^{-8}J/s m^2 K^4. It is assumed that Au-rich phases (η_6 and η_7) do not mechanically interact with Ti-rich solid η_1 at bottom boundary. Similarly, at top edge, η_1 does not interact with η_6 and η_7 i.e. mathematically,

$$\left(\frac{\partial \eta_1}{\partial n}\right)_{top} = 0$$
$$\left(\frac{\partial \eta_6}{\partial n}\right)_{bottom} = \left(\frac{\partial \eta_7}{\partial n}\right)_{bottom} = 0 \tag{25}$$

This boundary condition is helpful in suppressing the periodicity effect of microstructures. Natural boundary condition is set for composition variable at all edges. No-slip boundary condition is set for velocity at left, right and bottom edges.

3. Results and discussion

The heat distribution across the specimen during laser processing plays a crucial role in determining the thermo-physical property of the material being formed. Specially, the amount of deposited heat in the system directly influences the physical phenomenons such as melting, solidification, pore and precipitate formation, grain refinement, thermal distortion, and residual stress induction [89]. Additionally, the kinetics of these phenomenons namely: convection and diffusion are also affected by the supplied heat. Given the critical impact of heat distribution, this research aims to quantify the resulting physical changes in a computational model by examining two essential laser parameters: laser irradiance and scan speed. To achieve this, we conducted four sets of laser processing simulations on a geometrically identical model, varying the laser irradiance (134.6 kW/cm^2 and 150 kW/cm^2) and scan speed (4 nm/ms and 5 nm/ms).

We further incorporate the thermo-diffusion term into the phase field equations to account for the effects of non-isothermal heating within a finite domain. The presence of a spatial temperature gradient necessitates the incorporation of the term $\nabla T/T^2$ with the composition 'c' in the diffusion term, aligning with approaches demonstrated by Kunwar et al. [54], Mohanty et al. [90], and Oyedeji et al. [91]. Oyedeji et al. quantitatively integrate the driving forces for non-isothermal chemical and thermal diffusions, incorporating the 'T-c' cross term. Our model inherits this cross-effect through the terms $B_i(T - T_{eq}^i)^n$ in the equation of Gibbs energy (Eq. (4)). The presence of this thermal term in the driving force eventually affects the composition distribution in accordance to Eq. (9). Moreover, another term $C_i(c_iT)$ in Eq. (4) also displays the role of T variable in influencing the composition distribution in the alloy phases. These terms, although in over simplified form, capture the essential physics of phase evolution under thermal gradients. Future work will expand these terms to more accurately represent the physics of heat transfer and its impact on concentration gradients in non-isothermal systems.

Using different quantification techniques, such as time–temperature plots, free-energy versus phase stability graphs, and chemical diffusion versus heat transfer analyses, we aim to elucidate the correlation between these laser parameters and the resulting microstructural changes. These changes include intermetallic grain growth, melt pool dynamics (depth, width, and area), heat-affected zone stability, and overall microstructural evolution within the domain. These findings are discussed in detail in the following sections.

3.1. Scan-speed's influence on thermal history

To understand the effects of variations in laser scan speed within the computational domain, we conducted simulations while keeping all other model parameters identical. We ran two simulations with scan speeds of 4 nm/ms and 5 nm/ms. Fig. 3 shows the temperature distribution across the computational domain when a laser with a power density of 150 kW/cm^2 is applied at two distinct scan speeds: 4 nm/ms in **(a)** and **(b)**, and 5 nm/ms in **(c)** and **(d)**. To quantify the effects of laser scan speed, we selected two simulation instances at different time steps: one at the beginning of the laser treatment (t = 1 ms) and another at 190 ms into the simulation. Fig. 3**(a)** and **(c)** represent the simulation snapshot at t = 1 ms, while **(b)** and **(d)** correspond to t = 190 ms, respectively.

Initially, the effect of increased laser scan speed from 4 nm/ms to 5 nm/ms is not distinctly visible at the beginning. For both conditions, the maximum temperature attained by the domain was 2400 K, as illustrated in Fig. 3**(a)** and **(c)**. Similarly, the temperature gradient away from the laser beam spot (in both axes) is practically indistinguishable, as denoted by the temperature contour lines. This may be due to the fact that initially, the entire domain is at 300 K, and the heat energy from the laser incident on the left-top surface takes some time to diffuse throughout the computational domain, which cannot be fully captured within 1 ms. To observe and evaluate the actual effects caused by the difference in scan speed, we examined the temperature distribution at a later time step. Fig. 3**(b)** and **(d)** demonstrate the simulation snapshot at t = 190 ms, where the consequences of different laser speeds are more apparent. The first observable difference is the laser position; in **(d)**, with a higher scan speed, the laser traversed a greater distance from the left-top of the domain compared to **(b)**. The inset plots in Fig. 3**(b)** and **(d)** show the time–temperature graphs for three randomly selected spots at the top surface (P, Q, and R) inside the computational model. These plots indicate that the total simulation time required for the selected points to heat up and subsequently cool down to ambient temperature is longer (350 ms) for the slower scan speed compared to the faster one (300 ms). Since the laser irradiance is the same in both cases, the heat flux is higher for the lower speed than for the higher speed. This means the heat energy is imparted for a longer time at the point of beam incidence, consequently increasing the temperature of the domain. This phenomenon is observed in Fig. 3**(b)**, where the maximum temperature attained by the system is 1900 K, whereas at the same simulation time of t = 190 ms, in **(d)**, the system peaked at

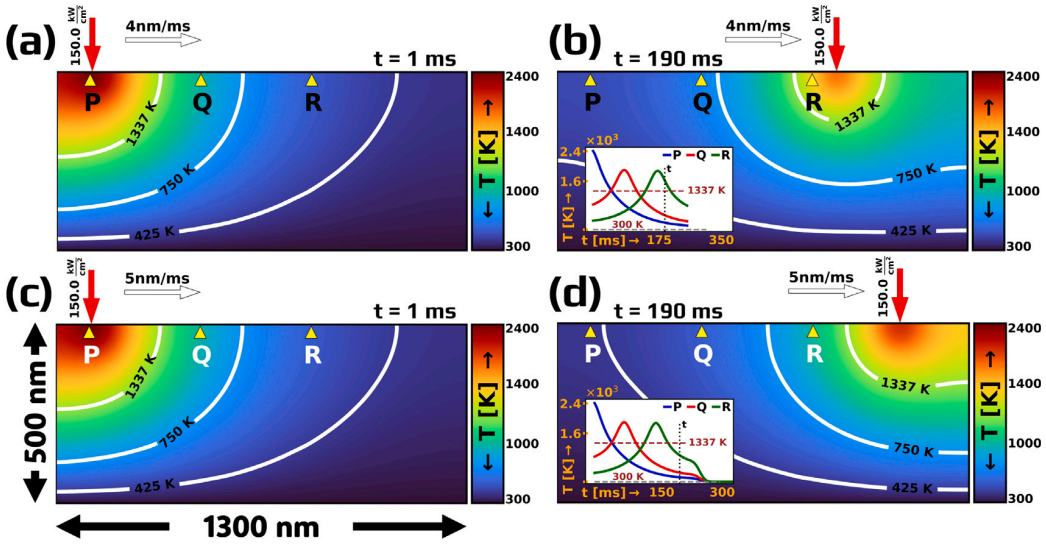


Fig. 3. Illustration of a composite set of four snapshots from phase-field laser simulations conducted on a 1300 nm × 500 nm computational domain, subjected to a laser irradiance of 150 kW/cm^2 at varying scan speeds of 4 and 5 nm/ms. The two images on top half depict snapshots from the same simulation with a scan speed of 4 nm/ms at two distinct time points: **(a)** t = 1 ms and **(b)** t = 190 ms, respectively. In **(a)**, the initial laser application results in a rapid temperature surge, peaking at approximately 2400 K, with a discernible temperature gradient away from the laser impact point. Figure **(b)** illustrates the temperature distribution after 190 ms of laser exposure, reaching a horizontal distance of 885 nm from the left edge. The temperature distribution averages out, peaking at 1900 K directly beneath the laser source. A time–temperature plot inset provides a temporal profile for three spatial points (P, Q, and R) on the system's top surface, each separated by 350 nm. The plot further indicates a total simulation duration of about 350 ms for these selected points to cool down to ambient temperature post-laser treatment. Similarly, bottom two images showcase snapshots from a different simulation with a faster scan speed of 5 nm/ms. Initially, at **(c)** t = 1 ms, the effects of the higher scan speed are indistinguishable, with a maximum temperature reaching a similar range of 2400 K at the beam focus. However, at **(d)** 190 ms, the impact of the higher scan speed becomes evident. The laser covered a greater distance of 1075 nm from the top left edge, and the maximum temperature at the laser illumination center is lower (1860 K) compared to the slower scan speed. This is attributed to the shorter laser exposure time due to the faster scan speed, resulting in less heat deposition into the specimen. The inset time–temperature plot within image **(d)** illustrates that the laser's overall traversal time for points P, Q, and R, with substantial cooldown to ambient temperature, is comparatively shorter (below 300 ms) than in previous case with a slower scan speed.

1860 K. The detailed simulation videos depicting the thermal history for two different scan speeds and two irradiance levels is available in the Appendix B. Videos B1, B2, B3, and B4 illustrate the temperature distribution across the simulation domain as the laser moves from left to right on the top surface, with scan speeds of 5 nm/ms and 4 nm/ms, and irradiance levels of 150 kW/cm^2 and 134.6 kW/cm^2, with all the combinations of these parameters respectively.

3.2. Effects of irradiance

Next, we discuss about the effects of the most critical laser processing parameter: irradiance or power-density [47,92] by exploring its impact on the computational model through a comparative study of laser irradiance at two levels: 150 kW/cm^2 and 134.6 kW/cm^2. Fig. 4**(a)** presents the time–temperature plot corresponding to three selected spots at the domain's top surface (P, Q, and R as shown in the inset picture) obtained from two separate simulations with different laser irradiance levels at a constant scan speed of 5 nm/ms. The solid lines represent points irradiated by a laser with 150 kW/cm^2, while the dotted lines represent points irradiated by a laser with 134.6 kW/cm^2.

The most noticeable differences in time–temperature plots for the two laser irradiance levels are in: (i) The peak temperature attained by the computational domain. and (ii) The duration for which the selected points stay above the thermal melting zone (>1337 K). It is evident that a higher temperature is attained by the simulated domain when irradiated by a laser with higher irradiance. As confirmed by Fig. 4**(a)**, all solid lines are above the dotted lines on the temperature scale. However, this increase in temperature has further impacts on the system that pose a greater challenge to quantify during actual laser experiments specifically, the duration for which any given point in the system remains above the thermal melting zone. Using post-processing tools in Python, we measured the total time during which the three selected points (P, Q, and R) remain above the theoretical melting temperature of gold (1337 K) as the laser traverses through these points. The measurement results indicate a similar trend to that of peak temperature: with higher laser irradiance, these points remain above the thermal melting zone for a longer duration (Q: 55 ms, R: 53 ms) compared to lower laser irradiance (Q: 42 ms, R: 41 ms).

While Fig. 4**(a)** visualizes the time–temperature profile at three specific points on the domain, Fig. 4**(b)** and **(c)** present the distribution of temperature at time t = 100 ms for two levels of laser irradiance: 134.6 kW/cm^2 and 150 kW/cm^2, respectively. At a constant scan speed of 5 nm/ms, the horizontal distance traversed by the laser is the same in both cases. Comparing the two snapshots, **(b)** and **(c)**, we can readily identify several key differences in temperature profiles between them. Firstly, the peak temperatures are 1650 K (for 134.5 kW/cm^2) and 1860 K (for 150 kW/cm^2). Secondly, the area of the domain lying inside the thermal melting zone of 1337 K is greater for the higher laser power than the lower one. This can be visually verified by the contour line of 1337 K covering a deeper and wider field (nearly touching point Q and P) in **(c)** than in **(b)**. Similarly, the contour line for 700 K touches point P in **(c)**, covering a larger area compared to **(b)** with lower laser irradiance.

Further, the effect of laser irradiance can be observed within the meltpool, where the flow velocity of the LIQUID phase is higher for high power density and lower for low power density. Fig. 5 illustrates the convective flow inside the meltpool at two levels of irradiance: **(a)** shows the flow characteristics for 150 kW/cm^2, and **(b)** for 134.6 kW/cm^2. The figure compares the maximum flow velocity in the LIQUID phase at a constant scan speed of 5 nm/ms, 144 ms into the simulation. For high laser irradiance, the maximum flow velocity inside the meltpool is nearly twice that for low irradiance. This demonstrates that not only are the size and shape of the meltpool directly associated with laser intensity, but the convective flow and its maximum magnitude inside the meltpool are also closely linked with laser power density.

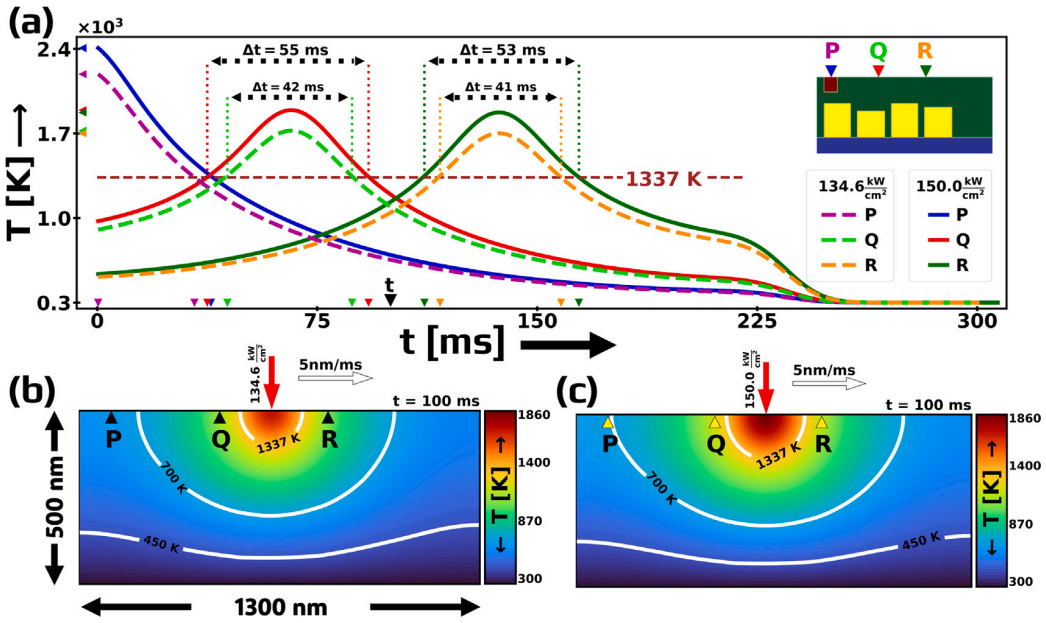


Fig. 4. Laser irradiance's effects on T profiles. **(a)** Plot illustrating the temporal temperature distribution at three specific spatial coordinates (P, Q, and R, as indicated in inset figure) located on the top (z = 500 nm) at x = 105, 455 and 805 nm respectively for two distinct irradiance levels. The continuous blue, red, and green lines represents the temperature variations at points P, Q, and R, under laser irradiance of 150 kW/cm^2 and a speed of 5 nm/ms. Conversely, the dashed magenta, light green, and orange lines represents the temperature profiles at the same points under 134.6 kW/cm^2 irradiance at the identical speed. Notably, at higher laser irradiance, all three location points remain above the melting temperature (1337 K) for a significantly longer duration: 38 ms, 55 ms, and 53 ms compared to the lower irradiance scenario where the same coordinates experience above melting temperatures only for 33 ms, 42 ms, and 41 ms, respectively. The graph emphasizes that not only does higher irradiance guarantee longer peak T in the material, but it also significantly alters the temporal status of the thermal melting zone, even at the exact same scan speed. **(b)** Snapshot of the temperature field distribution profile captured at 100 ms (during midway), employing an irradiance of 134.6 kW/cm^2 and a scan speed of 5 nm/ms. Notably, the computational domain reaches a maximum temperature of 1650 K at the laser impact point on the surface. Contour lines delineate three distinct temperature regimes at 450 K, 700 K, and the FCC melting point of 1337 K. Similarly, in **(c)**, the temperature distribution at the same time point (t = 100 ms) is visualized, maintaining the identical laser scan velocity but with a higher irradiance of 150 kW/cm^2. A visually distinctive feature is the extended region surpassing the melting point, with a general maximum temperature of 1860 K recorded at the laser-irradiated surface spot. Collectively, images (a), (b), and (c) intricately convey that the overall dynamics of heat transfer and melting point regime exhibit significant variation with laser power, even when the scanning speed is held constant.

With the consideration of temperature dependent free energy formulation we present a more realistic representation of temperature distribution across the meltpool and solid phases. Unlike other works [52, 57], where the thermal profile coupled with the phase field is taken at just two fixed temperature values, as shown in Fig. 6**(a)**, we present a fully coupled continuous temperature-phase-field system, allowing the temperature to vary according to the heat deposition by a Gaussian beam profile. The issue with considering a constant temperature within a phase in above mentioned studies is the lack of continuously differentiable free energy function dependent on temperature, which is primarily responsible in dictating the phase transitions. Hence, to interpolate phase field variables and associated material properties within phases, a fixed reference temperature is used in those studies. This assumption undermines the realistic representation of laser processing, as illustrated by the top-hat curves for phase (ϕ: sky blue line) and temperature (red line) in Fig. 6**(a)**, where it is observed that the phase changes occur instantaneously as the temperature shifts. In contrast, the formulation of a continuous function of temperature-dependent free energy in our work allows us not only to observe differences in heat flow and chemical diffusion but also to achieve a realistic temperature distribution (Gaussian profiled red line) and phase profile (blue line), as shown in Fig. 6**(b)**.

From these graphs of time–temperature, temperature distribution in Figs. 4, 6 and convective flow of Fig. 5, we can leverage laser irradiance for a tailored design approach to control the area of the heat-affected zone (HAZ), thermal melting zone, flow characteristics inside meltpool, as well as the time period for melting-solidification of any given spatial area of the domain.

3.3. Phase dynamics

With different laser parameters, we observed a different nature of microstructural growth of each phases. In Fig. 7, each yellow block indicates the Ti_3Au IMC grain marked as G_1, G_2, G_3, and G_4, the meltpool region is represented by dark red color with Au-rich FCC phase in green. The Ti-rich HCP phase is shown in blue, and the dotted contour lines inside the domain denotes the temperature distribution. The result from four different sets of simulation criteria are presented inside the dotted blocks with upper rectangular block representing phase evolution under laser power of 134.6 kW/cm^2, and the one in bottom corresponding to that of 150 kW/cm^2. Inside of each block, the first row corresponds to scan-speed of 5 nm/ms and second row to 4 nm/ms. To analyze the temporal evolution of Ti_3Au intermetallics, snapshot of the domain at two time stamps are presented in columns: **(a)** at t = 40 ms and **(b)** at t = 200 ms.

Analyzing the results from four simulations setup, it was found that IMC grain growth is largely enhanced by a higher value of irradiance at slower scan-speed. It can be observed that the under the influence of maximum heat flux condition ($\dot{Q}_{max}$) the overall growth of all the 4 grains is highest and in minimum flux condition ($\dot{Q}_{min}$) the grain grown is not so prevalent. The maximum and minimum heat flux conditions are a defined as a set of combination of laser irradiance and scan speed, for $\dot{Q}_{max}$ the irradiance is 150 kW/cm^2 with scan-speed 4 nm/ms and for $\dot{Q}_{min}$, the irradiance is 136.4 kW/cm^2 at a faster scan-speed of 5 nm/ms.

From the post-simulation calculation, for $\dot{Q}_{min}$ (topmost row) the area of meltpool is computed to be 48 × 10^3 nm^2 at t = 40 ms and 21 × 10^3 nm^2 at t = 200 ms, the lowest in all four simulation results. In the second row of Fig. 7, with a slower scan speed of 4 nm/ms, the heat

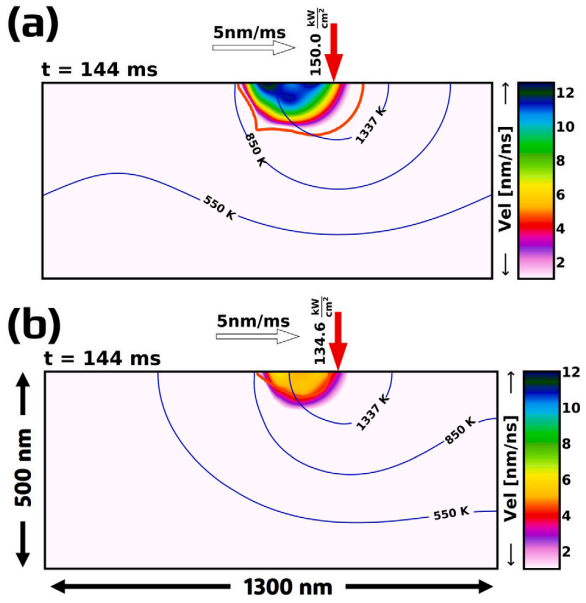


Fig. 5. Illustration of the effect of laser irradiance on convective flow inside the meltpool regime. **(a)** Shows the magnitude of flow velocity inside the liquid phase (marked by the orange contour line) for laser irradiance of 150 kW/cm^2. The maximum velocity magnitude is observed at the top surface of the domain with a value greater than 12 nm/ns, decreasing gradually with depth, and reaching zero outside the liquid phase. **(b)** depicts the convective flow velocity inside the meltpool for irradiance of 134.6 kW/cm^2. It is to be noted that the maximum velocity magnitude is nearly half (6 nm/ms) that of **(a)**. The scan speed for both simulations was set to 5 nm/ms, and the velocity profile snapshot is taken at 144 ms into the simulation.

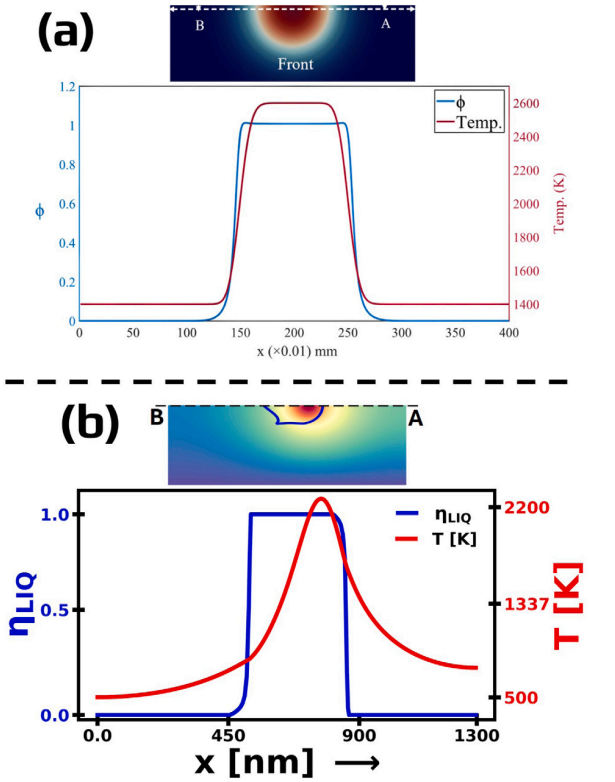


Fig. 6. Comparison of temperature distribution across the liquid (melt pool) and solid phases between the work of Darabi et al. [57] (**a**), which uses a constant temperature interpolation between phases, and our work (**b**), which employs a temperature-dependent free energy functional and material properties. **(a)** Plot of phase field and temperature variation graph along the A–B line in the melt pool boundary domain [57]. A fixed two-temperature model is illustrated by the uniform temperature of 2600 K across the entire melt pool regime (ϕ = 1), displaying a top-hat profile, and a temperature of 1400 K in the solidified region (ϕ = 0). **(b)** The phase field plot for the liquid phase and the temperature profile along the A–B line from our work. The bell-shaped temperature distribution demonstrates a smooth and continuous temperature profile across the melt pool. The spatial lead of the temperature profile relative to the liquid phase is due to differences in thermal and chemical diffusivity.

deposition increases compared to the $\dot{Q}_{min}$ condition. The meltpool area measures 54 × 10^3 nm^2 at t = 40 ms and 36 × 10^3 nm^2 at t = 200 ms. For the IMC grains, particularly grain G_1 is observed to be protruding further downward at the later time stamp. In the third row, with a higher laser irradiance of 150 kW/cm^2, the grains G_1 and G_2 start to grow and come in contact with each other at time t = 40 ms which indicates a preferential growth of IMC at an elevated temperature (800 K+). This growth is attributed to the lower Gibbs free energy (−12 kJ/mol) of IMC compared to near by FCC phase with free energy −8.5 kJ/mol at 800 K. At t = 200 ms, not only do all IMC grains evolve rapidly, but the meltpool area also increases to 39 × 10^3 nm^2 compared to that with irradiance of 134.6 kW/cm^2 at same scan-speed.

In the fourth row, an extreme phase morphology is observed throughout the simulation. The area of meltpool dominates all other phases with an area of 125 × 10^3 nm^2 at time t = 200 ms. Evolution of all the IMC grains is observed through the consumption of nearby FCC and HCP-rich regions. This particular snapshot of the simulation at $\dot{Q}_{max}$ condition also highlights an intriguing phenomenon where chemical diffusion lags behind heat flow, which is discussed further in Section 3.7.

3.4. Area evolution

Further quantification of individual phase growth in response to changes in laser parameters are discussed within this section primarily focusing on the growth and shrinkage of phase areas. With an area-time plot for two extreme cases of maximum ($\dot{Q}_{max}$) and minimum ($\dot{Q}_{min}$) heat flux Fig. 8 demonstrates the temporal growth of all the phases. Fig. 8**(a)**, corresponding to $\dot{Q}_{min}$ with an initial dominance of the Au-rich FCC phase (green line) undergoing transitions with an area of 3.4 × 10^5 nm^2 at t = 0 ms. As the laser irradiates the top surface of the domain, solid FCC melts to form LIQUID phase represented by red line peaking its area from 1 × 10^4 nm^2 initially to 5 × 10^4 nm^2 at t = 53 ms.

As the laser progresses through the domain, noteworthy growth in IMC grains is observed (yellow line) at t = 150 ms around mid-simulation. By 225 ms into the simulation, FCC phase reduces to its minimum with area of 2.6 × 10^5 nm^2, while the meltpool re-expands to 4 × 10^4 nm^2. During the end of the simulation (t = 300 ms), the meltpool solidifies back into the FCC phase, augmenting the Au-rich phase. Meanwhile, the IMC grains expansion slowly plateaus. For the HCP phase (blue line), its initial area of 1.3 × 10^5 nm^2, reduces to 7.4 × 10^4 nm^2 at t = 150 ms, and by the end at t = 281 ms it further drops to of 3 × 10^4 nm^2.

Similarly, in plot 8**(b)** the area-time profile under maximum heat flux conditions ($\dot{Q}_{max}$) is presented. Although the initial phase areas are identical to $\dot{Q}_{max}$ condition, a drastic differences in phase growth is observed. Starting with the FCC to LIQUID phase transition due to laser-induced melting, the Au-rich FCC phase undergoes a conspicuous 'U'-shaped dip in the area curve, reaching its all-time low presence of 9 × 10^4 nm^2 at t = 275 ms. At the same time, the meltpool area takes a sharp ascent, with a maximum area of 1.5 × 10^5 nm^2. Implying that higher laser power coupled with a slower scan speed exerts a more profound influence on phase morphologies compared to lower irradiation with a faster scan speed. After 275 ms, as the laser traverses fully through the domain, the meltpool solidifies decreasing its area from 4 × 10^4 nm^2 at 500 ms to near non-existent by the end with an increase in FCC phase area to 2.4 × 10^5 nm^2. Concurrently, the

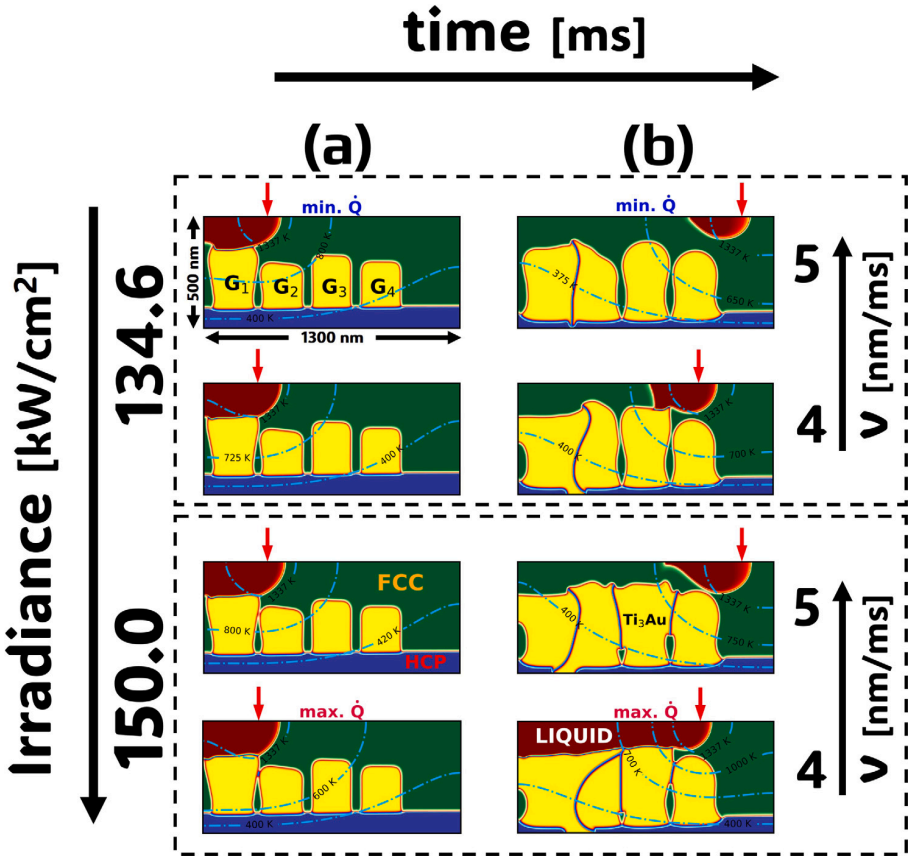


Fig. 7. Utilizing phase field simulations to explore the combined effects of irradiance and scan speed on phases/grain sizes and morphologies during transient heating process. For minimal boundary heat flux rate ($\dot{Q}$) condition (indicated by process parameters of 134.6 kW/cm^2, 5 nm/ms on the topmost images), the yellow colored IMC grains G_1, G_2, G_3 and G_4 of size and morphology quantified at **(a)** t = 40 ms, evolve to the nanostructures of different profile and dimensions at **(b)** t = 200 ms. Among the four grains, the grain G_1 being the first one to meet the melt pool since 40 ms takes the opportunity to not only become the largest and widest at 200 ms. When the $\dot{Q}$ is increased with only the decrease of scan speed at same irradiance (corresponding to 134.6 kW/cm^2, 4 nm/ms), it allows G_1 to expand laterally + vertically even bigger at the cost of adjacent phases and grains, thereby suggesting that the IMC grains appearing first to the slowly traveling heat source benefit the most at the fixed time duration of 200–40 = 160 ms. However, when irradiance is increased to 150 kW/cm^2 with scan speed maintained higher at 5 nm/ms, the grains G_2, G_3 and G_4 compete proportionately with G_1 for growth. Finally, as in the context of images in the bottommost part of the figure, when the maximal $\dot{Q}$ criterion is implemented (150 kW/cm^2, 4 nm/ms), the slowly moving and high powered laser beam again favors G_1 grain the most. Observing the melt pool profiles (red colored LIQUID phase) corresponding to 200 ms, the one for minimal $\dot{Q}$ condition is the smallest and touches none of the IMC grains, whereas the melt pool of maximal $\dot{Q}$ criterion is the largest, the longest and completely touches the three grains G_1, G_2 and G_3. It is to be noted that meltpool front for 5 nm/ms speed are ahead than those for 4 nm/ms. Comparing between the images at 200 ms, the FCC phase (green colored region) and HCP substrate (blue colored region) retain the largest areas for minimal $\dot{Q}$ criterion and the smallest areas for maximal $\dot{Q}$ condition.

cumulative are of Ti_3Au IMC grains peaks to 38×10^5 nm^2 at t = 275 ms and remains relatively constant till the end. Meanwhile for HCP phase, a sharp decrease in area is observed initially reducing to 2×10^4 nm^2, and after t = 275 ms it almost maintains constant area.

The simulation videos displaying phase evolution through animated area graphs are provided in the Appendix B. Videos B5, B6, B7, and B8 illustrate the growth and area evolution of individual phases. These videos correspond to the laser scan speeds of 5 nm/ms and 4 nm/ms, with irradiance levels of 150 kW/cm^2 and 134.6 kW/cm^2, respectively, representing all combinations of these parameters.

From a broader observation of simulation results in Figs. 7**(a) (b)** and 8**(a) (b)**, it can be noted that the area of intermetallic grains (Ti_3Au) grows with an increase in temperature of the simulation domain which is consistent with the two different experimental works from Karimi at al. and Lukose et al. [13,14]. The increase in temperature of the computational domain corresponds to a higher laser irradiance and a slow scan speed. Our numerical simulation is in agreement with these experimental observations that the increase in power input accelerates the morphological appearance of conspicuously columnar intermetallic grains.

3.5. Laser induced Meltpool characteristics

Understanding laser-induced meltpool characteristics such as shape, depth, width, and temperature is crucial in advancing the quality and efficacy of laser-based additive manufacturing processes [93]. Meltpool geometry and area are two highly influential factors determining the microstructure, along with the kinematics of solidification, cooling rate, phase transition and dendrite growth [94]. Tracking the interface via the phase field method, we measured the ever-changing dynamics of the LIQUID phase: the temporal evolution of the maximum width (x_{max}) and the changes in meltpool maximum depth (z_{max}). In addition, a comparative analysis of the time–temperature profile and free energy changes of the heat affected zone (HAZ) with that of meltpool region is done by selecting two study points (∘ and ×, as marked in the inset of Fig. 9**(a)**). These two selected points are 10 nm from the interface on either direction with each lying inside HAZ (FCC phase) and meltpool (LIQUID phase) at a fixed distance from the top surface. As, these points are linked to the FCC–LIQUID interface, their absolute coordinates inside the domain vary as the interface moves along the domain.

In Fig. 9**(a)**, the four subplots illustrate the changes in Gibbs free energy over time at ∘ and × with different laser parameter setup. A

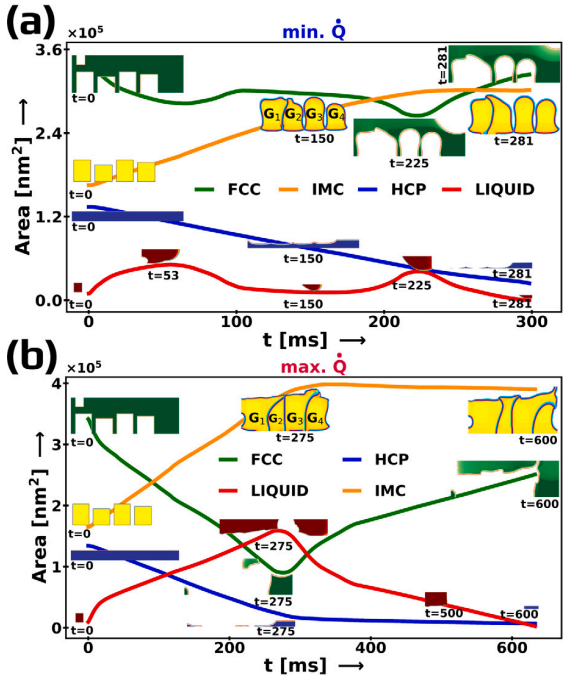


Fig. 8. Synopsis of temporal variation of the individual areas for LIQUID, FCC, IMC, and HCP phases for two conditions of boundary heat source - **(a)** $\dot{Q}_{min}$ (134.6 kW/cm^2, 5 nm/ms), and **(b)** $\dot{Q}_{max}$ (150 kW/cm^2, 4 nm/ms). The phase area of IMC is quantified as the total areas of the four grains G_1, G_2, G_3 and G_4. The time taken by the laser for **(b)** to reach the another end of the computational domain from the start position is twice that of **(a)**. At the time the laser finishes its journey, the IMC phase (orange colored lines) acquires the largest area in context of **(b)** $\dot{Q}_{max}$ criterion whereas FCC (green colored lines) retains its initial position in case of **(a)** $\dot{Q}_{min}$ criteria. Since LIQUID (red colored lines) and FCC phase replace each other during melting and resolidification, the increase in area of one of the two phases is marked by the decrease in the size of the another phase. In context of $\dot{Q}_{min}$ condition, the FCC phase area is always larger than the LIQUID area throughout the entire path of the laser, and with a difference of at least 2×10^5 nm^2. In $\dot{Q}_{max}$ condition, the difference of area is reduced as time passes till the meltpool (LIQUID phase) area temporarily exceeds that of the FCC area for a duration of 91.09 ms midway. Again the FCC phase area surpasses the LIQUID area till the end. The HCP phase being consumed by the growing IMC grains, keeps on ceding its area in both conditions but the loss rate is more pronounced in context of maximal heat source application criterion.

horizontal black dotted line is used to demarcate the zero free energy value, separating positive (unstable) and negative (stable) realms. Considering the tendency of reactions to minimize free energy for maximum stability, observing the temporal evolution of free energy graphs provides an insight into the phase stability of these points. Notably, in all four subplots of **(a)**, the free energy at the HAZ point marked by '×' is persistently large and positive, indicating its pronounced instability. In contrast, the point 'o' within the LIQUID phase consistently demonstrates significantly negative free energy, signifying stability. Thus, it can be inferred that as the laser advances, the phase at the HAZ proceeds to transition towards a more stable LIQUID phase. In Figures **(b)** and **(c)**, the time–temperature plots illustrate the thermal responses at two selected points under $\dot{Q}_{min}$ and $\dot{Q}_{max}$ conditions. As these points traverse along with the FCC–LIQUID interface during the simulation, observable temperature fluctuations manifest. Notably, both coordinates (∘ and ×) consistently register temperatures well above the FCC melting point, signaling an impending phase transition from the heat-affected zone to the LIQUID phase. The temperature–time diagrams between $\dot{Q}_{min}$ and $\dot{Q}_{max}$ conditions for these two points shows a observable difference in peak temperatures attained, with temperatures reaching approximately 2100 K for $\dot{Q}_{min}$ and around 2300 K for $\dot{Q}_{max}$. Additionally, the curves representing $\dot{Q}_{max}$ exhibits higher temperature for region of interest inside heat-affected zone compared to that inside LIQUID phase. Conversely, for $\dot{Q}_{min}$ conditions, a fluctuating competition emerges between point of interest inside the HAZ and that inside the LIQUID phase to achieving a higher temperatures.

The free energy and temperature evolution of the region around the FCC–LIQUID interface provide an essential insight into the potential development of the LIQUID phase during laser processing. To characterize the actual meltpool formed due to laser melting of the FCC-rich phase, we traced the maximum meltpool width and depth throughout the simulation at two laser irradiance levels (134.6 kW/cm^2 and 150 kW/cm^2) for same scan-speed of 5 nm/ms. We found that the relationship between x_{max} and z_{max} with the laser irradiance level is straightforward: the higher the irradiance, the greater the width and depth of the meltpool, aligning with the study by Li, et al. [95].

As shown in Fig. 9**(d)**, the maximum meltpool depth consistently surpasses at each time instance for higher laser power (red solid line), with a maximum depth of 180 nm at t = 225 ms, at the same time the dotted red line represents the lower irradiance level with a maximum depth of 158 nm. The meltpool width mimics the meltpool depth, i.e. higher laser irradiance yields larger x_{max} values at each time step (purple solid line peaking at 630 nm at t = 91 ms). In contrast, the x_{max} values for the lower irradiance of 134.6 kW/cm^2 peak at 72 ms in the simulation, registering a value of 525 nm, represented by the dashed light blue line. One key noticeable distinction between the curves of x_{max} for the two irradiance levels is the sharp decrease in meltpool width for higher irradiance (solid purple line) from t = 127 ms to t = 143 ms, which can be attributed to the separation of the meltpool at the trailing edge as a result of rapid solidification, while the leading front follows the laser. (The videos of these simulations analysis are provided as supplementary material and is also available at https://github.com/subediupadesh/MultiPhysics_MultiPhaseField_LaserProcessing/tree/main/3_Simulation_Video_Animations).

3.6. Interdiffusion and IMC growth at non-isothermal condition

One common theme that was observed in all four simulations performed with different laser processing parameters was the growth of Ti_3Au intermetallic grains. To understand the thermodynamic reason behind the observable grain growth, we need to focus on the interfacial region between IMC phase and other phases in contact. The non-isothermal conditions in the domain creates an unique effect on the driving force and evolving phases. To study the detail intricacies ongoing in the interfacial region, we proceed to calculate the free energy's numerical value at IMC interface and analyze the behavior of evolution with regards to free energy value. For this, a point in interface is selected for each IMC grain as marked by '×' in the inset of Fig. 10**(d)**. These marked points are dynamic in nature and shift their position as interface itself moves to minimize the free energy of the system.

In Fig. 10, the temporal changes in free energy values at the upper interface of IMC grains is presented. Fig. 10**(a)** showcases $\dot{Q}_{min}$ condition where consistently the lowest free energy value is calculated at the interface for all four IMC grains (yellow lines) implying the continuous growth of Ti_3Au intermetallics. Additionally, from the same graph it can deduced that there is only one grain G_1 interacting with the meltpool marked by the presence of red solid line in plot for G_1 and absence in all others. The interaction between meltpool and grain G_1 is very brief lasting only for 21.8 ms after which, the only interaction of all IMC grains including G_1 is with FCC phase (green line). Throughout the simulation, the free energies of interacting phases IMC grains and FCC is always minimum for IMC giving rise to its eventual growth. Similarly, for $\dot{Q}_{max}$ condition, the plot is presented in Fig. 10**(b)** where a distinct phenomenon is observed for grain G_1 and G_3. For grain G_1, at the beginning of simulation the LIQUID phase dominates the interfacial region resulting in meltpool area increase. After 22 ms into the simulation, the driving free energy at interface region shifts from LIQUID phase to IMC and hence IMC grain G_1 grows. For grain G_3, the

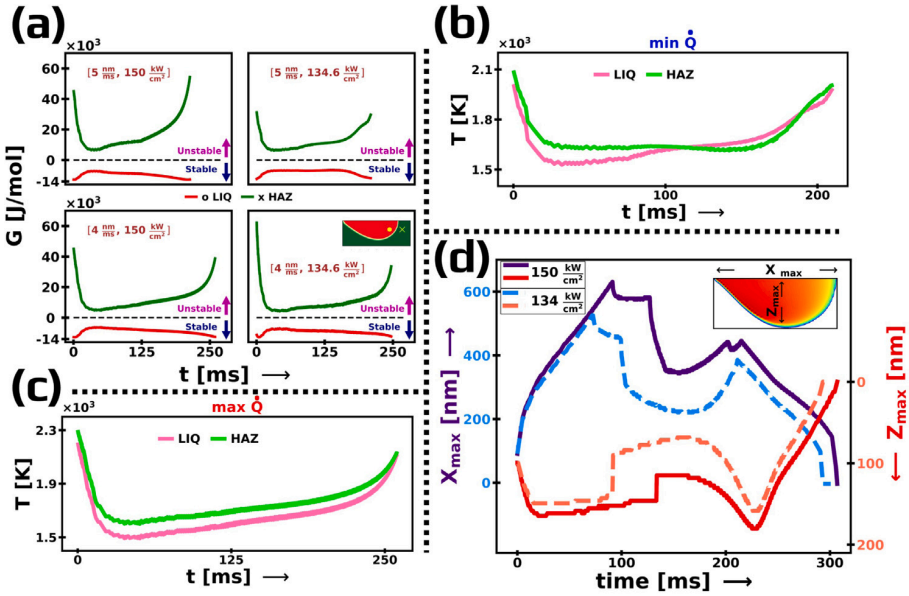


Fig. 9. Assessment of thermodynamic stability of meltpool is performed in **(a)–(c)**. The images in **(a)** demonstrate how laser irradiance and scan speed influences free energy profiles at the forefront of an advancing melt pool. The red colored free energy curves representing the position dot (∘) located within the LIQUID phase of the meltpool 10 nm inward from the phase interface are negative throughout the entire time duration. On the other hand, the cross (X) position located at the solid FCC phase 10 nm outward from the phase interface, has a positive valued F values through out the entire duration and thus indicates that it will be consumed by the advancing melt pool (relative position of dot 'o' and cross '×' is presented in the inset figure of **(a)**). The temperature values that dictate the F values for the two locations — one positioned at the LIQUID phase (LIQ) and another at heat affected zone (HAZ) of FCC phase, are plotted as functions of time for processing parameters of **(b)** 150 kW/cm^2, 4 nm/ms (max Q) and **(c)** 134.6 kW/cm^2, 5 nm/ms (min Q) criteria. The graph in **(d)** reveals how the transient melt pool size (characterized geometrically by horizontal span x_{max} and vertical depth z_{max}) is increased two-dimensionally by the amount of the irradiance values of a boundary heat source moving at a constant speed of 5 nm/ms. The magnitudes of x_{max} and z_{max} are differentiated through the colors of the labels in the vertical axes. The lengths (span and depth) for higher irradiance value of 150 kW/cm^2 are represented by solid lines whereas those for lower irradiance (134.6 kW/cm^2) are depicted by dotted lines. For applied irradiance of 150 kW/cm^2, the meltpool span achieves its peak value of 630 nm at 91 ms whereas the largest depth of 180 nm at 225 ms.

IMC interface comes into contact with meltpool mid-simulation (from 125 ms to 147 ms) elsewhere the phase in contact is FCC. Although the interface contact changes from FCC to LIQUID to FCC back again for grain G_3, the free energy at interface is measured to be minimum for IMC grain throughout the simulation. For grain G_2 and G_4, IMC grain evolves and grows in expense of FCC phase by maintaining the minimum free energy at IMC-FCC interface responsible for driving the phase transition.

Fig. 10**(c)** features two subplots with time–temperature graph of the marked point (×) at the IMC interface under $\dot{Q}_{min}$ and $\dot{Q}_{max}$ conditions. It can be observed that the maximum temperature attained by all four interfacial points is greater for $\dot{Q}_{max}$, compared to $\dot{Q}_{min}$. Similarly, under maximum heat flux, the time required for the interfacial points to reach maximum temperature and return to ambient temperature is longer than under minimum heat flux condition (380 ms and 300 ms, respectively). Whereas, Fig. 10**(d)** presents the growth of the inter-metallic compound's mean thickness (s) on application of two level of laser irradiance at fixed scan-speed of 5 nm/ms. The calculation of mean overall thickness is performed by dividing the total area of IMC grains by the combined bottom width (X_{max}^{IMC}) of all grains. For laser irradiance of 150 kW/cm^2 the grain growth exhibits a non-linear pattern (red line), featuring an initial surge followed by a plateau towards the simulation's end. Whereas, the growth of intermetallics is not so pronounced for lower laser irradiance (blue dashed line) only attaining a thickness (s) of 289 nm at 235 ms compared to 289 nm at 235 ms for higher irradiance level. Here, it can be observed that with just an 11.44% increase in laser irradiance level, the IMC thickness increased by a substantial 25.68% aiding to the conclusion that Ti_3Au intermetallics growth is highly sensitive towards deposited heat.

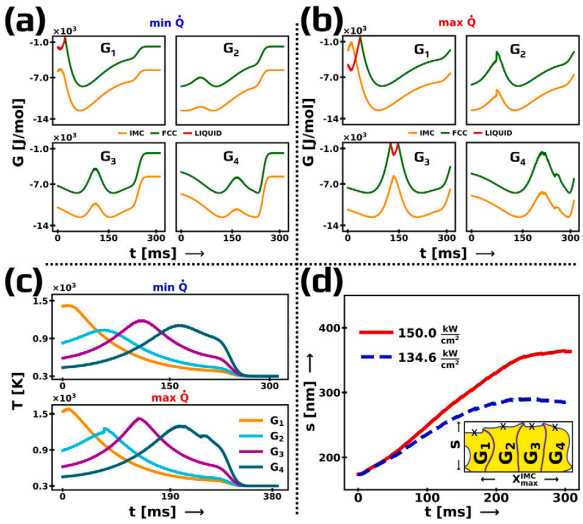


Fig. 10. Thermodynamic assessment at the top interface points of four IMC grains G_1, G_2, G_3, G_4 at **(a)–(c)** for two heat source parameters conditions — min Q̇ (134.6 kW/cm^2, 5 nm/ms) and max Q̇ (150 kW/cm^2, 4 nm/ms), reveals that IMC grains having a relatively lower free energy (F) values than FCC phase can grow at the latter's expense. In context of minimum boundary heat source criterion, as shown in **(a)** and **(c)** only the grain G_1's top interface reaches a higher temperature value (T > 1337 + K) at initial time momentarily when LIQUID phase is thermodynamically favorable as compared to the FCC phase. However, in case of maximum boundary heat source criterion, as shown in **(b)** and **(c)**, top interfaces of grains G_1 and G_3 reach the very high temperature condition in which LIQUID phase will momentarily get more favorable conditions than the FCC phase in terms of thermodynamic stability (quantified by the relative values of free energy). At a constant scan speed of 5 nm/ms, the image in **(d)** shows how a higher irradiance value of laser accelerates the total IMC layer thickness increment rate (s).

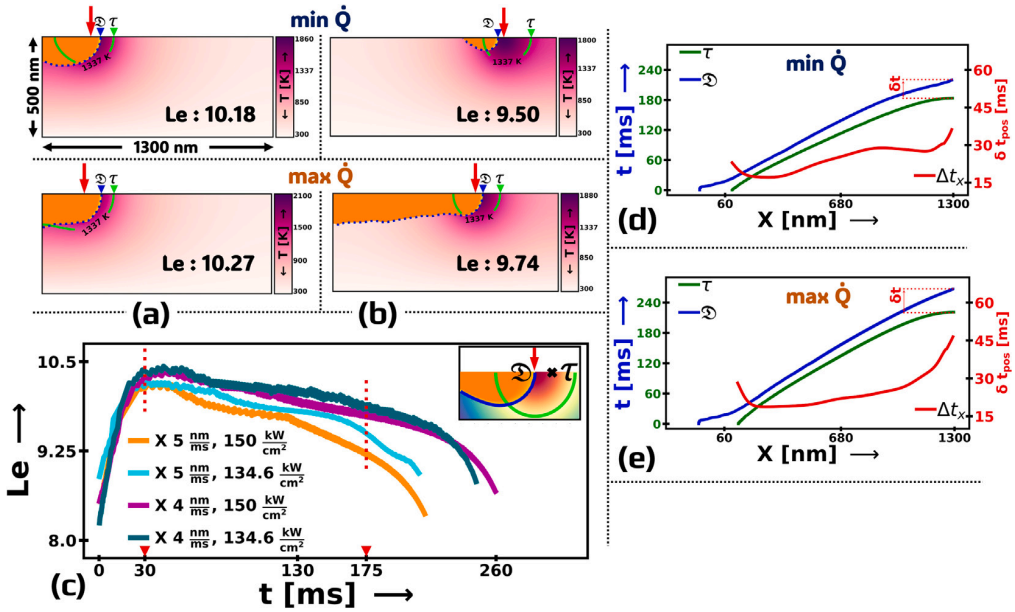


Fig. 11. The figures presented herein highlight our key findings regarding the distinction between thermal and chemical diffusion fronts, characterized by τ and $\mathfrak{D}$. In this context, τ marks the isotherm tip corresponding to the FCC-melting temperature (1337 K), while $\mathfrak{D}$ denotes the leading front of the meltpool. Subplots **(a)** and **(b)** chronicle the temporal evolution of τ and $\mathfrak{D}$ under minimum and maximum heat flux conditions per unit time, revealing the lead–lag dynamics. For instance, in **(a)** under $\dot{Q}_{min}$ (134.6 kW/cm^2 and 5 nm/ms) at t = 30 ms, the isotherm front (τ) precedes the meltpool front ($\mathfrak{D}$) with a Lewis number of 10.18, similar to the $\dot{Q}_{max}$ (150 kW/cm^2 and 4 nm/ms) scenario at the same time stamp but with a slightly higher Lewis number of 10.27. In **(b)**, under $\dot{Q}_{min}$ at t = 175 ms, the Lewis number decreases to 9.50, and the laser beam spot surpasses the chemical diffusion front τ. Notably, the meltpool area (inside dotted blue line) is distinctly smaller than the region above the melting temperature (green contour line) due to the $\dot{Q}_{min}$ condition. For $\dot{Q}_{max}$ at the same time stamp, the meltpool front precedes the laser beam spot, following the thermal front τ with a Lewis number of 9.74. Plot **(c)** illustrates the variation in Lewis number for different laser parameters over simulation time, highlighting the significant impact of scanning speed on Lewis number. Slower scanning speeds exhibit higher Lewis numbers, as seen in teal and magenta lines (4 nm/ms), compared to the faster scan speed of 5 nm/ms (orange and light blue lines). The inset schematics provide a visual representation of the thermal front (τ), meltpool front ($\mathfrak{D}$), and laser beam spot. Graphs **(d)** and **(e)** display positional time lags (δt_{pos}) between thermal and meltpool diffusion fronts against the domain's horizontal dimension. Under minimum heat flux per unit time in **(d)**, the meltpool front $\mathfrak{D}$ catches up to the isotherm front τ within 37.08 ms, while in **(e)** for maximum heat flux per unit time, the positional time lag reaches a maximum of 47.14 ms, as indicated by the red line.

3.7. Diffusion kinetics and Lewis number

In literature, the majority of numerical models for laser processing [56,57,61] assume that the melting of material correlates instantaneously with its theoretical melting temperature. This assumption might yield satisfactory results for scenarios where the laser heat source is stationary. However, for a moving laser heat source traversing through the material, the growth of the meltpool cannot simply be a function of temperature alone. Instead, the diffusion of heat and mass transfer come into play for the meltpool to trace the path of the moving laser [96]. Since the diffusion rates of heat and mass are different quantities, as shown in Eq. (26), the assumption that any region inside the domain where the temperature reaches the material's melting point will instantaneously change into meltpool becomes invalid. Thus the movement of the LIQUID phase is dictated by chemical diffusion rather than heat diffusion. And since heat transfer is faster than chemical diffusion [97], it leads to the conclusion that LIQUID phase lags behind the isotherm of melting temperature as laser moves across the domain. To model the real scenario accurately, we quantified the difference between the rates of heat diffusion and mass diffusion using the Lewis Number (Le), a non-dimensional measure of the heat flow-to-chemical diffusion ratio, as expressed in Eq. (26) [49]. This measure is capable of unraveling the dynamics of laser-induced diffusion fronts in the Ti–Au system.

$$Le_T = \frac{\alpha}{D} = \frac{k_{th}}{\rho Cp} \times \frac{1}{D} \tag{26}$$

where α is the heat diffusivity, D is the chemical diffusivity, k_{th} is the thermal conductivity, Cp denotes the specific heat capacity, and ρ is the density. In the above-mentioned equation subscript 'T' denotes that the associated material property is a function of changing temperature and is not constant during the transient heating via laser irradiance.

To clearly visualize the difference between temperature front and chemical diffusion phenomena during the simulation, we present Fig. 11, where we tracked two diffusion fronts corresponding to the meltpool ($\mathfrak{D}$) and the melting temperature of 'Au' (1337 K) (τ). Fig. 11**a** and **b** represent the dynamics of two diffusion fronts for $\dot{Q}_{min}$ and $\dot{Q}_{max}$ conditions at two time frames (11**a**: t = 30 ms, 11**b**: 175 ms). In the figures, it can be observed that initially at t = 30 ms, for both conditions, the gap between heat transfer and chemical diffusion (τ - $\mathfrak{D}$) is nearly equal. However, as the laser progresses (t = 175 ms), for $\dot{Q}_{min}$ the gap increases compared to the $\dot{Q}_{max}$ condition due to the rise in domain temperature with higher heat flux which increases the chemical diffusion rate allowing to catch up with heat flow front. Fig. 11**c** illustrates the dynamics of the changing Lewis number for the meltpool front and isotherm of 1337 K for all four simulation conditions.

Fig. 11**d** and **e** show the temporal progression of the two diffusion fronts at the top horizontal surface of the domain corresponding to $\dot{Q}_{min}$ and $\dot{Q}_{max}$ conditions. The green line denotes τ (isotherm at T = 1337 K) and the blue curve represents the meltpool front ($\mathfrak{D}$), whereas the positional time lag (δt_{pos}) between τ and $\mathfrak{D}$ is shown by the red curve (Δt_x). The quantity (δt_{pos}) represents the difference in time taken by the heat flow front (at 1337 K) and that by the meltpool front to reach a specific coordinate at the top horizontal surface of the numerical domain. Mathematically, it is given by the Expression (27). The simulation videos demonstrating the heat transfer and chemical diffusion lead–lag dynamics, along with plots of positional time-lag over time, are available in the Appendix B. The four videos, which cover combinations of two scan speeds (5 nm/ms and 4 nm/ms) and two irradiance levels (150 kW/cm^2 and 134.6 kW/cm^2), are represented by Videos B9, B10, B11, and B12, respectively.

$$\delta t_{pos} = t_{\mathfrak{D}} - t_{\tau} \tag{27}$$

here, $t_{\mathfrak{D}}$ and t_{τ} are the time taken by phase front and isotherm tip to reach any given spatial coordinate point on the top right surface of the domain. From Fig. 11, we can note that during mid-simulation, the δt_{pos} is lower for the $\dot{Q}_{max}$ condition, meaning the meltpool front catches up with the temperature flow front faster compared to that during the $\dot{Q}_{min}$ condition.

4. Conclusion

In this research work explores the computational aspect of laser processing parameter's effect on microstructural phase evolution in Ti–Au binary alloy system. Using a temperature-composition dependent free energy formulation for phase-field modeling we conducted four different simulations by varying laser irradiance and scan-speed. The quantitative analysis of thermal history, phase transition, area evolution of phases, meltpool dynamics and kinetics of heat and chemical diffusion is performed for combination of different laser parameters. It was observed that the higher laser heat flux condition is highly preferable for the growth of Ti_3Au intermetallic grains and even with the minimum heat flux condition of faster scan-speed at lower irradiance, the IMC grains tend to gradually grow. For FCC and LIQUID phases, they are found to grow inexpense of each other as laser melts the Au-rich FCC phase and as laser traverse the LIQUID phase transforms to solid FCC phase, whereas the Ti-rich HCP region continuously shrinks with the evolution of IMC phase at the HCP-FCC interface. The growth of Ti_3Au intermetallics is further backed by minimum value of free energy for intermetallic phase calculated at the contact point between other phases and IMC grains making the TI_3Au evolution more stable. Further more, we performed numerical analysis on meltpool depth and width with variation in scan-speed and irradiance with result showcasing that higher irradiance at slower scan-speed give rise to a wider and deeper LIQUID phase directly below the laser focus point. Similarly, the quantitative prediction of phase stability between meltpool and HAZ (FCC) region is made via the comparison of free energy values at these region as laser moves from left top edge to right top edge of the computational domain. Finally, we proceed to address the issue of heat flow and chemical diffusion difference which are not taken into consideration in contemporary research by calculating the Lewis Number to quantify the differences in chemical diffusion and heat flow fronts in the domain. We also defined a parameter called *positional time lag (δt_{pos})* that quantifies the time difference it takes for the phase (meltpool) to catch the isotherm of 1337 K (melting temperature of Au) at the spatial coordinate in the domain by combining the information of Lewis number with the phase-temperature lead–lag dynamics.

In conclusion, our work provides a comprehensive understanding of phase area evolution, free energy dynamics, and diffusion phenomena during laser processing of Ti–Au binary alloy system. With the quantification of interplay between heat flow and chemical diffusion, we have pushed the boundary of phase field modeling for non-isothermal laser processing, particularly in the context of unique intermetallic compound Ti_3Au. With the preliminary foundation of temperature-composition dependence free energy formulation in this work, we intend to extend this work in future with further refinements in multiphysics by combining surface-tension and other flow phenomenon in the meltpool. We also intend to combine the machine learning models trained on simulation data to construct a Digital Twin capable of taking input from thermal imaging cameras to predict different microstructural features and phase evolution in multi-alloy system.

CRediT authorship contribution statement

Upadesh Subedi: Investigation, Conceptualization, Methodology, Formal analysis, Writing – original draft, Visualization, Validation, Software, Data curation. **Nele Moelans:** Writing – review & editing, Formal analysis, Validation, Methodology. **Tomasz Tański:** Writing – review & editing, Visualization, Validation, Supervision. **Anil Kunwar:** Writing – review & editing, Validation, Supervision, Conceptualization, Project administration, Methodology, Funding acquisition, Data curation.

Declaration of competing interest

The authors declare that they have no known competing financial interests or personal relationships that could have appeared to influence the work reported in this paper.

Acknowledgments

This work was supported by the National Science Centre, Poland (UMO-2021/42/E/ST5/00339). The resources and services used in this work were provided by the VSC (Flemish Supercomputer Center), funded by the Research Foundation - Flanders (FWO), Belgium and the Flemish Government, Belgium.

Appendix A. The common tangent method and Gibbs free energy projections

The common tangent method is utilized to compute the τ parameter mention in Eq. (16) of main text. Fig. A.1 illustrates the concept of processes involving the calculation of τ parameter. The figure shows the equilibrium compositions as points on the composition axis: $c_{i,eq,j}$, $c_{j,eq,i}$, $c_{j,eq,k}$, and $c_{k,eq,j}$ at two temperatures (A.1**a** at 700 K and A.1**b** at 1500 K). The segment length $(c_{j,eq,i} - c_{i,eq,j})$ corresponds to the common tangent between phases i and j, while $(c_{k,eq,j} - c_{j,eq,k})$ corresponds to the common tangent between phases j and k. Their product captures the combined effect of the two common tangents, representing the variation of Gibbs free energy projected onto the composition axis. Averaging this product over all N temperature points gives τ, which characterizes how the Gibbs free energy projection changes with temperature.

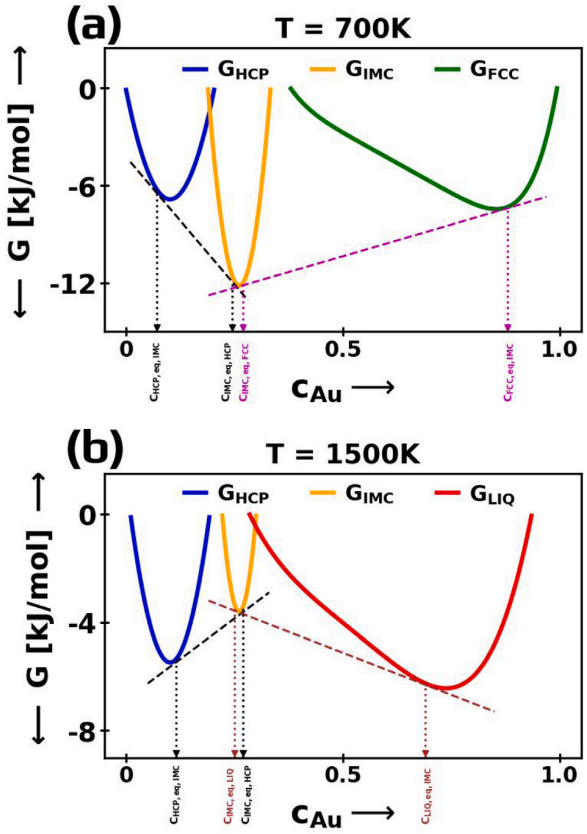


Fig. A.1. Common tangent construction for equilibrium compositions at **(a)** 700 K and **(b)** 1500 K. The segment lengths represent equilibrium composition differences used to compute the τ parameter, capturing Gibbs free energy variations with temperature.

Appendix B. Supplementary data

Supplementary material related to this article can be found online at https://doi.org/10.1016/j.commatsci.2025.113875.

Data availability

The data and codes for this work are available at https://github.com/subediupadesh/MultiPhysics_MultiPhaseField_LaserProcessing.

References

[1] P.J. Bania, Beta titanium alloys and their role in the titanium industry, JOM 46 (1994) 16–19, http://dx.doi.org/10.1007/BF03220742, URL https://link.springer.com/article/10.1007/BF03220742.

[2] T.S. Tshephe, S.O. Akinwamide, E. Olevsky, P.A. Olubambi, Dditive manufacturing of titanium-based alloys- A review of methods, properties, challenges, and prospects, Heliyon 8 (2022) e09041, http://dx.doi.org/10.1016/j.heliyon.2022.e09041, URL https://www.sciencedirect.com/science/article/pii/S2405844022003292.

[3] E. Marin, A. Lanzutti, Biomedical applications of titanium alloys: A comprehensive review, Mater. 17 (1) (2023) 114, http://dx.doi.org/10.3390/ma17010114, URL https://www.mdpi.com/1996-1944/17/1/114.

[4] E. Lautenschlager, P. Monaghan, Titanium and titanium alloys as dental materials, Int. Dent. J. 43 (3) (1993) 245—253, URL http://europepmc.org/abstract/MED/8406955.

[5] H.B. Mamo, U. Subedi, T. Poloczek, M. Adamiak, A.N.S. Appiah, M. Skonieczna, P.M. Nuckowski, Y. Geng, B. Haldar, A. Kunwar, Prototyping Ti2Cu intermetallic grain growth heterogeneously in Ti6Al4V matrix through laser additive manufacturing, Mater. Des. 246 (2024) 113312, http://dx.doi.org/10.1016/j.matdes.2024.113312, URL https://www.sciencedirect.com/science/article/pii/S0264127524006877.

[6] O. Bialas, A.N. Appiah, M. Wala, A. Kunwar, A. Woźniak, P.M. Nuckowski, W. Simka, P. Råback, M. Adamiak, Laser assisted fabrication of mechanochemically robust Ti3Au intermetallic at Au-Ti interface, Eng. Sci. Technol. Int. J. 42 (2023) 101413, http://dx.doi.org/10.1016/j.jestch.2023.101413, URL https://linkinghub.elsevier.com/retrieve/pii/S2215098623000903.

[7] N. Nohira, W.-T. Chiu, M. Tahara, H. Hosoda, Microstructural changes and mechanical property response to aging heat treatment in hypereutectoid Ti-Au-Mo biomedical alloys, Mater. Sci. Eng.: A 912 (2024) 146956, http://dx.doi.org/10.1016/j.msea.2024.146956, URL https://www.sciencedirect.com/science/article/pii/S0921509324008876.

[8] J. Liu, K. Wang, X. Li, X. Zhang, X. Gong, Y. Zhu, Z. Ren, B. Zhang, J. Cheng, Biocompatibility and osseointegration properties of a novel high strength and low modulus Beta- Ti10Mo6Zr4Sn3Nb alloy, Front. Bioeng. Biotechnol. 11 (2023) http://dx.doi.org/10.3389/fbioe.2023.1127929, URL https://www.frontiersin.org/journals/bioengineering-and-biotechnology/articles/10.3389/fbioe.2023.1127929.

[9] Y. Sun, Q. Liu, Z. Yu, L. Ren, X. Zhao, J. Wang, Study on osseointegration capability of beta-type Ti-Nb-Zr-Ta-Si alloy for orthopedic implants, Mater. 17 (2024) 472, http://dx.doi.org/10.3390/ma17020472, URL https://www.mdpi.com/1996-1944/17/2/472.

[10] E. Svanidze, T. Besara, M. Fevsi Ozaydin, C.S. Tiwary, J.K. Wang, S. Radhakrishnan, S. Mani, Y. Xin, K. Han, H. Liang, T. Siegrist, P.M. Ajayan, E. Morosan, High hardness in the biocompatible intermetallic compound b-Ti3Au, Sci. Adv. 2 (7) (2016) http://dx.doi.org/10.1126/sciadv.1600319, URL https://www.science.org/doi/10.1126/sciadv.1600319.

[11] C.C. Lukose, I. Anestopoulos, M.I. Panayiotidis, M. Birkett, Nanomechanical and microstructural characterization of biocompatible Ti 3 Au Thin Films Grown on Glass and Ti 6 Al 4 V Substrates, ACS Biomater. Sci. Eng. 10 (2024) 2935–2944, http://dx.doi.org/10.1021/acsbiomaterials.4c00070, URL https://pubs.acs.org/doi/10.1021/acsbiomaterials.4c00070.

[12] G.B. Kocabas, S. Yalcinkaya, E. Cetin, Y. Sahin, Energy absorption of a novel lattice structure-filled multicell thin-walled tubes under axial and oblique loadings, Adv. Eng. Mater. 26 (2024) http://dx.doi.org/10.1002/adem.202400483, URL https://advanced.onlinelibrary.wiley.com/doi/full/10.1002/adem.202400483.

[13] C.C. Lukose, I. Anestopoulos, L. Bowen, M.I. Panayiotidis, M. Birkett, Adatom controlled emergence of high hardness in biocompatible beta-Ti3Au intermetallic thin film surfaces, Surf. Interfaces 40 (2023) 103034, http://dx.doi.org/10.1016/j.surfin.2023.103034, URL https://linkinghub.elsevier.com/retrieve/pii/S2468023023004042.

[14] A. Karimi, C. Cattin, Intermetallic β-Ti3Au hard thin films prepared by magnetron sputtering, Thin Solid Films 646 (2018) 1–11, http://dx.doi.org/10.1016/j.tsf.2017.11.027, URL https://linkinghub.elsevier.com/retrieve/pii/S0040609017308726.

[15] L. Li, M. Hong, M. Schmidt, M. Zhong, A. Malshe, B.H. in'tVeld, V. Kovalenko, Laser nano-manufacturing - State of the art and challenges, CIRP Ann 60 (2011) 735–755, http://dx.doi.org/10.1016/j.cirp.2011.05.005, URL https://www.sciencedirect.com/science/article/pii/S0007850611002071.

[16] G.E. Moore, Cramming more components onto integrated circuits, reprinted from electronics, volume 38, number 8, April 19, 1965, pp.114 ff, IEEE Solid- State Circuits Soc. Newsl. 11 (2006) 33–35, http://dx.doi.org/10.1109/N-SSC.2006.4785860, URL https://ieeexplore.ieee.org/document/4785860.

[17] Y. Zhai, Z. Feng, Y. Zhou, S.-T. Han, Energy-efficient transistors: suppressing the subthreshold swing below the physical limit, Mater. Horizons 8 (2021) 1601–1617, http://dx.doi.org/10.1039/D0MH02029J, URL https://pubs.rsc.org/en/content/articlelanding/2021/mh/d0mh02029j.

[18] M. Boutinguiza, A. Riveiro, J. del Val, in: M. Boutinguiza, A. Riveiro, J. del Val (Eds.), Laser Synthesis of Nanomaterials, MDPI, 2023, http://dx.doi.org/10.3390/books978-3-0365-6928-4, URL https://www.mdpi.com/books/reprint/7067-laser-synthesis-of-nanomaterials.

[19] J. Meijer, K. Du, A. Gillner, D. Hoffmann, V. Kovalenko, T. Masuzawa, A. Ostendorf, R. Poprawe, W. Schulz, Laser machining by short and ultrashort pulses, state of the art and new opportunities in the age of the photons, CIRP Ann 51 (2002) 531–550, http://dx.doi.org/10.1016/S0007-8506(07)61699-0, URL https://www.sciencedirect.com/science/article/pii/S0007850607616990.

[20] R. Srinivasan, E. Sutcliffe, B. Braren, Ablation and etching of polymethylmethacrylate by very short (160 fs) ultraviolet (308 nm) laser pulses, Appl. Phys. Lett. 51 (1987) 1285–1287, http://dx.doi.org/10.1063/1.99001, URL https://pubs.aip.org/aip/apl/article-abstract/51/16/1285/52789.

[21] M. Koleva, A. Dikovska, N. Nedyalkov, T. Genova, G. Atanasova, Laser synthesis and processing of composite nanostructures, J. Chem. Technol. Met. 59 (2024) 831–839, http://dx.doi.org/10.59957/jctm.v59.i4.2024.11, URL https://j.uctm.edu/index.php/JCTM/article/view/411.

[22] L. Yang, J. Wei, Z. Ma, P. Song, J. Ma, Y. Zhao, Z. Huang, M. Zhang, F. Yang, X. Wang, The fabrication of micro/nano structures by laser machining, Nanomaterials 9 (2019) 1789, http://dx.doi.org/10.3390/nano9121789, URL https://www.mdpi.com/2079-4991/9/12/1789.

[23] M. Kim, S. Osone, T. Kim, H. Higashi, T. Seto, Synthesis of nanoparticles by laser ablation: A review, KONA Powder Part. J. 34 (2017) 80–90, http://dx.doi.org/10.14356/kona.2017009, URL https://www.jstage.jst.go.jp/article/kona/34/0/34_2017009/_article.

[24] L. Orazi, L. Romoli, M. Schmidt, L. Li, Ultrafast laser manufacturing: from physics to industrial applications, CIRP Ann 70 (2021) 543–566, http://dx.doi.org/10.1016/j.cirp.2021.05.007, URL https://www.sciencedirect.com/science/article/pii/S0007850621001232.

[25] Y. Rho, C.P. Grigoropoulos, Laser-Induced Processing of Nanoparticles and Growth of Nanowires, Springer International Publishing, Cham, 2020, pp. 1–39, http://dx.doi.org/10.1007/978-3-319-69537-2_28-1, URL https://link.springer.com/referenceworkentry/10.1007/978-3-319-69537-2_28-1.

[26] M.-L. Zheng, X.-M. Duan, Laser nano-manufacturing technology and applications towards optical functional nanostructures and devices, in: 2015 Opto-Electronics and Communications Conference, OECC, IEEE, 2015, pp. 1–3, http://dx.doi.org/10.1109/OECC.2015.7340195, URL https://ieeexplore.ieee.org/document/7340195.

[27] A. Klos, X. Sedao, T.E. Itina, C. Helfenstein-Didier, C. Donnet, S. Peyroche, L. Vico, A. Guignandon, V. Dumas, Ultrafast laser processing of nanostructured patterns for the control of cell adhesion and migration on titanium alloy, Nanomaterials 10 (2020) 864, http://dx.doi.org/10.3390/nano10050864, URL https://www.mdpi.com/2079-4991/10/5/864.

[28] J.F. De Almeida, D.C. Amaral, R.T. Coelho, Innovative framework to manage New Product Development (NPD) integrating additive manufacturing (AM) and agile management, Procedia CIRP 103 (2021) 128–133, http://dx.doi.org/10.1016/j.procir.2021.10.020, URL https://linkinghub.elsevier.com/retrieve/pii/S2212827121008611.

[29] J. Reichwein, S. Vogel, S. Schork, E. Kirchner, On the applicability of agile development methods to design for additive manufacturing, Procedia CIRP 91 (2020) 653–658, http://dx.doi.org/10.1016/j.procir.2020.03.112, URL https://linkinghub.elsevier.com/retrieve/pii/S2212827120308799.

[30] C. Klahn, B. Leutenecker, M. Meboldt, Design strategies for the process of additive manufacturing, Procedia CIRP 36 (2015) 230–235, http://dx.doi.org/10.1016/j.procir.2015.01.082, URL https://linkinghub.elsevier.com/retrieve/pii/S2212827115008938.

[31] P. Gradl, D.C. Tinker, A. Park, O.R. Mireles, M. Garcia, R. Wilkerson, C. Mckinney, Robust metal additive manufacturing process selection and development for aerospace components, J. Mater. Eng. Perform. 31 (8) (2022) 6013–6044, http://dx.doi.org/10.1007/s11665-022-06850-0, URL https://link.springer.com/10.1007/s11665-022-06850-0.

[32] T. Blachowicz, G. Ehrmann, A. Ehrmann, Metal additive manufacturing for satellites and rockets, Appl. Sci. 11 (24) (2021) 12036, http://dx.doi.org/10.3390/app112412036, URL https://www.mdpi.com/2076-3417/11/24/12036.

[33] M.H. Mobarak, M.A. Islam, N. Hossain, M.Z. Al Mahmud, M.T. Rayhan, N.J. Nishi, M.A. Chowdhury, Recent advances of additive manufacturing in implant fabrication – A review, Appl. Surf. Sci. Adv. 18 (2023) 100462, http://dx.doi.org/10.1016/j.apsadv.2023.100462, URL https://linkinghub.elsevier.com/retrieve/pii/S266652392300096X.

[34] H.B. Mamo, M. Adamiak, A. Kunwar, 3D printed biomedical devices and their applications: A review on state-of-the-art technologies, existing challenges, and future perspectives, J. Mech. Behav. Biomed. Mater. 143 (2023) 105930, http://dx.doi.org/10.1016/j.jmbbm.2023.105930, URL https://linkinghub.elsevier.com/retrieve/pii/S1751616123002837.

[35] M. Peters, J. Kumpfert, C. Ward, C. Leyens, Titanium alloys for aerospace applications, Adv. Eng. Mater. 5 (6) (2003) 419–427, http://dx.doi.org/10.1002/adem.200310095, URL https://onlinelibrary.wiley.com/doi/10.1002/adem.200310095.

[36] P. Nyamekye, S. Rahimpour Golroudbary, H. Piili, P. Luukka, A. Kraslawski, Impact of additive manufacturing on titanium supply chain: Case of titanium alloys in automotive and aerospace industries, Adv. Ind. Manuf. Eng. 6 (2023) 100112, http://dx.doi.org/10.1016/j.aime.2023.100112, URL https://linkinghub.elsevier.com/retrieve/pii/S2666912923000016.

[37] N. H.A. Besisa, T. Yajima, Titanium-based alloys: Classification and diverse applications, in: Titanium-Based Alloys - Characteristics and Applications [Working Title], IntechOpen, 2024, http://dx.doi.org/10.5772/intechopen.1005269, URL https://www.intechopen.com/online-first/1180817.

[38] U. Subedi, N. Moelans, T. Tański, A. Kunwar, Rapid portabilization of elasto-chemical evolution data for dental Ti-Cr alloy microstructure through sparsification and tensor computation, Scr. Mater. 244 (2024) 116027, http://dx.doi.org/10.1016/j.scriptamat.2024.116027, URL https://linkinghub.elsevier.com/retrieve/pii/S1359646224000629.

[39] S. Pothala, M. Jagannadha Raju, Recent advances of metallic bio-materials in additive manufacturing in biomedical implants–A review, Mater. Today: Proc. (2023) http://dx.doi.org/10.1016/j.matpr.2023.07.109, URL https://linkinghub.elsevier.com/retrieve/pii/S2214785323039780.

[40] Y. Liu, W. Wang, L.-C. Zhang, Additive manufacturing techniques and their biomedical applications, Fam. Med. Community Heal. 5 (4) (2017) 286–298, http://dx.doi.org/10.15212/FMCH.2017.0110, URL https://fmch.bmj.com/lookup/doi/10.15212/FMCH.2017.0110.

[41] N. Sommer, P. Kluge, F. Stredak, S. Eigler, H. Hill, T. Niendorf, S. Böhm, Additive manufacturing of compositionally-graded AISI 316L to CoCrMo structures by directed energy deposition, Crystals 11 (9) (2021) 1043, http://dx.doi.org/10.3390/cryst11091043, URL https://www.mdpi.com/2073-4352/11/9/1043.

[42] S. Liang, C. Wei, A. Kunwar, U. Subedi, H. Jiang, H. Ma, C. Ke, Phase field modelling combined with data-driven approach to unravel the orientation influenced growth of interfacial Cu6Sn5 intermetallics under electric current stressing, Surf. Interfaces 37 (2023) 102728, http://dx.doi.org/10.1016/j.surfin.2023.102728, URL https://linkinghub.elsevier.com/retrieve/pii/S2468023023000986.

[43] U. Subedi, Y.A. Coutinho, P.B. Malla, K. Gyanwali, A. Kunwar, Automatic featurization aided data-driven method for estimating the presence of intermetallic phase in multi-principal element alloys, Metals 12 (2022) 964, http://dx.doi.org/10.3390/met12060964, URL https://www.mdpi.com/2075-4701/12/6/964.

[44] S. Poudel, U. Subedi, M.O. Hamid, K. Gyanwali, N. Moelans, A. Timofiejczuk, A. Kunwar, AlloyManufacturingNet for discovery and design of hardness-elongation synergy in multi-principal element alloys, Eng. Appl. Artif. Intell. 132 (2024) 107902, http://dx.doi.org/10.1016/j.engappai.2024.107902, URL https://www.sciencedirect.com/science/article/pii/S0952197624000605.

[45] S. Poudel, R. Thapa, R. Basnet, A. Timofiejczuk, A. Kunwar, PiezoTensorNet: Crystallography informed multi-scale hierarchical machine learning model for rapid piezoelectric performance finetuning, Appl. Energy 361 (2024) 122901, http://dx.doi.org/10.1016/j.apenergy.2024.122901, URL https://www.sciencedirect.com/science/article/pii/S0306261924002848.

[46] U. Subedi, N. Moelans, T. Tánski, A. Kunwar, Foretelling microstructural interface with multi-generational convolutional-LSTM framework, Eng. Comput. (2025) http://dx.doi.org/10.1007/s00366-025-02117-z, URL https://link.springer.com/article/10.1007/s00366-025-02117-z.

[47] S. Liu, M. Lee, C. Choi, K. Shin, Effect of additive manufacturing of SUS316L using selective laser melting, J. Mater. Res. Technol. 24 (2023) 9824–9833, http://dx.doi.org/10.1016/j.jmrt.2023.05.160, URL https://linkinghub.elsevier.com/retrieve/pii/S2238785423011262.

[48] S. Ramadugu, S.R.K. Ledella, J.N.J. Gaduturi, R.R. Pinninti, V. Sriram, K.K. Saxena, Environmental life cycle assessment of an automobile component fabricated by additive and conventional manufacturing, Int. J. Interact. Des. Manuf. (IJIDeM) (2023) http://dx.doi.org/10.1007/s12008-023-01532-0, URL https://link.springer.com/10.1007/s12008-023-01532-0.

[49] F. Oueslati, B. Ben-Beya, T. Lili, Double-diffusive natural convection and entropy generation in an enclosure of aspect ratio 4 with partial vertical heating and salting sources, Alex. Eng. J. 52 (4) (2013) 605–625, http://dx.doi.org/10.1016/j.aej.2013.09.006, URL https://linkinghub.elsevier.com/retrieve/pii/S111001681300094X.

[50] Y. Yang, O. Ragnvaldsen, Y. Bai, M. Yi, B.X. Xu, 3D non-isothermal phase-field simulation of microstructure evolution during selective laser sintering, Npj Comput. Mater. 5 (1) (2019) 81, http://dx.doi.org/10.1038/s41524-019-0219-7, URL https://www.nature.com/articles/s41524-019-0219-7.

[51] J.Y. Choi, T. Xue, S. Liao, J. Cao, Accelerating phase-field simulation of three-dimensional microstructure evolution in laser powder bed fusion with composable machine learning predictions, Addit. Manuf. 79 (2024) 103938, http://dx.doi.org/10.1016/j.addma.2023.103938, URL https://linkinghub.elsevier.com/retrieve/pii/S2214860423005511.

[52] D. Liu, Y. Wang, Mesoscale multi-physics simulation of rapid solidification of Ti-6Al-4V alloy, Addit. Manuf. 25 (2019) 551–562, http://dx.doi.org/10.1016/j.addma.2018.12.005, URL https://linkinghub.elsevier.com/retrieve/pii/S2214860417306139.

[53] H. Azizi, A. Ebrahimi, N. Ofori-Opoku, M. Greenwood, N. Provatas, M. Mohammadi, Phase-field simulation of solidification behavior of AlSi10Mg alloys manufactured through direct metal laser sintering, in: Minerals, Metals and Materials Series, 2020, pp. 299–307, http://dx.doi.org/10.1007/978-3-030-36296-6_28, URL http://link.springer.com/10.1007/978-3-030-36296-6_28.

[54] A. Kunwar, J. Hektor, S. Nomoto, Y.A. Coutinho, N. Moelans, Combining multi-phase field simulation with neural network analysis to unravel thermomigration accelerated growth behavior of Cu6Sn5 IMC at cold side Cu–Sn interface, Int. J. Mech. Sci. 184 (2020) 105843, http://dx.doi.org/10.1016/j.ijmecsci.2020.105843, URL https://linkinghub.elsevier.com/retrieve/pii/S0020740320314466.

[55] X. Gong, K. Chou, Phase-field modeling of microstructure evolution in electron beam additive manufacturing, JOM 67 (5) (2015) 1176–1182, http://dx.doi.org/10.1007/s11837-015-1352-5, URL http://link.springer.com/10.1007/s11837-015-1352-5.

[56] S. Sahoo, K. Chou, Phase-field simulation of microstructure evolution of Ti–6Al–4V in electron beam additive manufacturing process, Addit. Manuf. 9 (2016) 14–24, http://dx.doi.org/10.1016/j.addma.2015.12.005, URL https://linkinghub.elsevier.com/retrieve/pii/S2214860415300051.

[57] R. Darabi, E. Azinpour, A. Reis, J.C. de Sa, Multi-scale multi-physics phase-field coupled thermo-mechanical approach for modeling of powder bed fusion process, Appl. Math. Model. 122 (2023) 572–597, http://dx.doi.org/10.1016/j.apm.2023.06.021, URL https://linkinghub.elsevier.com/retrieve/pii/S0307904X23002767.

[58] S.G. Kim, W.T. Kim, T. Suzuki, Phase-field model for binary alloys, Phys. Rev. E - Stat. Phys. Plasmas Fluids Relat. Interdiscip. Top. 60 (6) (1999) 7186–7197, http://dx.doi.org/10.1103/PhysRevE.60.7186, URL https://link.aps.org/doi/10.1103/PhysRevE.60.7186.

[59] K. Fitzner, O.J. Kleppa, Thermochemistry of binary alloys of transition metals: The Me-Ti, Me-Zr, and Me-Hf(Me=Ag, Au) systems, Met. Trans. A 23 (3) (1992) 997–1003, http://dx.doi.org/10.1007/BF02675574, URL https://link.springer.com/10.1007/BF02675574.

[60] G. Kim, S.V. Meschel, P. Nash, W. Chen, Experimental formation enthalpies for intermetallic phases and other inorganic compounds, Sci. Data 4 (1) (2017) 170162, http://dx.doi.org/10.1038/sdata.2017.162, URL https://www.nature.com/articles/sdata2017162.

[61] Z. Li, M. Greenwood, A. Phillion, A phase field methodology for simulating the microstructure evolution during laser powder bed fusion in-situ alloying process, IOP Conf. Ser.: Mater. Sci. Eng. 1281 (1) (2023) 012017, http://dx.doi.org/10.1088/1757-899X/1281/1/012017, URL https://iopscience.iop.org/article/10.1088/1757-899X/1281/1/012017.

[62] D. Gaston, C. Newman, G. Hansen, D. Lebrun-Grandié, MOOSE: A parallel computational framework for coupled systems of nonlinear equations, Nucl. Eng. Des. 239 (10) (2009) 1768–1778, http://dx.doi.org/10.1016/j.nucengdes.2009.05.021, URL https://linkinghub.elsevier.com/retrieve/pii/S0029549309002635.

[63] M.R. Tonks, D. Gaston, P.C. Millett, D. Andrs, P. Talbot, An object-oriented finite element framework for multiphysics phase field simulations, Comput. Mater. Sci. 51 (1) (2012) 20–29, http://dx.doi.org/10.1016/j.commatsci.2011.07.028, URL https://linkinghub.elsevier.com/retrieve/pii/S0927025611004204.

[64] A.D. Lindsay, D.R. Gaston, C.J. Permann, J.M. Miller, D. Andrš, A.E. Slaughter, F. Kong, J. Hansel, R.W. Carlsen, C. Icenhour, L. Harbour, G.L. Giudicelli, R.H. Stogner, P. German, J. Badger, S. Biswas, L. Chapuis, C. Green, J. Hales, T. Hu, W. Jiang, Y.S. Jung, C. Matthews, Y. Miao, A. Novak, J.W. Peterson, Z.M. Prince, A. Rovinelli, S. Schunert, D. Schwen, B.W. Spencer, S. Veeraraghavan, A. Recuero, D. Yushu, Y. Wang, A. Wilkins, C. Wong, 2.0 - MOOSE: Enabling massively parallel multiphysics simulation, SoftwareX 20 (2022) 101202, http://dx.doi.org/10.1016/j.softx.2022.101202, URL https://linkinghub.elsevier.com/retrieve/pii/S2352711022001200.

[65] D. Gu, Laser additive manufacturing (AM): Classification, processing philosophy, and metallurgical mechanisms, in: Laser Additive Manufacturing of High-Performance Materials, Springer Berlin Heidelberg, Berlin, Heidelberg, 2015, pp. 15–71, http://dx.doi.org/10.1007/978-3-662-46089-4_2, URL https://link.springer.com/10.1007/978-3-662-46089-4_2.

[66] R. Otis, Z.-K. Liu, Pycalphad: CALPHAD-based computational thermodynamics in python, J. Open Res. Softw. 5 (1) (2017) 1, http://dx.doi.org/10.5334/jors.140, URL https://openresearchsoftware.metajnl.com/article/10.5334/jors.140/.

[67] W. Luo, Z. Jin, H. Liu, T. Wang, Thermodynamic assessment of the Au-Ti system, Calphad: Comput. Coupling Phase Diagr. Thermochem. 25 (1) (2001) 19–26, http://dx.doi.org/10.1016/S0364-5916(01)00026-8, URL https://linkinghub.elsevier.com/retrieve/pii/S0364591601000268.

[68] N. Moelans, A quantitative and thermodynamically consistent phase-field interpolation function for multi-phase systems, Acta Mater. 59 (3) (2011) 1077–1086, http://dx.doi.org/10.1016/j.actamat.2010.10.038, URL https://linkinghub.elsevier.com/retrieve/pii/S1359645410007019.

[69] S. Poudel, N. Moelans, R. Thapa, A. Timofiejczuk, D. Panthi, A. Kunwar, Unraveling elastochemical effects in microstructural evolution of Al-Cu-Ni system through DFT-informed multi-phase field simulations, Int. J. Solids Struct. 300 (2024) 112894, http://dx.doi.org/10.1016/j.ijsolstr.2024.112894, URL https://www.sciencedirect.com/science/article/pii/S0020768324002531.

[70] C.N. Singman, Atomic volume and allotropy of the elements, J. Chem. Educ. 61 (2) (1984) 137–142, http://dx.doi.org/10.1021/ED061P137, URL https://pubs.acs.org/doi/abs/10.1021/ed061p137.
[71] W.H. Xiong, W. Liu, M.M. Dai, J.Q. Liu, X.G. Lu, Assessments of molar volumes of Co-, Ni- and Ti- related bcc and fcc phases, Calphad: Comput. Coupling Phase Diagr. Thermochem. 66 (2019) 101629, http://dx.doi.org/10.1016/j.calphad.2019.101629, URL https://linkinghub.elsevier.com/retrieve/pii/S0364591619300896.
[72] A. Kunwar, Y.A. Coutinho, J. Hektor, H. Ma, N. Moelans, Integration of machine learning with phase field method to model the electromigration induced Cu6Sn5 IMC growth at anode side Cu/Sn interface, J. Mater. Sci. Technol. 59 (2020) 203–219, http://dx.doi.org/10.1016/j.jmst.2020.04.046, URL https://linkinghub.elsevier.com/retrieve/pii/S1005030220305156.
[73] A. Kunwar, E. Yousefi, X. Zuo, Y. Sun, D. Seveno, M. Guo, N. Moelans, Multi-phase field simulation of Al3Ni2 intermetallic growth at liquid Al/solid Ni interface using MD computed interfacial energies, Int. J. Mech. Sci. 215 (2022) 106930, http://dx.doi.org/10.1016/j.ijmecsci.2021.106930, URL https://www.sciencedirect.com/science/article/pii/S0020740321006408 https://linkinghub.elsevier.com/retrieve/pii/S0020740321006408.
[74] J. Hektor, M. Ristinmaa, H. Hallberg, S.A. Hall, S. Iyengar, Coupled diffusion-deformation multiphase field model for elastoplastic materials applied to the growth of Cu6Sn5, Acta Mater. 108 (2016) 98–109, http://dx.doi.org/10.1016/j.actamat.2016.02.016, URL https://linkinghub.elsevier.com/retrieve/pii/S1359645416300933.
[75] S. Zhu, T.P. Chen, Z.H. Cen, E.S.M. Goh, S.F. Yu, Y.C. Liu, Y. Liu, Split of surface plasmon resonance of gold nanoparticles on silicon substrate: a study of dielectric functions, Opt. Express 18 (21) (2010) 21926, http://dx.doi.org/10.1364/OE.18.021926, URL https://opg.optica.org/oe/abstract.cfm?uri=oe-18-21-21926.
[76] D. Hwang, S.G. Ryu, N. Misra, H. Jeon, C.P. Grigoropoulos, Nanoscale laser processing and diagnostics, Appl. Phys. A: Mater. Sci. Process. 96 (2009) 289–306, http://dx.doi.org/10.1007/s00339-009-5207-1, URL https://link.springer.com/article/10.1007/s00339-009-5207-1.
[77] A.P. Joglekar, H. hua Liu, E. Meyhöfer, G. Mourou, A.J. Hunt, Optics at critical intensity: Applications to nanomorphing, Proc. Natl. Acad. Sci. 101 (2004) 5856–5861, http://dx.doi.org/10.1073/pnas.0307470101, URL https://www.pnas.org/doi/10.1073/pnas.0307470101.
[78] K. Sugioka, Progress in ultrafast laser processing and future prospects, Nanophotonics 6 (2017) 393–413, http://dx.doi.org/10.1515/nanoph-2016-0004, URL https://www.degruyter.com/document/doi/10.1515/nanoph-2016-0004.
[79] J.W. Peterson, A.D. Lindsay, F. Kong, Overview of the incompressible Navier–Stokes simulation capabilities in the MOOSE framework, Adv. Eng. Softw. 119 (2018) 68–92, http://dx.doi.org/10.1016/j.advengsoft.2018.02.004, URL https://linkinghub.elsevier.com/retrieve/pii/S0965997817310591.
[80] A. Kunwar, L. An, J. Liu, S. Shang, P. Råback, H. Ma, X. Song, A data-driven framework to predict the morphology of interfacial Cu6Sn5 IMC in SAC/Cu system during laser soldering, J. Mater. Sci. Technol. 50 (2020) 115–127, http://dx.doi.org/10.1016/j.jmst.2019.12.036, URL https://linkinghub.elsevier.com/retrieve/pii/S1005030220302279.
[81] J.Y. Huh, K.K. Hong, Y.B. Kim, K.T. Kim, Phase field simulations of intermetallic compound growth during soldering reactions, J. Electron. Mater. 33 (2004) 1161–1170, http://dx.doi.org/10.1007/s11664-004-0118-6, URL https://link.springer.com/article/10.1007/s11664-004-0118-6.
[82] M. Park, S. Gibbons, R. Arróyave, Prediction of processing maps for transient liquid phase diffusion bonding of Cu/Sn/Cu joints in microelectronics packaging, Microelectron. Reliab. 54 (2014) 1401–1411, http://dx.doi.org/10.1016/j.microrel.2014.02.023, URL https://www.sciencedirect.com/science/article/pii/S0026271414000791.
[83] T. Dubberstein, M. Schürmann, H. Chaves, H.P. Heller, C.G. Aneziris, A novel vibrating finger viscometer for high-temperature measurements in liquid metals and alloys, Int. J. Thermophys. 37 (10) (2016) 100, http://dx.doi.org/10.1007/s10765-016-2104-7, URL http://link.springer.com/10.1007/s10765-016-2104-7.
[84] A. Jain, S.P. Ong, G. Hautier, W. Chen, W.D. Richards, S. Dacek, S. Cholia, D. Gunter, D. Skinner, G. Ceder, K.A. Persson, Commentary: The materials project: A materials genome approach to accelerating materials innovation, APL Mater. 1 (1) (2013) http://dx.doi.org/10.1063/1.4812323, URL https://pubs.aip.org/apm/article/1/1/011002/119685/Commentary-The-Materials-Project-A-materials.
[85] R. Powell, R. Tye, The thermal and electrical conductivity of titanium and its alloys, J. Less Common Met. 3 (1961) 226–233, http://dx.doi.org/10.1016/0022-5088(61)90064-9, URL https://www.sciencedirect.com/science/article/abs/pii/0022508861900649.
[86] A. Khvan, I. Uspenskaya, N. Aristova, Q. Chen, G. Trimarchi, N. Konstantinova, A. Dinsdale, Description of the thermodynamic properties of pure gold in the solid and liquid states from 0 K, Calphad 68 (2020) 101724, http://dx.doi.org/10.1016/j.calphad.2019.101724, URL https://linkinghub.elsevier.com/retrieve/pii/S0364591619302858.
[87] M.W. Chase Jr., NIST-JANAF Thermochemical Tables, Monograph 9, fourth ed., Vol. 9, American Chemical Society, Washington DC, 1998, pp. 1–1951, URL http://www.nist.gov/srd/monogr.cfm.
[88] N. Zhao, Y. Zhong, M. Huang, H. Ma, W. Dong, Growth kinetics of Cu6Sn5 intermetallic compound at liquid-solid interfaces in Cu/Sn/Cu interconnects under temperature gradient, Sci. Rep. 5 (2015) 13491, http://dx.doi.org/10.1038/srep13491, URL https://www.nature.com/articles/srep13491.
[89] G.E. Bean, D.B. Witkin, T.D. McLouth, D.N. Patel, R.J. Zaldivar, Effect of laser focus shift on surface quality and density of Inconel 718 parts produced via selective laser melting, Addit. Manuf. 22 (2018) 207–215, http://dx.doi.org/10.1016/j.addma.2018.04.024, URL https://linkinghub.elsevier.com/retrieve/pii/S2214860417303044.
[90] R.R. Mohanty, J.E. Guyer, Y.H. Sohn, Diffusion under temperature gradient: A phase-field model study, J. Appl. Phys. 106 (3) (2009) http://dx.doi.org/10.1063/1.3190607, URL https://pubs.aip.org/aip/jap/article-abstract/106/3/034912/370423.
[91] T.D. Oyedeji, Y. Yang, H. Egger, B.X. Xu, Variational quantitative phase-field modeling of nonisothermal sintering process, Phys. Rev. E 108 (2) (2023) http://dx.doi.org/10.1103/PhysRevE.108.025301, URL https://journals.aps.org/pre/abstract/10.1103/PhysRevE.108.025301.
[92] M. Parsazadeh, S. Sharma, N. Dahotre, Towards the next generation of machine learning models in additive manufacturing: A review of process dependent material evolution, Prog. Mater. Sci. 135 (2023) 101102, http://dx.doi.org/10.1016/j.pmatsci.2023.101102, URL https://www.sciencedirect.com/science/article/pii/S0079642523000348.
[93] R.R. Kamath, H. Choo, K. Fezzaa, S.S. Babu, Estimation of spatio-temporal temperature evolution during laser spot melting using in situ dynamic X-Ray radiography, Met. Mater. Trans. A (2024) http://dx.doi.org/10.1007/s11661-024-07307-w, URL https://link.springer.com/article/10.1007/s11661-024-07307-w.
[94] W. Liu, J. DuPont, Effects of melt-pool geometry on crystal growth and microstructure development in laser surface-melted superalloy single crystals, Acta Mater. 52 (16) (2004) 4833–4847, http://dx.doi.org/10.1016/j.actamat.2004.06.041, URL https://linkinghub.elsevier.com/retrieve/pii/S1359645404003908.
[95] Y. Li, K. Zhou, S.B. Tor, C.K. Chua, K.F. Leong, Heat transfer and phase transition in the selective laser melting process, Int. J. Heat Mass Transfer 108 (2017) 2408–2416, http://dx.doi.org/10.1016/j.ijheatmasstransfer.2017.01.093, URL https://linkinghub.elsevier.com/retrieve/pii/S0017931016330290.
[96] X. Shi, D. Gu, Y. Li, D. Dai, Q. Ge, Y. Sun, H. Chen, Thermal behavior and fluid dynamics within molten pool during laser inside additive manufacturing of 316L stainless steel coating on inner surface of steel tube, Opt. Laser Technol. 138 (2021) 106917, http://dx.doi.org/10.1016/j.optlastec.2021.106917, URL https://linkinghub.elsevier.com/retrieve/pii/S0030399221000050.
[97] N. Provatas, K. Elder, Phase-Field Methods in Materials Science and Engineering, Wiley, 2010, http://dx.doi.org/10.1002/9783527631520, URL https://onlinelibrary.wiley.com/doi/book/10.1002/9783527631520.

ARTICLE V

Spatiotemporally learning the morphological and dynamic features of Au meltpool under different heat source types with phase-field informed U-Net framework

Computational Materials Science 263 (2026) 114456

Contents lists available at ScienceDirect

Computational Materials Science

journal homepage: www.elsevier.com/locate/commatsci

Full length article

Spatiotemporally learning the morphological and dynamic features of Au meltpool under different heat source types with phase-field informed U-Net framework

Upadesh Subedi [a,b,c,*], Aadya Bhattarai [d], Nele Moelans [c], Tomasz Tański [a], Anil Kunwar [b]

[a] Department of Engineering Materials and Biomaterials, Faculty of Mechanical Engineering, Silesian University of Technology, 44-100 Gliwice, Poland
[b] Scientific and Didactic Laboratory of Nanotechnology and Material Technologies, Faculty of Mechanical Engineering, Silesian University of Technology, 44-100 Gliwice, Poland
[c] Department of Materials Engineering, KU Leuven, Kasteelpark Arenberg 44 Bus 2450, 3001 Leuven, Belgium
[d] Department of Industrial and Management Systems Engineering, University of South Florida, Tampa, 33620 FL, United States

ARTICLE INFO

Dataset link: https://github.com/subediupadesh/AMTwinLab, https://github.com/AadyaBhattarai/PhaseVelNet

Keywords:
Moving heat source
Super Gaussian order
FCC Au
MicroTwin
Phase-informed FlowTwin
Conditional automation

ABSTRACT

The uncertainties in the interaction between laser and microstructural interfaces pose a major hindrance to precision engineering in additive manufacturing. Proper assessment of the role of laser heat source types on microstructure evolution and phase transitions is crucial for understanding the process-property relationship of 3D-printed parts. To address this, we present a multiphysics computational study that explores thermal distribution, phase transformation, and meltpool flow across different laser beam profiles and free energy expressions in a unary Au system. A detailed comparison of the microstructural pathways developed under four laser beam shapes (Gaussian, Flat-Top, Ring, and Bessel) was conducted, along with two different mathematical expressions for free energy. Furthermore, a two-stage U-Net architecture was implemented using the simulation data. The initial network predicted phase from temperature inputs, achieving accuracies of 0.9992, 0.9989, and 0.9979 for training, validation and testing sets, respectively. The second stage employed temperature and phase to predict velocity, yielding MSE of 0.068, MAE of 0.079, and R^2 of 0.999 on test data. For user-supplied temperature distribution array, the built primary MicroTwin can predict phase evolution, whereas a secondary FlowTwin informed by MicrosTwin's prediction is capable of estimating velocity selectively inside the liquid meltpool domain.

1. Introduction

The advancement of intelligent manufacturing has transformed conventional process design through the integration of computational modeling, machine learning, and real-time data analysis to achieve adaptive control and quantify uncertainties in complex fabrication processes [1]. In laser-aided Additive Manufacturing (AM), uncertainties in meltpool geometry, area, and morphology directly influence the resulting microstructure and mechanical performance of the fabricated component [2,3]. Addressing these uncertainties requires a detailed understanding of the coupled thermo-physical phenomena governing meltpool evolution under varying processing conditions. Recent progress in multi-physics simulations and data-driven approaches now enables the study of these phenomena across multiple spatio-temporal scales, paving the way for intelligent systems capable of predicting and controlling microstructural evolution in real-time [4]. The integration of unified phase-field modeling within an Integrated Computational Materials Engineering (ICME) framework has proven instrumental in accurately predicting microstructural evolution [5] and optimizing process parameters for high-performance alloys treated by lasers of varying heat source types.

Building, upon this motivation, this study presents a comprehensive computational analysis of how four different laser beam profiles affect the microstructure evolution in a unary Au-system during laser processing. Using Phase-Field (PF) simulations, we traced the meltpool geometry, its area, and the thermal history within the computational domain. A quantitative comparison between two different free energy

* Corresponding author at: Department of Engineering Materials and Biomaterials, Faculty of Mechanical Engineering, Silesian University of Technology, 44-100 Gliwice, Poland.
E-mail address: upadesh.subedi@polsl.pl (U. Subedi).
URLs: https://www.linkedin.com/in/upadesh-s-0b321a15b/, https://www.researchgate.net/profile/Upadesh-Subedi (U. Subedi).

https://doi.org/10.1016/j.commatsci.2025.114456
Received 27 October 2025; Received in revised form 13 December 2025; Accepted 15 December 2025
Available online 31 December 2025
0927-0256/© 2025 Elsevier B.V. All rights are reserved, including those for text and data mining, AI training, and similar technologies.

expressions driving the phase transition was also carried out. The first approach used a logarithmic-polynomial free energy function fitted to thermodynamic data (fine-tuned expression), while the second relied on case equations extracted directly from a Thermodynamic Database (TDB) file using a Python script. Comparisons of free energy expressions in phase-field modeling are rare, as exact thermodynamic expressions are difficult to obtain, leading most studies to rely on polynomial fits [6]. Moreover, many such studies are often limited to free energy expressions defined at two fixed temperatures for two phases [7]. In this work, we have integrated thermodynamic expressions for free energies as a function of temperature, making the phase transition process inherently non-isothermal. Our study employs the MOOSE Framework as the multi-physics simulation environment [8,9], where three coupled physical phenomenons are solved: heat-transfer, phase-field and fluid-flow, using Finite Element Method (FEM).

As described in our previous work [10], most computational studies of laser processing treats thermal and phase diffusion as identical. This assumption leads to the presumption that the LIQUID phase (meltpool) forms instantaneously upon reaching melting temperature, overlooking the real physical behavior in laser-based additive manufacturing where phase diffusion lags behind the thermal diffusion front [11]. In this study, we found that implementing the TDB-based free energy expression replicates the real-world behavior of the lead-lag dynamics between phase and thermal fronts. The main reason this distinction is often overlooked in contemporary research is likely computational cost and efficiency. However, ignoring it fails to capture the intricate interplay between the two diffusion fronts, which in turn influences other physical phenomena such as fluid flow, thermal conductivities, and phase densities. In addition to phase-field modeling, the FEM simulations generated data were used to train machine learning models capable of predicting the LIQUID phase, its shape, areas, and its velocity, using the temperature distribution of the domain as input.

This approach provides a foundation for realizing the conditional automation in additive manufacturing. Conditional automation refers to systems that adaptively control manufacturing processes based on real-time sensor inputs or evolving process conditions. Unlike fixed-sequence automation, these systems respond dynamically to parameters such as temperature, meltpool shape, or phase evolution, improving precision and consistency through live feedback control algorithms. Phase-field simulations and U-Net based architectures form the core building blocks for achieving such adaptive, data-driven process control conditional automation of additive manufacturing [12,13].

In the following section, we discuss in detail, the types of laser heat sources, the expressions for thermodynamic driving forces, temperature-dependent material properties, and machine learning architectures. We also outline the conceptualization of physics informed virtual digital-twin for laser processing using the trained ML model. Finally, in the Results and Discussion (Section 8), we explore the effects on phase evolution, temperature distribution, and meltpool flow characteristics under different laser heat sources, and distinct free-energy expressions. For comparison of the laser beam profiles, the laser power (P), scan speed (v), and beam outer radius (r_x) were kept constant across all simulations.

2. Initial and boundary conditions

Simulations were carried out in a computational domain of 1000 μm × 250 μm in the x–z plane, as shown in Fig. 1. The system consists of two phases: LIQUID representing molten gold, and FCC representing solid gold. At the initial time (t_0), a laser beam with power of 25 mW was irradiated on the top surface at a distance of 125 μm from the left, with a scan speed of 30 μm/s. The initial area of meltpool was designed to be 2500 μm^2. The computational domain is surrounded by an ambient environment at a temperature T_{air} = 300 K on three sides (left, right, and top), while the bottom rests on an interface with a heat transfer coefficient h_{int} = 11,500 W/m^2K [14]. The convective heat transfer coefficient of the surrounding air is taken as h_{amb} = 50 W/m^2K [15], while the emissivity for radiative heat transfer is set to 0.3 [16]. Similarly the meltpool velocity field is initialized to zero everywhere ($\vec{u}_{t_0} = \vec{0}$), reflecting a quiescent state prior to laser irradiation. The initial LIQUID phase starts at uniform temperature, inducing no initial gradients. Once the laser heat deposition (Q_{laser}) starts, it rapidly generates ∇T, which via temperature-dependent properties, triggers buoyancy and dominant Marangoni convection and the FEM solver evolves $\vec{u}$ self-consistently from this rest state, capturing ramp-up transients without spurious artifacts. To accurately assign the material properties of different phases, including densities, specific heat capacities, thermal conductivities, and meltpool viscosity, under non-isothermal conditions, these properties were defined as the function of temperature. The detailed formulations are provided in Section 6.

3. Non-isothermal phase field model

The phase field model consists of two phases: LIQUID (meltpool) and FCC (solid), which are represented by the non-conserved order parameter 'η' and '1 - η' respectively. The value of 'η' is set to 1 inside the LIQUID phase and 0 at the FCC phase. The conserved variable 'composition' remains constant throughout the domain as this work follows the evolution of phases in a single-component system. Thus, this study focuses on the two phases and their transformation induced by laser heat deposition. For this setup, a swift transition of material properties between phases with thermodynamic consistency is required which is achieved using the interpolation function $h_i(\eta)$ introduced by Moelans [17], as presented in Eq. (1).

$$h_i = \frac{\eta_i^2}{\sum_{k=1}^{N} \eta_k^2} \tag{1}$$

In the above equation, N and i represents total number of order parameters and specific phase in the system. The interpolation function h_i ensures a thermodynamically consistent transition in the mushy zone, where intermediate values of η ($0 < \eta < 1$) correspond to mixed solid-liquid regions with phase fractions h_{FCC} and h_{LIQUID}, facilitating smooth property blending without unphysical discontinuities. This diffuse interface representation, with an effective mushy zone thickness on the order of δ = 10 μm, aligns with experimental observations of solidification microstructures in alloys [18]. The driving force dictating the morphological changes of microstructure in the domain is the total free energy of the system. With an external heat source, the total free energy (F_{total}) can be modeled as the combination of bulk free energy (F_{bulk}) and interfacial free energy (F_{int}), as given by Eq. (2).

$$F_{total} = F_{bulk} + F_{int} = \int_V (f_{bulk} + f_{int}) dV \tag{2}$$

here, the bulk and interfacial energies are expressed in terms of free energy densities (energy per unit molar volume of Au). The bulk free energy density (f_{bulk}) is expressed in Eq. (3).

$$f_{bulk} = \sum_i h_i f_{bulk}^i = \sum_i h_i \frac{F_i(T)}{V_m} \tag{3}$$

In Eq. (3), h_i represents the interpolation function, whereas f_{bulk}^i denotes the bulk free energy density of the i^{th} phase. V_m is the molar volume of gold, with a value of 10.21 cm^3/mol [19], taken for both phases. Additionally, $F_i(T)$ represents the temperature-dependent Gibbs free energy of phase 'i'. The correct formulation of the Gibbs free energy is necessary for accurate description of the phase and meltpool evolution during laser processing of metallic microstructures. In Section 4, two variants of bulk free energy expressions: TDB-based ($F_{bulk} = F_\psi$) and fine-tuned ($F_{bulk} = F_\theta$) are formulated, for assessment of the quantitative aspects of the driving force in the evolution model. The latent heat (L_f) representing the enthalpy absorbed/released during the solid-liquid phase change [20] is thermodynamically encoded in the free energy expressions via the entropy discontinuity $\Delta S = L_f/T_m$ at melting. The expression for L_f, can be postprocessed in the phase

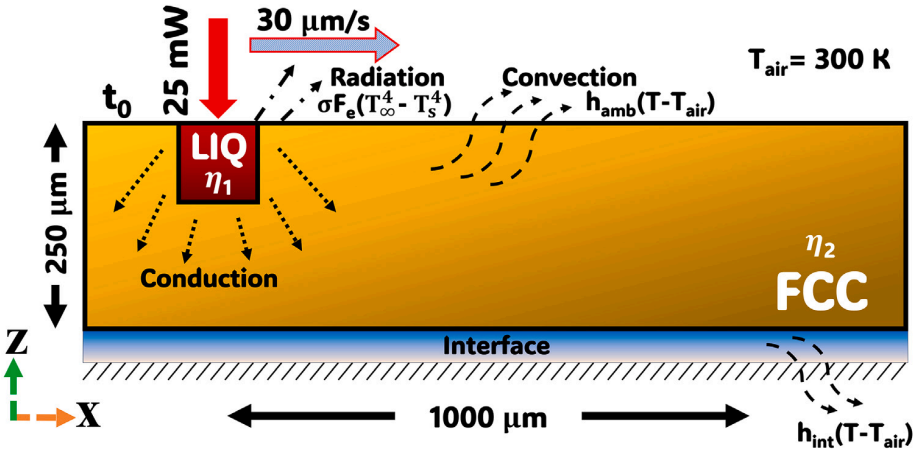


Fig. 1. Schematic of the computational domain setup showing laser-induced phase evolution in the Phase-Field Model at time t_0. The domain represents a 1000 µm × 250 µm section of a unary Au system in the x–z plane. The system rests on a fixed interface at the bottom, with ambient air on the remaining three sides. Heat enters the domain by conduction and exists through radiation and convection at the air and interface boundaries. A laser heat source of 25 mW irradiates the top surface positioned 125 µm from the top-left corner, moving at a scan speed of 30 µm/s (indicated by the red arrow above the LIQUID phase). The initial LIQUID phase region (η_1, 2500 µm^2) represents the meltpool shown in red, while the remaining solid region is the FCC phase (η_2 shown in yellow). The same computational setup, phase structure, and processing parameters (laser power and scanspeed) are maintained across all the simulations with different beam profiles.

field model as: $L_f = \frac{d\Delta F}{dT} T_m$, where ΔF is difference in gibbs free energy of FCC and LIQUID phases at the vicinity of the melting point and is provided in Fig. A.1 of Appendix A. A steeper $|d\Delta F/dT|$ implies a sharper ramp-up of $|\Delta F|$ above T_m, confining the effective transition to a narrow temperature window. In the phase-field model, L_f is thus implicitly incorporated through the temperature-dependent bulk free energy density $f_{\text{bulk}} = \sum_i h_i F_i(T)/V_m$ (Eq. (3)), which drives the order parameter evolution and ensures the integrated driving force over the full phase transition equals L_f per mole.

Similarly, the interfacial free energy density (f_{int}) in Eq. (2) is further expressed in Eq. (4).

$$f_{int} = m f_{barrier} + \frac{\kappa}{2} \sum_i (\nabla \eta_i)^2 \tag{4}$$

where, m and κ are the model parameters associated with interfacial energy (σ [J/m^2]) and diffused interface width (δ [m]) as follows:

$$m = \frac{6\sigma}{\delta} \tag{5}$$

$$\kappa = \frac{3}{4}\delta\sigma \tag{6}$$

In this study, we have set the value of the interface width δ to be 10 µm and the interfacial energy to 0.5 J/m^2. The term $f_{barrier}$ in Eq. (4) is a fourth-order Landau polynomial of the phase field variable, as expressed in Eq. (7) with the value of γ taken as 1.5 [21].

$$f_{barrier} = \sum_i \left(\frac{(\eta_i)^4}{4} - \frac{(\eta_i)^2}{2} \right) + \gamma \sum_i \sum_{j \neq i} \eta_i^2 \eta_j^2 + \frac{1}{4} \tag{7}$$

During laser processing, the spatio-temporal tracking of non-conserved phase field variable i.e., the order parameter (η), provides an accurate description of phase transformation. Eq. (8) describes such evolution of this variable as:

$$\frac{\partial \eta_i}{\partial t} = -L(\eta_1, \ldots, \eta_N) \left(\frac{\partial f_{bulk}}{\partial \eta_i} - \nabla \cdot \frac{\partial f_{int}}{\partial \nabla \eta_i} \right) \tag{8}$$

where, $L(\eta_1, \ldots, \eta_N) = L^i$ which is defined as follows:

$$L^i = \frac{\sum_{i=1}^{N} \sum_{j>1}^{N} L_{ij} \eta_i^2 \eta_j^2}{\sum_{i=1}^{N} \sum_{j>1}^{N} \eta_i^2 \eta_j^2} \tag{9}$$

The interfacial mobility in Eq. (9) is further approximated as follows:

$$L_{ij} = \frac{4m}{3\kappa} \times \frac{M^i + M^j}{2} \tag{10}$$

here, M^i and M^j are the phase mobilities of the two adjacent phases. Similarly, for the heat deposited by the laser source, heat transfer follows the partial differential equation presented in Eq. (11).

$$\rho^i C p^i \left(\frac{\partial T}{\partial t} + \vec{u} \cdot \nabla T \right) = k_{th}^i \nabla^2 T + Q_{laser} \tag{11}$$

In the above equation, temperature is denoted by T at time t. The density, specific heat capacity, and thermal conductivity of phase 'i' are represented by ρ^i, Cp^i, and k_{th}^i, respectively while the external laser heat source is denoted by Q_{laser}. The flow velocity inside the meltpool is given by $\vec{u}$ solved via Navier–Stokes Eq. (12) [22] assuming the flow as incompressible, which contributes to convective heat transfer. The viscosity, surface tension, and associated Marangoni effect inside the inside meltpool flow is further discussed in Section 6.

$$\begin{gathered} \nabla \cdot \vec{u} = 0 \\ \rho^{LIQ} \left[\frac{\partial \vec{u}}{\partial t} + (\vec{u} \cdot \nabla) \vec{u} \right] + \nabla \cdot \sigma - \vec{f} = 0 \\ \sigma = -p\boldsymbol{I} + \mu \left[\nabla \vec{u} + (\nabla \vec{u})^T \right] \end{gathered} \tag{12}$$

where, σ is total stress tensor, f includes the Boussinesq and gravity force terms, and μ is the dynamic viscosity.

4. Thermodynamic driving force formulations for heat-treated metallic gold

For computational efficiency and faster numerical convergence, polynomial expressions of free energy are often preferred, especially parabolic expressions of second-order polynomials, which are widely used for modeling binary and ternary alloy systems [23–25]. Although, polynomial expressions with n> 2 generally offer more accurate descriptions, they are computationally expensive due to the compositional complexities they introduce into the diffusion equations. In this study on laser processing of pure element, the free energy depends solely on temperature (T), with constant composition and pressure. This condition allows for the flexibility to expand the polynomial expression beyond traditional parabolic forms to include logarithmic terms.

Table 1
Coefficients of thermodynamic constants for the Free energy expressions.

Coeff.	LIQUID	FCC	Unit	Coeff.	LIQUID	Unit	FCC	Unit
A_θ	1337	300	J/mol	A_ψ	24.9435	J/mol K	24.9435	J/mol K
B_θ	24 474	515	J/mol	B_ψ	126.6874	K	126.6874	K
C_θ	16.2	−46.2	J/mol K	C_ψ	−0.12027		6103.6566	J/mol
D_θ	24.5	−13.5	J/mol K	D_ψ	19 700	K	−0.001281	J/mol K^2
E_θ	0.00214	0.1985	1/K	E_ψ	14.917		-4.02×10^{-7}	J/mol K^3
F_θ	0.04512	−0.001	J/mol K^2	F_ψ	0.00067	J/mol K^2	1.55×10^{36}	JK^{11}/mol
G_θ	1.9×10^{-5}	2.0×10^{-5}	J/mol K^3	G_ψ	326.3861	J/mol	-2.27×10^{18}	JK^5/mol
H_θ	−17.4	−0.001	JK/mol	H_ψ			−2.0566	J/mol K
T_0	2662	121	K	I_ψ			9.8072	J/mol K
T_{th}	10.412	9.03		J_ψ			3898.778	J/mol

Accordingly, the free energy for pure Au under temperature change is best described by the fine-tuned expression (F_θ), as presented in Eq. (13), derived in a manner similarly to [26,27]. Similarly, the TDB-extracted expressions (F_ψ) are piecewise continuous as presented in Eq. (13). These expressions are based on Thermodynamic Data Base file formulated by Khvan et al. [28]. In Eq. (13), the coefficients A, B, C, D, E, F, G, H, I, J and T_{th}, with subscripts 'θ' and 'ψ', represent the thermodynamic coefficients of the free energy function for the fine-tuned and TDB-based expressions, respectively. The coefficient values are listed in Table 1 for both the LIQUID and FCC phases. The variable 'T' depicts the temperature dependence of the free energy in both expressions.

$$F_\theta = T_{th}\Big[A_\theta - B_\theta - C_\theta(T-T_0) + D_\theta(T-T_0)\ln(E_\theta T) + F_\theta(T-T_0)^2 + G_\theta(T-T_0)^3 + H_\theta T^{-1}\Big]$$

$$F_\psi = \begin{cases} LIQUID & : A_\psi T\ln\left[1-\exp(-B_\psi T^{-1})\right] - RT\ln\left[1+\exp\left(C_\psi(D_\psi - E_\psi T)T^{-1}\right)\right] - F_\psi T^2 - G_\psi \\ FCC & : A_\psi T\ln\left(1-\exp(-B_\psi T^{-1})\right) - C_\psi + \begin{cases} T<1337.33 & : D_\psi T^2 - E_\psi T^3 \\ T>=1337.33 & : F_\psi T^{-11} - G_\psi T^{-5} \end{cases} - H_\psi T\ln(T) + I_\psi T + J_\psi \end{cases} \quad (13)$$

The two free-energy formulations were combined with four different laser beam profiles to analyze their effects on phase growth, while keeping other laser parameters constant. The plots for free energy expressions of Eq. (13) are presented in Fig. 2**(a)** and **(b)**. As shown in Fig. 2, the F_θ curves for the FCC and LIQUID phases display a distinct phase-change interval, while the F_ψ curves derived from the TDB expressions do not exhibit this feature.

A sharp or narrow phase-change interval, such as in pure metals, causes rapid phase transition during melting and solidification. This can result in residual stresses [29,30], and may complicate numerical convergence [31]. In contrast, when modeling compositionally-complex alloys, a broader phase-change interval can play an important role in ensuring stability and convergence. Thus, a fine-tuned (fitted) free energy function can be effectively applied to multicomponent system, even with only limited energy-temperature thermodynamic data are available. On the other hand, when a thermodynamic database (.TDB) file is available, free energy expressions can be extracted directly and implemented into a FEM solver using a simple Python script, thereby formulating the required temperature-dependent expressions. This direct TDB-based approach not only ensures thermodynamic consistency but also enhances the accuracy. As observed in Fig. 2**(b)**, the near absence of a phase-change interval implies a very narrow temporal range over which multiple phases co-exist. This leads to rapid interpolation of material and phase-dependent properties, thereby improving the numerical stability of the model.

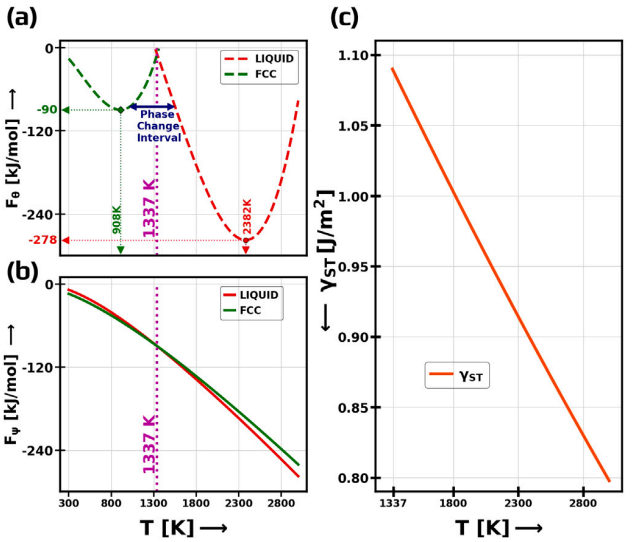


Fig. 2. Graphical representation of the two free energy expressions used for phase-field simulations of laser-processed unary Au. In **(a)**, the free energy curves are based on a higher-order polynomial-logarithmic function obtained from thermodynamic data fitting, referred to as the fine-tuned expression (F_θ, Eq. (13)). The dashed green and red curves corresponds to the FCC and LIQUID phases, respectively. Below the melting temperature (1337 K), the FCC phase is more stable, while above 1337 K, the LIQUID phase becomes stable. In **(b)**, the free energy expression extracted directly from the *.TDB* file, referred to as the TDB-based expression (F_ψ, Eq. (13)), is shown. Similar to **(a)**, the red curve represents the LIQUID phase and the green curve the FCC phase, but here the two curves interset at 1337 K without a distinct phase change interval. The presence or absence of this interval in **(a)** and **(b)** governs how thermal history influences structural evolution, leading to distinct simulation outcomes. **(c)** Variation of surface tension in the meltpool induced by the dynamic heat source, leading to thermo-capillary convection.

5. Laser beam heat source models

The Gaussian laser beam is the most widely used profile for modeling laser-based melting and solidification in additive manufacturing, owing to its simple mathematical form. The beam peaks intensity at the center and decays outwards exponentially, creating steep thermal gradients that influences microstructure evolution [32–34]. However, uniform heating is often desired in practice to reduce thermal gradients, motivating alternative beam profiles such as the Flat-Top beam, which truncates the Gaussian peak to produce a uniform intensity region, and the Ring-shaped beam, which distributes heat in an annular pattern with maximum intensity at a specific radius [35]. The Bessel beam combines both characteristics, featuring a Gaussian-like center surrounded by concentric rings defined by the zeroth-order Bessel function [36]. Experimental studies confirm that beam shape strongly affects meltpool

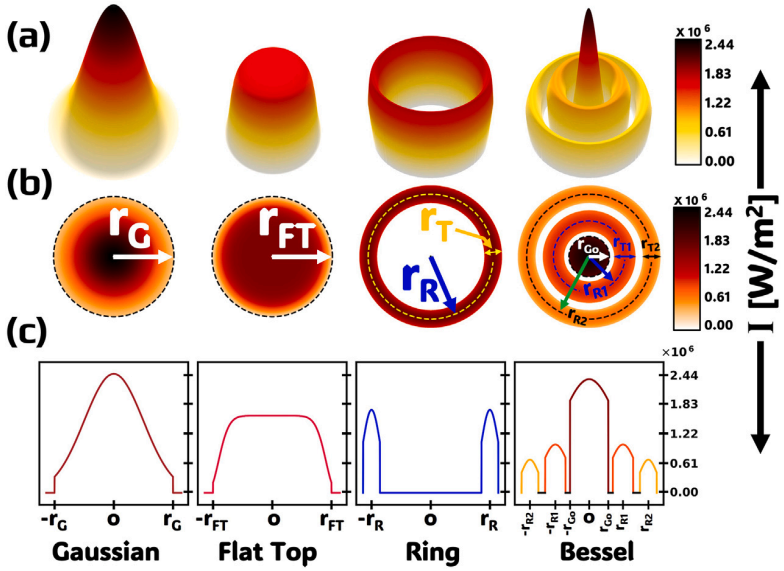


Fig. 3. Visualization of four laser beam profiles- Gaussian, Flat-Top, Ring, and Bessel, used for laser-aided phase-field simulations of unary Au. **(a)** 3D intensity maps of the four beam types, each with an equivalent outer radius of 70 μm. The peak intensities at the beam center are 2.44×10^6 W/m^2 for Gaussian, 1.58×10^6 W/m^2 for Flat-Top, 1.70×10^6 W/m^2 for Ring, and 2.33×10^6 W/m^2 for Bessel beam, as shown by the color scale. **(b)** Top-view intensity distributions for the same beams, where r_G and r_{FT} denotes the Gaussian and Flat-Top beam radii, respectively, and r_R and r_T indicates the Ring beam radius and thickness. For the Bessel beam with a central core and two outer rings, the core radius is r_{G_0}, while the outer rings have radii r_{R_1} and r_{R_2} with respective thickness r_{T_1} and r_{T_2}. **(c)** Side-view irradiance profile showing the variation of intensity with radial distance, where the y-axis represents irradiance and the x-axis represents the distance from the beam center.

geometry and microstructure: Galbusera et al. [37] showed that varying beam shape alters meltpool aspect ratio and depth, while Wischeropp et al. [38] found that donut-shaped beams reduce defects in AlSi10Mg. Tumkur et al. [39] further demonstrated that Bessel beam improve control over meltpool dynamics, lowering porosity and keyhole defects. These findings highlight the critical role of beam profile in determining microstructural and mechanical properties, underscoring the value of computational modeling for deeper insights into phase transformation, heat flow and defect prediction, areas difficult to probe experimentally. In this work, we compare four laser beam profiles: Gaussian, Flat-Top, Ring and Bessel, under identical process parameters in laser-aided phase-field simulations of a pure Au system. The effects on meltpool shape, area, flow and temperature distribution are analyzed, revealing a lead-lag dynamic between heat and mass diffusion fronts.

5.1. Gaussian beam

Among the four heat source types, the Gaussian beam serves as the reference case due to its simple formulation and well-understood thermal behavior [40–42]. It produces maximum irradiance at the center, decaying radially to form the characteristic Gaussian distribution. The irradiance (I_G) is defined in Eq. (14) [36,43], where r_G denotes the effective beam radius corresponding to $\frac{1}{e^2}$ of the peak intensity, P is the laser power, η_e is efficiency of laser power to heat conversion, and C_a and C_b are constants whose values are listed in Table 2. A representative Gaussian heat source is illustrated in Fig. 3 with a 3D and cross-sectional view.

$$I_G = \frac{P}{\pi r_G^2} C_a \eta_e \exp\left[-C_b\left(\frac{r^2}{r_G^2}\right)\right] \tag{14}$$

5.2. Flat-Top | Super Gaussian beam

The Flat-Top or Super-Gaussian beam provides a near-uniform intensity across its radius with a sharp drop at the edges, enabling more homogeneous heating of the material [43,44]. Its irradiance (I_{FT}) is defined in Eq. (15) [36,43,45,46], where r_{FT} is the effective beam radius. All other processing parameters P, η_e, C_a and C_b are kept identical for all four laser profiles, while the additional parameters k and $\Gamma(1/k)$ represents the super-Gaussian order ()set to 4.2 in this study) and gamma function respectively [36]. The Flat-Top beam profile is illustrated in the second column of Fig. 3, with 3D, top and side views.

$$I_{FT} = \frac{P}{\pi r_{FT}^2} \frac{k}{\Gamma(1/k)} C_a^{1/k} \eta_e \exp\left[-C_b\left(\frac{r^2}{r_{FT}^2}\right)^k\right] \tag{15}$$

5.3. Ring beam

The Ring laser beam features a hollow circular profile with maximum intensity along its circumference and minimal intensity at the center. This configuration promotes outward-to-inward heat flow, helping achieve more uniform temperature distribution and reduced thermal defects [47,48]. The beam introduces one additional process parameter, the ring width, which controls the energy spread across the domain [49,50]. The irradiance (I_R) for the ring beam is defined in Eq. (16) [34,35,51,52]. All parameters (P, η_e, C_a, C_b) are identical to those used in Gaussian and Flat-Top sources, while r_R and r_T represents the ring radius and ring thickness respectively.

$$I_R = \frac{P}{\pi r_T^2 Y(r_R, r_T)} C_a \eta_e \exp\left[-C_b\left(\frac{(r - r_R)^2}{r_T^2}\right)\right] \tag{16}$$

The radial distribution function $Y(r_R, r_T)$, as described by Moore et al. [34], accounts for the combined influence of ring radius and thickness through an exponential decay and complementary error function expressed as:

$$Y(r_R, r_T) = \exp\left(\frac{-r_R^2}{2r_T^2}\right) + \frac{r_R}{r_T}\sqrt{\frac{\pi}{2}}\,\mathrm{erfc}\left(\frac{-r_R}{\sqrt{2}r_T}\right)$$

A visual representation of the ring beam is shown in the third column of Fig. 3, including 3D, top and side views in **(a)**, **(b)** and **(c)** respectively.

Table 2
Laser processing parameters.

Coeff.	Gaussian	Flat-Top	Ring	Bessel	Unit
P	25	25	25	25	mW
C_a	2	2	2	2	
C_b	2	2	2	2	
η_e	0.75	0.75	0.75	0.75	
r_G	70	–	–	–	μm
r_{FT}	–	70	–	–	μm
k	–	4.2	–	–	
r_R	–	–	70	–	μm
r_T	–	–	20	–	μm
r_{G_0}	–	–	–	22.65	μm
r_{R_1}	–	–	–	40	μm
r_{T_1}	–	–	–	30	μm
r_{R_2}	–	–	–	70	μm
r_{T_2}	–	–	–	20	μm
a_0	–	–	–	0.1	
a_1	–	–	–	0.5	
a_2	–	–	–	0.4	

5.4. Bessel beam

The Bessel beam consists of a central core surrounded by concentric ring beams, with irradiance gradually decreasing radially outward. In this study, a central Gaussian-type beam with two concentric rings are considered, where each radius corresponds to the zeros of the zeroth-order Bessel function. While some studies define the core radius as the point where irradiance drops to $\frac{1}{e^2}$ of its peak [53], here it is taken at the first zero of the Bessel function, with the subsequent rings located at the second and third zeros. To ensure comparable processing conditions across all beam types, the laser power is divide among the three components of the Bessel beam using attenuation coefficients a_0, a_1, and a_2 which satisfy as $a_0 + a_1 + a_2 = 1$. The irradiance (I_B) is expressed in Eq. (17) [36,53]. Parameters P, η_e, C_a, and C_b are identical to other three beams. The core radius and the two ring radii are denoted by r_{G_0}, r_{R_1}, and r_{R_2}, with corresponding ring thickness r_{T_1}, and r_{T_2}. Numerical values of these parameters are listed in Table 2. The visual representation of the Bessel beam is provided in the fourth column of Fig. 3, showing its 3D, top and transverse profiles in **(a)**, **(b)**, and **(c)**, respectively.

$$\begin{aligned} I_B = & \frac{C_a a_0 P\alpha}{\pi r_{G_0}^2} \exp\left[-C_b\left(\frac{r^2}{r_{G_0}^2}\right)\right] \\ & + \frac{C_a a_1 P\alpha}{\pi r_{T_1}^2 Y(r_{R_1}, r_{T_1})} \exp\left[-C_b\left(\frac{(r-r_{R_1})^2}{r_{T_1}^2}\right)\right] \\ & + \frac{C_a a_2 P\alpha}{\pi r_{T_2}^2 Y(r_{R_2}, r_{T_2})} \exp\left[-C_b\left(\frac{(r-r_{R_2})^2}{r_{T_2}^2}\right)\right] \end{aligned} \tag{17}$$

6. Material properties

In laser-induced phase-field simulations, the material properties of each phase play a critical role in determining phase evolution and microstructural development. Parameters such as phase mobility, thermal conductivity, density, and specific heat capacity directly influence the kinetics of phase transformation. Since these properties vary with temperature, assigning constant values in a non-isothermal laser processing model can lead to significant inaccuracies. In this work, temperature-dependent thermodynamic expressions are used to define the properties of a unary Au system. The material parameters are specified for the two phases, LIQUID and FCC, and interpolated between them using the function described in Eq. (1). Table 3 lists the temperature-dependent expressions for density (ρ), specific heat (C_p), thermal conductivity (k_{th}), and phase mobility (M). Thermal conductivities of both phases are assumed isotropic. The free energy, which acts as the driving force for phase transformation, depends solely on temperature for this unary system as expressed in Eq. (13). To represent the diffuse interface between solid and liquid regions, a mushy zone is introduced. The temperature-dependent viscosity of the LIQUID phase (μ_{LIQ}) and the adjusted viscosity of this interface region μ_{adj} are both defined in Eq. (18) [56].

$$\begin{aligned} \mu_{LIQ} &= \exp\left(-0.1990 + \frac{2669}{T}\right) \\ \mu_{adj} &= 10 \times \mu_{LIQ} \times [h_{LIQ} \times (1 - h_{LIQ})] \end{aligned} \tag{18}$$

The adjustment factor [h_{LIQ} × (1 - h_{LIQ})] peaks at $\eta = 0.5$, representing a 50% solid-liquid mushy zone, which enhances numerical stability and captures viscous damping in the diffuse interface. This formulation is consistent with phase-field models for alloy solidification, where such interpolations reproduce experimental morphologies and mushy zone thicknesses [18]. Additionally, temperature-dependent surface tension at the meltpool surface gives rise to the Thermo-Capillary Convection (Marangoni effect). The governing relation is presented in Eq. (19), following Cairncross et al. [57], where H is the mean surface curvature, σ_{LIQ} the Cauchy stress tensor for the LIQUID phase at the free surface, γ_{ST} the surface tension, and $\nabla_s = (I - \vec{n}\vec{n}).\nabla$ is the surface gradient operator representing the Marangoni effect. This expression is implemented as a boundary condition in the MOOSE Framework. The second part of Eq. (19) defines the temperature-dependent surface tension of gold given by Aqra et al. [58] also visualized in Fig. 2, where ϕ denotes the area occupied by a single atom (7.74×10^{-16} cm^2/atom), k is the Boltzmann constant, V_{melt} is the molar volume of gold at its melting temperature, and $V(T) = M_{mol}/\rho(T)$ represents the temperature-dependent molar volume, with M_{mol} being the molar weight. E_s denotes the sublimation energy (368 kJ/mol).

$$\begin{aligned} \vec{n}.\sigma_{LIQ} &= -2H\gamma_{ST}\vec{n} - \nabla_s\gamma_{ST} \\ \gamma_{ST} &= \phi^{-1}\left(\frac{V_{melt}}{V(T)}\right)^2 kT\left[0.139\frac{E_s}{RT} - 0.053\right] \end{aligned} \tag{19}$$

7. Machine learning and digital twin

The integration of experiments with mathematical models in real time has enabled advanced process control in various industries [59]. For additive manufacturing, this creates a need for computational models that can operate alongside experiments, providing process-property insights at a comparable speed. Phase-field FEM simulation remains one of the most robust methods for predicting mesoscale microstructure evolution and phase transitions. When coupled with multiphysics modules such as heat transfer and fluid flow, the model can capture the dynamic behavior of material characteristics, including the influence of temperature and phase on grain growth, meltpool flow velocity, and thermal-phase diffusion. However, despite the high physical fidelity of phase-field simulations, their computational cost and time requirements make real-time prediction and digital twin implementation impractical. Relying solely on FEM calculations for real-time phase prediction or closed-loop feedback in additive manufacturing is currently unrealistic due to the immense computational demand. A more practical approach lies at the intersection of predictive accuracy and computational efficiency, using a machine learning model trained on simulation-generated data to drive Digital Twin applications.

This work outlines a framework for constructing a Digital Twin framework. It demonstrates a conceptual model capable of monitoring experimental setups and tracking variables in real time, including meltpool geometry, its area, phase transformations, flow velocity and the interaction between thermal and phase diffusion. With surface temperature data, such as from an infrared thermal camera as input, the trained ML model can predict meltpool area, solid-liquid phase distribution, and internal flow velocity. To illustrate the concept, we developed a virtual Digital Twin prototype capable of running on a *Raspberry Pi*. The system processes a temperature distribution (in *numpy* tensor format) as input to the ML model. For this virtual setup,

Table 3
Temperature dependent material properties of individual phases.

Properties	Unit	Phase	Expression	Reference
Density (ρ)	kg/m^3	LIQUID	$19325.28 - 1.44T$	[54]
		FCC	$19657.60 - 1.20T$	[54]
Specific Heat (Cp)	J/kg K	LIQUID	$158 + 5.08 \times 10^7 \exp(-0.0114T)$	[55]
		FCC	$132 + 2.5 \times 10^{-5}T^2 - 0.011T$	[55]
Thermal Conductivity (k_{th})	W/m K	LIQUID	$100 + 0.027397T$	[54]
		FCC	$338.91 - 0.0693T$	[54]
Phase Mobility (M)	m^5/Js	LIQUID	$2.90 \times 10^{-15} \exp\left(\frac{-3043}{8.31T}\right)$	[10]
		FCC	$4.88 \times 10^{-21} \exp\left(\frac{-2221}{8.31T}\right)$	[10]

Table 4
Model hyperparameters.

Hyperparameter	PhaseNet	VelNet
Batch Size	16	16
Learning Rate	1×10^{-3}	1×10^{-3}
Number of Epochs	200	200
Input Channels	1	2
Output Channels	1	1
Loss Function	BCEWithLogitsLoss	MSE
Optimizer	Adam	Adam
Test Split	15%	15%
Validation Split	15%	15%

the temperature data is generated from a separate laser simulation without phase-field and fluid-flow physics. The trained ML model then predicts the corresponding phase microstructure, meltpool region, and flow velocity field. The outputs, input temperature, predicted phases, area data, and velocity fields are displayed through an interactive web application. A quantitative comparison of the computational cost of FEM-based phase-field simulations versus ML inference, together with the ML training details, is provided in the Appendix D.1 to clarify the efficiency gains relevant for real-time deployment. The web app is designed for easy updates and future expansion to multiple alloy systems by simply retraining the ML model as more simulation data becomes available. This modular approach allows rapid adaptation of the Digital Twin to different materials and processing condition. Future work will extend the model's training dataset to include laser processing of multi-component alloys at various scales and laser parameters (power and scan-speed), advancing towards a comprehensive multi-material Digital Twin for Additive Manufacturing.

7.1. Training data and model architecture

In this study, data were generated from multiple FEM simulations by varying both the laser beam profile and the free energy expression. From eight distinct phase-field laser simulations, described in Sections 4 and 5, a total of 3220 observations of the temperature distribution and corresponding phase evolution, as well as the meltpool phase's velocity, were extracted from the exodus file produced by the FEM solver. These data were converted into a three-dimensional data tensor with dimensions *(x-coordinate, y-coordinate, time)*, containing numerical values of temperature, phase, and velocity at each spatial and temporal point. Two U-Net architecture based machine learning models were developed: '**PhaseNet**' for predicting the phase and its corresponding meltpool area, and '**VelNet**' for predicting flow velocity within the meltpool. The hyperparameters used in each of these models are tabulated in Table 4. Both PhaseNet and VelNet were trained using datasets generated from simulations under all four laser heat source types (Gaussian, Flat-Top, Ring, and Bessel). This design ensures that the models are generalizable and applicable to any of the laser heating conditions studied.

7.1.1. PhaseNet model: Meltpool morphology

The first model was developed to predict the phase distribution based on the temperature, and **so it can be considered as the architecture required to set up digital twin (MicroTwin) for quantifying 3D printed microstructure in real time** . The architecture of MicroTwin is represented by the portion within the red colored box (PhaseNet) in Fig. 4. This stage aims to identify the solid and meltpool regions at each spatial point as the temperature evolves during the process. Given that the simulation data are represented in a 2D grid structure similar to images and phase classification is binary (0 or 1), the U-Net's superior performance in image segmentation tasks makes it an appropriate choice for this application. The model takes a single-channel temperature grid as an input, and the output is a single-channel phase grid. The architecture of the model is represented in Fig. 4 within PhaseNet block. The architecture comprises of series of encoders and decoders with a bottleneck in between. The encoder pathway has three downsampling stages, each consisting of a 3×3 convolutional layer with batch normalization and *ReLU* activation function, followed by 2×2 pooling. The feature channel along the encoder increase from 32 to 64 and then to 128 across the 3 stages, while the spatial resolution decreases by half in each stage. At the bottleneck, there are 256 channels, and the spatial dimension is reduced to 1/8th of that of the original dimension. The decoder pathway then reconstructs the original spatial and feature map. It consists of three upsampling stages using 2×2 transposed convolution. At each stage, we have skip connections that bridge the encoder and decoder, allowing the decoder to recover important spatial information that might have been lost during the downsampling. The final layer outputs a raw phase logit that is passed through a sigmoid activation function to decode the phase values between 0 and 1. These values then classified into either solid or liquid based on the threshold of 0.5 as shown in the equation below:

$$\text{phase}(i,j) = \begin{cases} 1, & \text{if } \sigma(z_{i,j}) > 0.5, \\ 0, & \text{otherwise}, \end{cases} \tag{20}$$

where $\sigma(\cdot)$ denotes the sigmoid activation and $z_{i,j}$ is the raw output at pixel (i, j). The threshold ensures a separation between the solid and liquid phases, producing binary values of 0 and 1, which better reflects the actual physical state than the continuous probabilities.

7.1.2. VelNet model: Automated prediction of kinematic feature

The second model predicts the velocity field **using the temperature distribution externally and the phase information predicted by the PhaseNet Model internally via the MicroTwin**. This VelNet Model utilizes the same U-Net architecture, but with two input channels: one corresponding to temperature and the other to phase, and a single output channel representing the meltpool velocity. The VelNet architecture is the backbone software library for constructing the **FlowTwin** in additive manufacturing process. The VelNet architecture's dependence on PhaseNet for Physics-informing the domain with phase mask implies that FlowTwin is built on top of MicroTwin. In other words, the MicroTwin is hierarchically/vertically linked to FlowTwin in terms of information flow.

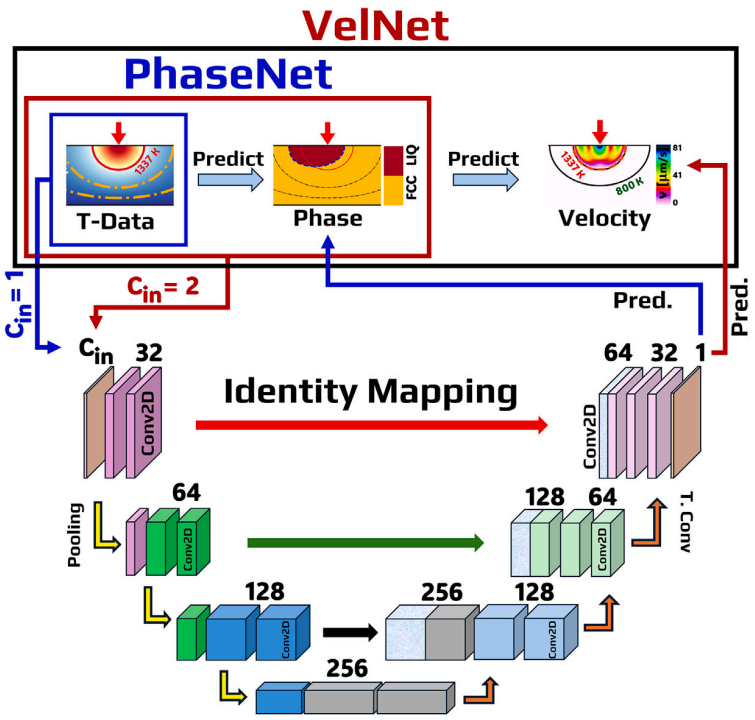


Fig. 4. Schematic of the customized multi-step U-Net architectures developed for predicting phase evolution and meltpool velocity. The PhaseNet model predicts the phase distribution from a single-channel temperature input (T-Data, C_{in} = 1), while the VelNet model predicts the meltpool velocity using two input channels, temperature (T-Data) and the PhaseNet-predicted phase (C_{in} = 2). Both models share the same encoder–decoder structure, consisting of convolutional and pooling layers that extract hierarchical spatial features. The encoder compresses spatial dimensions while increasing feature channels (C_{in}, 32, 64, 128), and the decoder restores spatial resolution through upsampling and skip connections (lateral arrows), reducing channels from 256 to 1. The primary difference between the two models lies in their training objectives: PhaseNet uses a binary cross-entropy loss for phase classification (LIQUID vs. FCC), whereas VelNet employs a mean squared error (MSE) loss for velocity regression, combined with a hard-pass filter to constrain predictions within the LIQUID phase region. The PhaseNet and VelNet programs are loaded on the Raspberry Pi microcomputer (refer Fig. 13) to render it as a physics-informed conditionally automated device.

The velocity prediction network shares the same U-Net encode-decoder framework as the PhaseNet model, as shown in Fig. 4, with modifications to accommodate two input channels performing regression rather than classification. The FlowTwin is represented by the black colored box (VelNet) in Fig. 4 and it is clear therein that it totally sits on top of MicroTwin. Specifically, the sigmoid activation function and binary cross-entropy loss were replaced with a linear output layer and mean squared error loss, respectively. However, there is another key modification in the output stage. We introduce a hard mask based on the laws of physics on the output velocity. As the velocity in the solid phase regions can be treated as non-existent (since they are nearly equal to zero), we multiply the final predicted velocity by the binary phase mask as follows:

$$v_{\text{pred}}(i,j) = \text{phase}(i,j) \times \hat{v}(i,j) \tag{21}$$

where $\hat{v}(i,j)$ is the VelNet model's predicted output velocity. This masking operation ensures that velocities are driven to zero wherever the phase (order-parameter) equals zero, which is represented by the solid FCC phase in the domain.

The complete model implementation, including encoder, bottleneck, and decoder blocks with their respective convolutional, max pooling, and upsampling layers, is available on the PhaseVelNet GitHub page, also referenced in Data availability section.

8. Result and discussion

This section presents the results obtained from phase-field simulations and machine learning model predictions. In Section 8.1, we analyze the thermo-phase response corresponding to different free energy expressions used during laser-induced simulations. Section 8.2 discusses the evolution of the meltpool, its area, and temperature distribution across the computational domain under various laser beam profiles. Similarly, Section 8.3 quantifies the uncertainties in peak temperature resulting from the choice of free energy expression. Finally, Section 8.4 presents the outcomes of the machine learning model trained on simulation data, demonstrating its capability to predict laser-induced multiphase behavior. We also outline the use of temperature distribution data tensors for rapid prediction of phase transformations through the trained ML models, along with the conceptualization of a virtual digital twin framework.

8.1. Effects on phase response by driving force formulations

Phase evolution is primarily governed by the system's free energy, the phase with the lowest free energy at a given temperature determines temporal stability. This study compares the phase response, stability, and transition behavior during non-isothermal laser processing using two Gibbs free energy formulations that dictates the phase-field dynamics. As shown in Graph 2, for the fine-tuned expression 2**(a)**, the free energy curves for the two phases are parabolic and intersect near the melting point of Au, T_{melt} = 1337 K, forming a small energy gap. In contrast, the TDB-based free energy curves (Fig. 2**(b)**) intersects directly at T_{melt} without a visible gap between the LIQUID and FCC phases. For the LIQUID phase evolution using the fine-tuned expression (F_θ), the results differ distinctly from those with the TDB-based expression (F_ψ), as seen in Fig. 5. The initial LIQUID region (2500 μm^2) grows into a semi-circular meltpool that follows the 1337 K contour at around 1 s of simulation time (Fig. 5**(a)**). The

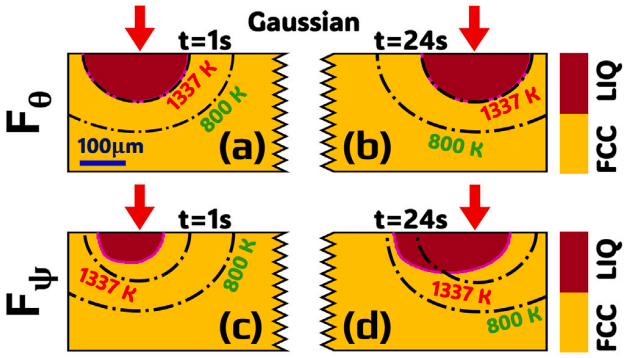


Fig. 5. Phase evolution in a unary Au system irradiated by a Gaussian laser beam (25 mW, 30 μm/s) scanning from the top left to the top right of the computational domain. Subplots **(a)** and **(b)** shows phase-field simulations using the fine-tuned free energy expression (F_θ) at t = 1 s and t = 24 s, respectively, where the LIQUID phase (dark red) aligns with the melting temperature contour of 1337 K. Subplots **(c)** and **(d)** presents results using the TDB-based free energy expression (F_ψ), indicating a time lag between thermal and phase diffusion, with thermal diffusion leading. At t = 1 s, the meltpool is 18484.18 μm^2 for F_θ and 7575.42 μm^2 for F_ψ, which converge to an average of ≈ 17,800 μm^2 by the end of the simulation, though the meltpool shape differ significantly. The results for Flat-Top, Ring and Bessel beam are provided in Fig. A.2 of Appendix A.

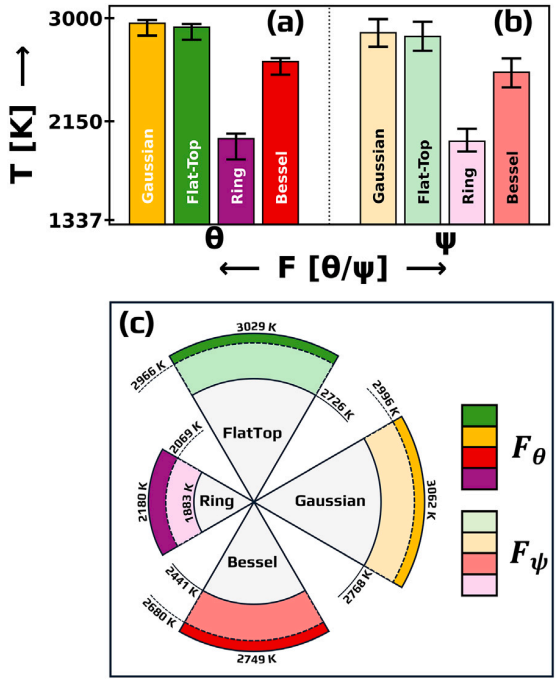


Fig. 6. Bar graph comparing the average peak temperature at the top surface of the computational domain as the laser scans from left to right during phase-field simulations. In **(a)**, results are shown for simulation using fine-tuned free energy expression (F_θ), where the Gaussian beam reaches the highest peak temperature of 3062 K, followed by Flat-Top (3029 K), Bessel (2749 K), and Ring (2180 K) profiles. In **(b)**, the results using the TDB-based free energy expression (F_ψ) shows a similar trend, with peak temperatures of 2996 K, 2966 K, 2680 K, and 2069 K for Gaussian, Flat-Top, Bessel, and Ring beams, respectively. Overall, simulations using F_θ yield consistently higher temperature values across all beam profiles compared to those using F_ψ. **(c)** The bird-eye overview of maximum temperature for four laser beam types with both free energy formulations in a radar chart.

meltpool boundary continues to trace this contour until the heat source is turned off Fig. 5**(b)**. In contrast, for F_ψ (Fig. 5**(c)**), the meltpool is not fully developed at 1 s, and the 1337 K thermal front leads the actual LIQUID front. This creates a physical separation between the temperature contour and the meltpool boundary, as shown in Fig. 5**(c)** and **(d)**, with red contours indicating the meltpool and black dotted lines the temperature field. This positional lag between thermal and phase diffusion, referred to as lead-lag dynamics described in detail in our previous work [10], is observed for F_ψ but not for F_θ. While Fig. 5 illustrates results for the Gaussian beam, similar distinctions in LIQUID phase evolution are observed for all other laser beams.

Another key difference between F_θ and F_ψ appears in the peak temperature range across the domain. Fig. 6 shows the variation of maximum surface temperature for both energy models: F_θ (Fig. 6**(a)**) consistently yield higher peak temperature than F_ψ (Fig. 6**(b)**). For instance, under the Gaussian beam, F_θ produces an *average peak temperature* of 2958 K, compared to 2880 K for F_ψ. Moreover, F_ψ exhibits a wider range of temperature fluctuations over time, as reflected by the larger error bars across all beam profiles. Similarly, Fig. 6 **(c)** presents the bird-eye view of the *maximum temperatures* attained by the four laser beam profiles with variations in two free expressions in a radar-chart.

Free energy formulation also influences meltpool flow velocity. Fig. 7**(a)** and **(b)** shows the velocity fields for F_θ under Bessel and Ring at t = 12.5 s while, Fig. 7**(c)** and **(d)** shows the same for F_ψ. For F_θ, the peak velocities are 81.17 μm/s (Bessel) and 18.90 μm/s (Ring). For F_ψ, these values are 56.29 μm/s and 23.71 μm/s respectively. The Ring beam is an exception, where the TDB based model (F_ψ) yields a higher flow velocity than (F_θ), a behavior discussed further in Section 8.2.

Another observation in simulation with F_ψ is the asymmetry in temperature distribution: the leading region (right of the moving laser) shows a wider thermal spread than the trailing region (left side). In Fig. 8**(c)** and **(d)**, the spatial gap between the 1337 K and 800 K contours at the leading surface (β_ψ and β'_ψ) is larger than at the trailing surface (α_ψ and α'_ψ). In contrast, for F_θ, these contours remains nearly symmetric ($\alpha_\theta \approx \beta_\theta$ and $\alpha'_\theta \approx \beta'_\theta$) as shown in Fig. 8**(a)** and **(b)**.

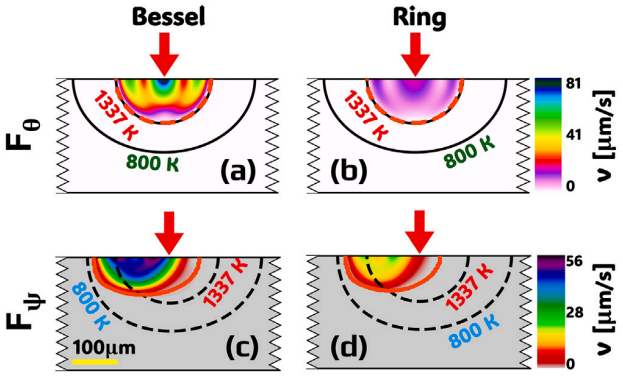


Fig. 7. Subplots showing the meltpool velocity profiles when the laser beam reaches the domain midpoint (500 μm from the top-left corner) at t = 12.5 s for two laser beam profiles under two free energy expressions. In **(a)** and **(b)**, the velocity distribution within the LIQUID phase is shown for Bessel and Ring beams using the fine-tuned free energy expression (F_θ). Similarly, **(c)** and **(d)** present results for the same beam profiles using the TDB-based expression (F_ψ). The meltpool velocity is consistently higher for the Bessel beam compared to the Ring beam across both free energy cases. For F_θ, the maximum velocities are approximately 81 μm/s (Bessel) and 18.90 μm/s (Ring), while for F_ψ, the respective maxima are 56 μm/s and 23.71 μm/s. Comparing the two energy expressions, F_θ yields higher flow velocities for the Bessel beam, whereas F_ψ produces greater meltpool flow for the Ring beam. The plots for Flat-Top and Gaussian beam are provided in Fig. A.3 of Appendix A.

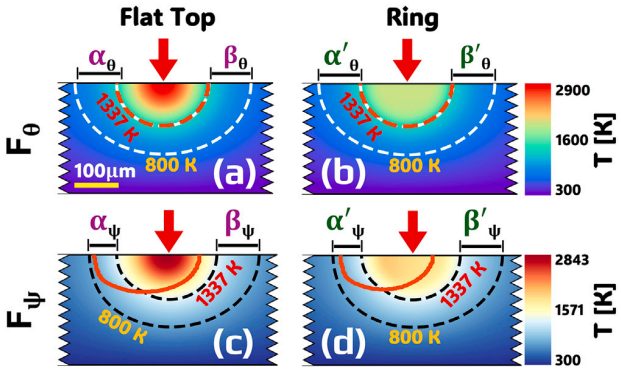


Fig. 8. Comparative illustration of temperature distribution for Flat-Top and Ring laser beam profiles at $t = 12.5$ s, when the laser reaches the midpoint of the top surface of the computational domain. Subplots **(a)** and **(c)** corresponds to the Flat-Top beam under fine-tuned (F_θ) and TDB-based (F_ψ) free energy expressions, respectively, while **(b)** and **(d)** represent the Ring beam under the same conditions. For F_θ, both Flat-Top and Ring profiles shows nearly symmetrical temperature contours at leading and trailing edges ($\alpha_\theta \approx \beta_\theta \approx 97.76$ μm) and ($\alpha'_\theta \approx \beta'_\theta \approx 92.27$ μm), with peak temperature of 2900 K and 1967 K, respectively. The 1337 K contour aligns precisely with the meltpool boundary (dashed red line), indicating no lag between phase and thermal fronts. In contrast, simulations with F_ψ show a clear offset between temperature and phase fronts (red and black-dashed lines) and asymmetry in the contour spacing. For Flat-Top, the leading edge gap ($\beta_\psi = 94.76$ μm) exceeds the trailing one ($\alpha_\psi = 62.34$ μm), and a similar trend appears for the Ring beam ($\beta'_\psi = 94.76$ μm, $\alpha'_\psi = 64.83$ μm). Overall, the Flat-Top beam produces higher temperature across the domain compared to the Ring beam, irrespective of the free energy expression.

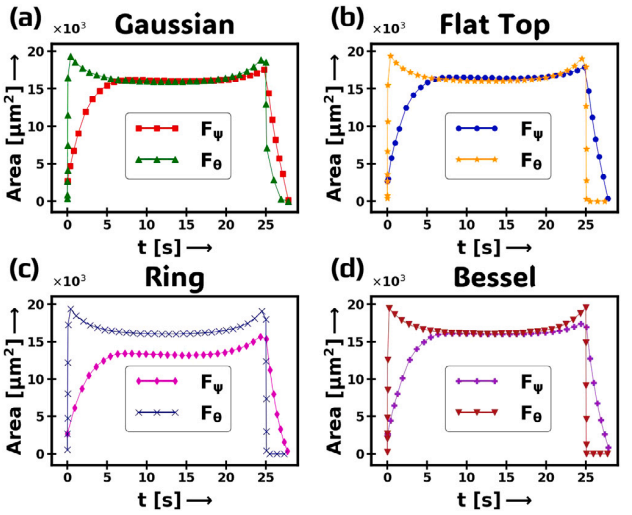


Fig. 9. Plots illustrating the evolution of meltpool (LIQUID) phase area over the simulation duration for four laser beam profiles and two free energy expressions. In **(a)**, the Gaussian beam shows that the fine-tuned free energy (F_θ) causes a rapid rise in meltpool area to 19422.59 μm², stabilizing around 16497.74 μm², while the TDB-based expression (F_ψ) produces a gradual growth reaching about 15551.55 μm² until the laser is turned off at $t = 25$ s. Similar behavior is seen for the Flat-Top **(b)** and Bessel **(d)** beams, both averaging near 16,500 μm², with F_θ showing an initial sharp rise and F_ψ a smoother increase. The Ring beam **(c)** deviates from this pattern: the F_θ simulation maintains an average meltpool area of 16549.60 μm², while the F_ψ simulation shows a smaller area averaging 12967.09 μm² and peaking near 16338.35 μm². A distinct delay is observed in meltpool formation and solidification for F_ψ, contrasting with the sharper transitions seen in F_θ.

8.2. How heat source type alters the morphology

This section discusses how four different laser beam profiles influences phase dynamics in the phase-field simulations. Starting with the temperature distribution, it is observed that the Gaussian beam produces the highest peak temperature, followed by the Flat-Top beam. The domain reaches a peak of 3062 K and 2996 K for F_θ and F_ψ respectively under the Gaussian beam, while the Flat-Top beam attains 3029 K and 2966 K (Fig. 6**(c)**). For the Bessel beam, the maximum temperature are 2749 K (F_θ) and 2680 K (F_ψ). Although these three beam produces comparable temperature range (above 2500 K), the Ring beam exhibits a distinct thermal response. Its peak temperature are notably lower, 2180 K and 2069 K for F_θ and F_ψ respectively, due to the unique way it distributes heat. Unlike Gaussian, Flat-Top and Bessel beams that deliver concentrated irradiance at the center, the Ring beam has near-zero central intensity, focusing energy along a circular ring. The resulting bidirectional heat flow- both inward and outward from the ring, creates a more uniform temperature field and prevents sharp temperature spikes. This behavior is clearly seen in Fig. 8**(b)** and **(d)**, where the Ring beam produces a smoother, radially symmetric temperature profile compared to the more peaked distribution of the Flat-Top beam in Fig. 8**(a)** and **(c)**. The temperature fields for Gaussian and Bessel beams at mid-simulation are shown in Fig. A.4 of Appendix A.

A similar, influence of beam shape is reflected in the evolution of the LIQUID phase. The meltpool area, tracked at each time step, is summarized in Fig. 9 for all beam types and both free energy expressions. For all beams except the Ring, the meltpool area evolves similarly in both F_θ and F_ψ simulations and converges by mid-simulation. However, for the Ring beam, the meltpool area with F_ψ remains significantly smaller than with F_θ. From these results, one can infer that beam shape directly impacts meltpool size and heat-affected zone (HAZ), guiding laser selection for specific additive manufacturing processes. For example, the Flat-Top beam produces the largest average meltpool area 16545.82 μm² (F_θ) and 15839.72 μm² (F_ψ), making it suitable for processes requiring larger meltpools or broader HAZ. Conversely, the Ring beam, with its uniform but smaller heating region, is more suitable where consistent temperature distribution and tighter HAZ control are desired.

The differences in temperature evolution across beam profiles are analyzed along the horizontal midline of the domain, indicated by the red arrow in Fig. 10. In all cases, temperature increases as the laser approaches the midpoint, peaks when the beam center passes over it, and decreases thereafter. Fig. 10**(a)** compares Gaussian and Ring beams; Fig. 10**(b)** compares Gaussian and Bessel; Fig. 10**(c)** compares Ring and Flat-Top; and Fig. 10**(d)** compares Flat-Top and Bessel. The Gaussian beam consistently produces higher peak temperature than other beams. In Fig. 10**(c)**, the Flat-Top beam heats the midpoint to 2843.02 K, while the Ring beam maintains a nearly constant temperature of 1958.09 K between $t = 10.61$ s to 14.39 s. This flattened thermal response of the Ring beam reflects steady and uniform heating, with gradual temperature rise and fall due to the ring's leading and trailing edges. Overall, Gaussian, Flat-Top, and Bessel beams produce a bell-shaped temperature profile at any surface point, while the Ring beam yields a steady, plateau-like profile.

For simulations using the fine-tuned free energy (F_θ), the beam-induced meltpool flow velocity follows the temperature trends. The Gaussian beam generates the highest average flow velocity of 123.75 μm/s (magenta line, Fig. 11**(a)**), followed by the Flat-Top beam at 119.94 μm/s (green line, Fig. 11**(b)**). The Bessel beam reaches a maximum of 84.65 μm/s (purple line, Fig. 11**(d)**), while the Ring beam produces the lowest velocity of 20.37 μm/s (cyan line, Fig. 11**(c)**). For the TDB-based energy model (F_ψ), the order of the flow velocity shifts slightly, Flat-Top records the highest (76.86 μm/s), followed by

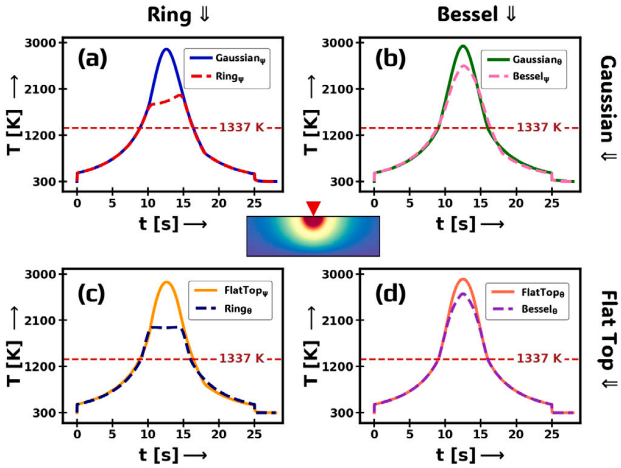


Fig. 10. Time-temperature plots for a spatial point located at the mid-top surface (inset). Subplot **(a)** compares Gaussian and Ring beams with F_ψ, showing a bell-shaped temperature curve for the Gaussian beam peaking at 2873.29 K, while the Ring beam exhibits a flatter profile with a peak of 1975.98 K. In **(b)**, the Gaussian beam with F_θ (green) reaches 2933.98 K, higher than the Bessel beam with F_ψ (pink, 2550.24 K). Subplot **(c)** compares Flat-Top (F_ψ) and Ring (F_θ) beams, where the Ring beam provides uniform heating (peak 1958.09 K) and the Flat-Top beam shows gradual heating and cooling (peak 2873.02 K). In **(d)**, both Flat-Top and Bessel beams with F_θ yield bell-shaped curves peaking at 2900.08 K and 2614.45 K, respectively. Readers are referred to Fig. 6**c** to obtain a bird-eye overview of the overall impact with different free energy expressions for each heat source types.

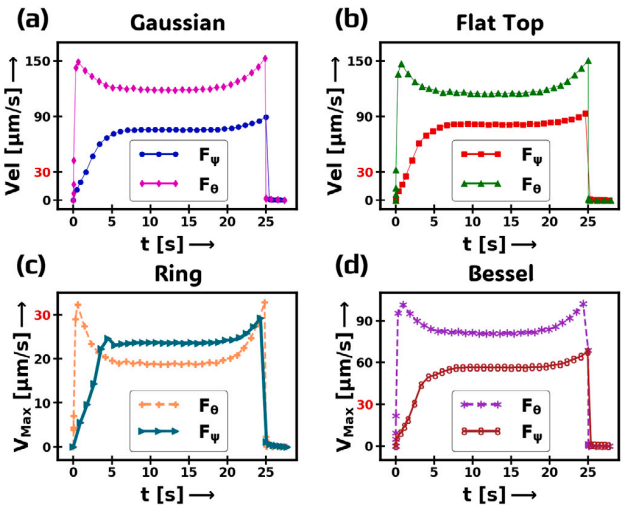


Fig. 11. Subplots showing the evolution of maximum meltpool velocity during simulation for different laser beam profiles and free energy expressions. In **(a)**, the Gaussian beam produces a higher peak velocity with F_θ (magenta line with diamond markers) than with F_ψ (blue line with circular markers), averaging 123.75 μm/s and 71.76 μm/s, respectively. A similar trend is seen for the Flat-Top beam in **(b)**, with average peak velocities of 119.94 μm/s (F_θ) and 76.86 μm/s (F_ψ). In contrast, for the Ring beam **(c)**, F_ψ yields slightly higher flow (22.65 μm/s) than F_θ (20.37 μm/s). For the Bessel beam **(d)**, the trend reverts to higher values with F_θ (84.65 μm/s) compared to F_ψ (52.39 μm/s). Note that the *y*-axis scale differs in **(c)** and **(d)** to account for the lower velocity range; a red marker at 30 μm/s is included across all subplots for reference.

Gaussian (71.76 μm/s), Bessel (52.39 μm/s) and Ring (22.65 μm/s), shown by red, blue, brown, and orange curves in Fig. 11**(b)**, **(a)**, **(d)** and **(c)** respectively. As also seen in the temperature data, the Ring beam remains an exception, its peak velocity is slightly higher in F_ψ (22.65 μm/s) than in F_θ (20.37 μm/s), consistent with its uniform and stable heating characteristics.

8.3. Uncertainty reduction in T-magnitudes

In laser AM, uncertainty in the prediction of peak meltpool temperatures is one of the major factors that limits build quality and process reliability. When thermodynamic models overestimate the temperature, often by several hundred kelvins, the melt pool becomes excessively hot. For metals such as Au or Ti-6Al-4V, temperatures above roughly 2000 K to 3000 K can lead to keyholing, where intense vapor recoil forms deep pores, spallation defects, and localized evaporation of low-boiling alloying elements. These effects alter the local chemistry, promote brittle phases, and ultimately compromise mechanical performance. If the model underpredicts the temperature, the opposite problem arises: insufficient melting causes lack-of-fusion defects, delamination between layers, and strongly anisotropic microstructures. These defects serve as preferred sites for fatigue cracking and can reduce component life by more than an order of magnitude. Even moderate temperature errors (100-200 K) can change melt-pool shape by 20%-30%, leading to irregular layer bonding and high build-failure rates in production environments. Additional consequences include wasted energy due to overheating and safety concerns from high-velocity spatter. Our TDB-based free-energy function, F_ψ, obtained directly from CALPHAD-consistent thermodynamic databases, substantially reduces these uncertainties. Compared with the empirically fitted free-energy expression F_θ, the TDB-based model predicts 60-100 K lower and more realistic peak temperatures as shown in Fig. 6.

The ramp-up rate of driving force for phase transition (Λ) near the melting temperature ($\pm\delta T_m$ = 5 K) is small for TDB based formulation (Λ_ψ = −9.511 J/mol/K) whereas, it is inflated by 81 times for fitted expression with Λ_θ = −770.45 J/mol/K as depicted in Fig. A.1 of Appendix A. This implies that during laser heating the fitted free energy based phase field model directly transforms FCC into LIQUID phase with a significantly sufficient barrier to resolidify, when the melting regime is reached and the temperature increases in the LIQUID phase faster. On the other hand, it might be possible for the material within the melting regime to remain in equilibrium between FCC and LIQUID phases incontext of the model using TDB expressions.

The temperature-slope of the thermodynamic driving force for the solid-liquid transition, ($\Lambda = d\Delta F/dT$), differs sharply between the two free-energy formulations. In the TDB-based model this slope is modest (Λ_ψ = −9.511 J/mol/K), while in the fitted expression it becomes **over 81 times steeper** (Λ_θ = −770.45 J/mol/K). Thermodynamically, this slope is tied to the entropy discontinuity at the melting point, ($\Delta S = L_f/T_m$), as the latent heat of fusion satisfies $L_f = \frac{d\Delta F}{dT}\Big|_{T_m}$, with ($\Delta F = F_{\mathrm{LIQ}} - F_{\mathrm{FCC}}$) being the Gibbs free-energy difference near (T_m). A steeper ($|d\Delta F/dT|$) corresponds to a higher effective latent heat and forces the transformation across an extremely narrow temperature range. In the fitted model, this exaggerated slope causes the driving force ($|\Delta F|$) to shoot upward as soon as the material enters the melting regime. As a result, the phase field quickly converts FCC to LIQUID, and because (ΔF) continues to increase unnaturally fast in the LIQUID phase, the model strongly suppresses solid-liquid coexistence. This creates a thermodynamically overstabilized LIQUID, which heats up more rapidly, trapping thermal energy and promoting unrealistic thermal overshoots. In contrast, the TDB-based formulation yields a much smoother and physically grounded variation of ($\Delta F(T)$). Its latent-heat signature is correctly distributed across a finite temperature window, enabling genuine thermodynamic coexistence of FCC and LIQUID phases with a sustained presence of high-conductivity solid near the melting point. Because the transition is not artificially compressed, a fraction of solid persists longer during heating. Solid gold has a thermal conductivity

of 246.3945 W/m K at $T = 1335$ K, more than that of the LIQUID (136.71 W/m K at $T = 1340$ K). The continued presence of the solid therefore enhances radial heat extraction, preventing localized heat accumulation and a broader latent-heat absorption interval. In the TDB formulation, the latent heat is absorbed over a physically meaningful temperature range rather than at an artificially sharp point. This effectively buffers incoming laser energy, delaying the temperature rise and flattening the thermal trajectory. The material spends more time in the mixed-phase regime where enthalpy is absorbed without a rapid temperature increase. Together, these thermodynamic effects result in 60-100 K lower peak temperatures in the TDB-based simulations compared with the fine-tuned model. The fine-tuned expression, by overstating the driving force slope, collapses the phase transition into a narrow band, suppresses the high-conductivity solid prematurely, and eliminates latent-heat buffering conditions that all amplify thermal overshoot. Conversely, the TDB formulation enforces CALPHAD-consistent phase equilibria, distributes latent heat realistically, preserves conductive solid for longer, and prevents artificial trapping of heat in low conductivity mushy zones. This combination stabilizes the thermal response, yielding peak temperatures far closer to experimentally observed values in laser melting of Au.

Ultimately, the strength of the TDB-based formulation is in providing thermodynamically consistent and reliably constrained temperature predictions. By embedding the correct latent-heat behavior, preserving realistic solid-liquid coexistence, and avoiding the artificial steepening of the driving force seen in the fitted model, the TDB approach delivers temperature fields that adhere closely to CALPHAD-based phase equilibria and thus markedly reduce the error margin in peak-temperature estimation. This reduction in uncertainty is critical for laser AM: accurate thermal predictions ensure that the process window is identified correctly, preventing inadvertent transitions into overheating regimes associated with keyholing, vapor-driven porosity, solute loss, and microstructural degradation, while also avoiding the under-melting conditions that cause lack-of-fusion defects and weak interlayer bonding. In contrast, the heuristically fitted free-energy expression injects substantial uncertainty into the temperature field-its exaggerated driving-force slope, compressed melting interval, and unrealistic thermal response amplify both over- and under-prediction risks. Such variability propagates directly into melt-pool geometry, defect formation, and build reliability. Therefore, the TDB-based formulation provides a more accurate, lower-uncertainty, and physically grounded foundation for predicting melt-pool temperatures, ultimately enabling more consistent, defect-resistant, and scalable additive manufacturing.

8.4. Learning the meltpool profile

The U-Net architectures predicting the microstructure phase and the meltpool flow velocity described in Section 7 were trained for 200 epochs on the data generated from FEM simulations. The training performance of both models are listed in Table 5. Both models exhibit good prediction capabilities across training, validation, and testing. PhaseNet achieved an accuracy score of 0.9992, 0.998, and 0.997 in training, validation and test dataset respectively. VelNet also showed similar performance with higher R^2, and lower loss across training (R^2=0.9994, MSE=0.045), validation (R^2=0.9992, MSE=0.060) and testing (R^2=0.999, MSE=0.068) indicating generalization capability and minimal overfitting.

Fig. 12**(a)** shows the microstructural similarity index (μ_{SIM}) calculated from the LIQUID phase predictions across 483 test samples. The μ_{SIM} values consistently exceed 0.995, with most values approaching 0.999. This high level of similarity indicates that the model accurately captures phase distribution patterns from the given temperature field inputs. The calculation method for μ_{SIM} is described in Appendix B. The training behavior of PhaseNet is presented in Fig. 12**(b)**, which displays the binary cross-entropy (BCE) loss and classification accuracy over 200 training epochs. The model converged rapidly, with both training and validation accuracy reaching approximately 0.999 within the first 50 epochs. These accuracy values remained stable throughout the remaining training period, showing only minor variations. The loss values followed a similar trend, decreasing from an initial value of about 0.25 to near zero within 50 epochs, after which they remained consistently low for the duration of training. The performance of VelNet is shown in Figs. 12**(c)** and **(d)**. Fig. 12**(c)** presents a parity plot that compares the predicted liquid phase velocities against the ground truth values for the test dataset. The predicted values align closely with the actual values along the diagonal, demonstrating the model's generalization capability. Fig. 12**(d)** shows the training performance of VelNet in terms of R^2 coefficient and mean squared error (MSE) loss. The training behavior of VelNet is similar to that observed for PhaseNet. Both the training and validation R^2 values rapidly increase to approximately 0.99 in the early epochs and stabilize near 1.0 for the remainder of the training period. The MSE loss curves show a corresponding pattern, with a sharp decrease in the initial epochs followed by convergence to near-zero values. Minor fluctuations in the loss values are observed primarily during the early training phase, after which the curves remain stable.

Table 5
Performance summary of PhaseNet (Phase Prediction) and VelNet (Velocity Prediction) models.

Dataset	PhaseNet		VelNet		
	Accuracy	BCE Loss	MSE	MAE	R^2
Training	0.9992	0.0016	0.045	0.062	0.9994
Validation	0.9989	0.0024	0.060	0.071	0.9992
Testing	0.9979	0.0060	0.068	0.079	0.9990

To further evaluate the model's predictive capability, a separate FEM simulation was conducted in the MOOSE Framework using only the heat transfer physics module. This setup computed the temperature distribution under a Bessel laser beam profile with the same power and scan speed as in the base phase-field simulations. An interpolation function (Eq. (22)) was applied to smoothly vary material properties-thermal conductivity, specific heat, and density, across the domain relative to the melting temperature of gold (1337 K).

$$h_T = \frac{1}{1 + e^{-10\left(\frac{T}{T_{\text{melt}}} - 1\right)}} \tag{22}$$

The resulting temperature data were converted into tensor format and fed as input to the MicroTwin (refer Fig. 13). The model-predicted meltpool phase evolution from the temperature history was compared against results from the full phase-field simulation. Fig. 14**(a)** shows the temperature field from the heat transfer simulation, while Fig. 14**(b)** presents the corresponding phase evolution from the full phase-field model. The predicted phase distribution from the trained PhaseNet model is shown in Fig. 14**(c)**, and the prediction error map in Fig. 14**(d)**. In this figure, green regions indicate *False Positives* (FP), where the model predicted the presence of meltpool phase absent in the phase-field result; red regions denote *False Negatives* (FN), where the model failed to identify the LIQUID phase; and light-yellow areas mark the *Correctly Predicted* (CP) regions where both results match. In addition, the LIQUID phase area at the presented time instant from the full phase-field FEM simulation was 17,363 μm^2, whereas PhaseNet predicted 18,046 μm^2, resulting in a meltpool area prediction error of about 3.93%. The temperature feature should be supplied as input feature whereas phase related features can be internally fed to the Flow Twin of Fig. 13. When the phase related features are supplied to the FlowTwin via the MicroTwin, the features are the machine learned ones. Also, it is possible to supply both temperature and phase features externally as input to the micro-computer. In this case, the phase features must be obtained from the FEM model. The phase features supplied to VelNet model (FlowTwin) to result in Fig. 14**(e)** were obtained from

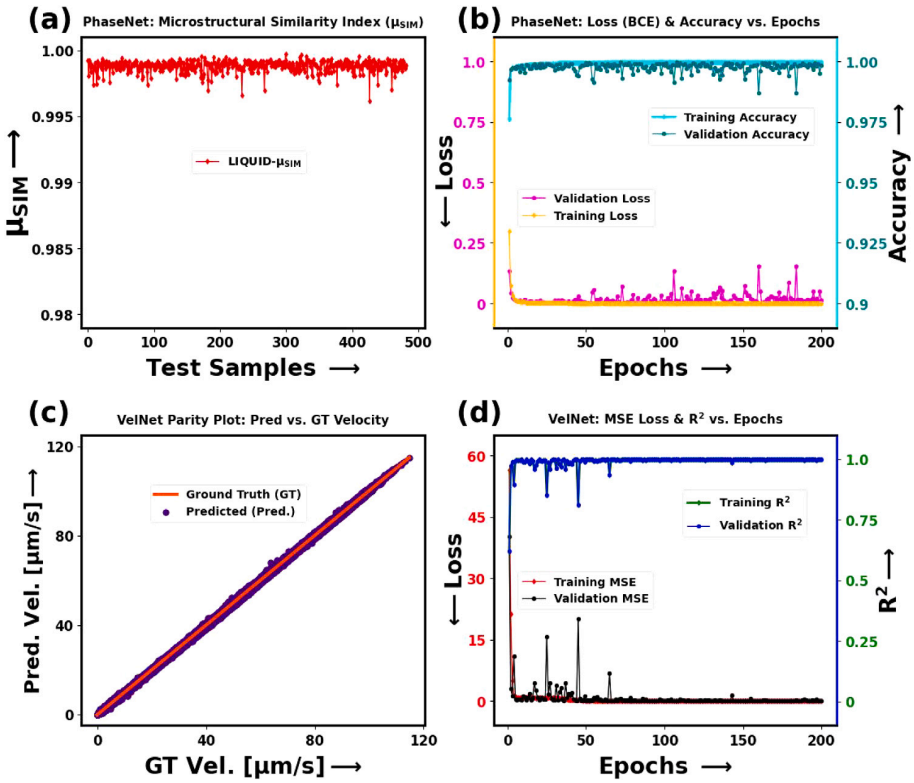


Fig. 12. Training, validation, and testing performance metrics of the machine learning models. **(a)** Microstructural similarity index (μ_{SIM}) between the ground truth and the PhaseNet-predicted LIQUID phase morphology for the test dataset. The high average μ_{SIM} value (0.995) across 483 test samples (15% of the total dataset) confirms the model's predictive accuracy on unseen data. **(b)** Training and validation accuracy and loss curves for the PhaseNet model over 200 epochs. Both metrics closely follow each other, reaching high accuracy and low loss for training and validation datasets. Loss is plotted along the left y-axis, while accuracy is shown on the right y-axis. **(c)** Parity plot comparing VelNet-predicted velocities with ground truth velocities at each spatial point within the LIQUID phase over a 1000 μm × 250 μm domain. The red line denotes ground truth, while purple dots represent the predicted velocities. **(d)** Training and validation loss (MSE) and R^2 metrics for the VelNet model over 200 epochs. Initial fluctuations stabilize after 50 iterations, showing consistently high R^2 and low loss, indicating robust training and validation performance.

MicroTwin. Fig. 14**(e)** shows the velocity field predicted by the VelNet model, while the corresponding full phase-field simulation result at the same time instance is presented in Fig. 14**(f)**. The absolute error between the predicted and simulated velocity fields is shown in Fig. 14**(g)**. For VelNet, the input variables were the temperature distribution from the stand-alone heat transfer simulation and the predicted phase data from PhaseNet. Thus, both the phase distribution and meltpool flow velocity can be inferred solely from the thermal distribution across the domain.

9. Virtual digital twin and outlook

The integration of IoT and remote sensing with digital twins offers an effective approach to minimizing laser-related hazards in industrial and research applications. Through real-time monitoring and predictive capability, digital twins can simulate laser-material interactions under varying conditions, reducing the risk of thermal damage, structural defects, and safety issues. IoT-enabled sensors provide continuous data streams, allowing adaptive control of laser parameters and improving overall process reliability [60,61].

Building on this, we propose a Digital Twin framework that employs training machine learning models to quantify and predict phase evolution, meltpool area, and velocity profiles in real time during additive manufacturing. The trained models can be deployed on a microcomputer such as a *Raspberry Pi*, connected to an infrared camera that records surface temperature data of the specimen. The model processes this temperature data and displays phase transformation details in real time.

To conceptualize this idea, a Virtual Digital Twin (VDT) [62] was developed with a web interface (WebApp), the working flow of this VDT is presented in Fig. C.1 of Appendix C. Instead of using infrared camera data, the virtual twin operates on temperature fields generated from a standalone laser heat-transfer simulation that excludes phase-field and fluid-flow physics (a Bessel beam is used as an example). The resulting temperature data are first passed to the trained PhaseNet model, which predicts the LIQUID and FCC phases and computes their respective areas. These outputs, together with temperature data, are then supplied to the VelNet model, which infers the velocity field within the meltpool region. The WebApp also incorporates the original phase-field simulation results (used to train ML models) to compute and visualize real-time error between simulated and predicted values for both phase and velocity fields. The Virtual Digital Twin WebApp is accessible at: VDTWebApp

This virtual twin framework can be readily extended to a physical digital twin by deploying the trained ML models on a *Raspberry Pi*. In this setup, actual thermal data are captured via infrared cameras, processed into numerical arrays, and used directly as model input.

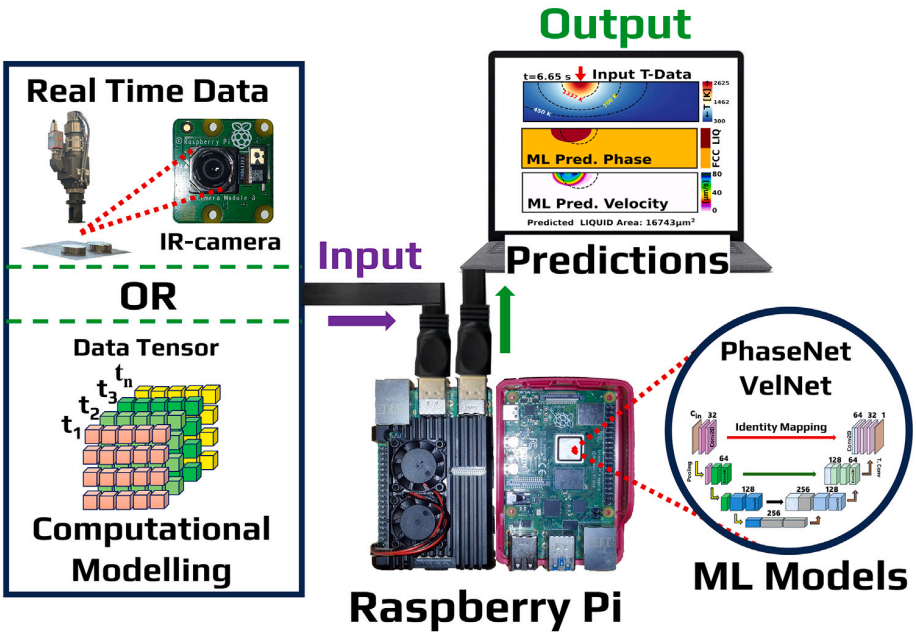


Fig. 13. The I/O interface of *Raspberry Pi* micro-computer consisting the PhaseNet and VelNet programs. The input (I) interface accepts the real time image data of temperature or the data tensor of the temperature. With the help of PhaseNet model, the micro-computer in the role of MicroTwin instantly outputs the phase at the Output (O). Interestingly, the U-Net architecture is reusable. The phase data from the MicroTwin can be channeled to the input (I) interface and together with the temperature feature, it could be utilized by FlowTwin (with VelNet architecture) to predict the meltpool dynamics (velocity) in accordance with Eq. (20). The predictions of the MicroTwin and FlowTwin are elaborated in Fig. 14.

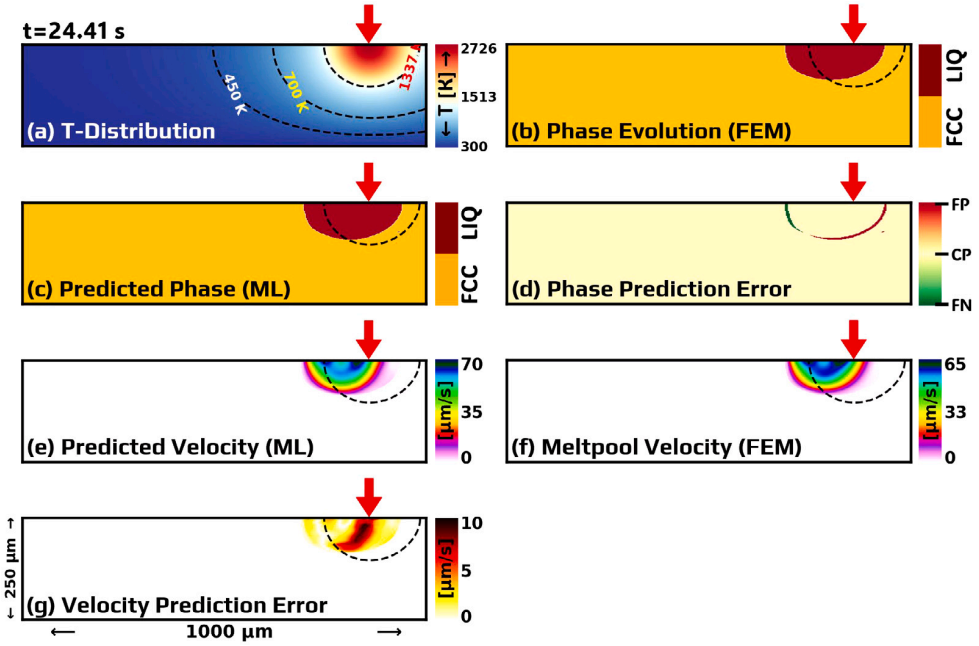


Fig. 14. Comparison of phase evolution and meltpool flow velocity predicted by the PhaseNet and VelNet models with FEM-based phase-field simulations. **(a)** Temperature distribution used as input to both ML models, obtained from a laser heat transfer simulation with a Bessel heat source and no phase-field coupling. In a real-time digital twin setup, similar data could be acquired from an IR camera and preprocessed on a microcomputer (e.g., *Raspberry Pi*) for model input. **(b)** FEM-based phase-field simulation result at $t = 24.41s$ showing a LIQUID phase area of 18,046 μm^2. **(c)** MicroTwin's PhaseNet-predicted phase distribution with a LIQUID phase area of 17,363 μm^2. **(d)** Comparison of PhaseNet predictions with FEM results, where CP (light yellow) denotes correctly predicted regions, FP (green) indicates false positives, and FN (red) marks false negatives. Most mismatches occur along the LIQUID-FCC interface. **(e)** FlowTwin's VelNet-predicted flow velocity within the LIQUID phase and **(f)** corresponding FEM-simulated melt pool velocity for identical laser parameters. **(g)** Absolute velocity prediction error between VelNet and FEM results at the same time step. The input temperature field originates from a stand-alone thermal FEM simulation not included in training, validation, or testing datasets, while the FEM-based phase and velocity fields used for comparison are part of the coupled-physics simulations used during training.

The prediction scope can be expanded in future work by training on data from multi-material systems (multi-component alloys) across different laser powers, scan speeds, and length scales, thereby enabling a generalized multi-material Digital Twin model.

In this context, the phase-field-informed U-Net architectures: PhaseNet and VelNet, running on a *Raspberry Pi* with infrared input exemplify conditional automation in additive manufacturing. PhaseNet takes temperature data and predicts structural features representing meltpool morphology, while VelNet uses temperature and phase data to infer meltpool velocity. The process is conditional because model outputs depend directly on the physical state encoded in the phase-field-based inputs. These networks learn mappings between phase-field states and meltpool behavior, which are key to additive manufacturing process control and optimization. Running the architecture on a portable device enables real-time, autonomous monitoring and remote prediction without manual intervention, achieving conditional automation by dynamically adapting predictions to input conditions.

Compared to to our previous work [10], where materials properties such as density, specific heat, free energy, and mobility were manually provided for FEM based phase prediction, the current approach eliminates the need for those external inputs. The trained ML models autonomously infer phase regions, areas, and meltpool velocity solely from laser-induced thermal data. Since additive manufacturing inherently involves laser-microstructure interactions, this autonomy, while still relying on external laser parameters, represents a step towards Conditional Automation (L3-Automation).

10. Conclusion

This study presented computational modeling of laser-induced phase transformation and microstructural evolution in a unary Au system. Simulations were performed using four laser beam profiles: Gaussian, Flat-Top, Ring, and Bessel, combined with two different free energy formulations. A fine-tuned logarithmic-polynomial fitted expression (F_θ) and a TDB-extracted expression (F_ψ).

The Gaussian, Flat-Top, and Bessel beams exhibited similar thermal and flow characteristics, with peak temperatures and maximum meltpool velocities concentrated at the beam center. In contrast, the Ring beam produced a more uniform temperature field within its radius. A key distinction was observed between the two free energy formulations: simulation using F_θ showed a precise alignment between the melting temperature contour (1337 K) and the LIQUID-FCC interface, while those using F_ψ revealed a noticeable lead-lag behavior between the thermal and phase fronts, attributed to differing diffusion rates of heat and phase fields.

Two U-Net based machine learning models, PhaseNet and VelNet, were trained on simulations datasets linking thermal histories to phase evolution and meltpool velocity. Using these models, a virtual digital twin framework was developed, capable of predicting phase and velocity evolution from temperature data inputs. This framework demonstrates a step towards constructing a physical Digital Twin for real-time experimental prediction using infrared camera data.

At present, the model is limited to a unary Au system, but future work will extend it to multi-component alloys and a wider range of laser processing parameters. The development of such multimodal Digital Twin systems is expected to accelerate real-time phase transformation prediction and advance precision control in additive manufacturing.

CRediT authorship contribution statement

Upadesh Subedi: Writing – original draft, Visualization, Validation, Software, Methodology, Investigation, Formal analysis, Data curation, Conceptualization. **Aadya Bhattarai:** Writing – review & editing, Visualization, Validation, Software, Investigation, Data curation. **Nele Moelans:** Writing – review & editing, Validation, Supervision, Methodology. **Tomasz Tański:** Writing – review & editing, Visualization, Validation, Supervision. **Anil Kunwar:** Writing – review & editing, Validation, Supervision, Project administration, Methodology, Funding acquisition, Data curation, Conceptualization.

Declaration of competing interest

The authors declare that they have no known competing financial interests or personal relationships that could have appeared to influence the work reported in this paper.

Acknowledgments

This work was supported by the National Science Centre, Poland (UMO-2021/42/E/ST5/00339). The authors acknowledge the use of computing time provided by GAIVI at the University of South Florida. The resources and services used in this work were provided by the VSC (Flemish Supercomputer Center), funded by the Research Foundation - Flanders (FWO) and the Flemish Government.

Appendix A

A.1. Ramp-up rate of driving force ($\Lambda_{\psi|\theta}$)

To quantify the discrepancy introduced by the fitted free-energy expression, we compare the temperature derivatives of the LIQUID-FCC free energy difference over a narrow interval if $\delta T = \pm 5K$ around the melting point $T_m = 1337K$ as presented in Fig. A.1. This analysis highlights how the physically consistent TDB-based formulation preserves the thermodynamically consistent ramp-up rate of the phase-transition driving force (Λ), whereas the polynomial fit introduces an unrealistically steep temperature dependence. Since the magnitude of the driving force $|\Delta F|$ directly determines the predicted phase-transition kinetics, even small distortions in $\frac{d\Delta F}{dT}$ can lead to order of magnitude error in phase front, underscoring the necessity of using thermodynamically grounded free energy models.

A.2. Complementary figures: Phase response to $F_{\psi|\theta}$

This section presents the complementary Figures and Plots A.2, A.3 and A.4, related to Sections 8.1 and 8.2.

Appendix B

B.1. Microstructural similarity index (μ_{SIM})

The Microstructural Similarity Index, μ_{SIM}, is computed using the formula shown in Eq. (B.1) [63,64]. In this expression, η_t corresponds to the ground-truth phase-field values obtained from the simulation, while η_t' represents the PhaseNet-predicted values of the phase variable η at time 't'.

$$\mu_{SIM}(\eta_t, \eta_t') = \frac{(2\mu_{\eta_t}\mu_{\eta_t'} + \alpha_{\eta_t})(2\sigma_{\eta_t\eta_t'} + \alpha_{\eta_t'})}{(\mu_{\eta_t}^2 + \mu_{\eta_t'}^2 + \alpha_{\eta_t})(\mu_{\eta_t}^2 + \mu_{\eta_t'}^2 + \alpha_{\eta_t'})} \tag{B.1}$$

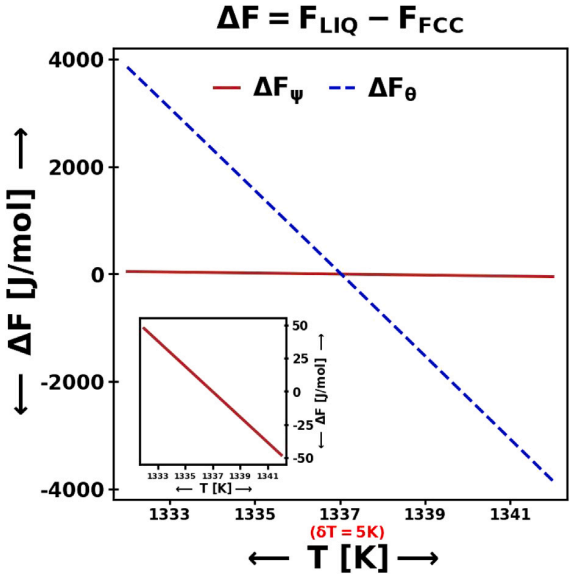


Fig. A.1. Comparison of the free energy ramp-up rate $\Lambda = \frac{d\Delta F}{dT}$ near melting point. The figure plots the temperature derivative of the LIQUID-FCC free energy differences, $\Delta F = F_{\text{LIQUID}} - F_{\text{FCC}}$, over a narrow interval of $\delta T = \pm 5K$ around $T_m = 1337$ K, comparing the TDB-based and fine-tuned (fitted) free energy expressions. The TDB-based formulation yields a physically consistent ramp-up rate of $\Lambda_\psi \approx -9.511$ J/mol/K. In contrast, the fitted expression produces an artificially steep slope of $\Lambda_\theta \approx -770.45$ J/mol/K, exaggerating the thermodynamic behavior by a factor of ≈ 81. The inset highlights only the TDB-based Λ_ψ curve to improve visibility of its small but physically meaningful temperature dependence. This discrepancy inflates the $|\Delta F|$ and thereby the phase-transition kinetics, resulting in absence of lead-lag dynamics in simulation performed with fine-tuned free energy expression.

The quantities μ_{η_t}, $\mu_{\eta_t'}$, $\sigma^2_{\eta_t}$, and $\sigma^2_{\eta_t'}$ denote the sample mean intensities and variances of the fields η_t and η_t', respectively, while $\sigma_{\eta_t\eta_t'}$ represents their cross-covariance. The constants α_{η_t} and $\alpha_{\eta_t'}$ are included to avoid division by zero. For the μ_{SIM} metric to be computed correctly, both ground truth distribution of η_t and predicted η_t' distribution must share the same data points in 2D domain of $N \times M$.

Appendix C

C.1. Virtual digital twin work flow

See Fig. C.1.

Appendix D

D.1. Computational cost comparison

The phase-field simulations were executed on a *Dell Precision 7920 Tower* using 10 CPU cores (2 threads each), 64 GB RAM, and an Intel Xeon Gold 5220R @ 2.20 GHz, launched via *mpiexec* within our MOOSE-based application. The average wall-clock time for a single FEM simulation was ≈12.5 h, and the eight simulations required for this study accumulated to roughly 4.5 days of compute time. In contrast, training the ML models (**PhaseNet** and **VelNet**) for 200 iterations on an

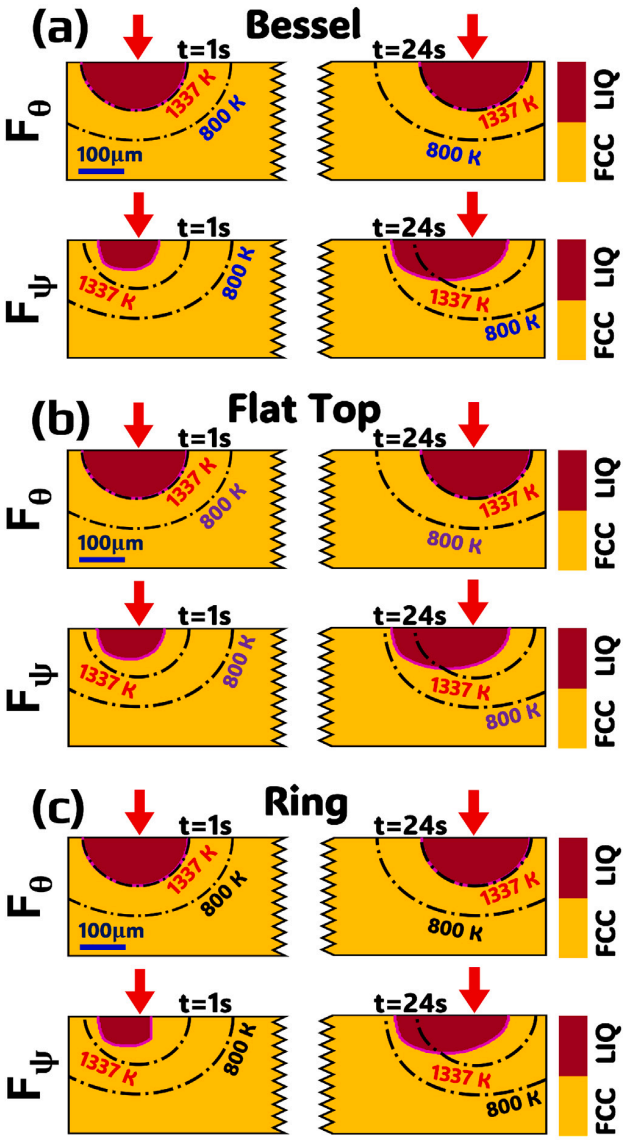


Fig. A.2. Visual illustration of laser induced phase evolution during the phase field simulation in unary Au system with different heat source profiles with different free energy expressions. **(a)** The four subplots depicts the growth of meltpool at time t=1s and t=25s under the Bessel beam with top row corresponding to fine-tuned free energy expression F_θ and bottom row with F_ψ. Similarly, in **(b)** the LIQUID phase status is presented for Flat-Top laser profile with F_θ and F_ψ as driving force for phase transformation in top and bottom row subplots. Finally **(c)** represents the meltpool phase growth similar to that of **(a)** and **(b)** but for the simulation with Ring laser beam under two free energy expressions. Although the different laser beam profile resulted in drastic temperature history and velocity profile inside the domain, the overall phase growth is in near similar fashion and is possible difficult to distinguish on a visual basis.

NVIDIA RTX A6000 required only 30-45 min. The largest performance gain arises during inference, where the trained ML models generate full spatiotemporal fields for new thermal inputs in **under 1 second**, representing a speed-up of five orders of magnitude relative to FEM simulations. This behavior was validated across multiple platforms,

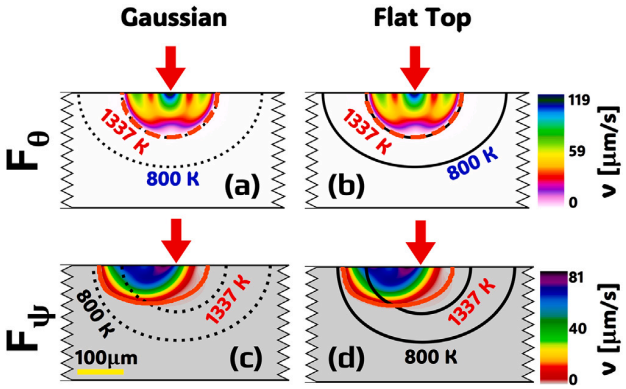


Fig. A.3. Illustration of velocity profile inside the meltpool when the laser traverses to domain midpoint. Subplot **(a)** and **(c)** are associated with simulation under the Gaussian heat source for F_θ and F_ψ respectively. The peak flow velocity for in the LIQUID phase for **(a)** and **(c)** are 119 μ m/s and 75.61 μ m/s respectively. In **(b)** and **(d)**, the flow profile for simulation conducted under the Flat-Top heat source for F_θ and F_ψ is presented.

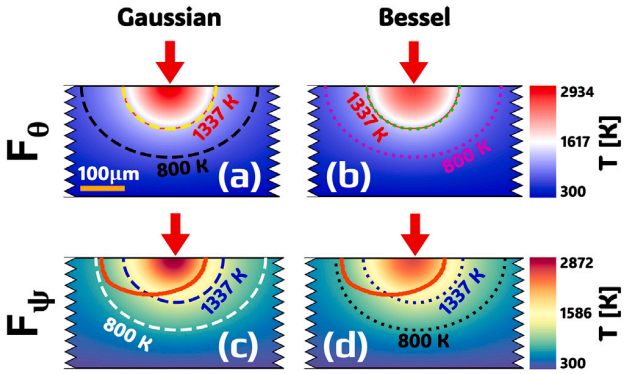


Fig. A.4. Visualization of thermal distribution across a cutout of simulation domain for Gaussian and Bessel laser sources. Plot **(a)** and **(c)** showcases the temperature profile for Gaussian heat source with driving force expression of F_θ and F_ψ respectively. Similarly, **(b)** and **(d)** represents the temperature inside the computational domain with Bessel heat source for F_θ and F_ψ correspondingly. A subtle difference in temperature profile can be noticed between Gaussian and Bessel based simulation results with a higher concentration of temperature distribution at the beam center for Gaussian beam, the peak temperature reached by the domain under Bessel beam are found to be 2613.11 K in **(b)** and 2548.95 K in **(d)**.

Table D.1
Inference time using trained ML model across different systems.

	Inference time
Raspberry Pi 4	≈0.265 s
Dell Precision 7920 Tower	≈0.192 s
Cloud Computing via Streamlit	≈0.397 s

including a *Raspberry Pi 4*, a high-performance workstation, and a freely hosted Streamlit web application, all achieving sub-second inference. Table D.1 summarizes these inference times.

These results demonstrate that the ML models enable real-time prediction of phase morphology, phase-fraction evolution, and meltpool flow velocity, in contrast to the hours-long FEM computations required for each new condition. This real-time capability is also integrated

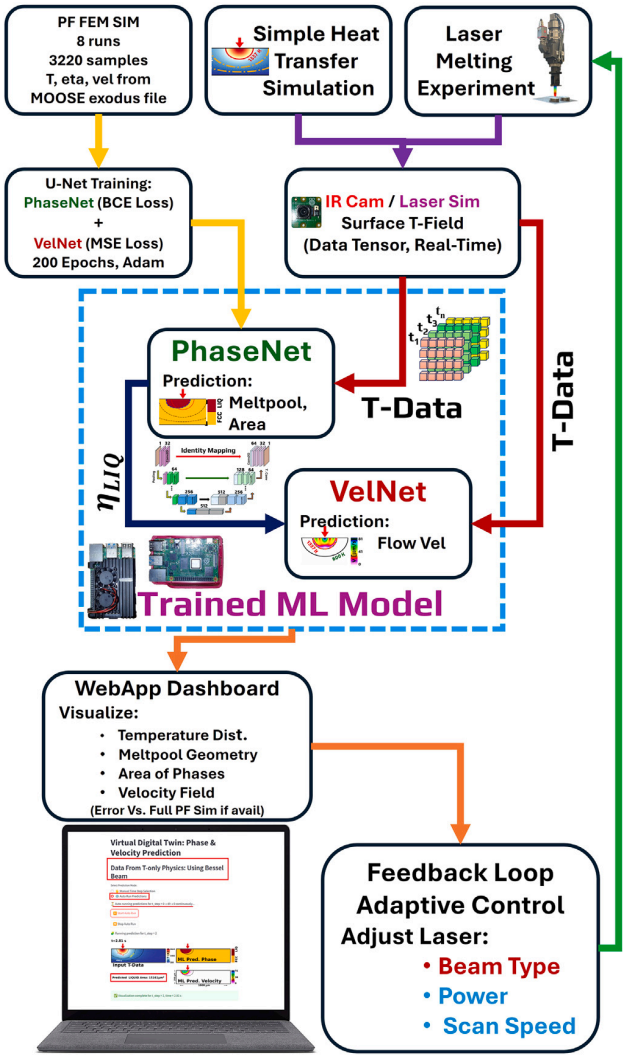


Fig. C.1. Flowchart of the Virtual Digital Twin framework for real-time meltpool prediction and laser control. High-fidelity Phase-Field (PF) simulations (8 runs, 3220 samples) provide temperature, phase, and velocity fields used to train two U-Net models: PhaseNet for melt-pool geometry and phase distribution (BCE loss) and VelNet for flow-velocity prediction (MSE loss). Independent temperature-field inputs, either from a simple heat-transfer laser simulation or real-time IR-camera measurements during laser melting, can be supplied to the trained models to infer melt-pool shape, phase area, and velocity fields. These predictions are displayed in a WebApp interface for visualization and optional comparison to PF simulations. The interface enables a feedback-loop adaptive control system that adjusts laser processing parameters (beam type, power, scan speed), closing the Virtual Digital Twin for real-time monitoring and control.

into the Virtual Digital Twin (VDT) interface, where inference time per prediction is displayed. Overall, the ML-based workflow provides a robust and quantitatively verified acceleration over FEM simulations, supporting its suitability for real-time process control and monitoring.

D.2. Convergence behavior across diffused-interface widths

See Fig. D.1.

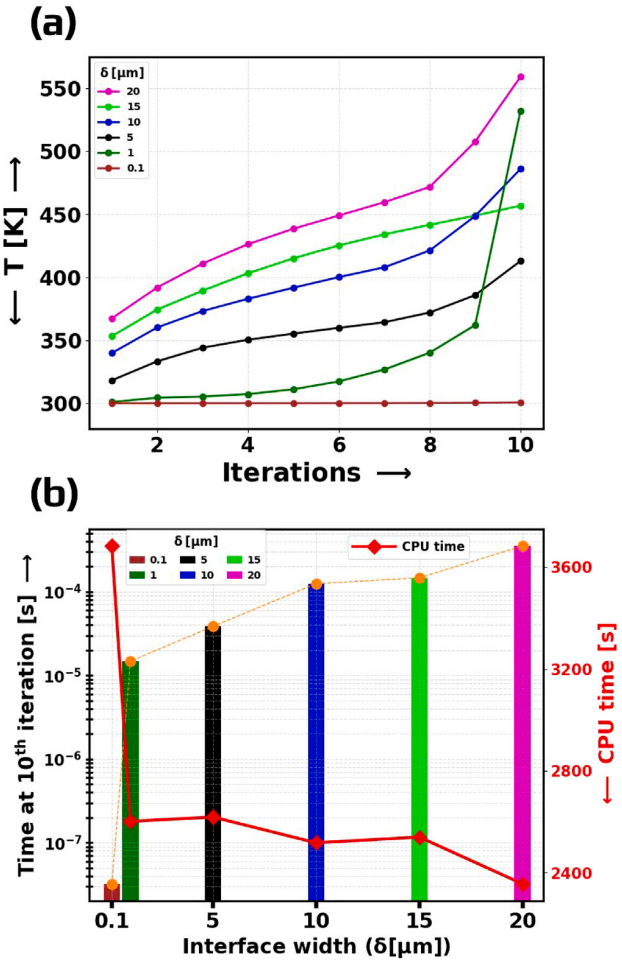


Fig. D.1. Effect of diffused-interface width δ on convergence behavior and computational cost. The same Gaussian TDB-based phase-field simulation was performed for δ = 0.1, 1, 5, 10, 15 and 20 μm, each run for 10 iterations. Subplot **(a)** shows the maximum temperature in the domain at the 10th iteration, demonstrating the simulations with larger diffused-interface widths reach higher temperatures more rapidly for the same iteration count. Subplot **(b)** explains this behavior via the actual physical simulation time (left y-axis) achieved after 10 iterations. For the smallest interface width (δ = 0.1 μm), the simulation advances only to $\sim 10^{-8}$s, because the sharp interface causes repeated convergence failure; the simulation therefore is programmed to reduce the timestep dt until convergence is possible, significantly increasing the wall clock time (right y-axis), which exceeds 3600s for 10 iterations. In contrast, larger δ values permit larger stable timesteps, leading to higher physical simulation times and substantially lower CPU times. Based on this balance between accuracy, convergence stability and computational efficiency, a diffused-interface width of δ = 10 μm was selected for the simulation in this work.

Data availability

The phase-field simulation codes, simulation video animations, and webapp for virtual digital twin along with the data used for this work is available at https://github.com/subediupadesh/AMTwinLab and the machine learning model source code is available at https://github.com/AadyaBhattarai/PhaseVelNet.

References

[1] B. Park, A. Chen, S. Mishra, Real-time melt pool homogenization through geometry-informed control in laser powder bed fusion using reinforcement learning, IEEE Trans. Autom. Sci. Eng. 22 (2025) 2986–2997, http://dx.doi.org/10.1109/TASE.2024.3386882, URL https://ieeexplore.ieee.org/document/10499998.

[2] N. Bastola, M.P. Jahan, N. Rangasamy, C.S. Rakurty, A Review of the Residual Stress Generation in Metal Additive Manufacturing: Analysis of Cause, Measurement, Effects, and Prevention, Micromachines 14 (7) (2023) 1480, http://dx.doi.org/10.3390/mi14071480, URL https://www.mdpi.com/2072-666X/14/7/1480.

[3] H. Zhao, C. Yu, Z. Liu, C. Liu, Y. Zhan, A novel finite element method for simulating residual stress of TC4 alloy produced by laser additive manufacturing, Opt. Laser Technol. 157 (2023) 108765, http://dx.doi.org/10.1016/j.optlastec.2022.108765, URL https://linkinghub.elsevier.com/retrieve/pii/S0030399222009112.

[4] S. Zhang, Y. Lu, H. Yang, Multiscale basis modeling of 3D melt-pool morphological variations for manufacturing process monitoring, Int. J. Adv. Manuf. Technol. 136 (9) (2025) 4055–4066, http://dx.doi.org/10.1007/s00170-024-13377-2, URL https://link.springer.com/article/10.1007/s00170-024-13377-2.

[5] Y. Zhao, T. Xin, S. Tang, H. Wang, X. Fang, H. Hou, Applications of unified phase-field methods to designing microstructures and mechanical properties of alloys, MRS Bull. 49 (6) (2024) 613–625, http://dx.doi.org/10.1557/s43577-024-00720-x.

[6] M.R. Tonks, A. Cheniour, L. Aagesen, How to apply the phase field method to model radiation damage, Comput. Mater. Sci. 147 (2018) 353–362, http://dx.doi.org/10.1016/j.commatsci.2018.02.007.

[7] R. Darabi, E. Azinpour, A. Reis, J.C. de Sa, Multi-scale Multi-physics Phase-field coupled Thermo-mechanical approach for modeling of powder bed fusion process, Appl. Math. Model. 122 (2023) 572–597, http://dx.doi.org/10.1016/j.apm.2023.06.021, URL https://linkinghub.elsevier.com/retrieve/pii/S0307904X23002767.

[8] D. Gaston, C. Newman, G. Hansen, D. Lebrun-Grandié, MOOSE: A parallel computational framework for coupled systems of nonlinear equations, Nucl. Eng. Des. 239 (2009) 1768–1778, http://dx.doi.org/10.1016/j.nucengdes.2009.05.021, URL https://linkinghub.elsevier.com/retrieve/pii/S0029549309002635.

[9] A.D. Lindsay, D.R. Gaston, C.J. Permann, J.M. Miller, D. Andrš, A.E. Slaughter, F. Kong, J. Hansel, R.W. Carlsen, C. Icenhour, L. Harbour, G.L. Giudicelli, R.H. Stogner, P. German, J. Badger, S. Biswas, L. Chapuis, C. Green, J. Hales, T. Hu, W. Jiang, Y.S. Jung, C. Matthews, Y. Miao, A. Novak, J.W. Peterson, Z.M. Prince, A. Rovinelli, S. Schunert, D. Schwen, B.W. Spencer, S. Veeraraghavan, A. Recuero, D. Yushu, Y. Wang, A. Wilkins, C. Wong, 2.0 - MOOSE: Enabling massively parallel multiphysics simulation, SoftwareX 20 (2022) 101202, http://dx.doi.org/10.1016/j.softx.2022.101202, URL https://linkinghub.elsevier.com/retrieve/pii/S2352711022001200.

[10] U. Subedi, N. Moelans, T. Tański, A. Kunwar, A non-isothermal multi-phase field approach to model the meltpool and IMC grains interaction in ti-au material, Comput. Mater. Sci. 255 (2025) 113875, http://dx.doi.org/10.1016/j.commatsci.2025.113875, URL https://www.sciencedirect.com/science/article/pii/S0927025625002186.

[11] Z. Li, M. Greenwood, A. Phillion, A phase field methodology for simulating the microstructure evolution during laser powder bed fusion in-situ alloying process, IOP Conf. Ser.: Mater. Sci. Eng. 1281 (1) (2023) 012017, http://dx.doi.org/10.1088/1757-899X/1281/1/012017, URL https://iopscience.iop.org/article/10.1088/1757-899X/1281/1/012017.

[12] C. Bonneville, N. Bieberdorf, A. Hegde, M. Asta, H.N. Najm, L. Capolungo, C. Safta, Accelerating phase field simulations through a hybrid adaptive Fourier neural operator with U-net backbone, Npj Comput. Mater. 11 (1) (2025) 14, http://dx.doi.org/10.1038/s41524-024-01488-z, URL https://www.nature.com/articles/s41524-024-01488-z.

[13] F. Ogoke, P. Pak, A. Myers, G. Quirarte, J. Beuth, J. Malen, A.B. Farimani, Deep learning for melt pool depth contour prediction from surface thermal images via vision transformers, Addit. Manuf. Lett. 11 (2024) 100243, http://dx.doi.org/10.1016/j.addlet.2024.100243, URL https://www.sciencedirect.com/science/article/pii/S2772369024000513.

[14] A. Kunwar, B. Guo, S. Shang, P.R. aback, Y. Wang, J. Chen, H. Ma, X. Song, N. Zhao, Roles of interfacial heat transfer and relative solder height on segregated growth behavior of intermetallic compounds in Sn/Cu joints during furnace cooling, Intermetallics 93 (2018) 186–196, http://dx.doi.org/10.1016/j.intermet.2017.11.021, URL https://www.sciencedirect.com/science/article/abs/pii/S0966979517309354.

[15] S. Chen, A. Lu, D. Yang, S. Lu, J. Dong, C. Dong, Analysis on flow pattern of bobbin tool friction stir welding for 6082 aluminum, Elsevier, 2013, pp. 353–358, http://dx.doi.org/10.1533/978-1-78242-164-1.353,

[16] N. Zhao, Y. Zhong, M. Huang, H. Ma, W. Dong, Growth kinetics of Cu6Sn5 intermetallic compound at liquid-solid interfaces in Cu/Sn/Cu interconnects under temperature gradient, Sci. Rep. 5 (2015) 13491, http://dx.doi.org/10.1038/srep13491, URL https://www.nature.com/articles/srep13491.

[17] N. Moelans, A quantitative and thermodynamically consistent phase-field interpolation function for multi-phase systems, Acta Mater. 59 (2011) 1077–1086, http://dx.doi.org/10.1016/j.actamat.2010.10.038, URL https://linkinghub.elsevier.com/retrieve/pii/S1359645410007019.

[18] Y. Zhao, K. Liu, H. Hou, L.-Q. Chen, Role of interfacial energy anisotropy in dendrite orientation in al-Zn alloys: A phase field study, Mater. Des. 216 (2022) 110555, http://dx.doi.org/10.1016/j.matdes.2022.110555, URL https://www.sciencedirect.com/science/article/pii/S0264127522001769.

[19] C.N. Singman, Atomic volume and allotropy of the elements, J. Chem. Educ. 61 (1984) 137–142, http://dx.doi.org/10.1021/ED061P137, URL https://pubs.acs.org/doi/abs/10.1021/ed061p137.

[20] Y. Zhao, Understanding and design of metallic alloys guided by phase-field simulations, Npj Comput. Mater. 9 (1) (2023) 94, http://dx.doi.org/10.1038/s41524-023-01038-z, URL https://www.nature.com/articles/s41524-023-01038-z.

[21] N. Moelans, B. Blanpain, P. Wollants, Quantitative phase-field approach for simulating grain growth in anisotropic systems with arbitrary inclination and misorientation dependence, Phys. Rev. Lett. 101 (2) (2008) 025502, http://dx.doi.org/10.1103/PhysRevLett.101.025502, URL https://journals.aps.org/prl/abstract/10.1103/PhysRevLett.101.025502.

[22] J.W. Peterson, A.D. Lindsay, F. Kong, Overview of the incompressible Navier–Stokes simulation capabilities in the MOOSE framework, Adv. Eng. Softw. 119 (2018) 68–92, http://dx.doi.org/10.1016/j.advengsoft.2018.02.004, URL https://www.sciencedirect.com/science/article/pii/S0965997817310591.

[23] A. Kunwar, E. Yousefi, X. Zuo, Y. Sun, D. Seveno, M. Guo, N. Moelans, Multi-phase field simulation of Al3Ni2 intermetallic growth at liquid al/solid Ni interface using MD computed interfacial energies, Int. J. Mech. Sci. 215 (2022) 106930, http://dx.doi.org/10.1016/j.ijmecsci.2021.106930, URL https://linkinghub.elsevier.com/retrieve/pii/S0020740321006408.

[24] S. Poudel, N. Moelans, R. Thapa, A. Timofiejczuk, D. Panthi, A. Kunwar, Unraveling elastochemical effects in microstructural evolution of Al–Cu–Ni system through DFT-informed multi-phase field simulations, Int. J. Solids Struct. 300 (2024) 112894, http://dx.doi.org/10.1016/j.ijsolstr.2024.112894, URL https://linkinghub.elsevier.com/retrieve/pii/S0020768324002531.

[25] H. Verbeeck, V. Feyen, I. Bellemans, N. Moelans, Multi-phase-field modeling of the dissolution behavior of stoichiometric particles on experimentally relevant length scales, Comput. Mater. Sci. 245 (2024) 113288, http://dx.doi.org/10.1016/j.commatsci.2024.113288, URL https://linkinghub.elsevier.com/retrieve/pii/S0927025624005093.

[26] F. Jing, Y. Liu, Y. Du, C. Shi, B. Hu, X. He, Phase Equilibria, Thermodynamics and Solidified Microstructure in the Copper–Zirconium–Yttrium System, Materials 16 (2023) 2063, http://dx.doi.org/10.3390/ma16052063, URL https://www.mdpi.com/1996-1944/16/5/2063.

[27] A. Dinsdale, SGTE data for pure elements, Calphad 15 (1991) 317–425, http://dx.doi.org/10.1016/0364-5916(91)90030-N, URL https://www.sciencedirect.com/science/article/abs/pii/036459169190030N.

[28] A. Khvan, I. Uspenskaya, N. Aristova, Q. Chen, G. Trimarchi, N. Konstantinova, A. Dinsdale, Description of the thermodynamic properties of pure gold in the solid and liquid states from 0 k, Calphad 68 (2020) 101724, http://dx.doi.org/10.1016/j.calphad.2019.101724, URL https://linkinghub.elsevier.com/retrieve/pii/S0364591619302858.

[29] B. Echebarria, R. Folch, A. Karma, M. Plapp, Quantitative phase-field model of alloy solidification, Phys. Rev. E 70 (6) (2004) 061604, http://dx.doi.org/10.1103/PhysRevE.70.061604, URL https://link.aps.org/doi/10.1103/PhysRevE.70.061604.

[30] T. Uehara, M. Fukui, N. Ohno, Phase field simulations of stress distributions in solidification structures, J. Cryst. Growth 310 (7–9) (2008) 1331–1336, http://dx.doi.org/10.1016/j.jcrysgro.2007.12.035, URL https://linkinghub.elsevier.com/retrieve/pii/S0022024807012109.

[31] X. Feng, A. Prohl, Analysis of a fully discrete finite element method for the phase field model and approximation of its sharp interface limits, Math. Comp. 73 (246) (2003) 541–567, http://dx.doi.org/10.1090/S0025-5718-03-01588-6, URL http://www.ams.org/mcom/2004-73-246/S0025-5718-03-01588-6/.

[32] S.A. Khairallah, A.T. Anderson, A. Rubenchik, W.E. King, Laser powder-bed fusion additive manufacturing: Physics of complex melt flow and formation mechanisms of pores, spatter, and denudation zones, Acta Mater. 108 (2016) 36–45, http://dx.doi.org/10.1016/j.actamat.2016.02.014, URL https://www.sciencedirect.com/science/article/pii/S135964541630088X.

[33] Y.-C. Wu, C.-H. San, C.-H. Chang, H.-J. Lin, R. Marwan, S. Baba, W.-S. Hwang, Numerical modeling of melt-pool behavior in selective laser melting with random powder distribution and experimental validation, J. Mater. Process. Technol. 254 (2018) 72–78, http://dx.doi.org/10.1016/j.jmatprotec.2017.11.032, URL https://linkinghub.elsevier.com/retrieve/pii/S0924013617305526.

[34] R. Moore, G. Orlandi, T. Rodgers, D. Moser, H. Murdoch, F. Abdeljawad, Microstructure-based modeling of laser beam shaping during additive manufacturing, Jom 76 (3) (2024) 1726–1736, http://dx.doi.org/10.1007/s11837-023-06363-8, URL https://link.springer.com/10.1007/s11837-023-06363-8.

[35] C. Wang, Z. Luo, J. Duan, L. Jiang, X. Sun, Y. Hu, J. Zhou, Y. Lu, Adjustable annular rings of periodic surface structures induced by spatially shaped femtosecond laser, Laser Phys. Lett. 12 (5) (2015) 056001, http://dx.doi.org/10.1088/1612-2011/12/5/056001, URL https://iopscience.iop.org/article/10.1088/1612-2011/12/5/056001.

[36] C. Lei, S. Ren, C. Yin, X. Liu, M. Chen, J. Wu, C. Han, Manipulating melt pool thermofluidic transport in directed energy deposition driven by a laser intensity spatial shaping strategy, Virtual Phys. Prototyp. 19 (1) (2024) http://dx.doi.org/10.1080/17452759.2024.2308513, URL https://www.tandfonline.com/doi/full/10.1080/17452759.2024.2308513.

[37] F. Galbusera, L. Caprio, B. Previtali, A.G. Demir, Analytical modeling and characterization of ring beam profiles for high-power lasers used in industrial manufacturing, J. Manuf. Process. 117 (2024) 387–404, http://dx.doi.org/10.1016/j.jmapro.2024.02.069, URL https://linkinghub.elsevier.com/retrieve/pii/S1526612524002093.

[38] T.M. Wischeropp, H. Tarhini, C. Emmelmann, Influence of laser beam profile on the selective laser melting process of alsi10mg, J. Laser Appl. 32 (2020) http://dx.doi.org/10.2351/7.0000100, URL https://pubs.aip.org/lia/jla/article-abstract/32/2/022059/225348/Influence-of-laser-beam-profile-on-the-selective.

[39] T.U. Tumkur, T. Voisin, R. Shi, P.J. Depond, T.T. Roehling, S. Wu, M.F. Crumb, J.D. Roehling, G. Guss, S.A. Khairallah, M.J. Matthews, Nondiffractive beam shaping for enhanced optothermal control in metal additive manufacturing, Sci. Adv. 7 (2021) http://dx.doi.org/10.1126/sciadv.abg9358, URL https://www.science.org/doi/10.1126/sciadv.abg9358.

[40] L.-E. Loh, C.-K. Chua, W.-Y. Yeong, J. Song, M. Mapar, S.-L. Sing, Z.-H. Liu, D.-Q. Zhang, Numerical investigation and an effective modelling on the selective laser melting (SLM) process with aluminium alloy 6061, Int. J. Heat Mass Transfer 80 (2015) 288–300, http://dx.doi.org/10.1016/j.ijheatmasstransfer.2014.09.014, URL https://linkinghub.elsevier.com/retrieve/pii/S0017931014008060.

[41] S. Chowdhury, N. Yadaiah, C. Prakash, S. Ramakrishna, S. Dixit, L.R. Gupta, D. Buddhi, Laser powder bed fusion: a state-of-the-art review of the technology, materials, properties & defects, and numerical modelling, J. Mater. Res. Technol. 20 (2022) 2109–2172, http://dx.doi.org/10.1016/j.jmrt.2022.07.121, URL https://linkinghub.elsevier.com/retrieve/pii/S2238785422011607.

[42] T. Kik, Heat source models in numerical simulations of laser welding, Materials 13 (11) (2020) 2653, http://dx.doi.org/10.3390/ma13112653, URL https://www.mdpi.com/1996-1944/13/11/2653.

[43] J. Wu, H. Wei, F. Yuan, P. Zhao, Y. Zhang, Effect of beam profile on heat and mass transfer in filler powder laser welding, J. Mater. Process. Technol. 258 (2018) 47–57, http://dx.doi.org/10.1016/j.jmatprotec.2018.03.011, URL https://linkinghub.elsevier.com/retrieve/pii/S092401361830116X.

[44] D.E. Jodi, T. Kitashima, Y. Koizumi, T. Nakano, M. Watanabe, Manufacturing single crystals of pure nickel via selective laser melting with a flat-top laser beam, Addit. Manuf. Lett. 3 (2022) 100066, http://dx.doi.org/10.1016/j.addlet.2022.100066, URL https://linkinghub.elsevier.com/retrieve/pii/S2772369022000408.

[45] W. Jiazhu, T. Liu, H. Chen, F. Li, H. Wei, Y. Zhang, Simulation of laser attenuation and heat transport during direct metal deposition considering beam profile, J. Mater. Process. Technol. 270 (2019) 92–105, http://dx.doi.org/10.1016/j.jmatprotec.2019.02.021, URL https://linkinghub.elsevier.com/retrieve/pii/S0924013619300779.

[46] D.L. Shealy, J.A. Hoffnagle, Laser beam shaping profiles and propagation, Appl. Opt. 45 (21) (2006) 5118, http://dx.doi.org/10.1364/AO.45.005118, URL https://opg.optica.org/abstract.cfm?URI=ao-45-21-5118.

[47] Z. Wang, M. Jiang, X. Chen, Y. Du, Z. Lei, S. Zhao, Y. Chen, Mitigating spatters in keyhole-mode laser welding by superimposing additional ring-shaped beam, Opt. Laser Technol. 168 (2024) 109869, http://dx.doi.org/10.1016/j.optlastec.2023.109869, URL https://linkinghub.elsevier.com/retrieve/pii/S0030399223007624.

[48] L. Yang, S. Geng, P. Jiang, Y. Wang, J. Xiong, Investigation on the keyhole/molten pool dynamic behavior during adjustable ring-mode laser welding of medium-thick aluminum alloy, Int. J. Therm. Sci. 196 (2024) 108723, http://dx.doi.org/10.1016/j.ijthermalsci.2023.108723, URL https://linkinghub.elsevier.com/retrieve/pii/S1290072923005847.

[49] I. Abdo, N. Ashry, M. Sadek, M. Abdel Hakim, D. Khalil, Effect of ring width on ring generated Bessel beam, in: A.V. Kudryashov, A.H. Paxton, V.S. Ilchenko (Eds.), 2012, 823608, http://dx.doi.org/10.1117/12.908956, URL http://proceedings.spiedigitallibrary.org/proceeding.aspx?doi=10.1117/12.908956.

[50] P. Pradhan, M. Sharma, B. Ung, Generation of Perfect Cylindrical Vector Beams With Complete Control Over the Ring Width and Ring Diameter, IEEE Photonics J. 10 (1) (2018) 1–10, http://dx.doi.org/10.1109/JPHOT.2018.2790175, URL https://ieeexplore.ieee.org/document/8252695/.

[51] A. Zapata, X.F. Zhao, S. Li, C. Bernauer, M.F. Zaeh, Three-dimensional annular heat source for the thermal simulation of coaxial laser metal deposition with wire, J. Laser Appl. 35 (1) (2023) http://dx.doi.org/10.2351/7.0000813, URL https://pubs.aip.org/jla/article/35/1/012020/2871665/Three-dimensional-annular-heat-source-for-the.

[52] M. Duocastella, C. Arnold, Bessel and annular beams for materials processing, Laser & Photonics Rev. 6 (5) (2012) 607–621, http://dx.doi.org/10.1002/lpor.201100031, URL https://onlinelibrary.wiley.com/doi/10.1002/lpor.201100031.

[53] G.S. Sokolovskii, V.V. Dudelev, S.N. Losev, K.K. Soboleva, A.G. Deryagin, K.A. Fedorova, V.I. Kuchinskii, W. Sibbett, E.U. Rafailov, Bessel beams from semiconductor light sources, Prog. Quantum Electron. 38 (2014) 157–188, http://dx.doi.org/10.1016/J.PQUANTELEC.2014.07.001.

[54] O. Bialas, A.N. Appiah, M. Wala, A. Kunwar, A. Woźniak, P.M. Nuckowski, W. Simka, P. Råback, M. Adamiak, Laser assisted fabrication of mechanochemically robust Ti3Au intermetallic at Au-Ti interface, Eng. Sci. Technol. an Int. J.

42 (2023) 101413, http://dx.doi.org/10.1016/j.jestch.2023.101413, URL https://linkinghub.elsevier.com/retrieve/pii/S2215098623000903.

[55] W. Luo, Z. Jin, H. Liu, T. Wang, Thermodynamic assessment of the au-ti system, Calphad 25 (2001) 19–26, http://dx.doi.org/10.1016/S0364-5916(01)00026-8, URL https://www.sciencedirect.com/science/article/pii/S0364591601000268.

[56] T. Dubberstein, M. Schürmann, H. Chaves, H.P. Heller, C.G. Aneziris, A novel vibrating finger viscometer for high-temperature measurements in liquid metals and alloys, Int. J. Thermophys. 37 (2016) 100, http://dx.doi.org/10.1007/s10765-016-2104-7, URL http://link.springer.com/10.1007/s10765-016-2104-7.

[57] R.A. Cairncross, P.R. Schunk, T.A. Baer, R.R. Rao, P.A. Sackinger, A finite element method for free surface flows of incompressible fluids in three dimensions. Part I. Boundary fitted mesh motion, Internat. J. Numer. Methods Fluids 33 (2000) 375–403, http://dx.doi.org/10.1002/1097-0363(20000615)33:3<375::AID-FLD13>3.0.CO;2-O, URL https://onlinelibrary.wiley.com/doi/abs/10.1002/1097-0363(20000615)33:3%3C375::AID-FLD13%3E3.0.CO;2-O.

[58] F. Aqra, A. Ayyad, Theoretical temperature-dependence surface tension of pure liquid gold, Mater. Lett. 65 (14) (2011) 2124–2126, http://dx.doi.org/10.1016/j.matlet.2011.04.063, URL https://www.sciencedirect.com/science/article/abs/pii/S0167577X1100440X.

[59] Siemens, A comprehensive Digital Twin, 2023, p. 1, URL https://www.siemens.com/global/en/products/automation/topic-areas/digital-enterprise/digital-twin.html. (Accessed 26 October 2025).

[60] X. Pei, J. Pei, H. Hou, Y. Zhao, Optimizing casting process using a combination of small data machine learning and phase-field simulations, Npj Comput. Mater. 11 (1) (2025) 27, http://dx.doi.org/10.1038/s41524-025-01524-6.

[61] N. Jyeniskhan, K. Shomenov, M.H. Ali, E. Shehab, Exploring the integration of digital twin and additive manufacturing technologies, Int. J. Light. Mater. Manuf. 7 (6) (2024) 860–881, http://dx.doi.org/10.1016/j.ijlmm.2024.06.004, URL https://www.sciencedirect.com/science/article/pii/S2588840424000556.

[62] M. Rezasefat, J.D. Hogan, Virtual rapid prototyping of materials with deep learning: spatiotemporal stress fields prediction in ceramics employing convolutional neural networks and transfer learning, Virtual Phys. Prototyp. 19 (2024) http://dx.doi.org/10.1080/17452759.2024.2399186, URL https://www.tandfonline.com/doi/full/10.1080/17452759.2024.2399186.

[63] Z. Wang, A. Bovik, H. Sheikh, E. Simoncelli, Image quality assessment: From error visibility to structural similarity, IEEE Trans. Image Process. 13 (2004) 600–612, http://dx.doi.org/10.1109/TIP.2003.819861, URL https://ieeexplore.ieee.org/document/1284395.

[64] S. van der Walt, J.L. Schonberger, J. Nunez-Iglesias, F. Boulogne, J.D. Warner, N. Yager, E. Gouillart, T. Yu, scikit-image: image processing in Python, PeerJ 2 (2014) e453, http://dx.doi.org/10.7717/peerj.453, URL https://peerj.com/articles/453.

APPENDIX B: DECLARATIONS OF CO-AUTHORS

Declaration statements form co-author's of published research articles with their credit and percentage contribution

Tomasz Tański, Ph.D, DSc., Eng.

Silesian University of Technology

Faculty of Mechanical Engineering

Department of Engineering Materials and Biomaterials - RMT1

Declaration

I hereby declare that my contribution percentages in the following publications were as follows:

1. U. Subedi, N. Moelans, T. Tański, A. Kunwar, *Rapid portabilization of elasto-chemical evolution data for dental Ti-Cr alloy microstructure through sparsification and tensor computation,* Scripta Materialia, 2024, 244, 116027.
   DOI: https://doi.org/10.1016/j.scriptamat.2024.116027 - **7 %**
   CRediT author contribution: Supervision, Validation, Visualization, Writing – review & editing.
2. U. Subedi, N. Moelans, T. Tański, A. Kunwar, *Foretelling microstructural interface with multi-generational convolutional-LSTM framework*, Engineering with Computers, 2025, 41:2593–2617.
   DOI: https://doi.org/10.1007/s00366-025-02117-z - **6 %**
   CRediT author contribution: Validation, Visualization, Writing- Review & Editing, Supervision
3. U. Subedi, N. Moelans, T. Tański, A. Kunwar, *A non-isothermal multi-phase field approach to model the meltpool and IMC grains interaction in Ti-Au material*, Computational Materials Science, 2025, 255, 113875
   DOI: https://doi.org/10.1016/j.commatsci.2025.113875 - **6 %**
   CRediT author contribution: Writing – review & editing, Visualization, Validation, Supervision
4. U. Subedi, A. Bhattarai, N. Moelans, T. Tański, A. Kunwar, *Spatiotemporally learning the morphological and dynamic features of Au meltpool under different heat source types with phase-field informed U-Net framework.* Computational Materials Science, 2026, 263, 114456
   DOI: https://doi.org/10.1016/j.commatsci.2025.114456 - **5 %**
   CRediT author contribution: Writing – review & editing, Visualization, Validation, Supervision

In particular, my primary contributions to the paper [1] were:

- Validation of the model's result, visualization of the data generated.

In particular, my main contributions to the paper [2] were:

- Visualization of the data, validation of the result and supervision

In particular, my primary contributions to the paper [3] were:

- Validation of the model, visualization of the data and supervision

In particular, my main contributions to the paper [4] were:

- Validation of the machine learning model, visualization of the model predicted results and supervision of the work.

Furthermore, I declare that I have been informed that the use of the above-mentioned publications in the doctoral dissertation of **Upadesh Subedi,** MSc, Eng., entitled:

"Towards Digital Twins for Quantifying Laser-Microstructure Interface in Multicomponent Alloys Using Thermodynamic Tensor Model"

_____

Tomasz Tański, Ph.D, DSc., Eng.

Anil Kunwar, Ph.D, Eng.

Silesian University of Technology

Faculty of Mechanical Engineering

Scientific and Didactic Laboratory of Nanotechnology and Material Technologies

Declaration

I hereby declare that my contribution percentages in the following publications were as follows:

1. U. Subedi, N. Moelans, T. Tański, A. Kunwar, *Rapid portabilization of elasto-chemical evolution data for dental Ti-Cr alloy microstructure through sparsification and tensor computation,* Scripta Materialia, 2024, 244, 116027.
   DOI: https://doi.org/10.1016/j.scriptamat.2024.116027 - **16 %**
   CRediT author contribution: Data curation, Funding acquisition, Methodology, Project administration, Supervision, Validation, Writing – review & editing.
2. H.B. Mamo, U. Subedi, T. Poloczek, M. Adamiak, A. Appiah, M. Skonieczna, P. Nuckowski, Y. Geng, B. Haldar, A. Kunwar, *Prototyping Ti2Cu intermetallic grain growth heterogeneously in Ti6Al4V matrix through laser additive manufacturing,* Materials & Design, 2024, 246, 113312.
   DOI: https://doi.org/10.1016/j.matdes.2024.113312 - **15 %**
   CRediT author contribution: Writing – review & editing, Supervision, Software, Project administration, Methodology, Investigation, Funding acquisition, Data curation, Conceptualization.
3. U. Subedi, N. Moelans, T. Tański, A. Kunwar, *Foretelling microstructural interface with multi-generational convolutional-LSTM framework*, Engineering with Computers, 2025, 41:2593–2617.
   DOI: https://doi.org/10.1007/s00366-025-02117-z - **17 %**
   CRediT author contribution: Conceptualization, Methodology, Validation, Data Curation, Supervision, Writing- Review & Editing, Project administration, Funding acquisition.
4. U. Subedi, N. Moelans, T. Tański, A. Kunwar, *A non-isothermal multi-phase field approach to model the meltpool and IMC grains interaction in Ti-Au material*, Computational Materials Science, 2025, 255, 113875
   DOI: https://doi.org/10.1016/j.commatsci.2025.113875 - **17 %**
   CRediT author contribution: Writing – review & editing, Validation, Supervision, Conceptualization, Project administration, Methodology, Funding acquisition, Data curation.
5. U. Subedi, A. Bhattarai, N. Moelans, T. Tański, A. Kunwar, *Spatiotemporally learning the morphological and dynamic features of Au meltpool under different heat source types with phase-field informed U-Net framework.* Computational Materials Science, 2026, 263, 114456
   DOI: https://doi.org/10.1016/j.commatsci.2025.114456 - **15 %**

CRediT author contribution: Writing – review & editing, Validation, Supervision, Conceptualization, Project administration, Methodology, Funding acquisition, Data curation.

In particular, my main contributions to the paper [1] were:

- Curating the methodology, validating the model results.

In particular, my main contributions to the paper [2] were:

- Methodology development, and conceptualization of the work.

In particular, my primary contributions to the paper [3] were:

- Conceptualization, methodology and validation of the models.

In particular, my primary contributions to the paper [4] were:

- Validation of the models, methodology curation

In particular, my main contributions to the paper [5] were:

- Conceptualization of the work, validation of the models.

Furthermore, I declare that I have been informed that the use of the above-mentioned publications in the doctoral dissertation of **Upadesh Subedi,** MSc, Eng., entitled:

"Towards Digital Twins for Quantifying Laser-Microstructure Interface in Multicomponent Alloys Using Thermodynamic Tensor Model"

_____

Anil Kunwar, Ph.D, Eng.

Nele Moelans, Ph.D.

KU Leuven

Faculty of Engineering Science

Department of Materials Engineering

Declaration

I hereby declare that my contribution percentages in the following publications were as follows:

1. U. Subedi, N. Moelans, T. Tański, A. Kunwar, *Rapid portabilization of elasto-chemical evolution data for dental Ti-Cr alloy microstructure through sparsification and tensor computation,* Scripta Materialia, 2024, 244, 116027.
   DOI: https://doi.org/10.1016/j.scriptamat.2024.116027 - **6 %**
   CRediT author contribution: Conceptualization, Methodology, Validation, Writing – review & editing.
2. U. Subedi, N. Moelans, T. Tański, A. Kunwar, *Foretelling microstructural interface with multi-generational convolutional-LSTM framework*, Engineering with Computers, 2025, 41:2593–2617.
   DOI: https://doi.org/10.1007/s00366-025-02117-z - **5 %**
   CRediT author contribution: Methodology, Validation, Writing – review & editing, Funding acquisition
3. U. Subedi, N. Moelans, T. Tański, A. Kunwar, *A non-isothermal multi-phase field approach to model the meltpool and IMC grains interaction in Ti-Au material*, Computational Materials Science, 2025, 255, 113875
   DOI: https://doi.org/10.1016/j.commatsci.2025.113875 - **7 %**
   CRediT author contribution: Writing – review & editing, Formal analysis, Validation, Methodology
4. U. Subedi, A. Bhattarai, N. Moelans, T. Tański, A. Kunwar, *Spatiotemporally learning the morphological and dynamic features of Au meltpool under different heat source types with phase-field informed U-Net framework.* Computational Materials Science, 2026, 263, 114456
   DOI: https://doi.org/10.1016/j.commatsci.2025.114456 - **5 %**
   CRediT author contribution: Writing – review & editing, Formal analysis, Validation, Methodology

In particular, my main contributions to the paper [1] were:

- Conceptualization and methodology development of the work.

In particular, my primary contributions to the paper [2] were:

- Methodology curation and validation of the models.

In particular, my main contributions to the paper [3] were:

- Analysis of simulation results, validation of the data generated.

In particular, my primary contributions to the paper [4] were:

- Validation of the model's result and development of methodological tools.

Furthermore, I declare that I have been informed that the use of the above-mentioned publications in the doctoral dissertation of **Upadesh Subedi,** MSc, Eng., entitled:

"Towards Digital Twins for Quantifying Laser-Microstructure Interface in Multicomponent Alloys Using Thermodynamic Tensor Model"

_____

Nele Moelans, Ph.D.

Marcin Adamiak, Ph.D, DSc., Eng.

Silesian University of Technology

Faculty of Mechanical Engineering

Materials Research Laboratory - RMT L1

Declaration

I hereby declare that my contribution percentages in the following publications were as follows:

1. H.B. Mamo, U. Subedi, T. Poloczek, M. Adamiak, A. Appiah, M. Skonieczna, P. Nuckowski, Y. Geng, B. Haldar, A. Kunwar, *Prototyping Ti2Cu intermetallic grain growth heterogeneously in Ti6Al4V matrix through laser additive manufacturing,* Materials & Design, 2024, 246, 113312.
   DOI: https://doi.org/10.1016/j.matdes.2024.113312 - **5 %**
   CRediT author contribution: Writing – review & editing, Supervision, Methodology, Conceptualization

In particular, my primary contributions to the paper [1] were:

- Conceptualization of experimental study, development of methodology, and supervision

Furthermore, I declare that I have been informed that the use of the above-mentioned publications in the doctoral dissertation of **Upadesh Subedi,** MSc, Eng., entitled:

"Towards Digital Twins for Quantifying Laser-Microstructure Interface in Multicomponent Alloys Using Thermodynamic Tensor Model"

_____

Marcin Adamiak, Ph.D, DSc., Eng.

Augustine Nana Sekyi Appiah, Ph.D, Eng.

Silesian University of Technology

Faculty of Mechanical Engineering

Department of Materials Research Laboratory – RMT L1

Declaration

I hereby declare that my contribution percentages in the following publications were as follows:

1. H.B. Mamo, U. Subedi, T. Poloczek, M. Adamiak, A. Appiah, M. Skonieczna, P. Nuckowski, Y. Geng, B. Haldar, A. Kunwar, *Prototyping Ti2Cu intermetallic grain growth heterogeneously in Ti6Al4V matrix through laser additive manufacturing,* Materials & Design, 2024, 246, 113312.
   DOI: https://doi.org/10.1016/j.matdes.2024.113312 **- 7 %**
   CRediT author contribution: Writing – review & editing, Investigation

In particular, my primary contribution to the paper [1] was:

- Experimental investigation and characterization

Furthermore, I declare that I have been informed that the use of the above-mentioned publications in the doctoral dissertation of **Upadesh Subedi,** MSc, Eng., entitled:

"Towards Digital Twins for Quantifying Laser-Microstructure Interface in Multicomponent Alloys Using Thermodynamic Tensor Model"

_____

Augustine Nana Sekyi Appiah Ph.D, Eng.

Barun Haldar, Ph.D, Eng.

Imam Mohammad Ibn Saud Islamic University

Mechanical Engineering Department

Declaration

I hereby declare that my contribution percentages in the following publications were as follows:

1. H.B. Mamo, U. Subedi, T. Poloczek, M. Adamiak, A. Appiah, M. Skonieczna, P. Nuckowski, Y. Geng, B. Haldar, A. Kunwar, *Prototyping Ti2Cu intermetallic grain growth heterogeneously in Ti6Al4V matrix through laser additive manufacturing,* Materials & Design, 2024, 246, 113312.
   DOI: https://doi.org/10.1016/j.matdes.2024.113312 - **5 %**
   CRediT author contribution: Writing – review & editing, Supervision, Methodology

In particular, my primary contribution to the paper [1] is:

- Experimental methodology development

Furthermore, I declare that I have been informed that the use of the above-mentioned publications in the doctoral dissertation of **Upadesh Subedi,** MSc, Eng., entitled:

"Towards Digital Twins for Quantifying Laser-Microstructure Interface in Multicomponent Alloys Using Thermodynamic Tensor Model"

_____

Barun Haldar, Ph.D, Eng.

Hana Beyene Mamo, MSc., Eng.

Silesian University of Technology

Faculty of Mechanical Engineering

Department of Materials Research Laboratory – RMT L1

Declaration

I hereby declare that my contribution percentages in the following publications were as follows:

1. H.B. Mamo, U. Subedi, T. Poloczek, M. Adamiak, A. Appiah, M. Skonieczna, P. Nuckowski, Y. Geng, B. Haldar, A. Kunwar, *Prototyping Ti2Cu intermetallic grain growth heterogeneously in Ti6Al4V matrix through laser additive manufacturing,* Materials & Design, 2024, 246, 113312.
   DOI: https://doi.org/10.1016/j.matdes.2024.113312 - **25 %**
   CRediT author contribution: Writing – original draft, Visualization, Validation, Software, Methodology, Investigation.

In particular, my primary contributions to the paper [1] were:

- Methodology development, experimental investigation and visualization of the experimental data

Furthermore, I declare that I have been informed that the use of the above-mentioned publications in the doctoral dissertation of **Upadesh Subedi,** MSc, Eng., entitled:

"Towards Digital Twins for Quantifying Laser-Microstructure Interface in Multicomponent Alloys Using Thermodynamic Tensor Model"

_____

Hana Beyene Mamo, MSc., Eng.

Magdalena Skonieczna, Ph.D, DSc.

Silesian University of Technology

Department of Engineering and Systems Biology

Declaration

I hereby declare that my contribution percentages in the following publications were as follows:

1. H.B. Mamo, U. Subedi, T. Poloczek, M. Adamiak, A. Appiah, M. Skonieczna, P. Nuckowski, Y. Geng, B. Haldar, A. Kunwar, *Prototyping Ti2Cu intermetallic grain growth heterogeneously in Ti6Al4V matrix through laser additive manufacturing,* Materials & Design, 2024, 246, 113312.
   DOI: https://doi.org/10.1016/j.matdes.2024.113312 **- 7 %**
   CRediT author contribution: Writing – review & editing, Investigation

In particular, my primary contributions to the paper [1] were:

- Experimental investigations

Furthermore, I declare that I have been informed that the use of the above-mentioned publications in the doctoral dissertation of **Upadesh Subedi,** MSc, Eng., entitled:

"Towards Digital Twins for Quantifying Laser-Microstructure Interface in Multicomponent Alloys Using Thermodynamic Tensor Model"

_____

Magdalena Skonieczna, Ph.D, DSc.

Paweł M Nuckowski Ph.D, Eng.

Silesian University of Technology

Faculty of Mechanical Engineering

Department of Materials Research Laboratory – RMT L1

Declaration

I hereby declare that my contribution percentages in the following publications were as follows:

1. H.B. Mamo, U. Subedi, T. Poloczek, M. Adamiak, A. Appiah, M. Skonieczna, P. Nuckowski, Y. Geng, B. Haldar, A. Kunwar, *Prototyping Ti2Cu intermetallic grain growth heterogeneously in Ti6Al4V matrix through laser additive manufacturing,* Materials & Design, 2024, 246, 113312.
   DOI: https://doi.org/10.1016/j.matdes.2024.113312 **- 7 %**
   CRediT author contribution: Writing – review & editing, Investigation

In particular, my primary contribution to the paper [1] was:

- Experimental investigation

Furthermore, I declare that I have been informed that the use of the above-mentioned publications in the doctoral dissertation of **Upadesh Subedi,** MSc, Eng., entitled:

"Towards Digital Twins for Quantifying Laser-Microstructure Interface in Multicomponent Alloys Using Thermodynamic Tensor Model"

_____

Paweł M Nuckowski Ph.D, Eng.

Tomasz Poloczek, Ph.D, Eng.

Silesian University of Technology

Faculty of Mechanical Engineering

Department of Welding Engineering - RMT 5

Declaration

I hereby declare that my contribution percentages in the following publications were as follows:

1. H.B. Mamo, U. Subedi, T. Poloczek, M. Adamiak, A. Appiah, M. Skonieczna, P. Nuckowski, Y. Geng, B. Haldar, A. Kunwar, *Prototyping Ti2Cu intermetallic grain growth heterogeneously in Ti6Al4V matrix through laser additive manufacturing,* Materials & Design, 2024, 246, 113312.
   DOI: https://doi.org/10.1016/j.matdes.2024.113312 **- 8 %**
   CRediT author contribution: Writing – review & editing, Validation, Investigation

In particular, my primary contributions to the paper [1] were:

- Experimental investigation and validation

Furthermore, I declare that I have been informed that the use of the above-mentioned publications in the doctoral dissertation of **Upadesh Subedi,** MSc, Eng., entitled:

"Towards Digital Twins for Quantifying Laser-Microstructure Interface in Multicomponent Alloys Using Thermodynamic Tensor Model"

_____

Tomasz Poloczek, Ph.D, Eng.

Yaoxiang Geng, Ph.D

Jiangsu University of Science and Technology

School of Materials Science and Engineering

Declaration

I hereby declare that my contribution percentages in the following publications were as follows:

1. H.B. Mamo, U. Subedi, T. Poloczek, M. Adamiak, A. Appiah, M. Skonieczna, P. Nuckowski, Y. Geng, B. Haldar, A. Kunwar, *Prototyping Ti2Cu intermetallic grain growth heterogeneously in Ti6Al4V matrix through laser additive manufacturing,* Materials & Design, 2024, 246, 113312.
   DOI: https://doi.org/10.1016/j.matdes.2024.113312 - **5 %**
   CRediT author contribution: Writing – review & editing, Supervision, Methodology, Funding acquisition

In particular, my primary contribution to the paper [1] is:

- Methodology development for experimental study.

Furthermore, I declare that I have been informed that the use of the above-mentioned publications in the doctoral dissertation of **Upadesh Subedi,** MSc, Eng., entitled:

"Towards Digital Twins for Quantifying Laser-Microstructure Interface in Multicomponent Alloys Using Thermodynamic Tensor Model"

_____

Yaoxiang Geng, Ph.D

Aadya Bhattarai, Ph.D. Student

University of South Florida, Tampa

Department of Industrial and Management Systems Engineering

Declaration

I hereby declare that my contribution percentages in the following publications were as follows:

1. Upadesh Subedi, A. Bhattarai, N. Moelans, T. Tański, A. Kunwar, *Spatiotemporally learning the morphological and dynamic features of Au meltpool under different heat source types with phase-field informed U-Net framework.* Computational Materials Science, 2026, 263, 114456
   DOI: https://doi.org/10.1016/j.commatsci.2025.114456 - **15 %**
   CRediT author contribution: Investigation, Software, Data Curation, Validation, Visualization, Writing – review & editing.

My primary contributions to the paper [1] were:

- Development, and training of the machine learning models, visualization of the generated data.

Furthermore, I declare that I have been informed that the use of the above-mentioned publications in the doctoral dissertation of **Upadesh Subedi,** MSc, Eng., entitled:

"Towards Digital Twins for Quantifying Laser-Microstructure Interface in Multicomponent Alloys Using Thermodynamic Tensor Model"

_____

Aadya Bhattarai, Ph.D. Student